

RADIATION RESILIENCE IN REDUCED DIMENSIONALITY SYSTEMS

By

Benjamin W. Jacobs

A DISSERTATION

Submitted to
Michigan State University
in partial fulfillment of the requirements
for the degree of

DOCTOR OF PHILOSOPHY

Department of Electrical and Computer Engineering

2007

UMI Number: 3298056

INFORMATION TO USERS

The quality of this reproduction is dependent upon the quality of the copy submitted. Broken or indistinct print, colored or poor quality illustrations and photographs, print bleed-through, substandard margins, and improper alignment can adversely affect reproduction.

In the unlikely event that the author did not send a complete manuscript and there are missing pages, these will be noted. Also, if unauthorized copyright material had to be removed, a note will indicate the deletion.

UMI[®]

UMI Microform 3298056

Copyright 2008 by ProQuest LLC.

All rights reserved. This microform edition is protected against unauthorized copying under Title 17, United States Code.

ProQuest LLC
789 E. Eisenhower Parkway
PO Box 1346
Ann Arbor, MI 48106-1346

ABSTRACT

RADIATION RESILIENCE IN REDUCED DIMENSIONALITY SYSTEMS

By

Benjamin W. Jacobs

Space based electronic systems such as communications satellites and interplanetary space probes have become increasingly important since their inception in the mid 20th century. However, as these systems become smaller and more sophisticated, the ability to carry radiation shielding to protect against the space radiation environment becomes more difficult. Therefore, new lightweight, radiation resilient electronics are needed to meet the demands of new probe designs. Current silicon based transistors rely on charged separated regions prone to radiation, which can disrupt normal operation. Novel nanomaterials that may be inherently radiation resilient offer promising alternatives. Recent research suggests that nanomaterials and nanomaterial based electronic devices may have inherent radiation resiliency due to their reduced dimensionalities, and in some cases enhanced self-healing due to their nanoscale sizes.

Low to high-Z heavy ion irradiation experiments, including heavy ion beams of krypton-86, krypton-78 and calcium-48, were conducted to explore fundamental heavy ion nanomaterial interactions. Nanomaterials irradiated included carbon nanotubes, gallium nitride nanowires and carbon onions. Real time gallium nitride nanowire-based circuit operation in radiation was also investigated using special vault. Results were highly encouraging and promise high payoff, given their high radiation resilience and superior materials and electronic performance.

Newly discovered gallium nitride (GaN) nanowires used in radiation investigations were unique multiphase nanowires that incorporated zinc-blende and wurtzite crystalline domains that grew in the longitudinal direction simultaneously. Structural properties of the multiphase nanowires were studied using high-resolution transmission electron microscopy. Plain-view high-resolution transmission electron microscopy (HRTEM) was used to identify the presence of both the zinc-blende and wurtzite crystalline phases present in the nanowire. Cross-section HRTEM was used to identify the domain orientation relationships within the nanowire. Scanning electron microscopy (SEM) investigations identified growth temperature dependence on GaN matrix features that led to the multiphase nanowire growth. HRTEM investigations of the sides of GaN hexagonal platelets, from which nanowires grew, revealed a network of nanoscale ledges. These ledges were identified as the nanowire nucleation sites.

Electronic properties of individual nanowires using nanomanipulator probes, cathodoluminescence, and nanowires integrated into devices were investigated. Using four-point probe techniques the intrinsic nanowire resistance was accurately measured. Using two-point probe techniques, evidence of single-phase transport was observed, where a large liquid protrusion emerged from the nanowire, while an outer structure remained in tact. Cathodoluminescence showed possible electron confinement effects and stress in the multiphase nanowire system. Gallium nitride nanowire-based field effect transistors were also fabricated and studied. All measurements indicated that the nanowires were capable of high current densities.

Copyright by
BENJAMIN W. JACOBS
2007

TABLE OF CONTENTS

LIST OF FIGURES	vii
1. INTRODUCTION.....	1
1.1 RADIATION RESILIENCY IN REDUCED DIMENSIONALITY SYSTEMS	4
1.2 CARBON NANOTUBES AND CARBON ONIONS.....	7
1.3 MULTIPHASE GALLIUM NITRIDE NANOWIRES	9
1.4 MULTIDISCIPLINARY RESEARCH APPROACH.....	11
1.5 SUMMARY OF LATER CHAPTERS	12
2. INSTRUMENTS AND METHODS	14
2.1 TRANSMISSION ELECTRON MICROSCOPY	16
2.1.1 <i>High-Resolution Transmission Electron Microscopy</i>	23
2.1.2 <i>Electron Diffraction</i>	24
2.1.3 <i>Energy Dispersive X-Ray Spectroscopy</i>	27
2.1.4 <i>Electron Energy Loss Spectroscopy</i>	29
2.2 FOCUSED ION BEAM	31
2.3 SCANNING ELECTRON MICROSCOPY	37
2.4 MICROFABRICATION PROCESS	41
2.4.1 <i>Photolithography</i>	41
2.4.2 <i>Electron Beam Lithography</i>	47
2.5 DEVICE CHARACTERIZATION TECHNIQUES.....	51
2.5.1 <i>Two-Point Probe</i>	51
2.5.2 <i>Four-Point Probe</i>	52
2.6 SCANNING PROBE MICROSCOPY	55
2.6.1 <i>Atomic Force Microscopy</i>	55
2.6.2 <i>Scanning Tunneling Microscopy</i>	58
2.7 RAMAN SPECTROSCOPY.....	60
2.8 CATHODOLUMINESCENCE AND PHOTOLUMINESCENCE.....	63
2.9 THERMOGRAVIMETRIC ANALYSIS	66
3. REDUCED DIMENSIONALITY SYSTEMS: FROM THREE-DIMENSIONS TO ZERO.....	71
4. ZINC-BLENDE WURTZITE MULTIPHASE GALLIUM NITRIDE NANOWIRES	78
4.1 NANOWIRE STRUCTURE INVESTIGATIONS.....	82
4.1.1 <i>Plain-View HRTEM</i>	82
4.1.2 <i>Cross-Section HRTEM</i>	94
4.2 NANOWIRE MATRIX INVESTIGATIONS	111
4.2.1 <i>SEM</i>	112
4.2.2 <i>HRTEM</i>	118
4.3 NANOWIRE GROWTH AND DISCUSSION	122

4.4	ELECTRONIC PROPERTIES	127
4.4.1	<i>Electronic Investigations of Multiphase GaN Nanowire-Based GaNFETs</i>	127
4.4.2	<i>Electronic Investigations of an Individual Multiphase GaN Nanowire</i>	132
4.4.3	<i>Cathodoluminescence</i>	141
5.	FUNDAMENTALS OF RADIATION INTERACTIONS IN REDUCED DIMENSIONALITY SYSTEMS.....	149
5.1	THE SPACE RADIATION ENVIRONMENT	149
5.1.1	<i>Single Event Effects and Total Ionizing Dose</i>	150
5.1.2	<i>Cosmic Rays</i>	151
5.2	ELECTRONICS IN SPACE	154
5.2.1	<i>Silicon Based Electronics</i>	154
5.2.2	<i>An Example: A MOSFET in Radiation</i>	156
5.3	THE NATIONAL SUPERCONDUCTING CYCLOTRON LABORATORY.....	160
5.3.1	<i>The Coupled Cyclotron</i>	160
5.3.2	<i>The Single Event Effects Testing Facility</i>	163
5.4	REDUCED DIMENSIONALITY MATERIALS IN HIGH RADIATION ENVIRONMENTS ..	168
5.4.1	<i>Materials</i>	169
5.4.2	<i>Experiments</i>	177
5.4.3	<i>Experimental Results and Discussion</i>	183
6.	FUTURE WORK.....	202
6.1	GALLIUM NITRIDE NANOWIRES	202
6.2	FUNDAMENTALS OF RADIATION INTERACTIONS IN REDUCED DIMENSIONALITY SYSTEMS.....	209
6.2.1	<i>Other Candidate Materials for High Radiation Environments</i>	212
6.2.2	<i>Other Candidate Devices for High Radiation Environments</i>	213
7.	CONCLUSION	217

LIST OF FIGURES

Chapter 2

Figure 2.1 JEOL 2200FS field-emission transmission electron microscope. (a) This particular TEM is in part controlled by computer. The computers used for imaging are shown on the right. (b) A TEM sample holder. The arrow indicates where a TEM grid is placed. Note its size. This restricts the size of the sample that can be placed in the TEM. (c) Close up of the TEM. The electron gun is at the top of the TEM and electrons are accelerated down the beam column and focused by the electromagnetic lenses. The sample holder indicates where the sample is located in the beam column. Images: B.W. Jacobs 19

Figure 2.2 Illustration of Bragg's law. An incoming wave will interact with the material and if the angle is correct it will satisfy the Bragg condition and strongly reflect at the same angle as the incident beam. Image: B.W. Jacobs 25

Figure 2.3 FEI Quanta 200 3D dual beam FIB with an integrated Omni Micromanipulator System at the Electron Microprobe Analysis Laboratory at University of Michigan. (a) The main components of a dual beam FIB are shown here. It is computer controlled. The electron gun is situated perpendicular to the sample as in a normal SEM. The ion gun is tilted 52° relative to the electron gun. The Pt source needle is next to the ion column. Manual stage control is on the front of the specimen chamber and is used in the cross-section preparation process. The micromanipulator is situated on the backside of the instrument. (b) A close up of the micromanipulator is shown here. The XYZ control is shown and consists of computer-controlled screws that move the needle. Image: B.W. Jacobs 32

Figure 2.4 The TEM cross-section preparation method using a FIB. (a) Nanowire sample. (b) Pt deposition on top of the nanowire to protect it from ion beam damage. A small amount of extra Pt is deposited on top of the nanowire to mark its exact location. (c) Creation of the trenches on either side of the Pt, perpendicular to the nanowire. (d) The U-cut. Two notches on either side are left to hold the sample in place. The superimposed needle indicates where it should be welded on the cross-section. (e) The extracted sample. (f) The extracted sample as it nears the TEM grid. (g) The sample is welded to the TEM grid. (h) Fine milling of the cross-section. It should be thin enough to be transparent in a TEM electron beam, less than 100 nm. (i) Ion beam image of the final nanowire cross-section. Images: B.W. Jacobs 35

Figure 2.5 Hitachi S-4700II FESEM at the W. M. Keck Microfabrication Facility at Michigan State University. (a) The SEM is controlled via software. On the right is the control computer. The left highlights several components of the SEM. The electron gun is at the top and accelerates electrons downward through a series of electromagnetic lenses and apertures. The sample is located at the base of the instrument. When

introducing a sample into the microscope it is first placed in an exchange chamber and then after rough pumping introduced into the specimen chamber shown in (b). (b) A close up image of the instrument shows the specimen chamber where imaging occurs and the lower and upper secondary electron detectors. Image: B.W. Jacobs.....38

Figure 2.6 Electron beam/sample interaction in the SEM. Electrons from the beam interact with the sample in a teardrop shaped volume. Variations in the surface topology cause thin points and edges to appear bright because electrons that enter this area can be scattered out more easily resulting in a higher number of detected electrons from those areas, and therefore a brighter spot. Image: B.W. Jacobs39

Figure 2.7 AB-M mask aligner at the W. M. Keck Microfabrication Facility at Michigan State University. (a) The instrument consists of a UV source that moves on rails to expose the photoresist on a wafer through a mask, located in the center of the instrument. An optical microscope on the right is used to align other masks used for multiple exposures for more complex features. (b) An example of a glass/chrome mask used in this research. Images: B.W. Jacobs42

Figure 2.8 Basic photolithography process. (a) A bare silicon wafer. (b) Silicon dioxide is grown on the surface and is used as an insulating layer. (c) Photoresist is spun on the wafer and it is exposed to UV light through a mask. (d) The developer removes the exposed resist. (e) A metal layer is deposited. (f) The remaining unexposed resist is taken off along with the metal layer that was on top of it, leaving the desired pattern. Images: B.W. Jacobs43

Figure 2.9 Edwards Auto 306 Thermal Evaporator at the W. M. Keck Microfabrication Facility at Michigan State University. (a) The cylindrical evaporation chamber is shown here. The sample holder is at the top of the chamber and is held upside down. The metal is at the bottom and evaporated metal drifts upward to the sample. (b) The sample holder is flipped up for easy access for sample mounting. (c) The evaporation mechanism is at the bottom of the chamber. The boat is screwed down and high current is passed through it to heat the metal. A detector is used to monitor the evaporation rate. A shutter is used to block the substrate from the source to stop metal deposition. (d) The evaporator controls. The current can be increased and decreased with a knob. The digital readouts of the rate monitor and vacuum control provide details of the evaporation conditions. Images: B.W. Jacobs45

Figure 2.10 Tri-layer photoresist stack. (a) After the first layer has been deposited and exposed, a 10 nm layer of Al is thermally evaporated. The second layer of resist is deposited and the stack is exposed under a mask. (b) After developing an undercut should be prevalent. (c) Metal is thermally evaporated with a large separation between the layer of metal on top of the resist stack and the layer on the bare substrate. (d) The top layers are removed and clean, sharp features are left. Images: B.W. Jacobs46

Figure 2.11 JEOL 840A SEM with integrated EBL capability at the W. M. Keck Microfabrication Facility at Michigan State University. (a) An SEM with a tungsten

filament is used for EBL. (b) A computer that is integrated into the SEM control system and is used to manipulate the beam according to a pre-defined pattern designed using a CAD program. Images: B.W. Jacobs48

Figure 2.12 Illustration of the electron beam lithography method. The beam flashes the sample at a point, moves a small distance flashes it again, and continues this way in a raster pattern. The spacing between the flashes can be defined in the point spacing and line spacing. Image: B.W. Jacobs49

Figure 2.13 The four-point probe resistance measurement technique. This technique uses four probes that are placed on the sample. The two outside probes pass a known current through the sample. The two inside probes measure a voltage. Very little current passes through the voltage probes. By dividing the known current into the measured voltage, an accurate resistance of the sample can be measured, with the contact resistances of the probes omitted. Image: B.W. Jacobs53

Figure 2.14 Diagram of basic AFM operation. The cantilever and tip are rastered along the sample surface. The variation in sample topology is detected by a reflected laser/photodiode system. The signal from the photodiode is then sent to the computer for digital image construction.....56

Figure 2.15 Veeco Instruments Nanoprobe III-A Multimode SPM at the Electronic and Biological Nanostructures Laboratory at Michigan State University. (a) This image shows an entire SPM setup. The SPM sits on top of several anti-vibration surfaces. An optical microscope is used to focus the sample surface and roughly focus the laser beam on the tip. The SPM is controlled via computer. (b) The head contains the laser, photodiode and provides the electrical connection to the tip. (c) A close up of the microscope shows the piezoelectric motion control and the head. (d) An AFM tip holder. (e) STM tip holder. Images: B.W. Jacobs57

Figure 2.16 STM operation. A metal tip is brought into close proximity to the sample surface. A tunneling voltage is applied, creating an electric field across the sample, and electrons tunnel out of the tip into the sample. The amount of tunneling current will depend on the variations in the electron density in the sample, i.e. the tunneling current over an atom will be different than the tunneling current between atoms. Image: adapted from original image, Michael Schmid, TU Wien59

Figure 2.17 Illustration of the basic theory of Raman scattering. In each case a photon causes electrons to enter a virtual energy state. The electron will then drop in energy either returning to the ground state or entering a higher vibrational energy state. Rayleigh scattering is the most common form of scattering and is caused by inelastic scattering. Stokes scattering is more common than anti-Stokes scattering. Image: B.W. Jacobs61

Figure 2.18 Kaiser Instruments micro Raman Spectrograph at the W. M. Keck Microfabrication Facility at Michigan State University. (a) The instrument consists of a mechanical stage control, laser source and detector, and a computer used for analyzing

data. (b) The laser used for exciting materials is focused through a microscope. This allows for very small areas of a sample to be analyzed. Image: B.W. Jacobs.....62

Figure 2.19 Illustration of the process involved in cathodoluminescence. Electrons represented by the black dots are excited to the conduction band, E_c , from the valence band, E_v , by the SEM electron beam. Electrons can be excited to states within the band gap, which can consist of impurities and defects in the material. Image: B.W. Jacobs...64

Figure 2.20 TGA instrument, Rigaku 8120 TG-DTA at the Tokura-Hirata Laboratory at Tokyo Institute of Technology. The sample material is packed into a small Pt pan and placed on precise balance. The pan is then put into a furnace and heated up. The arrow below the furnace label indicates the movement of the furnace. The furnace rides on two rails and encapsulates the samples in the furnace. The inset shows the whole instrument, with the furnace on the left and the balance mechanism on the right. A small tube for a desired gas is also indicated. Images: B.W. Jacobs67

Chapter 3

Figure 3.1 Examples of reduced dimensionality systems. From left to right: three-dimensional, two-dimensional, one-dimensional, and zero-dimensional. Images: B.W. Jacobs.....72

Figure 3.2 A quantum well. Particles in a quantum well are trapped in a confining potential. If the length of the well, L , is small enough, energy levels within the well will begin to separate and give rise to quantized energy levels. These energy levels are determined by the equation on the right, where n is the quantized energy level, h is Planck's constant, m is the mass of the particle, and L is the length of the well. Image: B.W. Jacobs73

Chapter 4

Figure 4.1 TEM and HRTEM images of a multiphase GaN nanowire that grew at 850° C. (a) The TEM image shows the width of the nanowire. Contrast variations indicate changes in thickness as well as phase across the nanowire. (b) An HRTEM image of the indicated boxed area in (a). The zinc-blende and wurtzite domains are clearly distinguishable in this image along with the sharp phase transition denoted by the dotted line. Images: B.W. Jacobs.....84

Figure 4.2 HRTEM image of a nanowire that grew at 850° C, and SAED and FFT analysis illustrating how the FFT can augment SAED patterns. (a) An HRTEM image of a nanowire shows the multiphase structure of the nanowire. (b) An SAED pattern of the nanowire showing both zinc-blende and wurtzite contributions. The zinc-blende SAED pattern was along the [001] axis and the wurtzite was along the [0001] axis. (c) FFT of the wurtzite phase taken from the boxed area in (a). (d) FFT of the zinc-blende phase

taken from the boxed area in (a). These FFTs separate out the zinc-blende and wurtzite contributions in the SAED pattern, and identified where these contributions were located in the nanowire. Images and interpretation: B.W. Jacobs 85

Figure 4.3 (a) An HRTEM image of a single-phase wurtzite nanowire grown at 1000° C. The wurtzite growth direction is the same as the nanowires grown at lower temperatures, $[2\bar{1}\bar{1}0]$. No zinc-blende phase was observed. (b) This SAED pattern was solved for the wurtzite crystal structure along the $[0001]$ zone axis. Images and interpretation: B.W. Jacobs..... 86

Figure 4.4 HRTEM images of nanowires grown at 1000° C and 850° C. (a) An HRTEM image of a nanowire grown at 1000° C. Zinc-blende and wurtzite phases were identified using FFTs taken from the indicated areas. A sharp phase transition was evident. The arrows indicate the nanowire growth direction for each phase. (b) An HRTEM image of a nanowire grown at 850° C. A very similar structure was observed, with similar FFTs and the same growth directions for each phase. Images and interpretation: B.W. Jacobs..... 87

Figure 4.5 TEM images of a nanowire grown at 1000° C. (a) A TEM images shows the nanowire end, with its tapered tip. It was about 700 nm wide. Its growth was along the $[0001]$ direction. (b) An HRTEM image taken from the boxed area in (a) shows a well-resolved lattice indicating the high crystal quality of the nanowire. (c) An SAED pattern was solved for the wurtzite structure along the $[01\bar{1}0]$ zone axis. Images and interpretation: B.W. Jacobs..... 88

Figure 4.6 Simulated diffraction patterns highlighting similar features found in some wurtzite and zinc-blende patterns. (a) $[0001]$ zone axis for the wurtzite structure. (b) $[111]$ zone axis for the zinc-blende structure. (c) $[10\bar{1}2]$ zone axis for the wurtzite structure. (d) $[112]$ zone axis for the zinc-blende structure. Images and interpretation: B.W. Jacobs 90

Figure 4.7 EDS spectrum of a GaN nanowire. The nitrogen and gallium peaks indicate the purity of these nanowires. A copper peak is also present due the copper TEM grid used to support the nanowire sample. Spectrum and interpretation: B.W. Jacobs 92

Figure 4.8 EELS spectra of a GaN nanowire. (a) The nitrogen core loss is located at 401 eV, and a strong signal was measured there indicating a significant presence of nitrogen. The oxygen core loss at 532 eV is located on this spectrum but no peak was detected confirming the lack of oxygen. (b) The gallium core loss is located at 1115 eV, and a strong signal was measured there indicating a significant presence of gallium. Spectra and interpretation: B.W. Jacobs 93

Figure 4.9 TEM images of cross-sections fabricated with the FIB. (a) Cross-section HRTEM image of a nanowire grown at 850° C. (b) Cross-section HRTEM image of a nanowire grown at 950° C. (c) Cross-section TEM image of multiple nanowires grown at 1000° C. (d) SEM image of the group of nanowires from which the cross-section was

taken. The dotted line denotes where the cross-section was taken. (e) A close up of this group shows each individual nanowire nucleating from the matrix. Both the large and small nanowires can be seen here. (f) An ion beam images shows the cross-section half way through the extraction process. The arrow points out where the three large nanowires were located. The nanowires were on top of a silicon substrate and under a thin layer of gold and a thick layer of platinum to protect them from ion beam damage. (g) A TEM image of a small nanowire. Its location within the nanowire group is indicated in (c). (h) A TEM image of a second small nanowire. Its location within the nanowire group is also indicated in (c). Images: B.W. Jacobs 96

Figure 4.10 Details of the cross-section taken from the nanowire grown at 850° C. This nanowire was separated into five regions corresponding to its distinct crystalline domains. These regions were divided along domain interfaces. FFTs from each region are shown on the right. Regions 1-4 were wurtzite and region 5 was zinc-blende. The arrows in the FFTs indicate the [0001] and [111] directions in the wurtzite and zinc-blende domains, respectively. Zinc-blende and wurtzite crystal models show which planes were responsible for faceting resulting in the triangular shape of the nanowire. In the wurtzite structure the $\{10\bar{1}1\}$ and (0001) planes faceted and were parallel with the growth direction, while the $\{2\bar{1}\bar{1}0\}$ planes were perpendicular to the growth direction. In the zinc-blende structure the $\{111\}$ planes faceted and were parallel to the growth direction, while the $\{011\}$ planes were perpendicular to the growth direction. Images and interpretation: B.W. Jacobs..... 98

Figure 4.11 HRTEM images of the cross-section taken from the nanowire grown at 850° C. (a) A close up from the corresponding boxed area in the center inset revealed several distinct crystalline domains with coherent and incoherent interfaces, as denoted by the solid and dashed lines, respectively. A dark contrast wurtzite domain was observed and could be due to a slightly different orientation. (b) The dark contrast wurtzite domain, from the corresponding boxed area in the center inset, is surrounded by both zinc-blende and wurtzite domains forming incoherent interface at every edge, as denoted by the dashed lines. The zinc-blende domains form coherent interfaces with the surrounding wurtzite domains, as denoted by the solid lines. (c) A close up of an incoherent interface, denoted by the dashed line, from the corresponding boxed area in the center inset. (d) This image shows the same incoherent interface at a different location. On the right side of this figure a long coherent interface that extends from the center of the nanowire to the outside edge forms between the (111) and (0001) planes, as denoted by the solid line. Images and interpretation: B.W. Jacobs 100

Figure 4.12 Details of the cross-section taken from the nanowire grown at 950° C. This nanowire was separated into six regions corresponding to distinct crystalline domains. These regions were divided along domain interfaces. FFTs from each region are shown on the right and bottom. Regions 1-5 were wurtzite and region 6 was zinc-blende. The arrows point in the [0001] and [111] directions in the wurtzite and zinc-blende domains, respectively, to emphasize differences in orientation. Images and interpretation: B.W. Jacobs..... 102

Figure 4.13 HRTEM images of the cross-section taken from the nanowire grown at 950° C. (a) A close up from the indicated area in the center inset revealed two distinct crystalline domains with incoherent interfaces. Possible stacking faults ran horizontally across the center of this image. (b) This image shows three distinct wurtzite domains with two incoherent interfaces. (c) Two wurtzite domains with an incoherent interface that changed its direction running from the center to the outside edge of the nanowire. (d) This image shows the center zinc-blende domain and a coherent interface between the zinc-blende and wurtzite domain. The top and bottom domain surrounding the zinc-blende domain were possible stacking faults that transitioned to wurtzite crystal structures. Images and interpretation: B.W. Jacobs 104

Figure 4.14 HRTEM images of the cross-section taken from the nanowire grown at 1000° C. (a) A large nanowire with a width of roughly 1.5 μm is shown. A wurtzite crystal model shows the facet planes parallel to the growth direction, $\{10\bar{1}0\}$, that resulted in the hexagonal cross-section shape, and the growth plane, (0001), perpendicular to the growth direction. (b) A high-resolution image of region 1 showing the high crystallinity of the nanowire. An FFT of region 1 that could be solved for the wurtzite crystal structure in the [0001] direction is shown in the inset. (c) A close up image of region 2 revealed a dark contrast wurtzite domain. (d) TEM image of the entire cross-section indicating where this nanowire cross-section was located. Images and interpretation: B.W. Jacobs..... 106

Figure 4.15 HRTEM images of the cross-section taken from the nanowire grown at 1000° C. (a) A small nanowire with a width of roughly 200 nm is shown here. It grew in the same direction as the nanowire shown in figure 4.15. It was divided into three regions. Regions 2 and 3 were lighter in contrast relative to the surrounding region 1. The FFTs shown on the right were all solved for the wurtzite structure along the [0001] direction. They were all in the same orientation. (b) A TEM image of the entire cross-section showing where this nanowire cross-section was located. (c) A close up of region 2 and 3 revealed that the light contrast regions were both hexagonal in shape. (d) A high-resolution image of region 1 showed the high crystallinity of the nanowire. Images and interpretation: B.W. Jacobs..... 107

Figure 4.16 HRTEM images of the cross-section taken from the nanowire grown at 1000° C. (a) A large “double” nanowire with a width of roughly 2 μm at its widest point is shown here. It grew in the same direction as the nanowire shown in figure 4.15 and 4.16. It was divided into four regions. Regions 1 and 2 are the left and right nanowires that made up the double nanowire. Regions 3 and 4 were areas with lighter contrast relative to the surrounding regions 1 and 2. The FFTs shown on the bottom of the image were taken from regions 1 and 2, and were solved for wurtzite structure along the [0001] direction. They were in the same orientation. (b) A TEM image of the entire cross-section indicates where this nanowire cross-section was located. (c) A close up of region 3 indicated that the light contrast region was hexagonal in shape. A small platelet was partially covering a hole in the center of the nanowire. (d) A close up of region 4 also shows an area of lighter contrast with a hole at its center. Images and interpretation: B.W. Jacobs..... 109

Figure 4.17 SEM images of the matrix that formed at 850° C. (a) The matrix is relatively uniform with feature sizes of around 200 nm to 1 μm in size. (b) A close up image shows the features in detail. There are many small and medium sized GaN crystal formations. Two nanowires in this image, as indicated by the arrows, have nucleated from the matrix. Images: K. McElroy 112

Figure 4.18 SEM images of the matrix that formed at 850° C. (a) A nanowire nucleated from the side of a hexagonal platelet. The arrows show the probable nanowire growth direction, $[2\bar{1}\bar{1}0]$ and the sides of the hexagonal platelet, $\{10\bar{1}0\}$. (b) A nanowire nucleated from the side of a hexagonal platelet. The arrows show the nanowire growth direction and sides of the platelet. Images: B.W. Jacobs 113

Figure 4.19 SEM images of the matrix that formed at 950° C. (a) The matrix is relatively uniform with feature sizes of around 200 nm to 1 μm in size, and similar to the matrix features formed at 850° C. (b) A close up image shows the features in detail. There are many small and medium sized GaN crystal formations. One nanowire in this image, as indicated by the arrow, has nucleated from the matrix. Images: K. McElroy 114

Figure 4.20 SEM images of the matrix that formed at 950° C. (a) A nanowire nucleated from the side of a hexagonal platelet. The arrows show the probable nanowire growth direction, $[10\bar{1}0]$ and the sides of the hexagonal platelet, $\{2\bar{1}\bar{1}0\}$. (b) A nanowire is also shown to have nucleated from the side of a hexagonal platelet. The arrows show the nanowire growth direction and sides of the platelet. Images: B.W. Jacobs 115

Figure 4.21 SEM images of the matrix that formed at 1000° C. (a) The matrix formed distinct features that could be divided into three regions. Region 1 indicates where the smallest features formed, region 2 the larger features, similar to those found in the matrix that formed at 850° C and 950° C and region 3 with the largest features. (b) A higher magnification image of regions 1 and 3 shows the features in more detail. The small features of region 1, in the foreground, are compared to the larger features of region 3, in the background. One nanowire in this image, as indicated by the arrow, has nucleated from region 1. (c) A higher magnification image of region 2 shows the features in more detail. This region is very similar to the matrix found to form at 850° C and 950° C. Three nanowire in this image, as indicated by the arrows, have nucleated from this region. (d) A higher magnification image of region 3 shows the features in more detail. The large crystal formations are easily seen here. A large rod is seen in the center of the image. These large rods were observed in the matrix that formed at 1000° C and not in the matrix that formed at the lower two temperatures. Images: K. McElroy 116

Figure 4.22 SEM and TEM images of the matrix that formed at 1000° C. (a) A SEM image of multiple nanowires that grew from the matrix. The arrow indicates where a nanowire nucleated from the top of a hexagonal platelet. (b) A SEM image of a possible nanowire nucleation site on the top of a hexagonal platelet. (c) A TEM image of the matrix showing large and small hexagonal holes, which may be sites where nanowires

nucleated and broke off. (d) A TEM image of the matrix also showing large and small hexagonal holes indicating possible nanowire nucleation sites. Images: (a),(b) K. McElroy, (c),(d) B.W. Jacobs 117

Figure 4.23 TEM images of a hexagonal platelet and its nanoscale ledges from matrix that formed at 850° C. (a) A TEM image shows a typical GaN hexagonal platelet. (b) HRTEM image of the indicated area in (a) revealed a network of nanoscale ledges. Images: B.W. Jacobs 118

Figure 4.24 HRTEM images of the nanoscale ledges from matrix that formed at 850° C. (a) An HRTEM image shows the side of a hexagonal platelet revealing the orientation of the nanoscale ledges. (b) An HRTEM image taken from a different area of the same hexagonal platelet revealed nanoscale ledges in a different but equivalent orientation as the ledges shown in (a) (c) An HRTEM image of a different platelet shows no nanoscale ledges revealing that not all hexagonal platelets have these features. (d) An HRTEM image of a different area on the same platelet in (c) shows the smooth edges of this platelet. Images: B.W. Jacobs 120

Figure 4.25 TEM images of hexagonal platelets and nanoscale ledges from matrix that formed at 1000° C. (a) Decomposed platelet resulting in the formation of nanoscale ledges. The dotted line indicates a fully formed platelet. (b) An HRTEM image of the area indicated in (a) shows the features and orientation of the ledges. (c) A TEM image of a different platelet indicates that nanoscale ledge formation can occur on the sides of platelets leading to a roughened edge. Images: B.W. Jacobs 121

Figure 4.26 Model showing the nanoscale ledges. The edges are the $\{10\bar{1}0\}$ planes and the peaks point in the $\langle 2\bar{1}\bar{1}0 \rangle$ direction. Nanoscale ledge growth occurred on the $\{10\bar{1}0\}$ planes and nanowire growth occurred along the $\langle 2\bar{1}\bar{1}0 \rangle$ direction. Image: B.W. Jacobs 122

Figure 4.27 SEM images indicating the evidence of the $\{10\bar{1}0\}$ growth. (a) The arrow indicates where the $\{10\bar{1}0\}$ platelet growth occurred, near the nanowire nucleation site, and the nanowire continuing to grow from there. (b) The arrow indicates a similar platelet growth in this image. The nanowire is shown to continue to grow from the base formation. Images: K. McElroy 123

Figure 4.28 SEM images showing the tapered tips of nanowires that grew at 1000° C along the $[0001]$ direction. The tips faceted on the $\{10\bar{1}1\}$ planes. Images: K. McElroy Interpretation: B.W. Jacobs 124

Figure 4.29 A typical GaNFET configuration. A highly doped silicon wafer was used as the substrate. SiO₂ was grown as the gate dielectric and a layer of metal was thermally evaporated on the backside of the wafer for the gate electrode. Nanowires were dispersed on top of the wafer and source and drain contacts were patterned with EBL. Image: B.W. Jacobs 128

Figure 4.30 I-V characteristics of a GaNFET. (a) The current was measured as V_{DS} was swept and V_{GS} stepped. The nonlinearity of the curves indicated Schottky barrier behavior. (b) This graphs emphasizes the change in current as a result of the change in V_{GS} . These data were extracted from the data in (a). I-V characteristics: B.W. Jacobs *et al. Nanotechnol.*, **18**, 475710 (2007) with permission 129

Figure 4.31 I-V characteristics of the circuit shown in the SEM image. (a) The nonlinear curve indicated that the nanowire-metal junction formed a Schottky barrier. At 6 V_{DS} over 70 μA of current was passing through the nanowire. (b) An SEM image shows the actual circuit. The SiO_2 insulating layer and Ti/Au contacts are labeled. The arrow shows the path current takes through the circuit. I-V characteristics, image and interpretation: B.W. Jacobs 130

Figure 4.32 I-V characteristics of a GaNFETs with three nanowires hooked in parallel. (a) The measured current was very high, over 400 μA , at 6 V_{DS} . (b) An SEM image shows the entire circuit. Photolithography (PL) was used to define the large contact pads where the contact probes were placed. The left and right boxes denote where close ups were taken in (c) and (d), respectively. (c) An SEM image showing two nanowires contacted in parallel. EBL was used to define the areas where metal was deposited on top of the nanowires. The bottom left pattern created with EBL is seen on top of an PL defined pattern. (d) A SEM image shows the third nanowire hooked in parallel and the EBL defined patterns that connected it. I-V characteristics, images and interpretation: B.W. Jacobs 131

Figure 4.33 The Zyvex S100 Nanomanipulator System. (a) The entire probing system is mounted in an SEM for high resolution imaging essential for nanoprobng and nanomanipulation. The arrows point out the four piezoelectrically controlled tungsten nanomanipulators. Images: R. Stallcup, A. Hartman and V.M. Ayres 133

Figure 4.34 SEM images showing the four-point probe configurations. Probes 1 and 4 were the current source probes, 2 and 3 were the voltage sense probes. (a) Configuration A, all probes were contacted to the contact pads. (b) Configuration B; current source probes were contacted to the contact pads, while the voltage sense probes were contacted to the nanowire. (c) Configuration C; all probes were contacted to the nanowire. (d) Configuration D; one current source probe was contacting the end of the nanowire and the other the contact pad, while the voltage sense probes were contacted to the nanowire. Images: B.W. Jacobs *et al. Nanotechnol.*, **18**, 475710 (2007) with permission 135

Figure 4.35 Four-point probe resistance measurements. (a) Configuration A, total system resistance measurement. Resistance values were between 3 and 5 $M\Omega$. Negative values corresponded to current sourced in the opposite direction. (b) Configuration C, NW resistance measurement, side contact. Resistance values were between 500 and 800 $k\Omega$. (c) Configuration D, NW resistance measurement, end contact. Resistance values were between 375 $k\Omega$ and 3 $M\Omega$. Below the resistance diagrams are the corresponding nanomanipulator nanoprobe placements for each configuration. Resistance measurements and diagrams: R. Stallcup, A. Hartman, V.M. Ayres and B.W. Jacobs .136

Figure 4.36 Two-point probe results. The graph shows the different voltage dependences of the current when the nanoprobe is on the Ti/Au contacts (dotted line, compliance was set to 250 nA) and directly on the nanowire (dashed line). Diagrams of the probe configurations are shown on the right. I-V characteristics and diagrams: K. McElroy and B.W. Jacobs 138

Figure 4.37 SEM images of the breakdown measurements, in configuration D. (a) The fractured nanowire. (b) The pull-apart between the voltage probes. The location of the pull-apart is shown in the inset. (c) Simultaneous onset of single-phase melt. The location of the melt is shown in the inset. (d) A larger amount of material melted and formed a protrusion outside the nanowire. Images: B.W. Jacobs *et al. Nanotechnol.*, **18**, 475710 (2007) with permission 140

Figure 4.38 Cathodoluminescence spectrum showing the double peak indicating the wurtzite and zinc-blende phases present in the nanowire. The band gap energies for each phase is blue-shifted on the order of 0.4 eV. Spectra: B.W. Jacobs *et al. Nano Lett.* **7**, 1435-1438 (2007) with permission 143

Chapter 5

Figure 5.1 The Space Radiation Environment. Galactic cosmic rays constantly bombard the Earth and surrounding space. The Earth's magnetic field, as indicated by the lines surrounding the Earth, protects it from harmful radiation. Image: NASA 150

Figure 5.2 n-type MOSFET. Radiation induced damage by an energetic heavy ion. As the heavy ion traverses through the semiconductor, it leaves a trail of defects. Images: B.W. Jacobs 158

Figure 5.3 Illustration of the particle acceleration process at the NSCL. Ions are sent from the source through attenuators to adjust the beam current. They are then injected into the K500 cyclotron and then the K1200 for acceleration. Degraders and attenuators adjust the beam properties, which is sent to the specified beam vault for experiments. The boxed area in the upper right represents the SEETF vault and its components. Image: adapted from R. Ladbury *et al. IEEE T. Nucl. Sci.* **51**, 3664 (2004) with permission 164

Figure 5.4 Image of the NSCL SEETF. Each main component of the SEETF is noted. The ion beam runs through the PPAC for analysis, exits through a zirconium foil, runs through the plastic scintillator, hits the target, and hits the graphite beam stop. Top image: B.W. Jacobs Bottom image: R. Ladbury *et al., IEEE T. Nucl. Sci.* **51**, 3664 (2004) with permission 166

Figure 5.5 The (n,m) CNT labeling system. T is the tube axis. C_h is the chirality vector and describes how to roll up the graphene sheet. a_1 and a_2 are the unit vectors of

graphene. (n,0) and (n,n) are special chirality vectors denoting zig-zag and armchair CNTs, respectively. The shaded box denotes the unit cell of the nanotube 170

Figure 5.6 Types of CNTs. There are three main types of CNTs, zig-zag, armchair, and the rest, chiral nanotubes 171

Figure 5.7 HRTEM images of SWCNTs and MWCNTs. (a) A single SWCNT can be seen in the middle of the image running nearly vertically. The single wall structure is easily seen. Disordered carbon is also seen on the surface of the nanotube. (b) The nested MWCNT structure is seen in this figure where each line indicates a wall. Images: B.W. Jacobs 172

Figure 5.8 HTREM image of carbon onions. (a) A single round carbon onion is shown in this figure. The inset shows a model of a C₆₀ molecule, which is the basis of carbon onions. (b) These carbon onions formed polygonal sides with some faceting on the outer layers. Images: B.W. Jacobs 174

Figure 5.9 HRTEM image of nanocrystalline diamond with diameters of 5 to 10 nm. Nanocrystalline diamond is used as a starting material for producing carbon onions. Images: B.W. Jacobs 176

Figure 5.10 The carbon samples were placed in quartz tubes and put in a close packed configuration. These samples were irradiated simultaneously. The heavy ions exited into air through a thin zirconium window and passed through the quartz tubes with an on target beam energy of over 11 GeV, as shown in the left image. The samples packed in the quartz tubes are shown on the right. Images: B.W. Jacobs..... 178

Figure 5.11 The carbon and gallium nitride nanowire samples were placed on a silicon wafer that was attached to a piece of particleboard with silicone adhesive. The particleboard was then screwed onto the SEETF movable stage. The samples were held in place by a small mica sheet that was attached to the silicon wafer with silicone adhesive. Each sample could then be separately irradiated with a specific dose. The heavy ions exited into air through a thin zirconium window and passed through the mica sheets with an on target beam energy of over 9.7 GeV, as shown in the left image. The samples that were placed on the silicon substrate are shown on the right. Images: B.W. Jacobs..... 180

Figure 5.12 The electronic characteristics of a GaNFET in radiated were measured. (a) The circuit was mounted in a ceramic package and mounted on particleboard and attached to the SEETF moveable stage. (b) A close up of the circuit shows its wire bonds. Images: B.W. Jacobs 181

Figure 5.13 TEM images of irradiated GaN nanowire. (a) A TEM image shows a plume of material, which may have resulted from heavy ion radiation. (b) An HRTEM image of the plume showing its amorphous character. The FFTs of the indicated areas show the

ring structure associated with amorphous and polycrystalline material. Image: B.W. Jacobs..... 184

Figure 5.14 TEM images of an irradiated nanowire. (a) The TEM image shows a nanowire with a rough outer surface, which may have resulted from heavy ion radiation. (b) HRTEM image of the boxed area in (a). An amorphous plume is shown here. An FFT taken from the boxed area shows a ring pattern associated with an amorphous and polycrystalline region. (c) HRTEM image taken from the boxed area in (a). The zinc-blende/wurtzite coherent interface is shown here. No damage is observed in this picture and FFTs do not show significant ring patterns. Images: B.W. Jacobs..... 185

Figure 5.15 Multiple V_{DS} sweep of a GaNFET in radiation. V_{GS} was kept constant at 9V. I-V Characteristics: V.M. Ayres *et al. Diam. Relat. Mater.* **15**, 1117-1121 (2006) 186

Figure 5.16 Raman spectra of irradiated SWCNTs. (a) Before and after krypton-78 irradiation. (b) Before and after calcium-48 irradiation. After all irradiation the SWCNTs indicated no observable damage. Spectra: B.W. Jacobs..... 188

Figure 5.17 SEM and HRTEM images of single walled CNTs before and after irradiation. (a) SEM before irradiation. (b) HRTEM before irradiation. (c) SEM after 1,000Gy krypton-78 irradiation. (d) HRTEM after 1,000Gy krypton-78 irradiation. (e) SEM after 10,000Gy krypton-78 irradiation. (f) HRTEM after 10,000Gy krypton-78 irradiation. Images: B.W. Jacobs 189

Figure 5.18 HRTEM image of SWCNT after 10,000Gy krypton-78 irradiation. This image shows carbon-60 packed into a SWCNT, a peapod, possibly due to heavy ion irradiation. Image: B.W. Jacobs..... 190

Figure 5.19 Raman spectra of MWCNTs before and after krypton-78 radiation. The D and G-peaks do not change significantly after each radiation dose compared to the un-irradiated sample. This indicates that the MWCNTs held up very well in the krypton-78 radiation and retained their multi walled structure. Spectra: B.W. Jacobs..... 191

Figure 5.20 SEM and HRTEM images of multi walled CNTs before and after irradiation. (a) SEM before irradiation. (b) HRTEM before irradiation. (c) SEM after 1,000Gy krypton-78 irradiation. (d) HRTEM after 1,000Gy krypton-78 irradiation. (e) SEM after 10,000Gy krypton-78 irradiation. (f) HRTEM after 10,000Gy krypton-78 irradiation. Images: B.W. Jacobs 192

Figure 5.21 Raman spectra of untreated and treated carbon onions before and after calcium-48 irradiation. (a) Untreated carbon onions. (b) Treated carbon onions. Spectra: B.W. Jacobs 193

Figure 5.22 HRTEM images of carbon onions before and after calcium-48 irradiation. (a) and (b) compares the before and after irradiation of the untreated carbon onions. (c)

and (d) compares the before and after irradiation of the carbon onions with oxidation treatment. The arrows in (b) and (d) denote modifications due to radiation that took the form of onion coalescence. Images: B.W. Jacobs..... 194

Figure 5.23 HRTEM images of carbon onions after calcium-48 irradiation. (a) Oxidation treated onions. The left most arrows point out outer layer discontinuities and the right points out onion coalescence. The inset also shows onion coalescence. (b) Untreated carbon onions. The arrow points out onion coalescence. The inset also shows onions coalescence. Both images indicate that that the overall onion structure was maintained. Onion structure modifications are consistent for both treated and untreated samples. Images: B.W. Jacobs 195

Figure 5.24 HRTEM images of untreated carbon onions grown at temperatures (a) 1700°C (b) 2000°C and (c) 2300°C show the evolution from spherical to polyhedral onions. The increased onion coalescence and outer layer discontinuities can be seen in (c). Images: B.W. Jacobs 196

Chapter 6

Figure 6.1 Bruker AXS high resolution XRD. (a) The X-ray source originates from the right. It hits the sample and is detected on the left. The detector sweeps in a counterclockwise direction detected reflected X-rays that meet the Bragg condition. (b) The X-ray detector. A reflected beam from the sample is detected. (c) The X-ray source. X-rays travel from the source to the sample. Images: B.W. Jacobs 205

Figure 6.2 Diagram of BEEM operation. The left image shows the physical setup of a BEEM. The tip interacts with the base metal surface passing electrons through gap between the tip and surface. I_c is the current coming out of the semiconductor collector, I_t is the current from the base metal resulting from electrons that were scattered in the metal and did not have enough energy to surmount the barrier, plus the collector current. The left image shows the energy diagram indicating each barrier. Electrons originate in the metal STM tip, tunnel through the vacuum gap and pass through the metal and into the semiconductor collector. E_f is the Fermi level of each material, and eV_b is the height of the metal-semiconductor Schottky barrier. The figure is not to scale. The vacuum gap is usually on the order of a few nanometers, and the metal base thickness is usually around 10nm. Image: B.W. Jacobs 207

Figure 6.3 Basic method of XPS sample spectrum acquisition. The X-rays are aimed at the sample surface at a known angle and interact with the surface inducing photo-emitted electrons. The photo-emitted electrons are collected and analyzed to determine their energy. A spectrum of the photo-emitted electrons is then created indicating what materials are on the sample surface, and the electronic state they are in 210

1. Introduction

Since the mid 20th century nanotechnology has emerged as a highly multidisciplinary research initiative spanning nearly all branches of science. The science of nanotechnology took off with the discovery of the C₆₀ molecule by Smalley, Kroto and Curl in the 1980's; a discovery that won the three scientists the 1996 Nobel Prize in Chemistry. The new molecule was named Buckminsterfullerene, or buckyball for short, after the architect Richard Buckminster Fuller who popularized the geodesic dome, which closely resembles the C₆₀ shape. These new molecules sparked a revolution in science that is still on the cutting-edge of research today, 20 years later. As a result, novel ideas and concepts are being developed across the globe that will find practical use in the next several decades.

Spanning many disciplines, nanotechnology has transformed science and engineering with an eminent influence in the electronics and materials industries. These industries in particular are on the cusp of a fundamental paradigm shift that will establish new ways of thinking about and solving the next generation problems in device design and materials engineering.

The search for new materials and systems with properties that meet or exceed the current state-of-the-art has gained significant momentum with the advent of the discoveries within the nanotechnology field. Many unexpected characteristics are continually discovered in these novel structures while working to uncover and understand their properties. There are several promising materials in particular that are spurring research for new applications. These materials, or nanomaterials, possess many interesting properties due to their small size. The resulting properties can only be

described using quantum mechanics. These properties lead to amazing new and unexpected characteristics, and exploiting these properties will drive innovation for many years.

As stated in the candidate's original thesis proposal, investigations of fundamental heavy ion radiation interactions with nanomaterials will be presented. In the first radiation experiments, carbon nanotubes were irradiated and their structural modifications, if any, were analyzed with several techniques. The results were very promising and additional experiments were planned and implemented. In the subsequent radiation experiments, gallium nitride (GaN) nanowires were also included. The GaN nanowire material performance, as well as devices that incorporated GaN nanowires as active elements, were investigated.

While analyzing these GaN nanowires used in the heavy ion radiation experiments, a previously unreported nanowire structure was discovered by the candidate. The details of this novel structure warranted further study, and a full investigation was initiated. A significant portion of this thesis presents results of this study obtained using several cutting-edge instruments and techniques.

Heavy ion radiation research involving reduced dimensionalities is also in its infancy with only a handful of groups contributing results at this time. This is an area of potentially national significance. There are several issues regarding nanomaterial and nanodevice heavy ion radiation experiment procedures that should be addressed and improved upon. Therefore, important problems, as well as recommendations for improvement, will be briefly discussed.

Specifics on how each investigated nanomaterial used in heavy ion radiation experiments was grown and characterized, as well as how devices that integrate nanomaterials were fabricated, are presented. The tools needed to characterize the nanomaterials and fabricate devices will also be discussed. Without these highly sophisticated tools, methods, and the ability to operate them and interpret results correctly, this thesis research would not have been possible. The methods are valuable in themselves, and are aimed at helping provide a baseline for future work in this area.

1.1 Radiation Resilience in Reduced Dimensionality Systems

Since the dawn of satellite communications and interplanetary space exploration, organizations from around the world have sent sophisticated electronic systems into space with increasing regularity. Though highly shielded and equipped with radiation hardened electronics and high redundancy, these systems are still prone to radiation induced upset. For satellites in near Earth orbit, the magnetic field induced by the Earth's core provides some protection. However, in years of increased solar activity these near Earth satellites are affected by radiation produced by the Sun, and instances of complete satellite failure due to solar radiation are not uncommon. Increased shielding and redundancy are not long-term solutions to this problem. Custom radiation hardened electronics and redundant systems are expensive to develop and implement. Shielding adds a substantial amount of weight, which translates to expensive added fuel costs, and adding increased shielding to new smaller space microprobe designs is increasingly difficult.

In order to reduce shielding requirements and the need for highly complex redundant systems, electronics should be inherently radiation resilient in their individual device critical components. With current trends in silicon transistor technology, where gate thickness and conducting channel length are getting ever smaller, already sensitive areas are becoming more susceptible to radiation induced upset. The gate thickness and channel length reduction also leads to lower operating voltages, which amplifies device sensitivity in radiation. As length scales are reduced by one order of magnitude, the frequency of radiation induced upset, and the magnitude at which damage is incurred, increases.

Novel nanomaterials, on scales two orders of magnitude smaller than current state-of-the-art feature sizes of silicon based devices, may be inherently radiation resilient. These radiation resilient properties may be inherent to their structure characteristics. Recent investigations suggesting that radiation interactions and damage propagation mechanisms in nanomaterials differ from bulk materials in ways that result in enhanced radiation resilience^{1,2,3}.

Promising nanomaterials, which can be defined as a material with at least one reduced dimensionality component, are finding use in a variety of applications. They have been recognized for their excellent electrical, optical, and mechanical properties. Nanomaterials utilized in devices can enhance system performance due to their reduced dimensionality components. This enhanced performance is an important consideration in finding alternative technologies to the current state-of-the-art. These systems must outperform current technologies in order to be viable in future systems. Recently electronic devices have been shown to be faster and operate at lower voltages⁴, chemical sensors are much more sensitive to specific species⁵, and optical devices are more efficient⁶ compared with current state-of-the-art technologies. Therefore, current silicon based technologies will inevitably be augmented with or replaced by these emerging devices that incorporate nanomaterials as key device components. With enhanced device performance and inherent radiation resilience, nanomaterials, and their use in new electronic, optical, and mechanical devices, are excellent candidates for next generation space applications.

Reduced dimensionality systems will inevitably become the mainstream in the electronics industry. If these systems are proven to be inherently radiation resilient, the

ability to use off the shelf electronic parts for new space based systems will significantly reduce the cost of system implementation. Shielding and redundancy could be reduced and the need for customized radiation hardened electronics will be mitigated.

Several types of nanomaterials and nanodevices have been explored in this research initiative. Specifically carbon nanotubes, carbon onions, gallium nitride nanowires, and gallium nitride nanowire transistors have been tested in heavy ion irradiation. The results of each nanomaterial and nanodevice performance, when irradiated with specific species and doses of highly energetic heavy ions, will be presented. Discussion of results will follow with possible explanations for these results will be given.

1.2 Carbon Nanotubes and Carbon Onions

Carbon nanotubes are a widely researched nanomaterial with many interesting properties. Carbon nanotubes are essentially a single sheet of graphene that self-assemble into a seamless cylinder around 1 nm in diameter with lengths reaching several millimeters. Officially discovered in 1991⁷, nanotubes have drawn an enormous amount of attention in scientific research. Due to their small size and unique structure, nearly all properties of carbon nanotubes, including their electrical, chemical, optical, and mechanical properties, have exhibited interesting, and many times very unexpected, properties that larger, bulk materials simply do not possess.

Carbon nanotubes are excellent candidates for harsh environments due to their robust structure and wide variety of possible applications. Possibly the most interesting property important for radiation resiliency, is their ability to self-heal after heavy ion damage. Carbon nanotubes were irradiated with three heavy ion beams, krypton-86, krypton-78, and calcium-48. The candidate helped design and implement these experiments, and analyzed irradiated nanomaterial.

Carbon onions are similar to carbon nanotubes, but instead of a seamless cylinder of graphene, they are nested seamless spheres of graphene. Their name comes from the similarity in structure of an onion of the vegetable variety, when cut in half, the concentric onion layers can easily be seen. Similarly, if a carbon onion could be cut in half, the concentric layers of graphene could easily be identified.

The round structure of carbon onions gives them the ability to provide a low friction interface between two surfaces, and they are small enough to fill cracks in those surfaces. Carbon onions were therefore tested for viability as a solid lubricant. It has

been shown that they work well as a lubricant in vacuum, and with a similar structure as carbon nanotubes, they may have the ability to self-heal after heavy ion radiation damage. Carbon onions were irradiated with calcium-48.

1.3 Multiphase Gallium Nitride Nanowires

A long solid structure comprised of a semiconducting or metallic material, nanowires have recently become a widely researched structure for electronic, mechanical, and sensor devices. Gallium nitride nanowires in particular are promising due to their versatility in devices. Gallium nitride (GaN) has a wide, direct band gap, and is inherently n-type, making it viable in many optical and electronic applications. The GaN nanowires investigated in this thesis research were found to have an interesting structure. Grown via a novel catalyst-free technique, the candidate identified a multiphase nanowire that incorporated the zinc-blende and wurtzite crystal structures simultaneously. The multiphase structure spanned the entire length of the nanowire, which can grow to 100s of microns in length. He identified possible nanowire nucleation sites responsible for the multiphase nanowire growth. The candidate has fabricated and tested many devices using the multiphase nanowire as the active element, and the first characterization as an electronic material and as an electronic element within a nanodevice will be presented.

Structural and electronic investigations were done with several instruments specially designed for characterizing nanosystems. Using these instruments several new and exciting results were obtained that would otherwise not have been possible using traditional characterization tools. High-resolution transmission electron microscopy, focused ion beam techniques, scanning probe microscopy, and a nanomanipulation system integrated with a low noise electronic characterization system were crucial in discovering and understanding the new properties these multiphase GaN nanowires.

GaN nanowires were also irradiated with a krypton-78 beam. Their subsequent material modifications, as a result of heavy ion radiation, were investigated by the

candidate and will be presented. GaN nanowire based circuits were fabricated by the candidate and also tested in real time in radiation.

1.4 Multidisciplinary Research Approach

Research and project development in nanotechnology requires a comprehensive understanding of a variety of disciplines as well as a highly interdisciplinary team working closely together in order for complex research initiatives to be successful. This multidisciplinary approach is quickly becoming the status quo in research labs investigating nanotechnology issues. Interdepartmental and inter-institutional national, as well as international, collaborations are becoming more common in nanotechnology research efforts, as was the case with this thesis research, combining expertise from a several scientific backgrounds.

In this thesis several different scientific disciplines are discussed including electrical engineering, materials science, chemistry, mechanical engineering, high-energy particle physics and quantum mechanics. Collaboration with scientists and engineers from these disciplines was required to accurately understand and describe material and device phenomena occurring in these new systems. This highly collaborative expertise was essential in the success of this research. These partnerships included inter-departmental collaboration with Chemical Engineering and Material Science and the National Superconducting Cyclotron Laboratory at Michigan State University, inter-institutional academic collaboration with Howard University and Tokyo Institute of Technology, government collaboration with NASA Goddard Space Flight Center and Jet Propulsion Laboratory, and industry collaboration with Keithley Instruments and Zyvex Corporation. The candidate was essential in the success of this group effort. He learned a great deal from these collaborations through direct interactions with members as well as acting as a liaison with all collaborators.

1.5 Summary of Later Chapters

In the second chapter several current analysis techniques used in characterizing nanomaterials, along with devices and systems that integrate nanomaterials, will be discussed. In the third chapter implications of size restrictions on specific materials will be introduced to explain how reduced dimensionalities affect certain material properties. In the fourth chapter a comprehensive analysis and discussion of a recently discovered multiphase gallium nitride nanowire homostructure will be presented. This includes discussions on the growth, structural and electronic characteristics pertaining to experimental results. In the fifth chapter, an overview of the heavy ion radiation experiments at the National Superconducting Cyclotron Laboratory (NSCL) will be discussed. Operation of the NSCL as well as the Single Event Effects Testing Facility, where the experiments were conducted, will be summarized so that basic knowledge of each facility is acquired. Results of GaN nanowire, carbon nanotube and carbon onion as well as GaN-based electronic devices in heavy ion irradiation will be presented. Chapters 6 and 7 will contain future work and a conclusion, respectively.

References

1. R. Leon, S. Marcinkevicius, J. Siegert, B. Cechavicius, B. Magness, W. Taylor, C. Lobo, "Effects of proton irradiation on luminescence emission and carrier dynamics of self-assembled III-V quantum dots," *IEEE Trans. Nucl. Sci.*, **49**, 2844-2851 (2002)
2. P. G. Piva, R. D. Goldberg, I. V. Mitchell, D. Labrie, R. Leon, S. Charbonneau, Z. R. Wasilewski, S. Fafard, "Enhanced degradation resistance of quantum dot lasers to radiation damage," *Appl. Phys. Lett.*, **77**, 624-626 (2000)
3. M. P. Petkov, L. D. Bell, H. A. Atwater, "High total dose tolerance of prototype silicon nanocrystal non-volatile memory cells," *IEEE Trans. Nucl. Sci.*, **51**, 3822-3826 (2004)
4. S. J. Wind, J. Appenzeller, R. Martel, V. Derycke, P. Avouris, "Vertical scaling of carbon nanotube field-effect transistors using top gate electrodes," *Appl. Phys. Lett.*, **80**, 3817-3819 (2002)
5. F. Patolsky, C. M. Lieber, "Nanowire nanosensors," *Mater. Today*, **8**, 20-28 (2005)
6. F. Qian, S. Gradeak, Y. Li, C-Y. Wen, C. M. Lieber, "Core/Multishell Nanowire Heterostructures as Multicolor, High-Efficiency Light-Emitting Diodes," *Nano Lett.*, **5**, 2287-2281 (2005)
7. S. Iijima, "Helical microtubules of graphitic carbon," *Nature*, **354**, 56-58 (1991)

2. Instruments and Methods

With the increasing complexity and unexpected properties of nanomaterials and nanosystems, a wide variety of instruments and methods are required to understand the fundamental characteristics of a given sample. Recently, in response to new instrument requirements brought about by the need to characterize novel materials and devices, specialized tools that can measure, probe, manipulate, and create on the nanoscale have been invented and many existing tools have been further customized and improved upon. Due to the wide variety of materials and systems investigated in this research, the use of many different instruments was required. During the development of this thesis research special instrumentation at several different sites was used. A description of the instruments and methods used, and the role they played in the candidate's thesis research, will provide necessary background information needed to understand later research results and discussions.

There are many instruments used for nanomaterial analysis. Several key instruments and methods used in this research are discussed here. Using these instruments, material structure, surface topology, elemental composition, etc. can be analyzed. With this fundamental information as a starting point in the design process, new devices and systems that utilize these nanomaterials can be successfully implemented in real world applications.

Many of the instruments discussed were located in different facilities and labs at Michigan State University. These facilities included the W. M. Keck Microfabrication Facility, the Center for Advanced Microscopy, the National Superconducting Cyclotron Laboratory, and the Electronic and Biological Nanostructures Laboratory. Additional

instrumentation was located at other institutions including the Electron Microbeam Analysis Laboratory at the University of Michigan, the Tokura-Hirata Lab at Tokyo Institute of Technology, Keithley Instruments in Cleveland, Ohio, and Zyvex Instruments in Richardson, Texas.

2.1 Transmission Electron Microscopy

The transmission electron microscope (TEM) is a highly versatile tool used for materials analysis. It is virtually indispensable for material identification, structure and defect analysis, material chemistry, and a host of other applications. This instrument has improved a great deal over the past few decades and has become a primary tool for analyzing very small structures. The TEM is one of the most important tools used in this thesis research. All the materials discussed have been analyzed in some way in the TEM. The TEM was able to resolve intricate features, leading to an enhanced understanding of the samples analyzed.

The TEM, as the name implies, uses electrons for image creation and sample analysis. Electrons can be used for imaging, because like all matter, they possess wave-particle duality. This means that electrons act as waves and particles simultaneously. The wavelength of an electron is inversely proportional to its momentum, in accord with the de Broglie hypothesis¹,

$$\lambda = \frac{h}{p}.$$

In this relationship λ is the particle wavelength, h is Planck's constant, and p is the particle momentum. Since the resolution of an imaging system depends on the wavelength of the incident beam, be it photons, electrons, neutrons, etc., shorter wavelengths lead to higher resolution². Therefore, if the electron wavelength decreases, the momentum of the electron increases and the resolution increases accordingly. Electron wavelengths can be less than .037 Å for acceleration voltages of 100 kV and above, much shorter than the range of wavelengths for visible light, which is around 400-700 nm.

The electron is also a charged particle. Therefore, electrons can interact with electromagnetic focusing fields in the TEM and with the sample, which also contains charged particles in the form of atomic nuclei and electron clouds surrounding the nuclei. These atomic interactions allow for specific sample material information to be obtained.

Electrons in the TEM are produced using one of three sources. A very common source is the tungsten filament used for thermionic emission. The filament is heated by passing a large current, which in turn produces electrons with enough energy to overcome the work function of tungsten. The work function is defined as the amount of energy needed for an electron to escape from a given material. The work function of tungsten is around 4.5 eV. By applying a high positive voltage to an anode near the filament, the electrons are attracted to the anode and pass through a small aperture. The high voltage on the anode is also responsible for the required electron acceleration. Tungsten filaments, however, produce a rather high distribution of electron energies, called the electron energy spread. This spread can cause electrons with different energies to be focused slightly different. This is called chromatic aberration and reduces resolution in the TEM. Tungsten filaments are quite inexpensive and last about 100 hours. A second method used for electron generation is the lanthanum hexaboride (LaB_6) tip. Similar to the tungsten filament in operation, it also uses thermionic emission, but it is brighter, meaning it emits more electrons due to its lower work function, 2.5 eV. It lasts roughly 10-15 times longer than the tungsten filament and has a smaller electron energy spread, but it is more expensive. A third way to produce electrons, and wholly different from thermionic emission, is to use a field-emission source. A field-emission source is usually made of tungsten that has a very sharp tip. When an electric field is applied, it is

concentrated at the sharp point of the field-emission tip. In response to this concentrated electric field, electrons at the tip of the tungsten source tunnel out of the material and are accelerated to the desired energy by the anode. Field-emission sources have become very popular, since they have a very low electron energy spread, are very bright, and provide excellent high-resolution images. They are, however, very expensive.

After the electrons have been accelerated through the anode, they are focused using a series of electromagnetic lenses and apertures. The physical location of these lenses and apertures are shown in figure 2.1. An electromagnetic lens essentially consists of a copper wire winding with a hole in the center that surrounds the electron beam. When a current is passed through the wire, a magnetic field is produced that can interact with and manipulate the electron beam. Apertures are used to block the transmission of unwanted electrons from contributing to the final image. The system of focusing electrons in electromagnetic lenses is nearly identical in concept to focusing photons in a glass optical lens. Using an electromagnetic lens, however, one has the ability to change the magnetic field strength by altering the current passing through the copper windings. In this way the beam can be manipulated, resulting in, for instance, a change in the magnification, without having to switch to a different lens, as in optical microscopy.

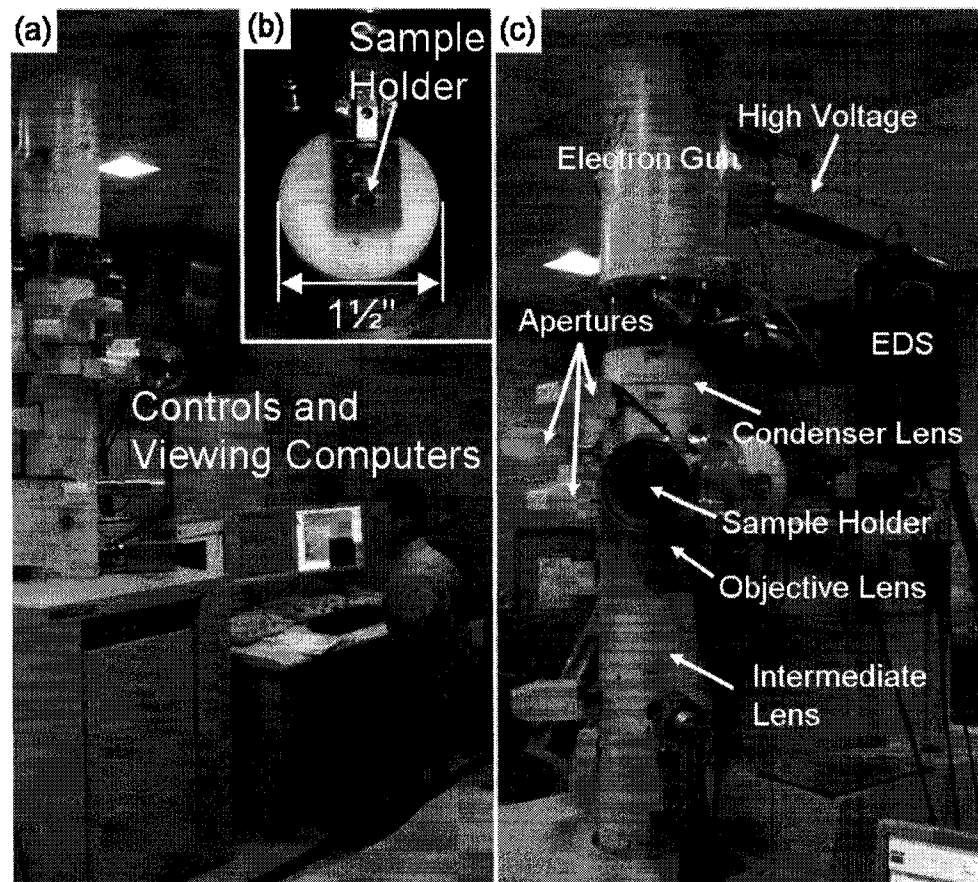


Figure 2.1. JEOL 2200FS field-emission transmission electron microscope at the Center for Advanced Microscopy at Michigan State University. (a) This particular TEM is in part controlled by computer. The computers used for imaging are shown on the right. (b) A TEM sample holder. The arrow indicates where a TEM grid is placed. Note its size. This restricts the size of the sample that can be placed in the TEM. (c) Close up of the TEM. The electron gun is at the top of the TEM and electrons are accelerated down the beam column and focused by the electromagnetic lenses. The sample holder indicates where the sample is located in the beam column. Images: B.W. Jacobs

In the TEM electromagnetic lens system the electron beam is first focused using a condenser lens so that a parallel beam is created. A parallel beam maximizes coherence and sample contrast. The condenser aperture is used to block stray electrons. The beam must also be circular so that astigmatism effects are mitigated. A non-circular beam will be focused differently since the magnetic field is stronger at the edge of the lens. After the beam passes through the sample, the objective lens is used to focus the image. The objective aperture and selected area diffraction aperture below the sample can further restrict the electron beam. The objective aperture is used to enhance the image contrast

and select certain diffracted beams used in advanced imaging techniques. The selected area diffraction aperture is used to select a certain area for diffraction studies and will be discussed later. The final lens normally used in image formation is the intermediate lens, which determines the magnification.

The electromagnetic lenses used in the TEM, however, are far from ideal. Unlike optical lenses that can be made nearly perfect, maximizing achievable resolution using the visible light spectrum, electromagnetic lenses fall far short of achieving this maximum possible resolution using electrons. A primary issue in electromagnetic lenses is the non-uniformity of the magnetic field around the lens. This causes electrons at different areas in the beam to be focused differently. The further out an electron is from the center of the beam, the stronger it is deflected. This phenomenon is called spherical aberration. This is a critical problem limiting the resolution of the modern TEM, restricting the resolution to around $.5 \text{ \AA}$ for acceleration voltages of 200 keV and an electron wavelength of $.0251 \text{ \AA}$. Although atomic scale resolution is possible, the maximum theoretical resolution using 200 keV electrons would easily be great enough to pick out fine details of atomic structure. The improvement of electromagnetic lenses and spherical aberration compensation has made significant progress, and new TEMs are able to resolve finer and finer detail in samples.

Preparing samples for imaging in the TEM poses several obstacles. The sample must meet several criteria before images can be taken. First and foremost it must be thin enough to be transparent to the TEM electron beam, and the thinner the sample is, the better. The sample should be less than 100 nm thick depending on the transparency of the material. The transparency depends on the sample material, i.e. its density, atomic

number, etc. The sample must also be small, since the TEM sample holder is only around 3 mm in diameter. The sample must be able to hold up in the high-energy electron beam so that imaging can take place. Samples will inevitably be damaged, so the electron beam should stay as defocused, or spread out, as much as possible. These criteria significantly restrict the type of samples that can be analyzed, and it complicates sample preparation.

Several techniques exist for preparing samples, including ion milling, microtome cross-sections, and chemical etching, to name a few. When imaging many nanomaterials in the TEM, however, these preparation techniques may not be needed because the samples are already very small. Usually in preparing a nanomaterial, such as nanowires or nanotubes, for imaging, an ethanol suspension containing the sample is placed on a TEM sample support and imaged. The sample support usually consists of a round copper or nickel grid with a fine mesh of square holes several hundred microns wide. A very thin carbon film with many holes only a few microns wide, which provides the actual sample support, spans the copper mesh. Ideally the sample material will span a hole in the carbon film so that maximum beam current will pass through the sample resulting in brighter, higher resolution images. This is the primary nanomaterial sample preparation technique used in this thesis research. Another primary sample preparation technique used in this research is nanowire cross-sectioning using a focused ion beam. This technique will be discussed in detail later the chapter.

In forming a sample image, electrons interact with atomic nuclei and electrons surrounding the nuclei resulting in elastic or inelastic scattering. Elastic scattering is the primary scattering process in the TEM². In order to understand how images are formed,

the wave nature of electrons, from the wave-particle duality concept, must be invoked. As the electron beam passes through a sample and scatters elastically, usually at very small angles, the resulting image will typically contain areas of light and dark contrast corresponding to the specific properties of that sample. There are two primary types of contrast that occur when forming an image, amplitude contrast and phase contrast. Phase contrast is important in high-resolution TEM and will be discussed later in the chapter. Amplitude contrast can be further divided into two groups, mass-thickness and diffraction contrast. Mass-thickness contrast primarily arises due to thickness variations in the sample. When the sample is thicker, there is a higher likelihood of multiple scattering events that cause electrons to significantly deviate from the beam axis and not contribute to the final image. Different elements present within the sample will also affect the contrast, since the electron beam will scatter differently off different elements. The amount of electron scatter depends on the atomic number of the specific element in the sample. Scattered electrons that are incoherent form mass-thickness contrast. In other words, there is no constructive or destructive interference in forming the image. In diffraction contrast, however, the sample is tilted so that two strong beams are obtained, one diffracted beam and the transmission beam, called a two-beam condition. Scattered electrons are coherent and as a result constructively and destructively interfere. Diffraction contrast is important for defect analysis and determining thickness variations on the sample. Diffraction contrast is similar to phase-contrast imaging used for high-resolution TEM, which is discussed next.

2.1.1 High-Resolution Transmission Electron Microscopy

High-resolution TEM (HRTEM) is a very useful tool when analyzing nanomaterials and nanostructures. Atomic scale resolution is obtainable if the sample material is thin enough. The local structure of materials can then be analyzed in detail. The JEOL 2200FS at the Center for Advanced Microscopy at Michigan State University was the primary HRTEM used in this research.

Usually HRTEM is thought to be synonymous with phase-contrast images. Actually, HRTEM is possible as a result of phase-contrast imaging. Phase-contrast images are formed when multiple coherent beams are allowed to constructively and destructively interfere. This is similar to diffraction contrast when two beams are allowed to interfere, but in phase-contrast images, many more beams interfere. Phase-contrast does occur in all TEMs, but not all TEMs have the capability to resolve atomic scale features.

This constructive and destructive interference of coherent beams is described by the transfer function,

$$T(u) = 2A(u)\sin\chi(u);$$

where $A(u)$ is the aperture function and $\chi(u)$ is the phase-distortion function². The transfer function is a function of spatial frequency, u , which is a reciprocal lattice vector, and is related to $1/x$, where x is a distance. Reciprocal space is discussed in the next section. The phase-distortion function, $\chi(u)$, takes the form of a phase shift. If the phase-distortion function is compared to the contrast transfer function, which describes the periodic nature, or bands, of contrast corresponding to areas of good transmission and zero transmission, the contrast transfer function has maximum transfer of contrast when

the phase-distortion function has multiple odd values of $\pm\pi/2$ and zero contrast when the function has values of $\pm\pi$. In other words when the value of $\sin\chi(u)$ is equal to $\pm\pi/2$, $T(u)$ is maximized corresponding to bright contrast and when $\sin\chi(u)$ is equal to $\pm\pi$, $T(u)$ is minimized corresponding to dark contrast. $\chi(u)$ depends on the defocus of the beam, and is a complicated function. In short, to achieve maximum resolution and contrast, an optimum value for $\chi(u)$ and therefore an optimum value of defocus can be determined. This is called the Scherzer defocus. The maximum resolution of a TEM is determined using this value. It depends on the spherical aberration, C_s , and electron wavelength, λ ,

$$\Delta f_{Sch} = -1.2\sqrt{C_s\lambda}.$$

So it is important to know what this value is and to be able to obtain it, in order to maximize resolution in the HRTEM.

The interpretation of HRTEM images, however, is not as straightforward as one might expect. Complex interference patterns give rise to misleading images that are not directly representative of the sample. Aberrations in the lenses also complicate images. Therefore, many additional considerations must be taken into account when imaging with HRTEM that are not issues with normal TEM imaging.

HRTEM has proven very useful in analyzing the nanomaterials used in this research. Since the materials studied in this research are very small, the HRTEM provided essential details of the structure of these materials. Many times certain material structures are too small to reliably produce informative diffraction patterns. Therefore post-processed FFTs of HRTEM images, further discussed in chapter 4, provide details of the sample material. Without the resolution capability of the HRTEM for material and FFT analysis, much of this research would not have been possible.

2.1.2 Electron Diffraction

Diffraction is one of the most important and useful technique used in the TEM, and is the basis of modern crystallography. Diffraction patterns are extremely useful in determining a material's properties including its structure, orientation, lattice constants, grain boundaries and so on.

Electrons in the TEM are able to form diffraction patterns due to their wave nature. When interacting with a given crystalline material, electron waves scatter off of specific atomic planes in the material, according to Bragg's law.

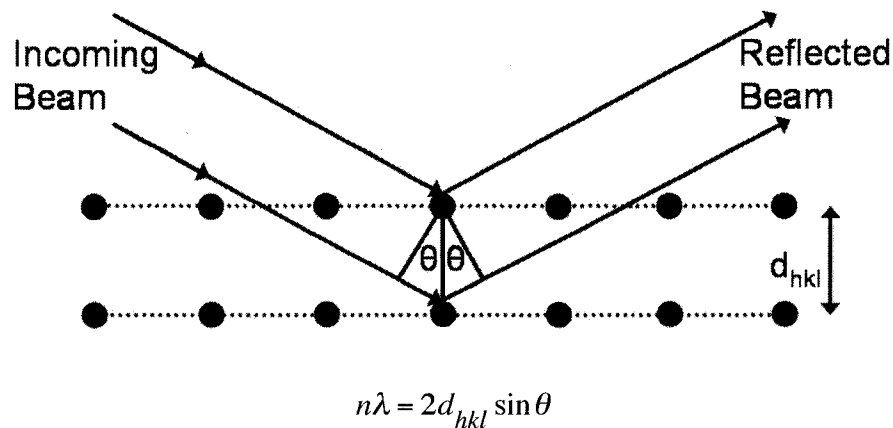


Figure 2.2. Illustration of Bragg's law. An incoming wave will interact with the material and if the angle is correct it will satisfy the Bragg condition and strongly reflect at the same angle as the incident beam. Image: B.W. Jacobs

In Bragg's law n is any integer, usually equal to 1, λ is the electron wavelength, d_{hkl} is the interplanar spacing in the crystal lattice, and θ is the Bragg angle. When a beam of electrons interacts with a crystalline material, and if the angle is correct, it will reflect strongly off the atomic planes at the same angle as the incident beam. This strong reflection results because at angles and interplanar spacing that satisfy Bragg's law,

constructive interference will occur. This correct combination of incident angle and interplanar spacing is called a Bragg condition and is the basis of diffraction.

For a crystalline material, the diffraction pattern, a collection of diffracted beams that meet the Bragg condition, will create a pattern of bright spots. With the exception of the center spot, which is the transmitted spot, each bright spot corresponds to specific atomic planes in the material. The location and relative brightness of each spot is a result of the crystal properties of the sample material. The information contained in the diffraction pattern represents the crystal structure in inverse space or reciprocal space. The spot pattern represents the atomic plane arrangement in real space. The distance between diffraction spots is measured in inverse meters and represents the spacing between the planes in real space. The diffraction pattern effectively represents the crystal structure in a way that is easier to analyze and quantify than real space images. Using diffraction techniques many properties of the crystal structure can be identified, such as orientation relationships, crystal type, and defects. For further information on reciprocal space see references 2 and 3. Diffraction patterns are formed with an aperture called the selected area diffraction aperture, which is used to select a certain area of interest in the material. The area selected is then projected to the viewing screen in reciprocal space.

Fast Fourier transforms are another tool useful for determining a material's crystallography. The information contained in a fast Fourier transform (FFT) is similar to the information contained in a diffraction pattern, but a FFT is a post-processed software technique. A diffraction pattern is purely physical, while a FFT is purely mathematical. After a high-resolution, atomic scale image has been taken, a FFT can be used to simulate a diffraction pattern, or determine the reciprocal space pattern of a real space image.

FFT's are excellent companions to diffraction patterns and augment diffraction data. FFT's are also indispensable when analyzing very small crystalline areas. Diffraction patterns are somewhat limited spatially, and sometimes diffraction spots from unwanted areas can appear. So if high quality, high-resolution TEM images can be obtained, FFT's do an excellent job in providing essential crystal data. The FFT is an excellent tool, but real diffraction patterns are far superior in the information they provide, so whenever possible, take a diffraction pattern.

Diffraction patterns and FFT's were a very important tool in this research. Without the use of diffraction patterns and FFT's, the crystallography of the GaN nanowires would have been extremely difficult if not impossible to solve. The small crystalline domains found in the nanowires were many times too small to use diffraction, so FFT's were ultimately heavily relied upon, but were backed up indirectly using real diffraction patterns.

2.1.3 Energy Dispersive X-Ray Spectroscopy

Energy dispersive x-ray spectroscopy (EDS) is a technique used in the TEM to determine the elemental composition of a given sample. Using the same high-energy electrons it uses to create images, electrons in the TEM cause electrons in core atomic orbitals of the sample material to be ejected. This causes an electron from a higher energy to drop into the "hole" left by the ejected electron. Since energy must be conserved, the electron that drops into the hole must release energy. This energy is equal to the difference between the ejected electron energy and the energy of the electron that dropped in energy to fill the hole. Energy is conserved through the emission of a photon.

The photon emitted will have a wavelength in the X-ray regime. The energy of the X-ray is specific to each element in the periodic table. The X-ray is detected and a computer plots a spectrum with peaks associated with each element present in the material. Using this technique one can very quickly and easily obtain the elemental makeup of a given material. EDS is generally used in conjunction with other techniques such as EELS to obtain a great deal of information about a given material.

This method is particularly useful when the composition of a material is not known. Instead of painstakingly solving diffraction patterns and comparing known diffraction patterns for material identification, EDS provides the user with valuable elemental information almost instantly. It is capable of estimating the elemental constituents of a material if the thickness and density is known. Small areas of only a few nanometers of material can also be analyzed since the TEM electron beam can be highly focused.

This technique has proved useful on several occasions. The stoichiometry of the GaN nanowires was initially called into question and EDS was one technique used to estimate the nanowire elemental constituents. Another occasion in particular was the discovery of gallium oxide (Ga_2O_3) nanowires, when gallium nitride nanowires were expected. In analyzing these nanowires, the structure looked somewhat different than what was usually observed for GaN nanowires. An EDS spectrum was taken, and in less than five minutes the structure was determined to contain gallium and oxygen in a 2:3 ratio. Therefore, taking an EDS spectrum on a given sample to analyze its structure is quick, easy, and usually highly beneficial.

2.1.4 Electron Energy Loss Spectroscopy

Electron energy loss spectroscopy (EELS) is a technique used to analyze the electronic structure of a given material in the TEM. Electrons in the TEM beam will undergo some inelastic scattering as a result of electron interactions with the sample material. These electrons will exit the material with a lower energy that is specific to the interaction within the sample. Electrons from the TEM beam can interact with the sample material electrons in several ways, including inner shell ionizations, plasmon excitations, phonon excitations, and energy band transitions. The plasmon excitations and inner shell ionizations are particularly important and provide information about the elemental composition, chemical bonding, valence and conduction band properties, and so on. Since these interactions are specific to the elements present in the material, quantitative information about the sample can be obtained using this technique.

The detection of electrons that are subjected to inelastic scattering in the sample material is done with magnetic prism located at the bottom of the microscope or with an in column omega filter, so named due to its close resemblance to the uppercase Greek letter Ω . Since electrons have a distribution of kinetic energies after passing through the sample relative to the incident beam, the energies can be segregated. Electrons with different kinetic energies can be therefore be detected with resolutions of around 1 eV⁴. The kinetic energy distribution of the scattered electrons is then plotted in a spectrum with peaks corresponding to scattered electrons with the same kinetic energy. Elemental mapping and EDS can be used in conjunction with EELS to obtain spatial mappings of specific elements within a sample.

An EELS spectrum can be difficult to obtain, because TEM beam stability and alignment can be finicky and thin samples are needed. However, with some patience and a stable beam, EELS spectra can provide a wealth of information about a sample. Usually the beam should be at the operating voltage for at least 8 hours for maximum stability before EELS is to be done.

EELS has proven particularly useful in the analysis of carbon onions. EELS is highly sensitive to the bond structure present in the carbon system and can easily distinguish between sp^2 and sp^3 hybridizations. When combined with Raman spectroscopy and XPS, both discussed later, EELS provided an excellent quantitative analysis of the sp^2 to sp^3 ratio. EELS also provided an independent verification of the presence of gallium and nitrogen in the GaN nanowires, as well as the lack of impurities such as oxygen.

2.2 Focused Ion Beam

A focused ion beam (FIB) system uses an ion beam, usually consisting of gallium ions, to create sample images. Gallium ions are accelerated and focused in electromagnetic lenses, just as in the scanning electron microscope (SEM), discussed next, and can produce images similar to those created in the SEM. Imaging with ions, however, can be very destructive to the sample. Therefore, a FIB is generally used for sample manipulation and preparation, due to its ion beam sputtering capability. In the sputtering process energetic Ga ions bombard the sample and eject atoms off the surface into a gas phase. In this way, patterns on the sample surface can be made. However, due to the inherent destructive nature of the ion beam, the dual beam FIB has been developed. Coupled with an electron beam, i.e. an SEM, a dual beam FIB can use the ion beam for sputtering and use the SEM for imaging. This minimizes damage imparted on the usually already delicate sample. An example of a dual beam FIB system is shown in figure 2.3.

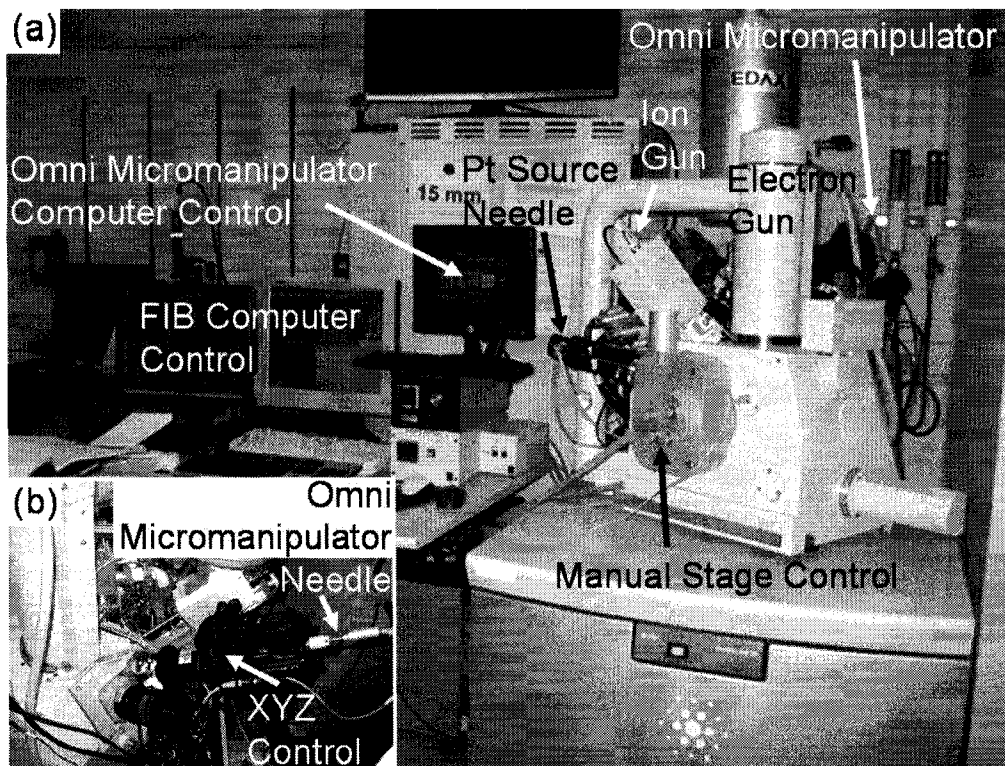


Figure 2.3. FEI Quanta 200 3D dual beam FIB with an integrated Omni Micromanipulator System at the Electron Microprobe Analysis Laboratory at University of Michigan. (a) The main components of a dual beam FIB are shown here. It is computer controlled. The electron gun is situated perpendicular to the sample as in a normal SEM. The ion gun is tilted 52° relative to the electron gun. The Pt source needle is next to the ion column. Manual stage control is on the front of the specimen chamber and is used in the cross-section preparation process. The micromanipulator is situated on the backside of the instrument. (b) A close up of the micromanipulator is shown here. The XYZ control is shown and consists of computer-controlled screws that move the needle. Image: B.W. Jacobs

The primary use of the FIB in this research has been TEM sample preparation. It was used to create cross-sections of GaN nanowires for HRTEM imaging. Using this cross-section technique the crystallography within the nanowires could be determined. Samples that have been prepared using the FIB have provided a wealth of information about the nanowires internal structure. Details of this structure will be discussed at length in chapter 4. Here the details of FIB sample preparation and implementation developed by the candidate for cross-section nanowire analysis are discussed.

When preparing a nanowire cross-section sample for HRTEM analysis, a dispersion of nanowires is first placed on a small silicon wafer. A 100-200 nm layer of

gold is thermally evaporated over the nanowires and silicon to initially protect the nanowires from ion beam damage in the FIB, figure 2.4(a). A layer of platinum is then deposited through reactive gas/ion Pt deposition; a 4-6 μm thick layer of Pt is sufficient. This layer provides the necessary protection for the nanowire through the entire cross-section preparation process. A few extra microns of Pt is added to the area directly over the nanowire to mark its location, see figure 2.4(b). After the necessary Pt metal is deposited, two trenches perpendicular to the nanowire and parallel to the Pt metal are sputtered, figure 2.4(c). These trenches are around 20-25 μm wide and 10 μm long on one side and 5 μm long on the other. The depth is 10 μm on either side, and tapers upward away from the deposited Pt. The sample is roughly milled at this time, to around 1 μm in thickness. After the trenches are complete, the sample is tilted and a “U-cut” around the bottom and sides of the sample is done, figure 2.4(d). This U-cut should penetrate through to the other side of the sample, and partially release the sample from the substrate. This is a very important step. The U-cut must extend completely through the base and sides of the sample. Small notches are left on each edge of the sample to hold it in place. A needle attached to a micromanipulator comes down and touches the top of the sample. The needle is superimposed in figure 2.4(d) to indicate where it would be placed directly prior to extraction. The needle is then welded to the Pt protection layer with additional Pt. The notches are sputtered away with the ion beam and the sample should be free, attached only to the needle. When sample extraction takes place, there should not be any material left attached to the substrate. The sample stage is then lowered using the manual stage control on the front of the microscope, and the sample extraction is complete. The sample can then be transferred to the TEM grid. A special

SEM sample holder is used so that the extracted cross-section sample can be transferred from the substrate to the TEM grid without the need to evacuate the specimen chamber. The sample should be brought to the TEM grid with extreme care. It is connected only to the needle at one delicate point, and any vibration or jarring could easily knock it loose resulting in a lost sample, see figure 2.4(e-f). When the sample just touches the side of the TEM grid it should be immediately welded and secured, figure 2.4(g). After welding the needle is cut with the ion beam and the sample is left welded to the TEM grid. Fine milling of the sample can now take place. The sample thickness must be thin enough to be transparent to the TEM electron beam. Therefore it must be less than 100 nm thick. It must be milled to the point where it seems that it cannot be milled further. It must be milled as absolutely thin as possible, see figure 2.4(h). A completed sample is shown in figure 2.4(i).

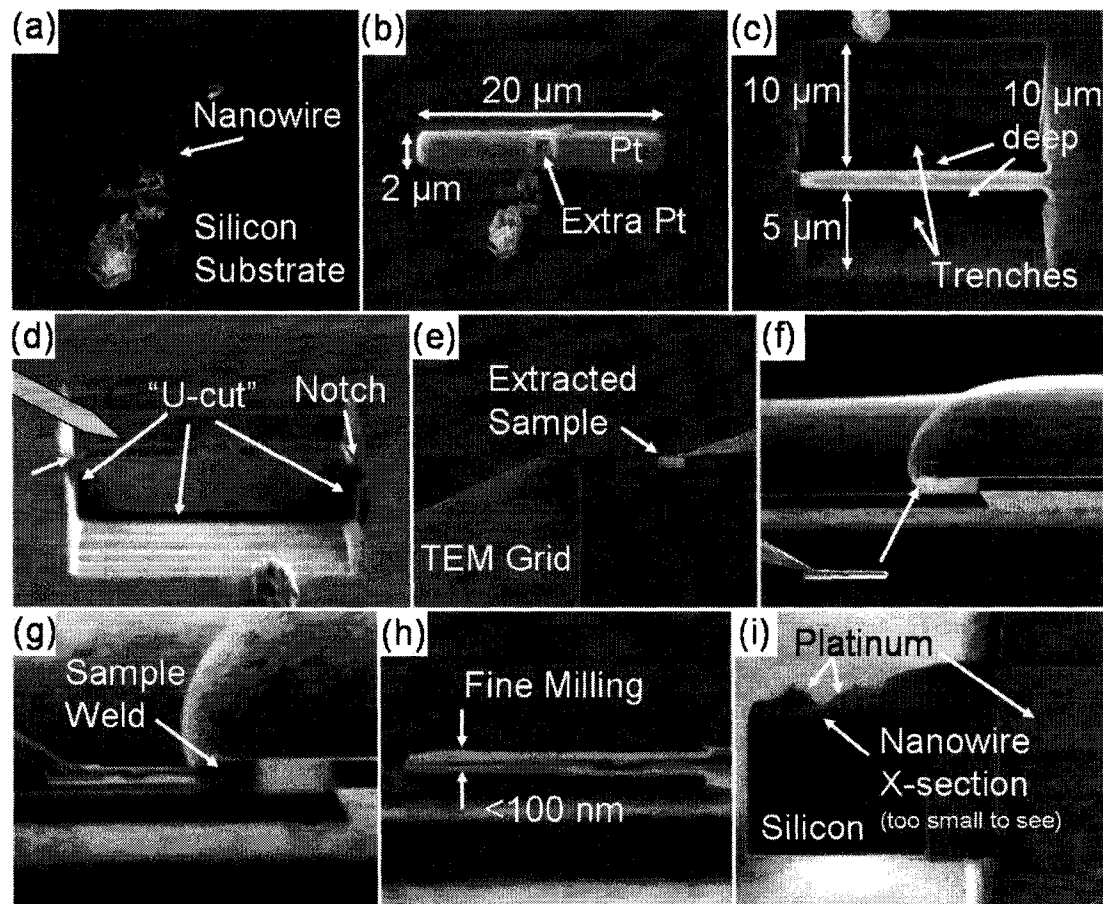


Figure 2.4. The TEM cross-section preparation method using a FIB. (a) Nanowire sample. (b) Pt deposition on top of the nanowire to protect it from ion beam damage. A small amount of extra Pt is deposited on top of the nanowire to mark its exact location. (c) Creation of the trenches on either side of the Pt, perpendicular to the nanowire. (d) The U-cut. Two notches on either side are left to hold the sample in place. The superimposed needle indicates where it should be welded on the cross-section. (e) The extracted sample. (f) The extracted sample as it nears the TEM grid. (g) The sample is welded to the TEM grid. (h) Fine milling of the cross-section. It should be thin enough to be transparent in a TEM electron beam, less than 100 nm. (i) Ion beam image of the final nanowire cross-section. Images: B.W. Jacobs

After fine milling is complete, the sample can be analyzed in the TEM. It is important to thoroughly weld the cross-section to the TEM grid so that it can withstand the process of taking it in and out of the TEM. Note the amount of Pt deposited on the right side of the cross-section in figure 2.4(i). Therefore, extra time and care must be taken when preparing these samples if quality high-resolution images are to be obtained.

The FIB allows for unique samples to be imaged in the TEM that would otherwise be nearly impossible due to size and thickness constraints. The FIB has traditionally been used in the semiconductor industry to image such structures as transistors and heterostructures to determine thin film thicknesses and to analyze interfaces and defects. The dual beam system has added further versatility to the FIB, which has increased in popularity due to the added SEM functionality and with the need to analyze new types of materials. The FIB has provided a truly unique twist on how materials analysis in this research has been conducted. It has helped uncover an interesting phenomenon in the GaN nanowires, which might not have been completely understood without the use of the FIB. The primary FIB used in this thesis research was a FEI Quanta 200 3D Dual Beam at the Electron Microbeam Analysis Laboratory at University of Michigan. These results will be discussed at length in chapter 4.

2.3 Scanning Electron Microscopy

Scanning electron microscopy is a very popular surface imaging technique. Using electrons for imaging, it is capable of high-resolution, topographical views of a sample. The electron beam in an SEM is produced via similar means as the TEM, by using a tungsten filament, LaB₆, or field emission tip. An anode accelerates the emitted electrons at a bias voltage between 1-50 kV depending on the instrument and user requirements. Although an SEM, like a TEM, uses electrons to image a sample, that is where the similarity ends.

After acceleration, electrons in an SEM are focused through a condenser lens and condenser aperture and an objective lens and objective aperture, see figure 2.5. However, unlike a TEM, where electrons pass through the sample and are diffracted, electrons are either backscattered or generate secondary electrons from the sample. The electromagnetic lenses used in the SEM are only used for incident beam manipulation, i.e. focusing and scanning the beam. The lenses in the SEM do not directly contribute to image formation in any way like the objective and intermediate lenses in the TEM.

The incident electron beam interacts with sample electrons and atomic nuclei, where the size of the interaction volume depends on the sample density, on target energy of the electron, and atomic number of the sample material. The material should be sufficiently conducting or SEM imaging would be difficult. An insulating material can be imaged in the SEM if a thin layer of conducting material, such as 20 nm of gold, is first deposited on the sample surface. SEMs that utilize a field emission gun, however, can image insulating samples even at low acceleration voltages.

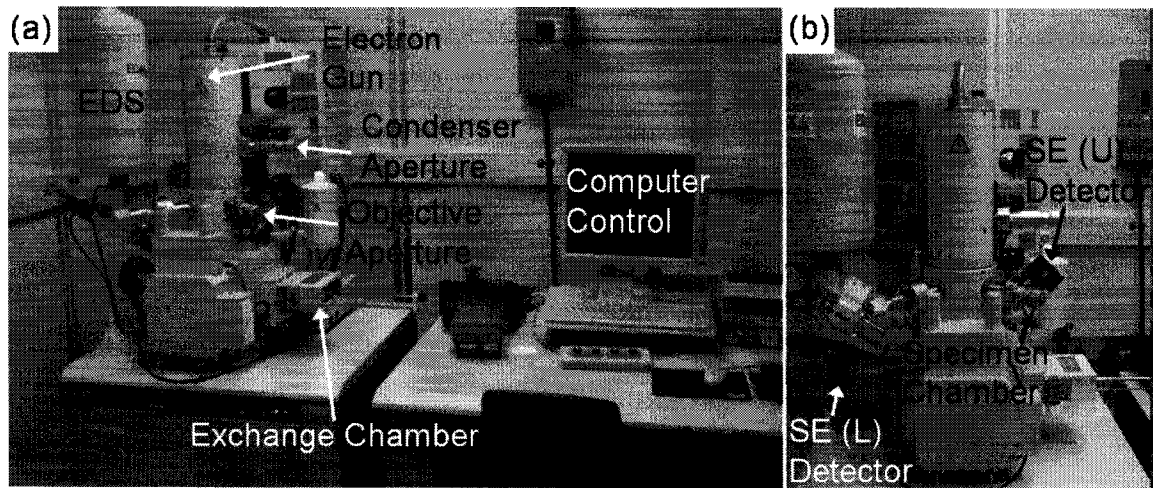


Figure 2.5. Hitachi S-4700II FESEM at the W. M. Keck Microfabrication Facility at Michigan State University. (a) The SEM is controlled via software. On the right is the control computer. The left highlights several components of the SEM. The electron gun is at the top and accelerates electrons downward through a series of electromagnetic lenses and apertures. The sample is located at the base of the instrument. When introducing a sample into the microscope it is first placed in an exchange chamber and then after rough pumping introduced into the specimen chamber shown in (b). (b) A close up image of the instrument shows the specimen chamber where imaging occurs and the lower and upper secondary electron detectors. Image: B.W. Jacobs

In forming an image, the SEM electron beam is rastered across the sample, and a detector collects secondary or backscattered electrons emitted from the sample. This detector consists of a scintillator, which converts electrons into photons. The electrons are attracted to the scintillator using a Faraday cage that is tuned to a certain voltage potential and is also used to mitigate the scintillator/incident beam interactions. After the scintillator converts an electron to a photon, a photomultiplier amplifies the signal and converts the photon into an electrical signal, which is displayed on a CRT or digital imaging device.

The two main types of electron scattering in the SEM, backscattered and secondary, can be used to determine different properties in the sample. When viewing the secondary electron image, areas of dark and bright contrast indicate edges or points on the sample. This contrast variation is a result of the incident electron beam interaction with the sample. If a sample is flat, the teardrop shaped volume of interaction restricts

the number of secondary electrons emitted. However, if an edge or point is being imaged, secondary electrons can escape the sample volume much easier since the volume of interaction is smaller, see figure 2.6. Therefore, a larger number of secondary electrons are collected, creating an area of bright contrast.

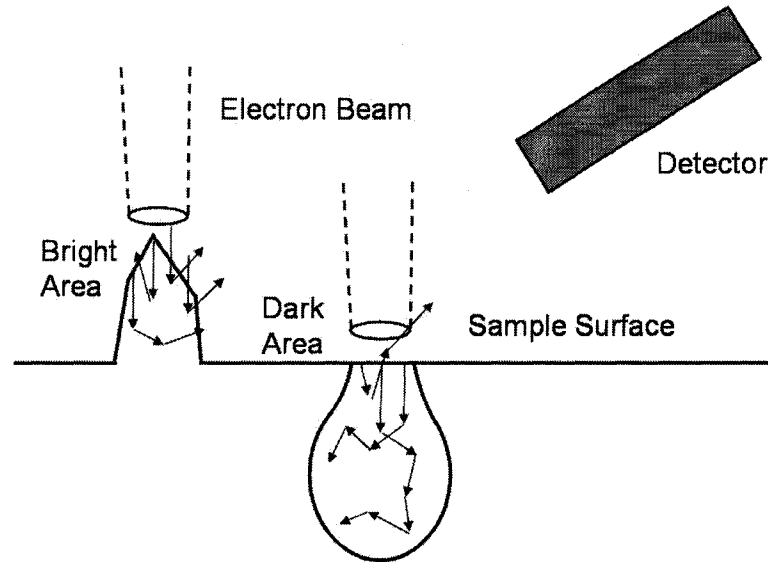


Figure 2.6. Electron beam/sample interaction in the SEM. Electrons from the beam interact with the sample in a teardrop shaped volume. Variations in the surface topology cause thin points and edges to appear bright because electrons that enter this area can be scattered out more easily resulting in a higher number of detected electrons from those areas, and therefore a brighter spot. Image: B.W. Jacobs

When viewing the backscattered electron image, areas of dark and bright contrast indicate different elements within the sample. A backscattered image is formed through the different interaction characteristics of the incident electron beam with the elemental constituents in the sample. For example, an electron will more effectively scatter off an element with a high atomic number, such as gold, and appear as a bright area in the image, as opposed to a lighter element, such as aluminum, which will appear darker relative to gold.

Backscattered electrons can also be used to form diffraction patterns. For crystalline or polycrystalline materials, electron backscatter diffraction (EBSD) can determine crystal orientation, be used in defect analysis, crystalline phase determination and so on. An EBSD image is formed by tilting a sample to a high angle, $\sim 70^\circ$ relative to the electron beam. The beam will diffract off the sample with varying intensity depending on the orientation of the crystal. The beam will diffract strongly when a Bragg condition is met, as is the case with electron diffraction in the TEM, and weakly when the condition is not met. EBSD can also be coupled with EDS, resulting in a powerful tool for materials characterization.

The SEM has been very useful in characterizing materials and devices used in this research. Located in the W. M. Keck Microfabrication Facility, the Hitachi S-4700II field emission SEM was the primary SEM used in this research. It was used to analyze features of fabricated GaN nanowire devices to assess fabrication quality. The SEM was also essential in materials characterization, including identifying nanowire nucleation sites, surface features on the sides of nanowires, and helped identify the triangular and hexagonal cross-section shape of many nanowires. These images resulted in many important findings and new information, making the SEM a very important tool in this research.

2.4 Microfabrication Process

Microfabrication encompasses a wide range of techniques for creating devices and systems on a small scale. Most of these techniques are geared toward the fabrication of electronics, such as microprocessors and optical devices. However, in recent years the microfabrication process has lent itself to the creation of a wide variety of mechanical devices. These devices include, temperature, pressure and acceleration sensors, actuators and inkjet nozzles for printers. The art of microfabrication is rooted deep in the semiconductor industry and has become highly developed and precise process through years of research and development. All devices were fabricated at the W. M. Keck Microfabrication Facility at Michigan State University, which is a class 100/1000 clean room facility.

2.4.1 Photolithography

Photolithography is by far the most common microfabrication process and is used almost exclusively by chip manufacturing companies to fabricate intricate electronic devices. These devices are usually created using silicon. Since the invention of the integrated circuit in the early 1960's, silicon has dominated as the material of choice for nearly all such devices through the present era. Photolithography, along with integrated circuits, has grown in complexity many times over. The integrated circuit, comprised of many individual on/off switches (transistors) has shrunk ever smaller as the desire for faster and faster devices increases with each passing year. Making transistors smaller increases the speed at which it can change state, i.e. how fast it can turn from off to on

and vice versa. A detailed discussion on the operation of a transistor will be discussed in chapter 5.

Photolithography uses light to expose specific areas of a special light sensitive material, called photoresist, which is on the surface of a substrate, usually a silicon wafer. These exposed areas then break down and become soluble in a developer and wash away leaving the unexposed photoresist remaining on the surface. Using this method, very intricate patterns can be made. Photolithography is done using a glass plate, called a mask, with a pattern of clear windows and opaque areas consisting of the desired pattern, see figure 2.7(b). This pattern is then transferred to the photoresist, exposing certain areas with UV light, figure 2.7(a), through the clear window on the mask and blocking certain areas with the opaque areas⁵. This is basically the same process that major semiconductor manufacturers use to produce highly complex integrated circuits.

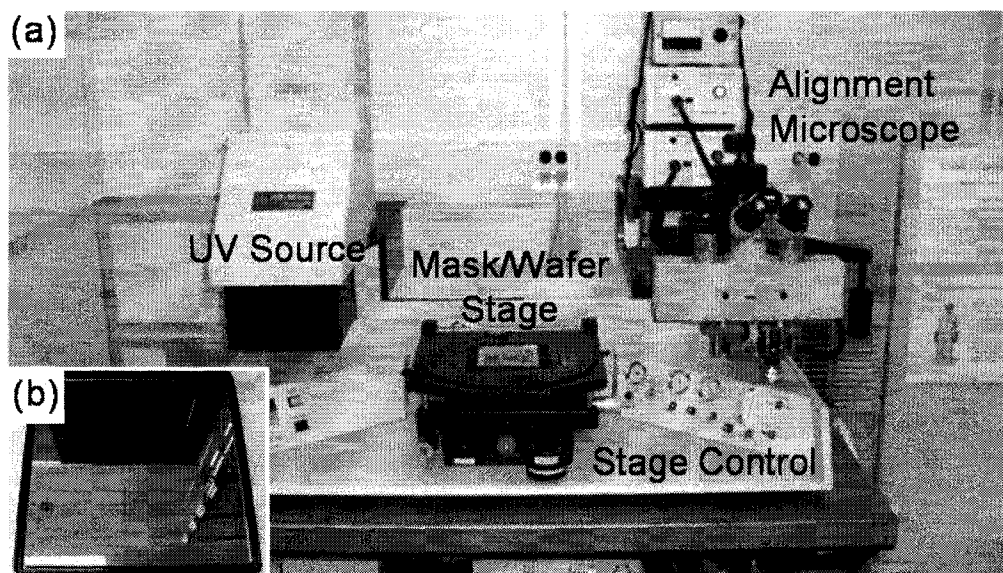


Figure 2.7. AB-M mask aligner at the W. M. Keck Microfabrication Facility at Michigan State University. (a) The instrument consists of a UV source that moves on rails to expose the photoresist on a wafer through a mask, located in the center of the instrument. An optical microscope on the right is used to align other masks used for multiple exposures for more complex features. (b) An example of a glass/chrome mask used in this research. Images: B.W. Jacobs

In the basic photolithography process used in this research, a bare silicon wafer is used as the substrate, see figure 2.8. A layer of silicon dioxide is grown on the surface and a layer of photoresist is spun on at 4000 RPM for maximum uniformity and consistent thickness. The photoresist is exposed to UV light through a mask with predefined windows, transferring the mask pattern to the photoresist. The exposed photoresist breaks down and can be removed with a developer. A metal can then be deposited and the areas with remaining photoresist can be removed along with the metal that was on top of those areas leaving the desired pattern.

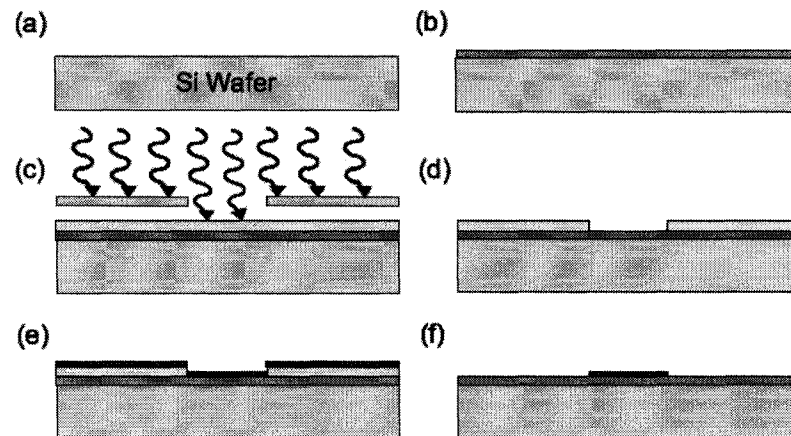


Figure 2.8. Basic photolithography process. (a) A bare silicon wafer. (b) Silicon dioxide is grown on the surface and is used as an insulating layer. (c) Photoresist is spun on the wafer and it is exposed to UV light through a mask. (d) The developer removes the exposed resist. (e) A metal layer is deposited. (f) The remaining unexposed resist is taken off along with the metal layer that was on top of it, leaving the desired pattern. Images: B.W. Jacobs

As silicon based integrated circuits continue to shrink, however, photolithography as well as silicon itself, is reaching a limit. The minimum feature sizes of patterns created with photolithography are highly dependent on the wavelength of incident light and the numerical aperture according to:

$$F = k \frac{\lambda}{N_A};$$

where F is the feature size in nanometers, k is process related and is approximately equal to 0.5, λ is the wavelength of the incident light and N_A is the numerical aperture. This is somewhat similar to the situation in the TEM, where resolving power depends on the wavelength of the incident beam. In order to achieve smaller and smaller feature sizes, semiconductor manufacturers have been reducing the wavelength of light used in photolithography. The use of shorter and shorter wavelengths, however, is proving to be problematic and expensive due to the light sources needed. The introduction of immersion lithography has been used in reducing feature sizes. Since the feature size is also dependent on the numerical aperture, which is dependent on the refraction index of the medium in which the lens is working, an increase in the index of refraction reduces the feature size. This development has helped photolithography extend its reign in integrated circuit fabrication.

When producing patterns with photolithography for creating devices in this research, it is only used to deposit metal on a substrate. There are several considerations to keep in mind when carrying out this process. Thermal evaporation is usually used to deposit metal in predefined patterns corresponding to the mask pattern. Evaporation of metal is done in high vacuum using a small filament consisting of a metal with a high melting point, molybdenum or tantalum for example, called a boat, see figure 2.9. The metal to be evaporated is placed on the boat and a high current is passed through heating the boat to a high enough temperature to evaporate the metal. Usually a thin film of titanium is deposited first as an adhesion layer and gold is then subsequently evaporated.

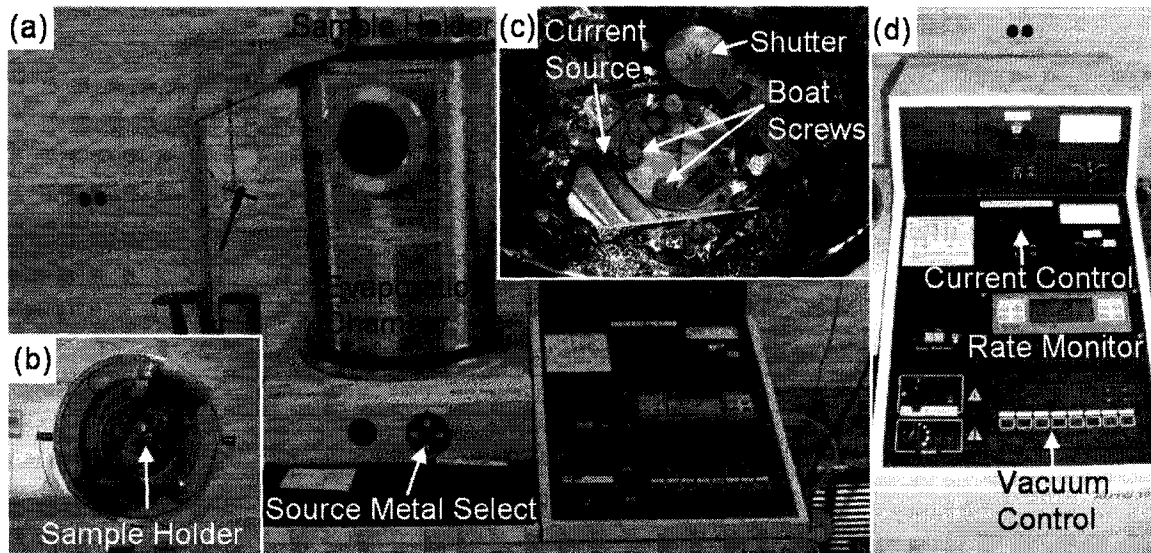


Figure 2.9. Edwards Auto 306 Thermal Evaporator at the W. M. Keck Microfabrication Facility at Michigan State University. (a) The cylindrical evaporation chamber is shown here. The sample holder is at the top of the chamber and is held upside down. The metal is at the bottom and evaporated metal drifts upward to the sample. (b) The sample holder is flipped up for easy access for sample mounting. (c) The evaporation mechanism is at the bottom of the chamber. The boat is screwed down and high current is passed through it to heat the metal. A detector is used to monitor the evaporation rate. A shutter is used to block the substrate from the source to stop metal deposition. (d) The evaporator controls. The current can be increased and decreased with a knob. The digital readouts of the rate monitor and vacuum control provide details of the evaporation conditions. Images: B.W. Jacobs

In order for the thermal evaporation process to be successful and to produce clean, sharp features, a dual resist layer is required, see figure 2.10. This method is used so that an undercut separates the unwanted metal layer on top of the resist with the layer that is to remain on the substrate. The undercut is created a bottom resist layer that develops faster than the top layer. This undercut provides added separation resulting in much cleaner, sharper features. The dual resist stack can be achieved in a few different ways. A special resist that inherently develops faster than the top resist is available, but is expensive. A tri-layer stack is also possible and was used for device fabrication in this research. First a layer of normal photoresist is deposited and exposed to light without a mask, i.e. the entire substrate and photoresist layer is exposed. Then a thin layer of aluminum, roughly 10 nm, is thermally evaporated. Aluminum is used because the

developer can etch it. A top layer of photoresist is deposited and the substrate is exposed to light under the mask as described above. Since the bottom layer is exposed to light twice it will develop quicker than the top layer, and the aluminum acts as a buffer to prevent mixing of the top and bottom layers of photoresist. This process has proven successful, is a much cheaper alternative to the special undercut photoresists and a large undercut can be obtained. After developing, the titanium/gold metal stack can be thermally evaporated and the remaining resist and aluminum can be removed leaving the desired pattern.

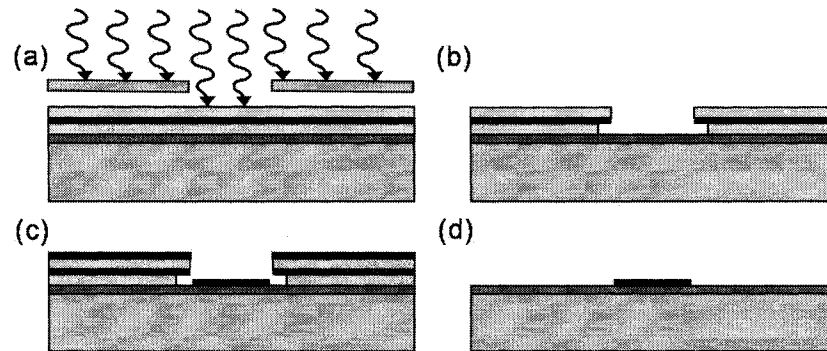


Figure 2.10. Tri-layer photoresist stack. (a) After the first layer has been deposited and exposed, a 10 nm layer of Al is thermally evaporated. The second layer of resist is deposited and the stack is exposed under a mask. (b) After developing an undercut should be prevalent. (c) Metal is thermally evaporated with a large separation between the layer of metal on top of the resist stack and the layer on the bare substrate. (d) The top layers are removed and clean, sharp features are left. Images: B.W. Jacobs

Reproducible patterns made with photolithography techniques are essential for making devices that function properly. A strict regiment of process steps should be followed to produce successful results. Since lithography plays such a large role in this research a process tailored by an individual should always be followed so that the yield is maximized and the time needed to produce working circuits is minimized.

Photolithography was used to pattern larger areas for placing characterization probes.

Smaller more intricate features were patterned with electron beam lithography, discussed next.

2.4.2 Electron Beam Lithography

Instead of using light for exposing photoresist in creating patterns on a substrate, electron beam lithography uses highly focused electrons. Electron beam lithography (EBL) is usually done in a SEM, where a highly focused beam of electrons is available, see figure 2.11. This process is similar to photolithography in that it uses electron beam sensitive resist (e-beam resist) to produce pre-defined patterns. The EBL process is mask-less, however. It uses the SEM beam deflectors to manipulate the beam position and the beam blanker to expose only certain areas of the e-beam resist using a computer control system. The e-beam resist is not exposed all at once, like in the photolithography system, where a wide area of parallel light beams is used to expose the masked surface. The small beam probe meticulously “writes” out the pattern sequentially, point by point. After the beam has written the desired pattern, a developer is used to wash away the exposed areas, just as in the photolithography process.

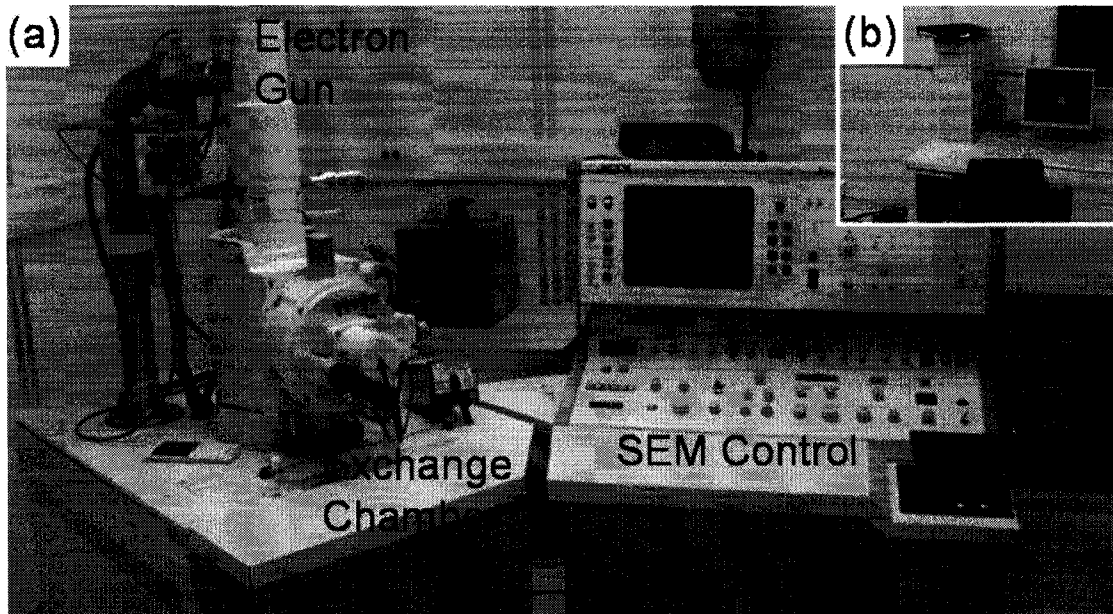


Figure 2.11. JEOL 840A SEM with integrated EBL capability at the W. M. Keck Microfabrication Facility at Michigan State University. (a) An SEM with a tungsten filament is used for EBL. (b) A computer that is integrated into the SEM control system and is used to manipulate the beam according to a pre-defined pattern designed using a CAD program. Images: B.W. Jacobs

There are several factors in EBL one must consider to develop consistent, reproducible results. First the ability to produce sharp, small feature sizes depends on the electron beam parameters and how much the electron radiation the e-beam resist is exposed to. In exposing a sample the round electron beam essentially flashes the resist one small spot at a time, see figure 2.12. It exposes one round area for a certain amount of time, called the dwell time, then moves a set distance, called the point spacing. After writing one line, the beam then moves a set distance to the next line, called the line spacing, and continues this way in a raster pattern. The SEM electron beam current plays a very important role in the exposure process and is used to calculate the dose a sample receives. These parameters: dwell time, point spacing, line spacing, beam current and the dose, are all essential considerations for obtaining successful results. They should be used consistently after a successful combination has been found so that device yield is maximized.

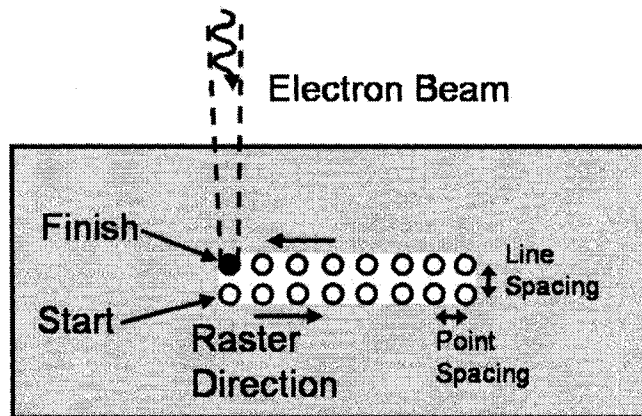


Figure 2.12. Illustration of the electron beam lithography method. The beam flashes the sample at a point, moves a small distance flashes it again, and continues this way in a raster pattern. The spacing between the flashes can be defined in the point spacing and line spacing. Image: B.W. Jacobs

EBL has several advantages when compared to photolithography. Since the electron beam probe in the SEM is highly focused and small, just a few nanometers in diameter, very small feature sizes on the order of 10 nm or less are possible⁶. Second, EBL is mask-less. Therefore, custom circuit designs can be created and many variations can be made with little or no extra cost for fabrication. This makes EBL invaluable for academic and research laboratories.

EBL has several disadvantages, however. Feature size limitations due to electron backscatter and secondary electron emissions, the basis of SEM image formation as discussed in section 2.3, from the substrate causes a proximity effect that exposes additional resist. This same phenomenon limits the ultimate feature sizes by causing patterns that are close together to be affected by additional electron exposure when the adjacent pattern is being written. The electromagnetic lenses are also a source of problems in EBL. As previously mentioned these lenses are far from perfect and small variations in their magnetic field create inconsistencies across multiple exposed samples. The low throughput is the main reason why the semiconductor industry has not adopted

EBL in mass production of integrated circuits. Integrated circuits need an extraordinarily high level of consistency, reproducibility and speed in fabrication.

EBL is one of the primary tools used in this research. All of the GaN nanowire devices studied in this thesis research have been fabricated with EBL, with a JEOL 840A SEM located in the W.M. Keck Microfabrication Laboratory at Michigan State University. The mask-less system has made it an invaluable tool for nanowire devices because nanowires are placed on the substrate in random locations. Because a custom pattern can be created with EBL each and every time a new circuit is to be made, it is an excellent tool for fabricating working devices.

2.5 Device Characterization Techniques

Characterizing devices that incorporate nanoscale materials pose significant challenges. Many properties of such a device are much different than traditional macroscopic devices. These properties include fundamental differences in device physics due to reduced dimensionality components, such as ballistic transport, carrier confinement, and other quantum mechanical effects. Devices that incorporate these reduced dimensionality components usually operate at lower currents and voltages and can operate at higher frequencies. So the need for sensitive, low noise measurement instruments is essential for achieving accurate and meaningful results.

Probe and contact coupling to these nanoscale materials is an important research issue and must also be taken into account⁷. For example, when a macroscopic, three-dimensional probe contacts a one-dimensional carbon nanotube or nanowire, the junction characteristics between the nanotube and nanowire are fundamentally different than in a planar system, such is the case in current transistors. Electron transport through a macroscopic contact to a nanotube or nanowire is also an issue since the available electron states in the macroscopic contact is different than in the nanoscopic nanotube or nanowire. Instrument developers, as well as researchers who seek high-quality, accurate and meaningful measurements of test devices, should keep these issues in mind when testing devices.

2.5.1 Two-Point Probe

Several properties of a device can be measured using two probes. By applying a voltage across two probes in a device and measuring the current, or by passing a current

through two probes in a device and measuring the voltage, a resistance can be obtained. Using this technique several important properties of a device can be measured. Current-voltage (I-V) measurements are probably the most common two-point probe measurement. Much information about the device properties can be obtained from an I-V measurement, and it is one of the main tests used to characterize a transistor. If a voltage across the transistor gate is also varied, the I-V measure will change according to the voltage on the gate. Therefore, the gate voltage influence on the amount of transistor current allowed to pass can be quantitatively determined. Two-point probe investigations using a low noise Keithley 4200-SCS at Keithley Instruments in Cleveland, Ohio, characterized several GaN nanowire-based transistors confirming gate modulation and their ability to carry a large current density. In addition to I-V, capacitance-voltage (C-V) measurements also yield important junction capacitance information as a function of voltage applied.

2.5.2 Four-Point Probe

In determining the resistance of a device element, the four-point probe technique produces more accurate results when compared to the two-point probe technique. As the name implies the four-point probe technique uses four probes in taking measurements. The two outside probes source a known current, while the two inside probes measure a voltage, as shown in figure 2.13. The voltage probes carry very little current so only a voltage drop is measured. Since a known current is passing through the sample, the measured voltage can be divided by the current and an accurate resistance calculated. By

using the voltage probes to measure the only the voltage drop across the sample and not the current, the resistance of the contacts is omitted.

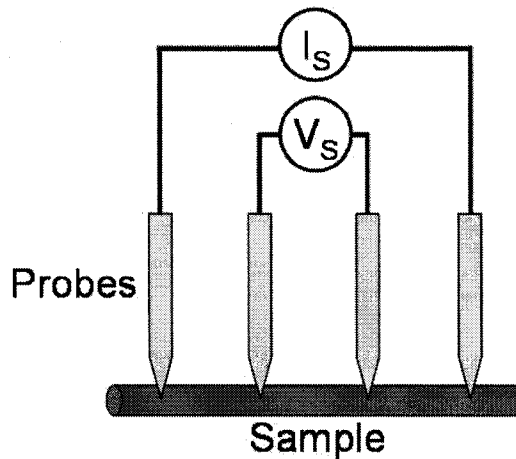


Figure 2.13. The four-point probe resistance measurement technique. This technique uses four probes that are placed on the sample. The two outside probes pass a known current through the sample. The two inside probes measure a voltage. Very little current passes through the voltage probes. By dividing the known current into the measured voltage, an accurate resistance of the sample can be measured, with the contact resistances of the probes omitted. Image: B.W. Jacobs

Four-point probe is a powerful technique when the resistance of just the sample is required. However, several issues involving probe coupling to the sample arise due to the small size of the samples used in this thesis research. As mentioned above, if a macroscopic probe contacts a nanoscopic element, the change in dimensionality will introduce added effects. In order to address this issue, instrument manufacturers have designed probes with tip sizes on the nanoscale. This reduces the effects of the probes, making them less invasive, so a more accurate four-point probe measurement can be taken.

The opportunity to use a state-of-the-art Zyvex KZ-100 nanomanipulation system, as Zyvex Co. in Richardson, Texas, that incorporated these nanoscale probes connected to a low-noise Keithley 4200-SCS was afforded to this research. Resistance

measurements of a GaN nanowire using this nanomanipulation system were taken with real-time visual inspection with an SEM. Intriguing phenomena was observed, which would not have been possible with traditional probing instruments. These results will be discussed at length in chapter 4.

The two and four-point probe techniques represent very important device characterization methods essential for producing real world devices and systems. New and custom instruments designed to accurately and precisely measure nanoscale devices and systems must be utilized to obtain accurate measurements.

2.6 Scanning Probe Microscopy

The scanning probe microscope is a powerful ultra-high-resolution surface characterization technique that is highly versatile. The scanning probe microscope (SPM) encompasses several different techniques designed to obtain different characteristics of a given material. The first SPM was the scanning tunneling microscope invented in 1972 by Russell Young and colleagues at the National Institute of Standards and Technology (NIST), and further developed by Gerd Binnig and Heinrich Rohrer at the IBM Zurich Research Laboratory in Switzerland. The scanning tunneling microscope (STM) is used to detect weak electrical currents in a material and will be discussed later in this chapter. Binnig and Rohrer's STM won them the Nobel Prize in Physics in 1986. Since then a wide variety of SPMs have been invented and highly creative ways of using them have revolutionized the way materials are imaged and manipulated.

2.6.1 Atomic Force Microscopy

The atomic force microscope (AFM) is probably the most common form of SPM. The AFM is a surface scanning technique capable of creating a three-dimensional image of a sample surface with atomic resolution in the z-direction, or height. In creating an image, the AFM uses a sharp probe tip at the end of a cantilever that is rastered across the sample surface in the x and y-direction. The probe tip is raised and lowered following the height variations of the sample surface, however it does not actually touch the sample surface. The tip-sample interaction forces can be of several different types, including electrostatic, Van der Waals, magnetic, and so on. A laser that is focused on the end of the cantilever above the tip is reflected to a photodiode, and changes in sample height

deflect the laser to different angles, see figure 2.14. The photodiode can detect the variations in the location of the laser resulting from different tip positions. The photodiode signal is sent to the computer so that a digital image of the sample surface can be constructed.

The lateral resolution, or resolution in the x and y-directions, however, is highly dependent on the size of the tip. A smaller tip radius yields better lateral resolution. The AFM is not generally used for high-resolution imaging in the x and y-directions. Recent work, however, using certain molecules⁸ or carbon nanotubes⁹ as tips, has drastically increased the lateral resolution of the AFM, and atomic scale imaging has been achieved.

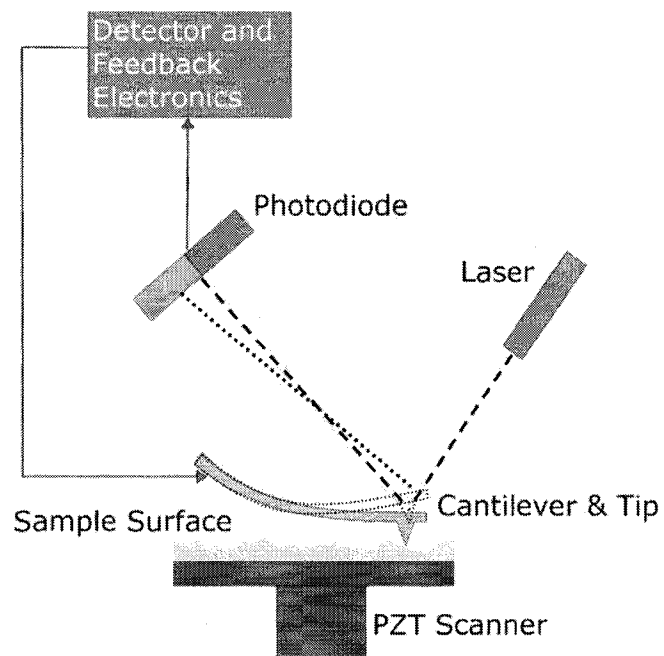


Figure 2.14. Diagram of basic AFM operation. The cantilever and tip are rastered along the sample surface. The variation in sample topology is detected by a reflected laser/photodiode system. The signal from the photodiode is then sent to the computer for digital image construction.

Two basic modes of AFM are used for sample analysis, contact and tapping.

Contact mode uses a cantilever with a known spring constant. It rasters across a sample

surface and detects variation in height. The cantilever is deflected when a change in height is encountered, resulting in a deflection of the reflected laser, which is detected by the photodiode. Height is also controlled via a feedback loop, which is an essential element in all modalities of the SPM. Cantilevers with several different spring constants are available. Certain cantilevers tend to work better on certain surfaces than others. The cantilever is rastered across the surface and the cantilever is deflected at variations on the surface according to Hooke's law, $F = -kx$, where k is the spring constant of the cantilever and x is the distance of deflection. Tapping mode uses a cantilever that oscillates up and down at a high frequency, usually at few 100 kHz, or close to the resonance frequency of the cantilever. As the cantilever is rastered across the sample it taps along the surface detecting variations in sample height.

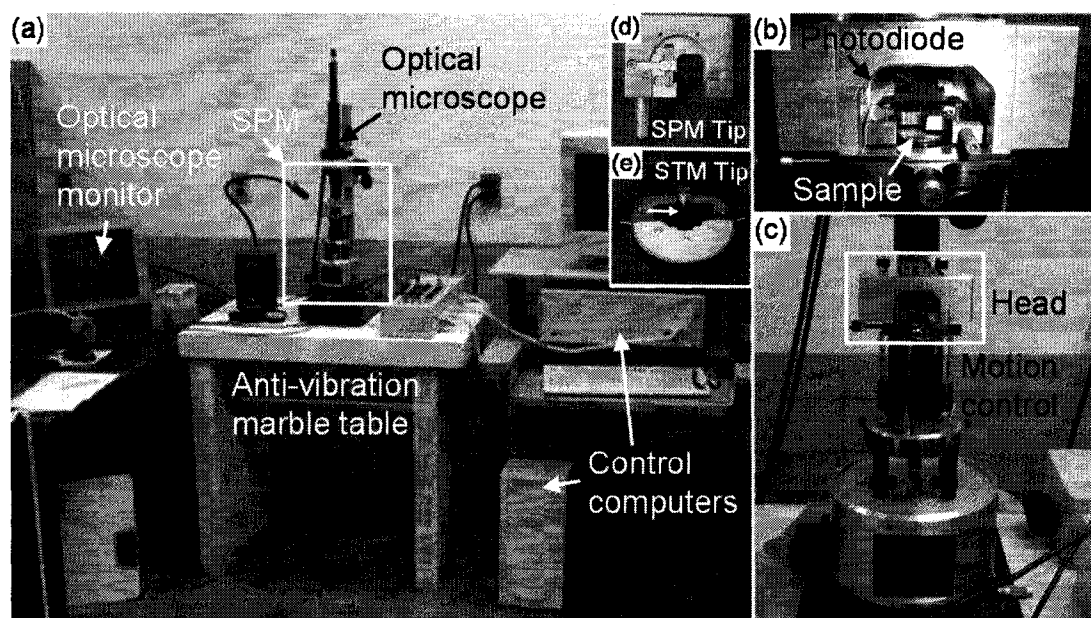


Figure 2.15. Veeco Instruments Nanoprobe III-A Multimode SPM at the Electronic and Biological Nanostructures Laboratory at Michigan State University. (a) This image shows an entire SPM setup. The SPM sits on top of several anti-vibration surfaces. An optical microscope is used to focus the sample surface and roughly focus the laser beam on the tip. The SPM is controlled via computer. (b) The head contains the laser, photodiode and provides the electrical connection to the tip. (c) A close up of the microscope shows the piezoelectric motion control and the head. (d) An AFM tip holder. (e) STM tip holder. Images: B.W. Jacobs

2.6.2 Scanning Tunneling Microscopy

The scanning tunneling microscope is used for imaging atomic scale features in electrically conducting samples. The conducting tip, usually platinum iridium, is atomically sharp, only one atom in diameter, providing an extremely small probe size. Due to this small probe, the STM is one of the highest resolution microscopes available. Similar to AFM, the STM tip rasters across the sample to form an image. The tip is brought close to the sample surface and an electric field is applied across the sample, see figure 2.16. Electrons are then emitted from the tip, tunnel through the gap between the tip and sample surface and enter the sample.

Variations in tunneling current through the sample are measured and depend on electron density within the sample. For example, tunneling current will be reduced when the tip is near an atom and is increased in between atoms. The sample can be imaged keeping either the current or height constant through the use of the feedback loop. Tunneling current also depends on the square of the distance from the sample surface making this an extremely sensitive technique.

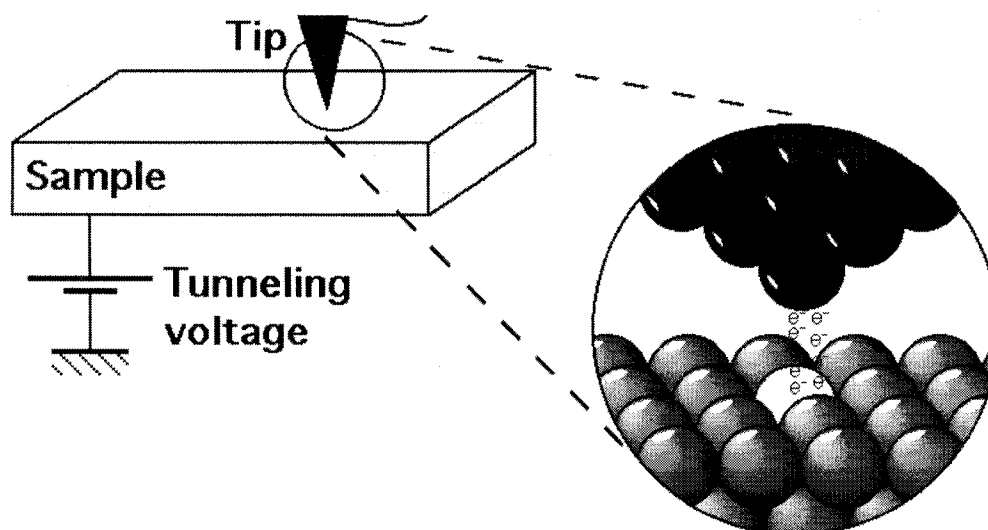


Figure 2.16. STM operation. A metal tip is brought into close proximity to the sample surface. A tunneling voltage is applied, creating an electric field across the sample, and electrons tunnel out of the tip into the sample. The amount of tunneling current will depend on the variations in the electron density in the sample, i.e. the tunneling current over an atom will be different than the tunneling current between atoms. Image: adapted from original image, Michael Schmid, TU Wien.

The SPM has been used to image nanoscale features of several types of nanomaterials used in this research, including carbon nanotubes, carbon onions, GaN nanowires and GaN nanowire growth matrix. All SPM investigations have been done with a Veeco Instruments Multimode Nanoscope IIIa located at the Electronic and Biological Nanostructures Laboratory at Michigan State University. It provides surface data in great detail and augments other material characterization instruments such as the TEM and SEM. Due to the extreme resolution in height, much information regarding the surfaces of nanomaterials can be uncovered.

2.7 Raman Spectroscopy

Raman spectroscopy is used to study the molecular composition of solid samples. It uses a beam of laser light, usually in the visible regime, to induce vibrations, or phonons, in a sample. These phonons are material specific and depend on atomic mass, bond order, molecular constituents, molecular geometry, and hydrogen bonding.

When the photons from the laser interact with electrons surrounding atomic nuclei of a sample material, photons are usually elastically scattered. This means they will have the same energy and wavelength before and after the interaction. This is called Rayleigh scattering, as shown in figure 2.17. In rare instances the photons will be scattered through an inelastic process and lose some energy to the material. This process can happen in one of two primary ways: Stokes scattering and anti-Stokes scattering¹⁰. In Stokes scattering an electron will absorb some energy from a photon and go from the vibrational ground state to a higher virtual energy state. The electron will reduce in energy and fall back into a vibrational state higher than the ground state. The energy that is transferred to the electron is equal to the difference in energy of the incident beam and the scattered beam of laser light. This loss in energy will cause the scattered photon to have a longer wavelength than the incident photon. This change in wavelength can be detected, and is referred to as the Raman shift, measured in inverse centimeters.

Anti-Stokes scattering is a very similar process. In anti-Stokes scattering an electron that is already in an excited vibrational energy state will absorb some energy from a photon and go from its excited state to a higher virtual energy state. The electron will reduce in energy and fall back below its initial excited state to the ground state. This process will give the photon more energy and shorten its wavelength. The magnitude of

the change in photon energy for both Stokes and anti-Stokes scattering is the same but has opposite signs. However, at room temperature anti-Stokes scattering is much less frequent. Electrons at room temperature are not often at an excited vibrational energy state above the ground state, so anti-Stokes scattering does not usually significantly contribute to a Raman spectrum. Anti-Stokes scattering can be a measure for how materials respond to temperature.

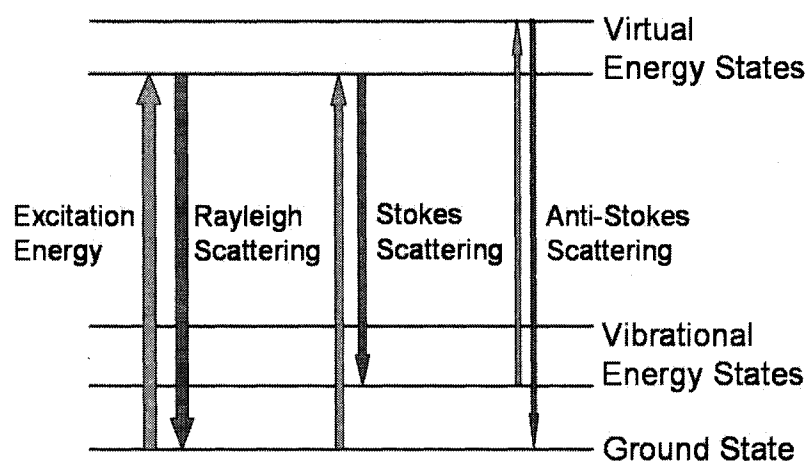


Figure 2.17. Illustration of the basic theory of Raman scattering. In each case a photon causes electrons to enter a virtual energy state. The electron will then drop in energy either returning to the ground state or entering a higher vibrational energy state. Rayleigh scattering is the most common form of scattering and is caused by inelastic scattering. Stokes scattering is more common than anti-Stokes scattering. Image: B.W. Jacobs

Most materials have specific phonon modes and therefore have specific, measurable Raman shifts. Raman spectroscopy is an excellent tool for analyzing organic materials, such as carbon, and has been extensively used in this research for analyzing the different allotropes of carbon, such as carbon nanotubes and carbon onions. Figure 2.18 shows a typical micro Raman instrument. All Raman investigations were done using this instrument, the Kaiser Optical micro Raman Spectrograph at the W.M. Keck

Microfabrication Facility at Michigan State University. It uses a frequency doubled YAG laser with a wavelength of 532 nm.

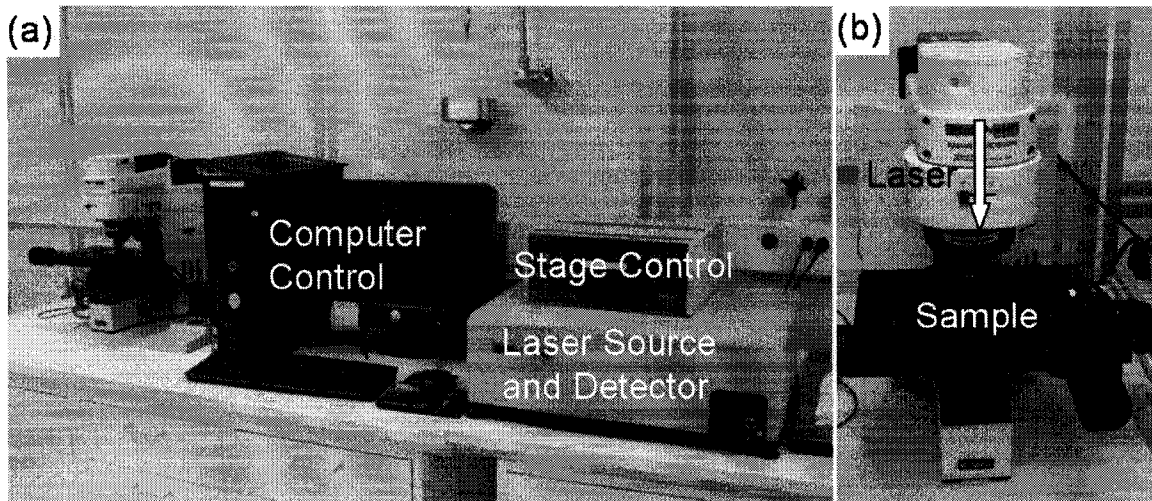


Figure 2.18. Kaiser Instruments micro Raman Spectrograph at the W. M. Keck Microfabrication Facility at Michigan State University. (a) The instrument consists of a mechanical stage control, laser source and detector, and a computer used for analyzing data. (b) The laser used for exciting materials is focused through a microscope. This allows for very small areas of a sample to be analyzed. Image: B.W. Jacobs

There has been much work done involving carbon nanomaterials and Raman spectroscopy. Many highly specific material characteristics can be determined using Raman spectroscopy and since the discovery of the carbon nanotube, it has proved an invaluable tool in analyzing and understanding their properties¹¹.

2.8 Cathodoluminescence and Photoluminescence

Cathodoluminescence (CL) is a technique used to determine the electronic structure characteristics of a material. It uses energetic electrons, usually from a SEM, which impart enough energy to excite electrons in the material from the valence band, where electrons are bound to atomic nuclei, into the conduction band, where they are free to move about the material. This energy transition is material specific. The amount of energy, measured in electron volts (eV), electrons need to be raised into the conduction band from the valence band is called the band gap. Inside this energy gap there are no available energy states for the electron, so in order to enter the conduction band an electron must gain at least the amount of energy equal to the band gap.

In CL electrons are given enough energy through the electron beam-sample interactions to be excited into the conduction band, as shown in figure 2.19. An excited electron will leave an empty state, or hole, in the valence band. The electron will quickly fall back into the valence band since it will always try to minimize its energy. Because energy is always conserved, this energy loss is converted into a photon equal to the loss of energy experienced by the electron. The photon energy will usually equal the band gap. The emitted photon is detected, and its energy, and therefore the sample material band gap, can be determined.

This technique can also determine the purity of a sample. If the material contains impurities, the impurities will also emit light with a different wavelength, because usually the energies of the impurities will lie within the band gap of the material. Defects also cause luminescence in differing wavelengths depending on where the defect lies within the band gap.

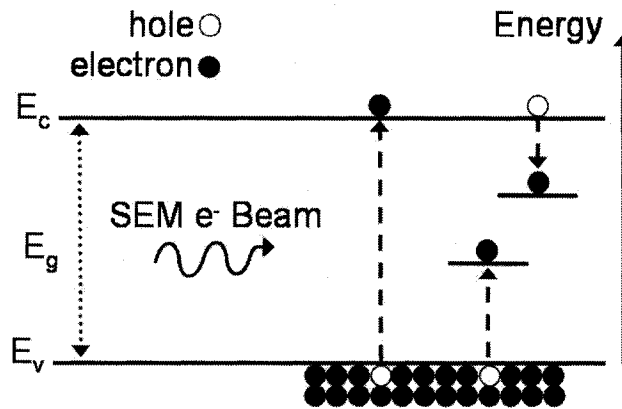


Figure 2.19. Illustration of the process involved in cathodoluminescence. Electrons represented by the black dots are excited to the conduction band, E_c , from the valence band, E_v , by the SEM electron beam. Electrons can be excited to states within the band gap, which can consist of impurities and defects in the material. Image: B.W. Jacobs

Photoluminescence (PL) is a very similar technique as CL and provides much of the same information. PL measures electron transitions in a material just as in CL, but it uses photons instead of electrons to probe the material. There are subtle differences between the two techniques, however.

In CL the electron beam induces excitations and emission from all the luminescent mechanisms within the material. This includes band-edge, valence to conduction band, emission as previously mentioned, defect induced emission, where defects with energies within the band gap are excited, as well as other recombination centers present in the material¹². This is due to the high energy of the electron beam. CL also provides depth-resolved luminescence information by varying the electron beam energy. When using a SEM to perform CL measurements a high spatial resolution is also available, where small areas of a material can be probed, which provides a spatial map of the sample luminescence.

PL excitation wavelengths, on the other hand, can be highly selective and can resolve specific luminescence mechanisms within a material¹³. This is important when

the band-edge emission and other luminescence mechanisms such as defects within the band gap need to be distinguished. Defect energies usually lie within the band gap of a material. Wavelengths that are too low in energy to excite band-edge luminescence can be used to distinguish these lower energy mechanisms. Therefore, if a defect with lower energy than the band gap is to be investigated, the excitation wavelength must be higher than the defect energy but lower than the band gap.

CL and PL are very important characterization tools in semiconductor engineering. They provide critical information, such as band gap energies, defect and recombination center details and the particulars of emission efficiency of materials. A LEO Supra 50 VP SEM in conjunction with a Gatan MonoCL system with a Hamamatsu R5509 photomultiplier located at Jet Propulsion Lab was used for the CL measurements. PL has as yet not been used in this thesis research.

Since this research deals heavily with GaN, which is a very promising optical material for blue and UV devices, CL and PL investigations are of utmost importance in characterizing the optical properties of the GaN nanowires. CL was also an independent experiment that identified both the wurtzite and zinc-blende phases in the multiphase nanowires, as will be discussed in chapter 4.

2.9 Thermogravimetric Analysis

Thermogravimetric analysis is used to determine the thermal stability of a given material. This is done with a highly precise balance and furnace. In sample testing the furnace temperature increases at a specified rate and at a given temperature the sample will begin to lose mass through vaporization. After a certain temperature is reached the sample will quickly vaporize. Throughout the temperature cycle, the precise balance measures the rate at which the material vaporizes, see figure 2.21. The furnace chamber can also be purged with an inert gas, water vapor, oxygen or other gas depending on the desired reaction. The resulting mass loss curves may also need further post processing to bring out subtle variations. The derivative of the mass curves is often used in uncovering these variations and to determine the point at which mass loss rate is greatest.

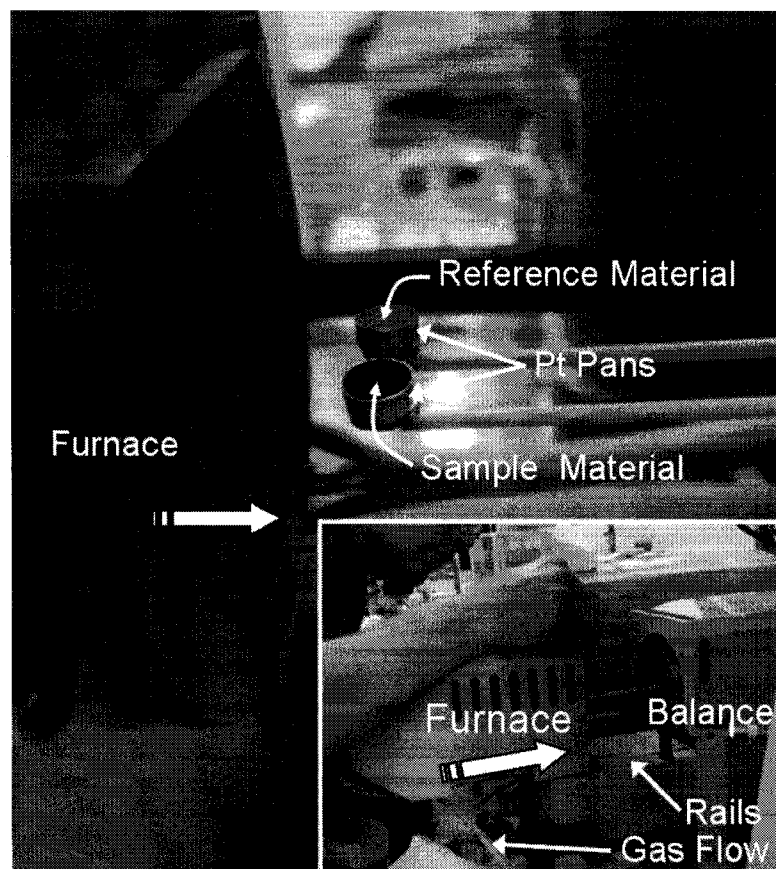


Figure 2.20. TGA instrument, Rigaku 8120 TG-DTA at the Tokura-Hirata Laboratory at Tokyo Institute of Technology. The sample material is packed into a small Pt pan and placed on precise balance. The pan is then put into a furnace and heated up. The arrow below the furnace label indicates the movement of the furnace. The furnace rides on two rails and encapsulates the samples in the furnace. The inset shows the whole instrument, with the furnace on the left and the balance mechanism on the right. A small tube for a desired gas is also indicated. Images: B.W. Jacobs

The TGA was primarily used to analyze carbon onion samples. The TGA system used was a Rigaku 8120 TG-DTA located in the Tokura-Hirata Laboratory at Tokyo Institute of Technology. Multiple carbon onion samples were produced from a variety of different starting materials and at different temperatures. In order to gain insight into the quality of carbon onions produced, and to determine the optimum starting material and temperature, TGA was used. Early on, the carbon onions were heated without the use of a flowing gas. The results were inconclusive, and the rate at which the temperature could be increased was much too low. The rate at which the temperature can be increase must

be such that a smooth loss in mass results. That way more consistent results and critical points such as the point at which mass loss is greatest can be more easily determined. Therefore purified air was passed through the furnace chamber at .2 l/min. The oxygen in the purified air caused the onions to oxidize into a gas form thereby reducing the mass. Initial mass reduction occurred at a lower rate and more consistent results were obtained, which will be discussed in chapter 5.

In addition to the flowing gas, there are several other considerations one must take into account when doing TGA. A consistent sample weight must be used, which must be the maximum amount the pan can accommodate, since carbon onions are very light and fluffy. They can also be pressed so that more material can be placed into the pan. All procedures must be as consistent as possible if reproducible results are to be obtained.

Using this procedure one can quantify the quality of as grown onions. If the carbon onions have outer layer defects, such as facet points or discontinuities in the wall structure, they will oxidize at lower temperatures¹⁴. The findings were compared with results from such studies as HRTEM imaging or Raman spectra, and an overall picture of onion growth characteristics were obtained.

Each instrument described above provided essential details of analyzed samples. These details could then be pieced together to gain an overall picture. Many times in uncovering and understanding new materials and material phenomena, several independent tests are need to provide a clear explanation for the observed phenomena. This was the case, for instance, for the new GaN nanowire structure and carbon onion modifications due to heavy ion radiation, results from several instruments were needed to compare the observations. Each instrument described above provided important results.

Additional instruments and methods will be described in chapter 6 that could provide further important details of these materials and devices discussed in this thesis research. The candidate investigated the materials and devices using all the instruments and methods described above.

References

1. D. J. Griffiths, "Introduction to Quantum Mechanics," Benjamin Cummings, San Francisco, 2004.
2. D. B. Williams, C. B. Carter, "Transmission Electron Microscopy," Plenum Press, New York, 1996.
3. R. F. Pierret, "Advanced Semiconductor Fundamentals," Prentice Hall, Upper Saddle River, 2003.
4. R. F. Egerton, *Electron Energy Loss Spectroscopy in the Electron Microscope*, Plenum Press, New York, 1986
5. M. J. Madou, "Fundamentals of Microfabrication: The Science of Miniaturization," CRC Press, Boca Raton, 2002.
6. K. A. Valiev, "The Physics of Submicron Lithography," Plenum Press, New York, 1992.
7. "Nanotechnology Measurement Handbook," Keithley Instruments, Inc., Cleveland, 2007.
8. F. Kühner, L. T. Costa, P. M. Bisch, S. Thalhammer, W. M. Heckl, H. E. Gaub, "LexA-DNA Bond Strength by Single Molecule Force Spectroscopy," *Biophys. J.*, **87**, 2683-2690 (2004)
9. J. S. Bunch, T. N. Rhodin, P. L. McEuen, "Noncontact-AFM imaging of molecular surfaces using single-wall carbon nanotube technology," *Nanotechnol.*, **15**, S76-S78 (2004)
10. R. L. McCreery, "Raman Spectroscopy for Chemical Analysis," John Wiley & Sons, New York, 2000.
11. M. S. Dresselhaus, G. Dresselhaus, A. Jorio, "Unusual Properties and Structure of Carbon Nanotubes," *Annu. Rev. Mater. Res.*, **34**, 247-278 (2004)
12. B. G. Yacobi, D. B. Holt, "Cathodoluminescence Microscopy of Inorganic Solids," Plenum Press, New York, 2002.
13. "Optical Radiation Measurements, Vol. 3, Measurement of Photoluminescence," Ed. K. D. Mielenz, Academic Press, London, 1982.
14. S. Osswald, G. Yushin, V. Mochalin, S. O. Kucheyev, Y. Gogotsi, "Control of sp²/sp³ Carbon Ratio and Surface Chemistry of Nanodiamond Powders by Selective Oxidation in Air," *J. Am. Chem. Soc.*, **128**, 11635-11642 (2006)

3. Reduced Dimensionality Systems: From Three Dimensions to Zero

As current silicon based devices are facing an inevitable end due to size limitations, novel materials and device concepts are being explored as successors to silicon technologies. The materials that seem to be the most promising usually have reduced dimensionality components. Essentially, a reduced dimensionality component, either engineered or inherently present in a material, has spatial dimensions that are so small that quantum mechanical confinement effects begin to play a significant role in determining the properties of the material. These quantum mechanical properties can enhance the performance of a material in a device, invoking properties that are not found in the same device made from the same material in bulk form. Such enhancements include faster electronics, brighter more efficient lasers and light emitting diodes, and sensors with extremely high sensitivity to a given compound.

Starting from a bulk material and working down, reducing one dimension at a time and discussing important properties at each step, will help clarify the importance of these systems, and the concept of reduced dimensionalities. Starting with a bulk block of material, the behavior of electrons will be explained as the spatial dimensions are shrunk as an illustrative example. This shrinking of dimensions is actually much more complex than it initially seems with intriguing quantum mechanical induced effects, but these effects are beyond the scope of this example.

Starting with a three-dimensional n-type semiconducting material, excess electrons can more or less freely move and bounce throughout the material. When an electron is in a three-dimensional material it acts much like a particle bouncing about through the lattice, interacting with the larger fixed atoms. If there is an external

perturbation, such as an applied electric field, the electron will randomly bounce through the lattice with an average motion opposite to the electric field.

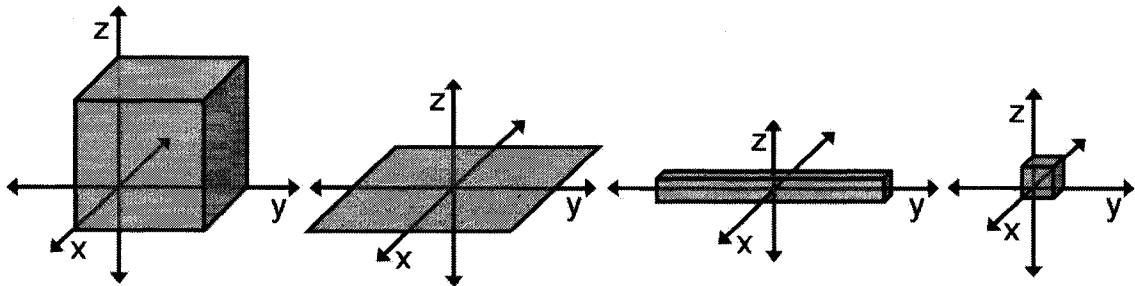


Figure 3.1 Examples of reduced dimensionality systems. From left to right: three-dimensional, two-dimensional, one-dimensional, and zero-dimensional. Image: B.W. Jacobs

If one spatial dimension is reduced, a very thin sheet of material will be formed, similar to a sheet of paper. In this case one spatial dimension is confined, i.e. it has one reduced dimensionality component. If we assign the z-direction of a three-dimensional coordinate system normal to this thin film, and assign the x and y-directions to the plane of the film, this system is considered to be confined in the z-direction. If this spatial confinement is sufficiently small, the electron energy landscape in this system will change relative to the three-dimensional, bulk system, i.e. electrons will not be able to freely move throughout the material. This spatial restriction will reduce the amount of available energy states accessible to the electrons, and electrons can only exist where there is available energy. If this spatial dimension is reduced beyond a certain point, the available electron energies will begin to separate. There will no longer be a continuous range of energy. A distinguishable set of energies, or energy levels, will begin to arise. This is called energy level quantization, and as the space gets ever smaller, the energy levels become more separated. However, let us not forget the energy landscape the in x

and y-directions. In plane with the surface of the thin film, electrons will move much like they did in the bulk material. This quantization of energy levels in the z-direction is purely a quantum mechanical phenomenon and can be explained by a relatively simple and very common model in quantum mechanics called a quantum well.

The quantum well is used to describe the behavior of trapped particles, including electrons. Figure 3.2 shows a one-dimensional quantum well with a length, the x-axis, and energy, the y-axis. This figure shows 4 energy levels stacked on top of one another depicting how the energy of the electrons arrange in such a configuration. As previously mentioned, electrons can only exist where there is available energy, so only a specific number of electrons can exist in a well. These energy levels depend on the inverse length, L , of the well. As this length decreases it increases the energy level spacing and reduces the number of available energy levels within the well. This concept is used in a variety of models in quantum mechanics and can be used to approximate energy levels in reduced dimensionality systems.

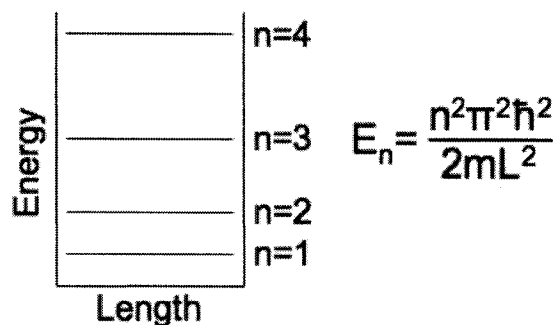


Figure 3.2 A quantum well. Particles in a quantum well are trapped in a confining potential. If the length of the well, L , is small enough, energy levels within the well will begin to separate and give rise to quantized energy levels. These energy levels are determined by the equation on the right, where n is the quantized energy level, h is Planck's constant, m is the mass of the particle, and L is the length of the well. Image: B.W. Jacobs

Two-dimensional systems are very popular in many systems and devices. In heterostructures a thin sheet of material sandwiched between two layers of material of a larger band gap, creates a quantum well in the thin, two-dimensional material. This thin material can be used as an optical device, efficiently creating certain colors of light. Two-dimensional materials can also be used in high power devices. If a two-dimensional material is again sandwiched between two materials with a larger band gap, a large amount of current can pass through the thin area. This device is called a high electron mobility transistor (HEMT) and is described in detail in chapter 6.

If a spatial dimension in the two-dimensional system were reduced, a one-dimensional system would result. This system consists of a line or very skinny wire of material, usually called a quantum wire or nanowire. This wire will restrict the energy levels in two-dimensions, i.e. it has two reduced dimensionality components. Electrons in this system are only free to move in the x-direction if the spatial dimension is reduced in the y direction. Two quantum wells, one in the z-direction, as in the thin film case, and in the y-direction, dictate the energy landscape. This has significant implications on electron conduction in such a system. The nanowire can only accommodate a set number of quantized energy levels in which electrons can travel, because of the quantum wells in the y and z directions. These quantized energy levels are called conduction channels. Carbon nanotubes are considered to be one of the best models of a one-dimensional system and are discussed in chapter 5. The GaN nanowires used in this thesis research are a pseudo one-dimensional system, because they do possess some one-dimensional quantum phenomena, but are quite large compared to a nanotube.

Electron injection into the one-dimensional system from a three-dimensional metal, which is usually used to connect the nanowires in devices, is fundamentally different than in a classical case due to the finite number of conduction channels in the reduced dimensional system. The three-dimensional metal essentially has an infinite number of conduction channels, so when electrons are injected into a one-dimensional system there will be a resistance. There will also be a resistance when the electron travels out of the one-dimensional system into the three-dimensional metal. For efficient junctions to low-dimensional materials, a so-called conduction channel-matching situation would be ideal. If the both the contact metal and one-dimensional wire had the same number of conduction channels there would theoretically be no resistance¹. This situation simply does not exist in macroscopic electronics. It is important to note, this is one of the main problems facing nanoelectronics, namely creating good contacts from the macroscopic world to the reduced dimensional system.

In reducing the final dimension, we are left with a zero-dimensional system, or a small box, called a quantum dot. This system has quantum wells in each of the three directions, confining electrons to a very small area with a small number of available energy levels. Quantum dots have excellent optical properties and have been shown to be efficient LEDs² and lasers³. Quantum dots have also been shown to be good photovoltaic cells.

Most future electronic devices will have some reduced dimensionality, or quantum component. Each reduced dimensionality has unique properties due to quantum mechanical induced effects, and specific devices can exploit these properties in niche applications. These properties are too numerous to discuss in full. This thesis discusses

original work in GaN nanowires, carbon nanotubes and carbon onions, all reduced dimensionality systems, and their applicability in next generation systems and devices.

References

1. S. Datta, *Electronic Transport in Mesoscopic Systems*, Cambridge: Cambridge University Press 1995
2. R. Schmidt, U. Scholz, M. Vitzethum, R. Fix, C. Metzner, P. Kailuweit, D. Reuter, A. Wieck, M. C. Hübner, S. Stufler, A. Zrenner, S. Malzer, G. H. Döhler, "Fabrication of genuine single-quantum-dot light-emitting diodes," *Appl. Phys. Lett.*, **88**, 121115 (2006)
3. M. Sugawara, N. Hatori, M. Ishida, H. Ebe, Y. Arakawa, T. Akiyama, K. Otsubo, T. Yamamoto, Y. Nakata, "Recent progress in self-assembled quantum-dot optical devices for optical telecommunication: temperature-insensitive 10 Gb s⁻¹ directly modulated lasers and 40 Gb s⁻¹ signal-regenerative amplifiers," *J. Phys. D*, **38**, 2126-2134 (2005)

4. Zinc-Blende Wurtzite Multiphase Gallium Nitride Nanowires

This chapter discusses all original research contributed by the candidate. Recent discovery of the multiphase nanowires by the candidate and subsequent investigations of the nanowire structure, growth and electronic characteristics will be thoroughly discussed.

Semiconducting nanowires have gained enormous popularity due to their versatility in multiple applications. Semiconductor nanowire versatility translates directly from the bulk semiconductor counterparts, providing a wide assortment of band gaps, hole and electron mobilities, and mechanical properties that can be utilized in device engineering. Many nanowire properties are even improved by confinement effects in comparison to semiconductor bulk properties. Various research groups have grown a wide variety of semiconductor nanowire structures including ZnO¹, Si², Ge³, GaAs⁴ and InN⁵ nanowires. Nanowire heterostructures^{6,7} and nanotubes^{8,9} also represent important steps forward toward practical device applications in nanowire engineering.

Gallium nitride has gained much interest in recent years, due to its desirable characteristics in electronic and optical devices. It is a direct, wide band gap semiconductor, 3.299 eV in bulk zinc-blende and 3.437 eV in bulk wurtzite¹⁰, and is inherently n-type with a doping concentration of around 10^{18} cm^{-3} present due to nitrogen vacancies^{11,12}. Gallium nitride (GaN) nanowires are currently being used in and developed for a wide variety of applications. GaN nanowire field effect transistors¹³ have demonstrated high transconductance and good switching behavior. Complementary logic¹⁴ and optical¹⁵ devices have been fabricated using p-type dopants in nanowire growth¹⁶, further enhancing the versatility of these nanowires in devices. Mechanical

properties of GaN nanowires have also been investigated for use in mechanical resonators¹⁷. GaN also has the ability to form in two different crystalline phases, zinc-blende, the metastable phase, and wurtzite, the stable phase.

In order to develop GaN nanowire devices with high levels of performance, nanowires must be of high crystalline quality and material purity. Therefore, a precisely tuned nanowire growth process must be implemented in order to achieve this quality and purity. Many research groups have successfully grown GaN nanowires using several methods of growth^{18,19,20}. These methods can be split into two basic categories, vapor-liquid-solid (VLS) and vapor-solid (VS)²¹. In VLS growth a catalyst particle is used for nanowire nucleation. The catalyst, usually a transition metal such as nickel or iron in liquid form, decomposes vapor-phase growth constituents on its surface, then supersaturates with the radicalized constituents, which is followed by re-assembly and continuous extrusion of a solid crystalline nanowire with correct stoichiometry. In VS growth, nanowire constituents decompose from pre-existing solid crystalline elements and at active sites on the surface of the same crystalline elements. These pre-existing crystalline elements are called a matrix.

The GaN nanowires that were investigated in this thesis research are distinctly unique; they naturally grow incorporating both the zinc-blende and wurtzite crystalline phases simultaneously in longitudinal crystal domains. This multiphase nanowire structure was obtained through a catalyst-free VS growth mechanism in a direct reaction of gallium metal with ammonia (NH₃) in a quartz tube furnace^{22,23}. Growth temperatures ranged between 850-1000° C with the ammonia flow rates around 20 sccm and pressures between 5 and 15 Torr. Nanowire growth can be broken into three basic stages. In the

first stage, an amorphous GaN matrix forms. In the second stage, GaN hexagonal crystal platelets form within the amorphous matrix. In the third and final stage the nanowires grow from the sides and corners of the GaN hexagonal platelets. By tuning growth parameters, different nanowire structures have been obtained, including the zinc-blende/wurtzite multiphase nanowires as well as wurtzite single-phase nanowires. Temperature seemed to be the strongest controlling parameter and extensive SEM and HRTEM analysis based on growth temperatures of 850° C, 950° C and 1000° C revealed distinct differences in growth matrix properties. The differences in growth matrix properties resulted in variations in nanowire structure as will be discussed.

The structure of the multiphase nanowires was studied using plain-view HRTEM images to understand the longitudinal structure configuration. Understanding and reconstructing this multiphase structure using plain-view HRTEM, which included diffraction patterns and FFTs, proved difficult. So further investigations using cross-section HRTEM nanowire samples fabricated with a FIB were invaluable in understanding the nanowire internal structure.

The electronic properties of these multiphase nanowires were also investigated using several techniques. Nanowires were used as the semiconducting element in field effect transistors, and the performance of these devices was assessed. Nanowire resistance measurements were done using nanoscale probes so an accurate, non-invasive measurement could be obtained. Unexpected transport characteristics were also observed while measurements took place, and indicated phase-specific transport. Cathodoluminescence studies were carried out to obtain electronic structure information including the band gap and if impurities were present.

In this chapter two terms that distinguish specific crystal elements of the nanowire will be used: phase and domain. Phase is used to distinguish between the zinc-blende and wurtzite crystalline structures. Therefore the term multiphase is used to describe the two different phases that exist in the nanowire. The term domain will be used to distinguish different crystalline structures within the nanowire that are separated by a boundary or interface. Domain can be used to distinguish, for instance, two wurtzite, two zinc-blende or one wurtzite and one zinc-blende crystalline structure that are separated by an interface.

4.1 Nanowire Structure Investigations

The nanowire structure was primarily investigated with TEM techniques, including plain-view HRTEM, selected area electron diffraction (SAED) patterns, fast Fourier transforms (FFTs), energy dispersive x-ray spectroscopy (EDS), electron energy loss spectroscopy (EELS), and cross-section HRTEM. Investigations of nanowires that grew at 850° C, 950° C, and 1000° C were carried out. Multiphase nanowires were observed at each temperature, but wurtzite single-phase nanowires were also observed at 1000° C. This was confirmed by cross-section HRTEM investigations where results from multiphase nanowires from 850° C and 950° C as well as wurtzite single-phase nanowires that grew at 1000° C were observed and will be presented. EDS and EELS were used for elemental composition confirmation.

4.1.1 Plain-View TEM

Extensive plain-view TEM studies were done in order to solve the crystallography of the multiphase nanowire structure²⁴. In these investigations the multiphase structure of the nanowires and the nanowire growth directions of both the zinc-blende and wurtzite phases were identified. This nanowire structural analysis was done using HRTEM images, SAED patterns, FFTs, EDS, and EELS. Each technique was critical in assessing the crystallography and stoichiometry of the nanowire. SAED patterns and FFTs of HRTEM images were used to distinguish the zinc-blende and wurtzite phases and to determine the growth direction of each phase. EDS was used to estimate the elemental composition. EDS spectra consistently showed, within an acceptable margin of error of

$\pm 10\%$, that the nanowires contained gallium and nitrogen in a 1:1 ratio. EELS was used to confirm the presence of gallium and nitrogen along with the lack of oxygen.

Nanowire TEM sample preparation consisted of just a few steps. First the nanowire/matrix sample was placed in a small plastic vial filled with ethanol. Ultrasonication of the nanowire/matrix/ethanol mixture for 1-3 seconds released nanowires from the matrix into suspension. Once in suspension the nanowires were pipetted out and dropped onto a copper TEM grid with carbon lacy support film spanning the holes on the grid. The TEM grid was allowed to dry for a few minutes and was left with several nanowires as well as many bits of matrix on the support film.

A typical HRTEM image of a multiphase nanowire that grew at 850°C is shown in figure 4.1. The multiphase structure is clearly evident in this image. Figure 4.1(a) shows a TEM image indicating the width, roughly 120 nm, of the nanowire. Figure 4.1(b) shows an HRTEM image of the area indicated in 4.1(a). A distinct phase transition between the zinc-blende and wurtzite crystalline phases can be seen and is indicated by the dashed line. It was very sharp, only a few atomic layers thick, with no observable defects.

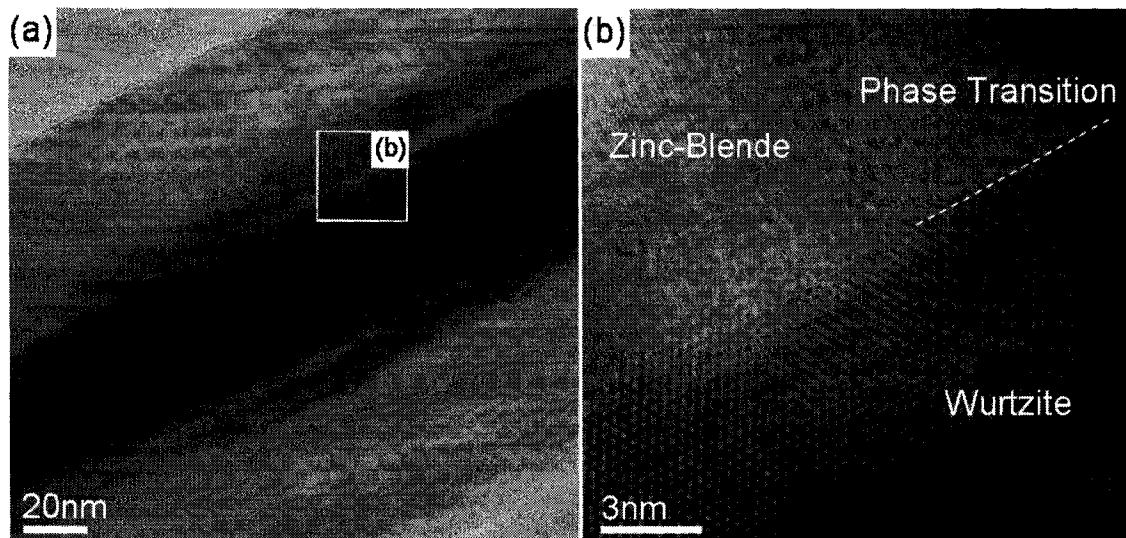


Figure 4.1. TEM and HRTEM images of a multiphase GaN nanowire that grew at 850° C. (a) The TEM image shows the width of the nanowire. Contrast variations indicate changes in thickness as well as phase across the nanowire. (b) An HRTEM image of the indicated boxed area in (a). The zinc-blende and wurtzite domains are clearly distinguishable in this image along with the sharp phase transition denoted by the dotted line. Images: B.W. Jacobs

An example of multiphase nanowire crystal phase and orientation determination using an SAED pattern and FFTs is shown in figure 4.2. Using diffraction, different crystalline domains can be distinguished and their orientations relative to the nanowire growth direction and their orientations relative to each other can be identified. A typical HRTEM image of a nanowire that grew at 850° C is shown in figure 4.2(a). It indicates the complicated structure of the nanowire where multiple crystalline domains in different orientations can contribute to the image. The wave-like features in the bottom right are likely moiré fringes resulting from similar stacked periodic structures²⁵. Figure 4.2(b) shows an SAED pattern taken of this nanowire. A zinc-blende phase and a wurtzite phase contributed to this pattern. The zinc-blende pattern is along the [001] zone axis and the wurtzite pattern is along the [0001] zone axis and it has been solved accordingly. Figures 4.2(c) and 4.2(d) are FFTs taken from the indicated areas in figure 4.2(a). These FFTs identified the zinc-blende and wurtzite domains that contributed to the SAED

pattern. The growth direction of this nanowire was along the $[2\bar{1}\bar{1}0]$ direction in the wurtzite phase and along the $[011]$ direction in the zinc-blende phase as indicated by the SAED pattern.

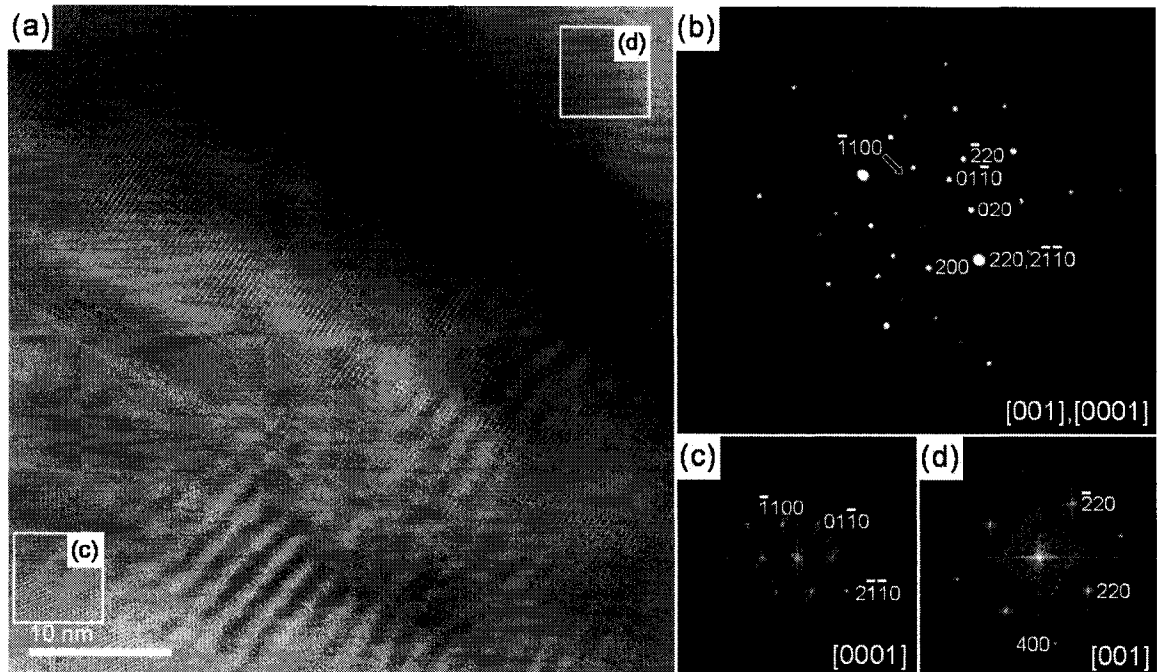


Figure 4.2. HRTEM image of a nanowire that grew at 850°C , and SAED and FFT analysis illustrating how the FFT can augment SAED patterns. (a) An HRTEM image of a nanowire shows the multiphase structure of the nanowire. (b) An SAED pattern of the nanowire showing both zinc-blende and wurtzite contributions. The zinc-blende SAED pattern was along the $[001]$ axis and the wurtzite was along the $[0001]$ axis. (c) FFT of the wurtzite phase taken from the boxed area in (a). (d) FFT of the zinc-blende phase taken from the boxed area in (a). These FFTs separate out the zinc-blende and wurtzite contributions in the SAED pattern, and identified where these contributions were located in the nanowire. Images and interpretation: B.W. Jacobs

Every nanowire grown at 850°C imaged to date has been multiphase. Figure 4.3 shows an HRTEM image of a nanowire grown at 1000°C with a wurtzite single-phase structure. The growth direction of this nanowire is the same wurtzite growth direction for the nanowires grown at 850°C , $[2\bar{1}\bar{1}0]$. The moiré fringes may result from different domain orientations within the nanowire. The formation of the single-phase nanowire may have to do with different growth kinetics present at higher temperatures.

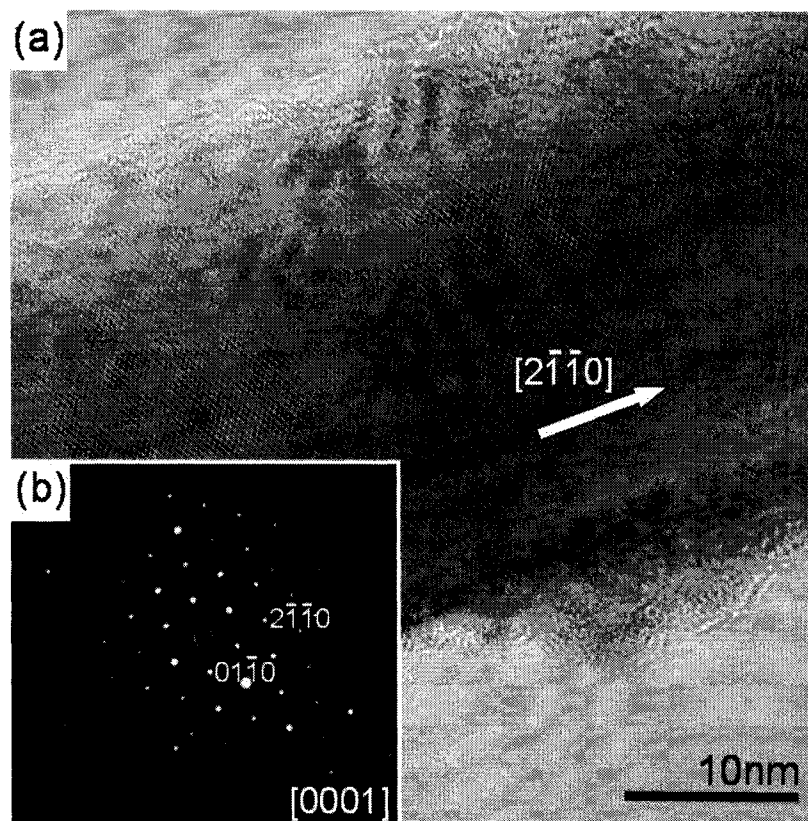


Figure 4.3. (a) An HRTEM image of a single-phase wurtzite nanowire grown at 1000° C. The wurtzite growth direction is the same as the nanowires grown at lower temperatures, $[2\bar{1}\bar{1}0]$. No zinc-blende phase was observed. (b) This SAED pattern was solved for the wurtzite crystal structure along the $[0001]$ zone axis. Images and interpretation: B.W. Jacobs

Multiphase nanowires with very similar structures to those found at 850° C were observed at 1000° C in addition to the single-phase nanowires. In comparing a multiphase nanowire grown at 1000° C, figure 4.4(a), to one grown at 850° C, figure 4.4(b), they were very similar. The sharp transition between the zinc-blende and wurtzite phases is evident in each figure. The nanowire growth directions are the same, and similar FFTs indicate similar crystal orientations.

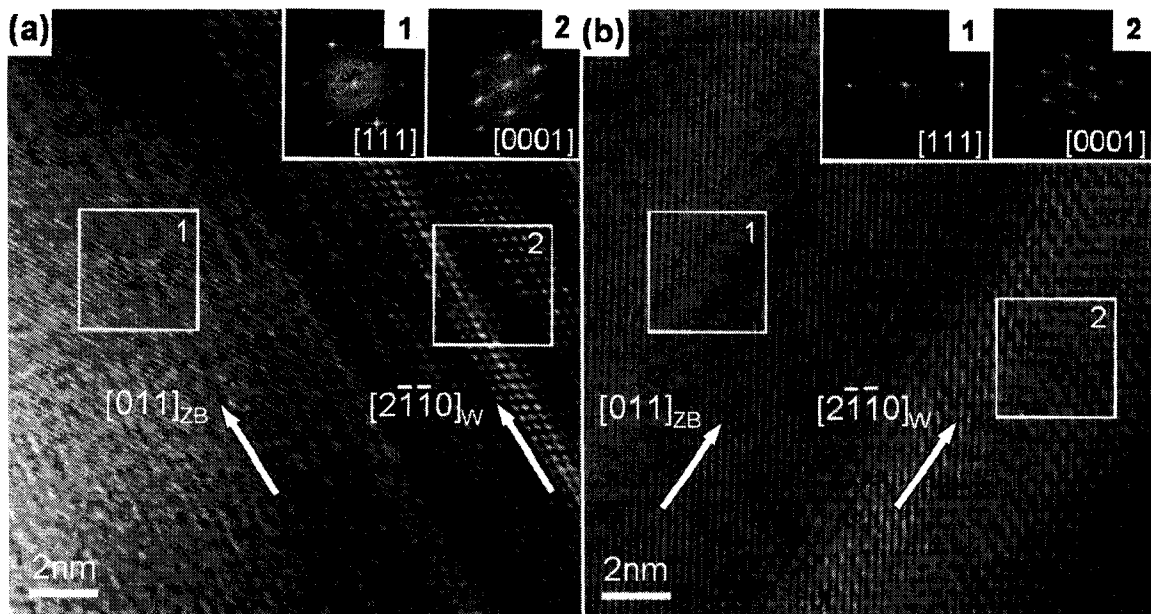


Figure 4.4. HRTEM images of nanowires grown at 1000° C and 850° C. (a) An HRTEM image of a nanowire grown at 1000° C. Zinc-blende and wurtzite phases were identified using FFTs taken from the indicated areas. A sharp phase transition was evident. The arrows indicate the nanowire growth direction for each phase. (b) An HRTEM image of a nanowire grown at 850° C. A very similar structure was observed, with similar FFTs and the same growth directions for each phase. Images and interpretation: B.W. Jacobs

Single-phase wurtzite nanowires grown at 1000° C, which had a different growth direction than the nanowire shown in figure 4.3, were also observed. With growth along the [0001] direction, these nanowires tended to be much thicker in width, ranging from 200 nm to 10 μ m. Figure 4.5(a) shows a single-phase nanowire grown at 1000° C with growth along the [0001] direction. Note the tapered tip of the nanowire; this feature will be discussed in section 4.3. Figure 4.5(b) shows an HRTEM image taken from the boxed area in 4.5(a) with a well-resolved lattice indicating the high crystal quality of the nanowire. Figure 4.5(c) shows an SAED pattern and was solved for the wurtzite structure along the $[01\bar{1}0]$ zone axis. Nanowires with this growth direction were specific to this growth temperature, and no nanowires have been observed to date with this growth direction at the lower temperatures.

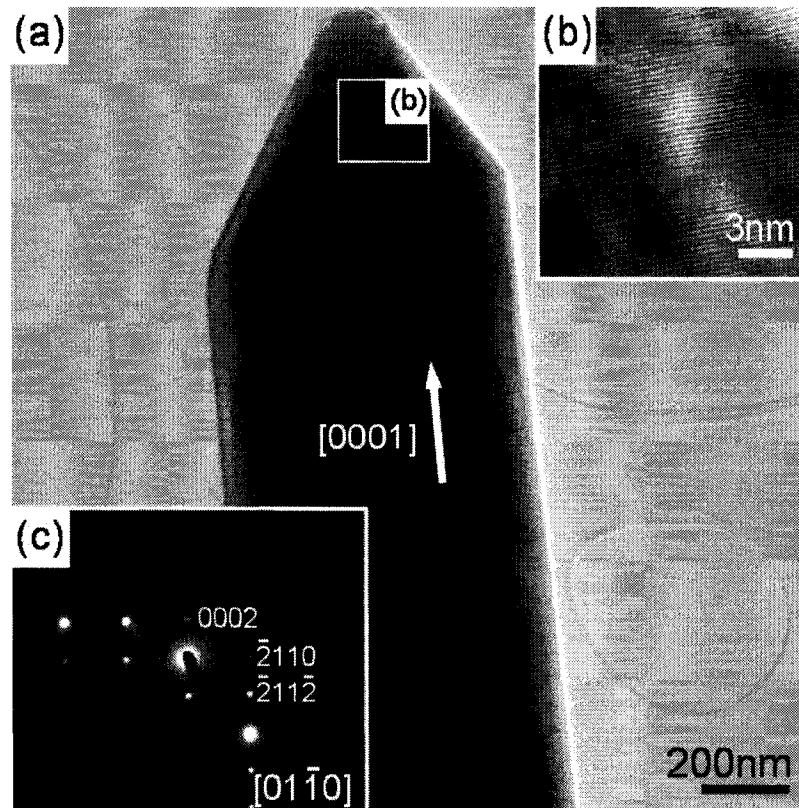


Figure 4.5. TEM images of a nanowire grown at 1000° C. (a) A TEM images shows the nanowire end, with its tapered tip. It was about 700 nm wide. Its growth was along the [0001] direction. (b) An HRTEM image taken from the boxed area in (a) shows a well-resolved lattice indicating the high crystal quality of the nanowire. (c) An SAED pattern was solved for the wurtzite structure along the $[01\bar{1}0]$ zone axis. Images and interpretation: B.W. Jacobs

Obtaining HRTEM images of the nanowires, as shown in the figures above, was not usually difficult. Many nanowires were very thin, roughly 60-150 nm in width, with edges thin enough to obtain high-resolution images. The center of the nanowires is normally too thick to obtain clear HRTEM images. Usually, when imaging in the TEM, tilting to a low index zone axis, such as [111] or [001] in zinc-blende, is done to understand the orientation of the crystal and to obtain the clearest high-resolution images. This is very difficult to do when imaging nanowires, however. As mentioned, the nanowire was usually very thin, so when tilting, the nanowire tended to move out of the viewing area and above or below eucentric height. Eucentric height is when the sample

is in focus and the objective lens current is at its optimum value. Therefore, the nanowire must be continually moved back into the viewing area and its location within the objective lens continually adjusted to eucentric. Many times, simply due to the multiphase structure of the nanowire, the orientation of one domain will allow for clear high-resolution images. Tilting to a low index zone axis can be done but requires patience on the part of the user.

Adding to the difficulty of obtaining clear images at a specific zone axis, the zinc-blende and wurtzite crystalline structures are quite similar, and the distinction between certain diffraction patterns may not always be clear. Several important diffraction patterns in the zinc-blende and the wurtzite phases are very similar, as shown in figure 4.6. When analyzing similar patterns, the spot intensity can be used as a clue as to which pattern is which. However, since the TEM beam is usually not exactly perpendicular to a set of low index planes, the Bragg condition may not be exactly met, giving different spot intensities than expected. Stacked domains can complicate the pattern. Also multiple reflections that have the same interplanar spacing and are at the same orientation will add to the spot intensity making it much brighter, as shown in figure 4.2(b). So after a diffraction pattern is obtained, special care must be taken in determining which phase it corresponds to.

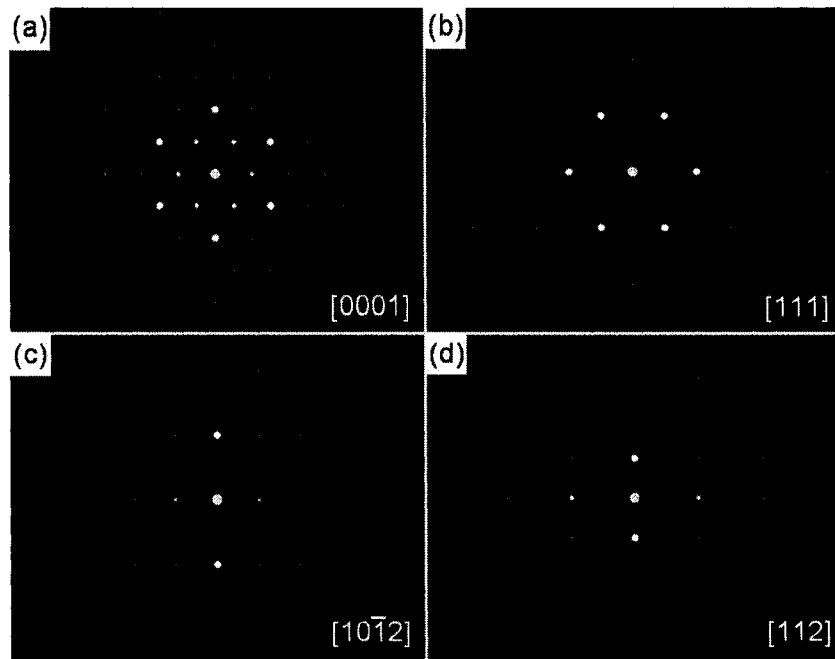


Figure 4.6. Simulated diffraction patterns highlighting similar features found in some wurtzite and zinc-blende patterns. (a) [0001] zone axis for the wurtzite structure. (b) [111] zone axis for the zinc-blende structure. (c) $[10\bar{1}2]$ zone axis for the wurtzite structure. (d) [112] zone axis for the zinc-blende structure. Images and interpretation: B.W. Jacobs

FFTs play an important role in multiphase nanowire crystal analysis since many times the different crystalline domains within the nanowire are too small to easily distinguish in a SAED pattern. Therefore, using FFTs taken from HRTEM images, SAED patterns can be linked to specific phases and domains within the nanowire, as shown in figure 4.2. However, FFTs do have their drawbacks. No specific spatial information is contained in an FFT. In real diffraction patterns, information about the spatial scale, based on the magnification and how far the diffraction pattern image is projected below the sample, called the camera length, is provided. Using this information the interplanar spacing for a given material can be calculated with a high degree of accuracy and compared against known values for confirmation. This information is key in determining the crystallography of a material. FFTs do not provide this information

directly. In order to successfully confirm the pattern generated with an FFT, it must be backtracked to a known diffraction pattern.

If the FFT can be backtracked to a known diffraction pattern, an FFT can be a powerful tool. For example, if an FFT is backtracked to a real diffraction pattern it can be compared against other FFTs that are taken at the same magnification and from the same size area. To take an FFT of an HRTEM image, a certain area of an HRTEM image is selected in a program such as ImageJ²⁶. This size of this area, usually a square, determines the size of the FFT along with the magnification of the image. As long as the same size square at the same magnification is used spatial information can be extracted from FFTs, making them an invaluable tool for crystal analysis, augmenting SAED patterns.

In addition to structural analysis, EDS in the TEM was used to investigate the elemental composition of the nanowires. It was essential to verify the purity of the GaN nanowires. Possible nanowire impurities, such as oxygen, were purposely removed from the growth chamber, and of the lack of these impurities in the nanowires needed verification. A common nanowire is gallium oxide (Ga_2O_3), and oxygen was not observed in the EDS spectra. Figure 4.7 shows an EDS spectrum with peaks occurring at specific energies corresponding to the elements present within the nanowire. Other peaks including copper and carbon were present as a result of the copper TEM grid and carbon lacy support film spanning the copper grid holes. The EDS spectra measured gallium and nitrogen in a 1:1 ratio.

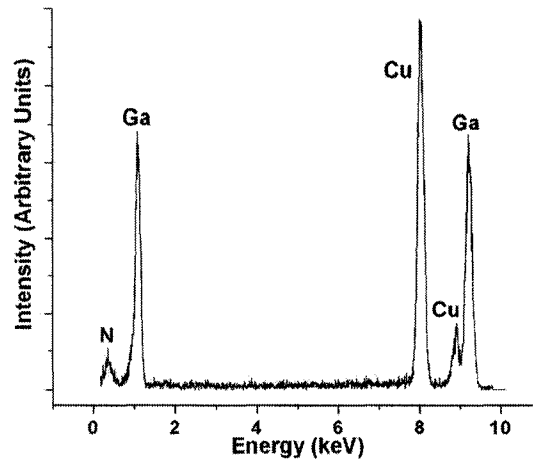


Figure 4.7. EDS spectrum of a GaN nanowire. The nitrogen and gallium peaks indicate the purity of these nanowires. A copper peak is also present due the copper TEM grid used to support the nanowire sample. Spectrum and interpretation: B.W. Jacobs

EELS was also used in elemental confirmation. EELS is very sensitive technique that can detect small amounts of a given element within a material. Using EELS, the presence of nitrogen, figure 4.8(a), and gallium, figure 4.8(b), were detected along with the absence of oxygen. Oxygen was an unwanted impurity and great care was taken to eliminate oxygen in nanowire growth.

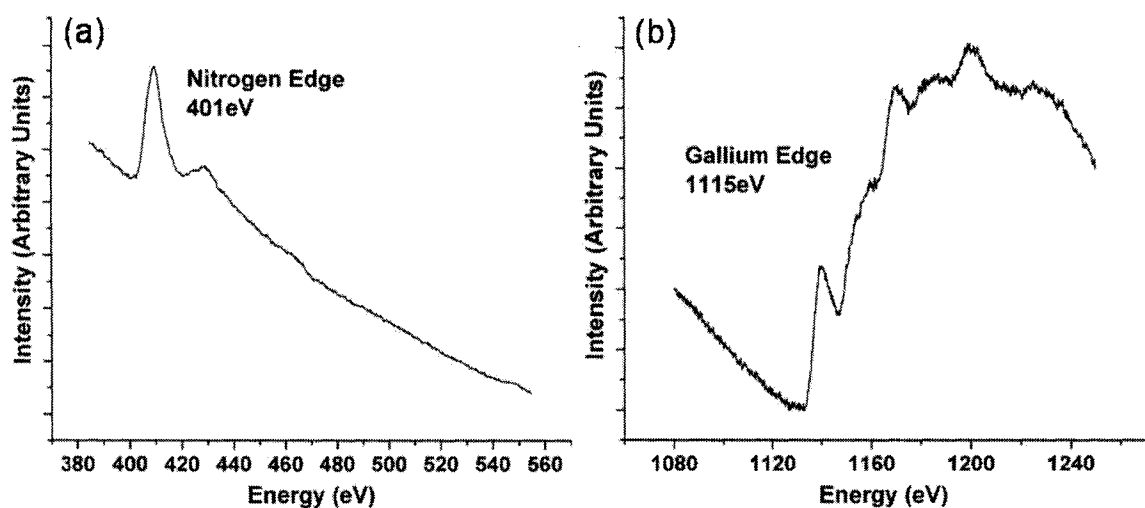


Figure 4.8. EELS spectra of a GaN nanowire. (a) The nitrogen core loss is located at 401 eV, and a strong signal was measured there indicating a significant presence of nitrogen. The oxygen core loss at 532 eV is located on this spectrum but no peak was detected confirming the lack of oxygen. (b) The gallium core loss is located at 1115 eV, and a strong signal was measured there indicating a significant presence of gallium. Spectra and interpretation: B.W. Jacobs

Plain-view HRTEM analysis proved very beneficial in determining the structure and stoichiometry of the multiphase nanowires. The multiphase structure was identified in HRTEM images and using SAED patterns and FFTs. The nanowire purity was verified using EELS and EDS. However, several questions remained after plain-view HRTEM analysis. Namely, how the nanowire crystalline domains were oriented relative to each other, and if sharp defect-free zinc-blende to wurtzite interfaces always formed. Usually the HRTEM images were too complicated to answer these questions and only so much information could be extracted from them. Therefore, other sample preparation techniques were discussed and explored. Cross-section HRTEM analysis proved the best possibility for obtaining further structural information and was pursued.

4.1.2 Cross-Section HRTEM

The internal structure of the multiphase nanowires was difficult to determine using only plain-view HRTEM techniques. Complicated SAED patterns were often difficult to solve since multiple crystalline domains could contribute to the pattern. SAED patterns could also be somewhat distorted because the low index crystal orientation may not be perpendicular to the electron beam resulting in a Bragg condition that was not exactly met. Therefore, in order to gain a better understanding on how these nanowires form, on axis, or cross-section HRTEM nanowire studies were considered.

Several techniques can be used for cross-section TEM sample preparation. A popular method is embedding a sample in hard resin and using a diamond tipped blade to cut very thin cross-sections. Another method involves placing the sample in liquid nitrogen and using a mortar and pestle to grind the sample in hopes of getting a small enough cross-sectioned piece of material. The former technique was attempted in making a cross-section of a GaN nanowire, but proved difficult. A third technique was then explored: using a focused ion beam to prepare individual nanowire cross-sections. This sample preparation technique has been explained in detail in chapter 2. This method proved difficult at first, but after many failed attempts successful samples were fabricated with spectacular results.

Cross-sections were fabricated from the three different growth temperatures mentioned above, 850° C, 950° C and 1000° C. Figure 4.9 shows a cross-section from each growth temperature. The cross-sections taken from the nanowires grown at 850° C and 950° C were single nanowires, and the cross-sections from each temperature had a unique structure, but both had a triangle shaped cross-section. A multiple nanowire

cross-section was obtained from nanowires grown at 1000° C. This was made possible by a small group of nanowires that held together at the matrix base after ultrasonication. These nanowires also had unique features, as will be discussed.

Figure 4.9(a) shows a cross-section taken from a nanowire grown at 850° C. Figure 4.9(b) shows a cross-section taken from a nanowire grown at 950° C. These two multiphase nanowires had the same growth directions, $[2\bar{1}\bar{1}0]$ for the wurtzite phase and $[011]$ zinc-blende phase. They had multiple wurtzite and zinc-blende domains in unique configurations, which will be discussed in detail. Figure 4.9(c) shows a cross-section taken from a group of multiple nanowires grown at 1000° C. There are five individual nanowires all with hexagon-shaped cross-sections. The very large nanowire on the left was likely two nanowires that grew together. The individual nanowires in this cross-section ranged between about 200 nm to 1.5 μm in width. These nanowires were single-phase wurtzite with growth in the $[0001]$ direction. Figure 4.9(d) shows an SEM of the group of nanowires. A dotted line denotes where the cross-section was taken. Figure 4.9(e) shows a close up of where the cross-section was taken. The silicon substrate on which the nanowires were placed, was tilted 52° relative to the electron beam in this image. The small nanowires are more easily seen here and the nanowire nucleation sites are also apparent. Figure 4.9(f) shows the nanowires embedded within the Pt/Au stack midway through the cross-section extraction process. The trenches on either side of the cross-section have been sputtered away, and at this stage the cross-section was ready for the U-cut. An arrow points out the location of the three large nanowires. The ion beam was used to create this particular image. Figures 4.9(g) and 4.9(h) are close ups of the two small nanowires, and their locations in the cross-section are indicated in 4.9(c).

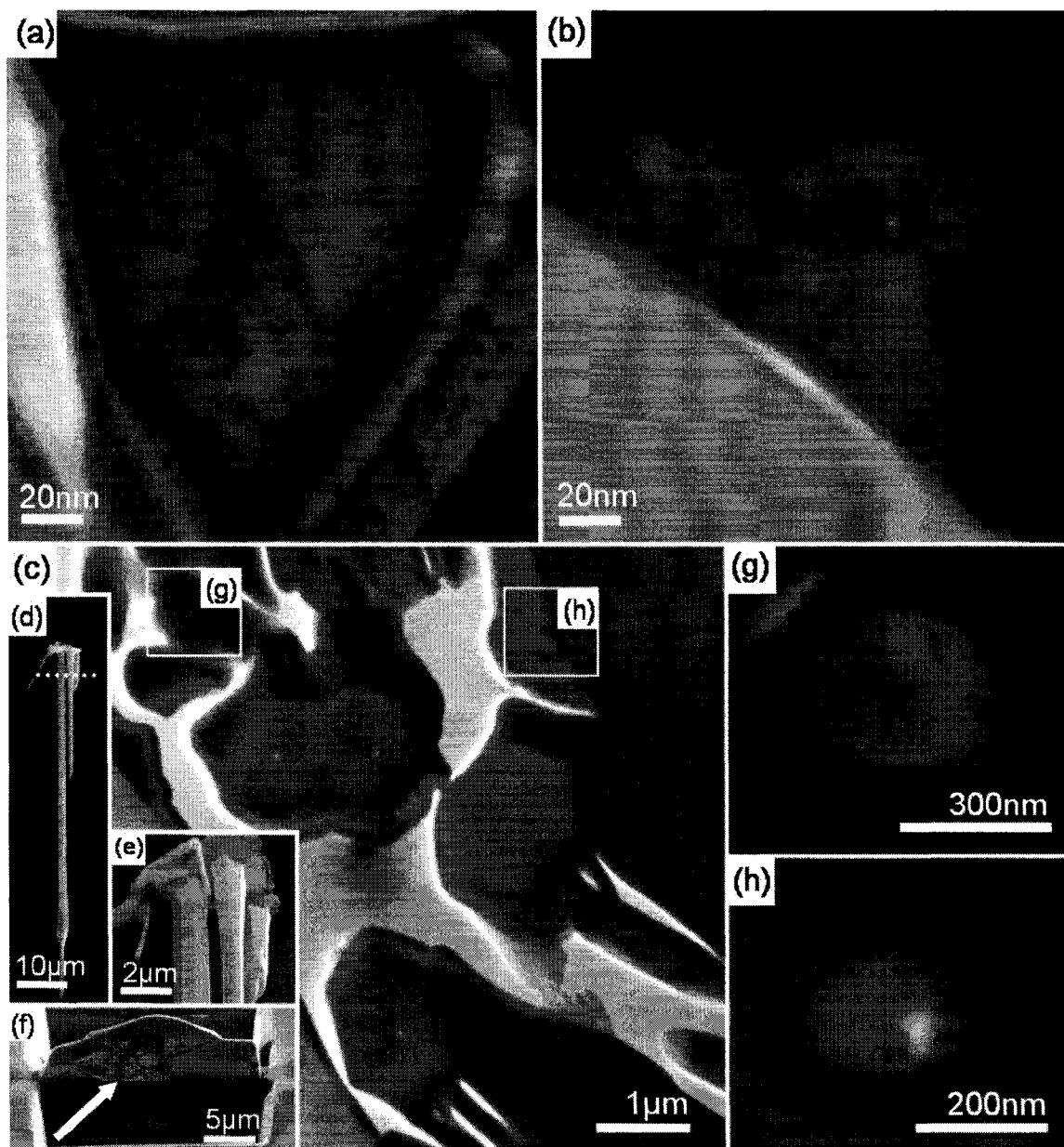


Figure 4.9. TEM images of cross-sections fabricated with the FIB. (a) Cross-section HRTEM image of a nanowire grown at 850° C. (b) Cross-section HRTEM image of a nanowire grown at 950° C. (c) Cross-section TEM image of multiple nanowires grown at 1000° C. (d) SEM image of the group of nanowires from which the cross-section was taken. The dotted line denotes where the cross-section was taken. (e) A close up of this group shows each individual nanowire nucleating from the matrix. Both the large and small nanowires can be seen here. (f) An ion beam images shows the cross-section half way through the extraction process. The arrow points out where the three large nanowires were located. The nanowires were on top of a silicon substrate and under a thin layer of gold and a thick layer of platinum to protect them from ion beam damage. (g) A TEM image of a small nanowire. Its location within the nanowire group is indicated in (c). (h) A TEM image of a second small nanowire. Its location within the nanowire group is also indicated in (c). Images: B.W. Jacobs

Detailed HRTEM analysis of a cross-section taken from a nanowire grown at 850° C is shown in figure 4.10. The nanowire was divided into five distinct regions that separated each crystal domain present in the nanowire. These regions were distinguished by domain interfaces denoted by the dotted line in the HRTEM image in figure 4.10. FFTs taken from each region are shown on the right. FFTs of regions 1-4 were solved for the wurtzite structure along the $[2\bar{1}\bar{1}0]$ direction, which coincided with the growth direction for the wurtzite phase found in the plain-view TEM investigations described in the previous section. The FFT from region 5 was solved for the zinc-blende structure along the $[011]$ direction, which also coincided with the growth direction for the zinc-blende phase found in the plain-view TEM investigations. The arrows in the FFTs point in the $[0001]$ and $[111]$ directions in the wurtzite domains and the zinc-blende domain, respectively, to emphasize the different orientation of each domain.

Low energy planes parallel to the nanowire growth direction faceted, which resulted in the overall triangular cross-section shape as well as in the individual triangular domains. In each wurtzite domain these planes were the $\{10\bar{1}1\}$, which made up two sides of the triangle and the (0001) plane, which made up the third side. Note, however, that the (0001) planes were always found as internal interfaces, they were never found as external facet planes. In the zinc-blende structure the $\{111\}$ planes faceted, and in region 5 are responsible for the diamond shaped domain. The crystal models at the bottom of this figure indicate which planes were responsible for faceting as well as the growth planes in both the zinc-blende and wurtzite structures perpendicular to the nanowire growth direction. The metal layers on top of the nanowire are also indicated. Titanium, gold and platinum were deposited on the nanowire to protect it from ion beam damage.

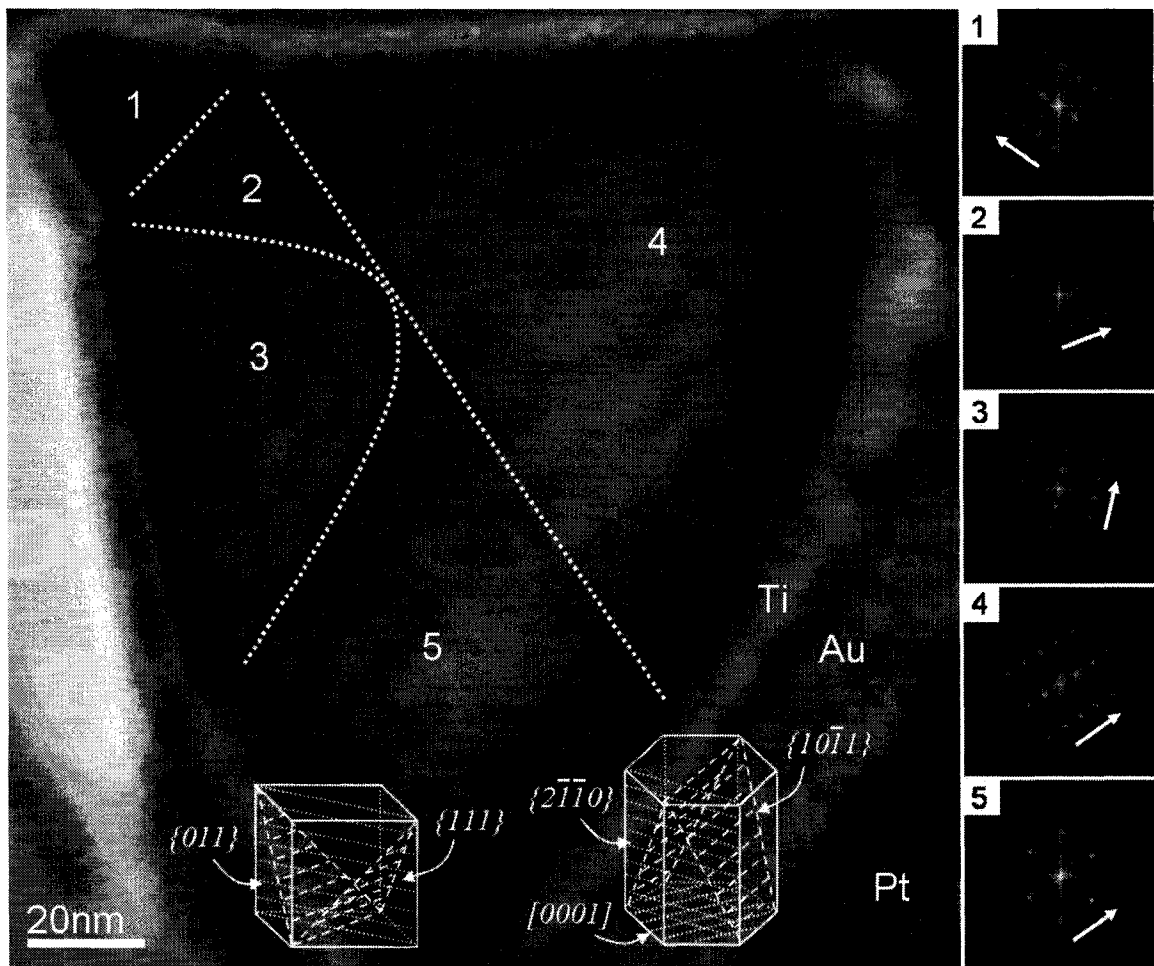


Figure 4.10. Details of the cross-section taken from the nanowire grown at 850° C. This nanowire was separated into five regions corresponding to its distinct crystalline domains. These regions were divided along domain interfaces. FFTs from each region are shown on the right. Regions 1-4 were wurtzite and region 5 was zinc-blende. The arrows in the FFTs indicate the [0001] and [111] directions in the wurtzite and zinc-blende domains, respectively. Zinc-blende and wurtzite crystal models show which planes were responsible for faceting resulting in the triangular shape of the nanowire. In the wurtzite structure the $\{10\bar{1}1\}$ and (0001) planes faceted and were parallel with the growth direction, while the $\{2\bar{1}\bar{1}0\}$ planes were perpendicular to the growth direction. In the zinc-blende structure the $\{111\}$ planes faceted and were parallel to the growth direction, while the $\{011\}$ planes were perpendicular to the growth direction. Images and interpretation: B.W. Jacobs

Figure 4.11 shows four HRTEM images of certain areas of the cross-section taken from the nanowire grown at 850° C, as indicated by the boxed areas in the center inset. These images highlight the coherent and incoherent interfaces present within the nanowire, as well as the different orientations of each crystalline domain. Multiple interfaces seen within the nanowire in previous plain-view HRTEM investigations were

clearly delineated in these cross-section HRTEM images. Multiple coherent interfaces were seen, which explained the extremely sharp, defect free phase transitions observed in the plain-view images. In figure 4.11(a) several coherent and incoherent interfaces are denoted by the solid and dashed lines, respectively. A crystalline domain with dark contrast is apparent in this figure and in figure 4.11(b), and consisted of a wurtzite structure, possibly in a slightly different orientation, giving it darker contrast than the surrounding areas. There are two zinc-blende domains on the top and left of the dark wurtzite domain that formed coherent interfaces with the surrounding wurtzite domains denoted by the solid lines. The dark wurtzite domain formed incoherent interfaces with all domains that surround it as denoted by the dashed lines. In figure 4.11(c) a long incoherent interface between a wurtzite and zinc-blende domain is denoted by the dashed line. Figure 4.11(d) is an image taken further along this incoherent interface and also shows a long coherent interface between the [111] and [0001] planes in the zinc-blende and wurtzite domain, respectively, as denoted by the solid line. This interface extended from the center of the nanowire 80 nm to the external edge of the nanowire. Each HRTEM image had well resolved lattices indicating the high crystal quality of each domain.

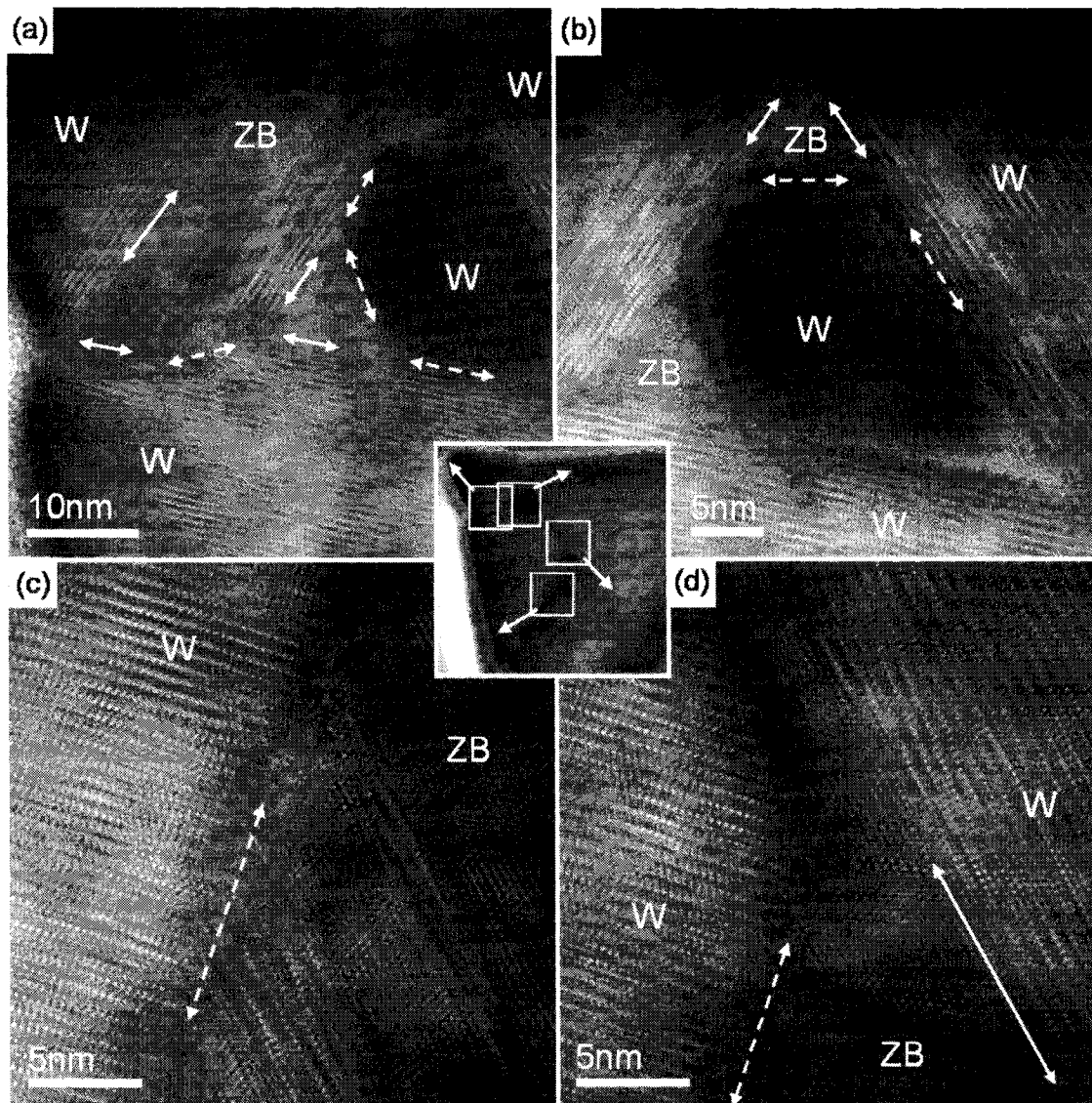


Figure 4.11. HRTEM images of the cross-section taken from the nanowire grown at 850° C. (a) A close up from the corresponding boxed area in the center inset revealed several distinct crystalline domains with coherent and incoherent interfaces, as denoted by the solid and dashed lines, respectively. A dark contrast wurtzite domain was observed and could be due to a slightly different orientation. (b) The dark contrast wurtzite domain, from the corresponding boxed area in the center inset, is surrounded by both zinc-blende and wurtzite domains forming incoherent interface at every edge, as denoted by the dashed lines. The zinc-blende domains form coherent interfaces with the surrounding wurtzite domains, as denoted by the solid lines. (c) A close up of an incoherent interface, denoted by the dashed line, from the corresponding boxed area in the center inset. (d) This image shows the same incoherent interface at a different location. On the right side of this figure a long coherent interface that extends from the center of the nanowire to the outside edge forms between the (111) and (0001) planes, as denoted by the solid line. Images and interpretation: B.W. Jacobs

Detailed HRTEM analysis of the cross-section taken from the nanowire grown at 950° C is shown in figure 4.12. The nanowire was divided into six distinct regions that

separated each crystal domain present in the nanowire. These regions were distinguished by domain interfaces denoted by the dotted line in the HRTEM image in figure 4.12. FFTs taken from each region are shown on the right and bottom. FFTs of regions 1-5 were solved for the wurtzite structure along the $[2\bar{1}\bar{1}0]$ direction. The FFT from region 6 was solved for the zinc-blende structure along the $[011]$ direction. These directions corresponded to the growth directions found for multiphase nanowires in the plain-view HRTEM investigations. The arrows in the FFTs point in the $[0001]$ and $[111]$ directions in the wurtzite domains and the zinc-blende domain, respectively, to emphasize the different orientation of each domain.

Similar to the cross-section shown in figure 4.10, this nanowire faceted on the same wurtzite planes, the $\{10\bar{1}1\}$ and (0001) . There was also a zinc-blende domain in the center of the nanowire that faceted internally on the $\{111\}$ planes and was also diamond shaped. Similar to the cross-section shown in figure 4.10, the (0001) planes were all found as internal interfaces.

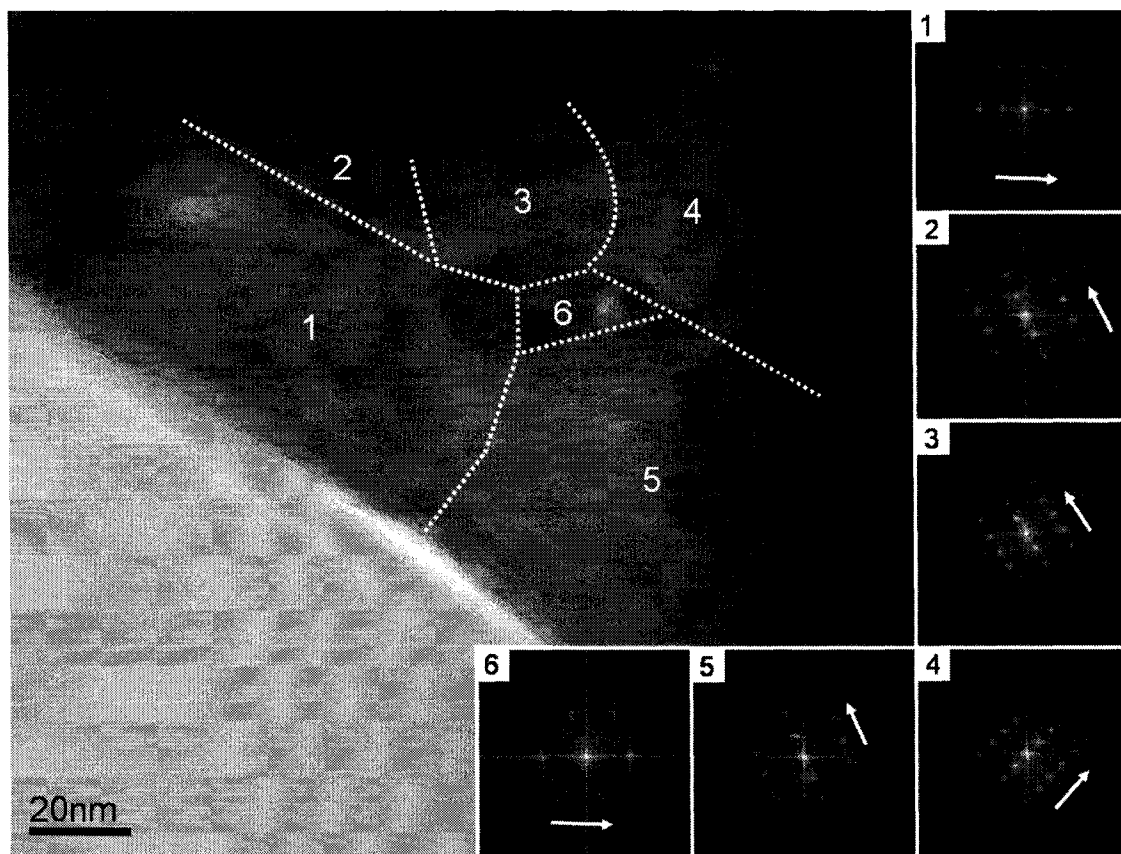


Figure 4.12. Details of the cross-section taken from the nanowire grown at 950° C. This nanowire was separated into six regions corresponding to distinct crystalline domains. These regions were divided along domain interfaces. FFTs from each region are shown on the right and bottom. Regions 1-5 were wurtzite and region 6 was zinc-blende. The arrows point in the [0001] and [111] directions in the wurtzite and zinc-blende domains, respectively, to emphasize differences in orientation. Images and interpretation: B.W. Jacobs

Figure 4.13 shows four HRTEM images of certain areas of the cross-section taken from the nanowire grown at 950° C, as indicated by the center inset. These images highlight the coherent and incoherent interfaces present within the nanowire, as well as the different orientations of each crystalline domain. Figure 4.13(a) shows an incoherent interface between two wurtzite domains. Stacking faults were also seen in this image, and ran horizontally through the center of the figure. In figure 4.13(b) two incoherent interfaces are shown between 3 wurtzite domains. The areas shown in this image also show possible stacking faults on the left and bottom of the figure that transitioned to wurtzite crystal structures. Figure 4.13(c) shows two wurtzite domains with an

incoherent interface. Possible stacking faults were seen in the right hand side of this image. The amount of zinc-blende crystal structure relative to the wurtzite structure was much lower than in the cross-section shown in figure 4.10, and was only observed in region 6, which was found in the very center of the nanowire, as shown in figure 4.13(d). This zinc-blende domain formed a coherent interface with region 1 between the (111) and (0001) planes. A region of light contrast was observed in the right side of this figure. This may be due to a thinner area resulting in lighter contrast relative to the surrounding areas. Each HRTEM image had well resolved lattices indicating the high crystal quality of each domain.

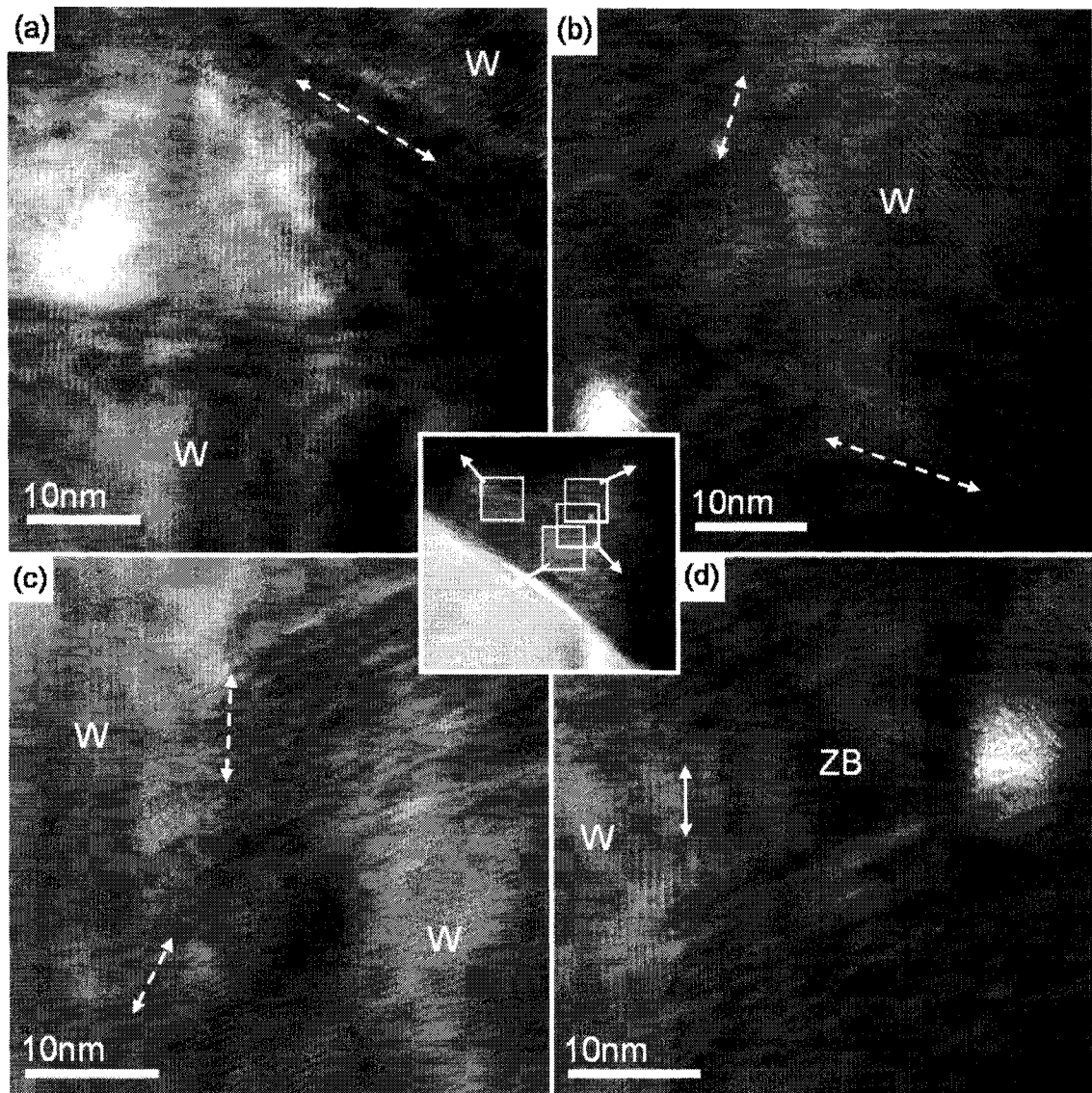


Figure 4.13. HRTEM images of the cross-section taken from the nanowire grown at 950° C. (a) A close up from the indicated area in the center inset revealed two distinct crystalline domains with incoherent interfaces. Possible stacking faults ran horizontally across the center of this image. (b) This image shows three distinct wurtzite domains with two incoherent interfaces. (c) Two wurtzite domains with an incoherent interface that changed its direction running from the center to the outside edge of the nanowire. (d) This image shows the center zinc-blende domain and a coherent interface between the zinc-blende and wurtzite domain. The top and bottom domain surrounding the zinc-blende domain were possible stacking faults that transitioned to wurtzite crystal structures. Images and interpretation: B.W. Jacobs

Detailed analysis of three nanowires in the cross-section taken from nanowires grown at 1000° C revealed a different nanowire growth direction from those grown at the two lower temperatures. With hexagon-shaped cross-sections these nanowires grew in the [0001] direction, and were all wurtzite single-phase nanowires. Nanowires that grew

in this direction had a larger range of observed widths, roughly 200 nm to several microns, than the nanowires grown at the lower two temperatures. The single-phase nanowires that grew in the [0001] direction also tended to have larger widths on average than the multiphase nanowires grown at this temperature as well as the lower two temperatures.

Figure 4.14 shows details of a large nanowire, roughly 1.5 μm in width. The nanowire was divided into two regions, as shown in figure 4.14(a). The wurtzite crystal model at the right of this figure showed that the planes parallel to the growth direction, the {1010} planes, faceted. The (0001) planes were perpendicular to the growth direction. Figure 4.14(b) shows an HRTEM image of region 1 with a well-resolved lattice that indicated the high crystal quality of the nanowire. The FFT of region 1 was solved for the wurtzite structure along the [0001] direction. Figure 4.14(c) shows a close up image of region 2, which revealed a small wurtzite domain with darker contrast than the surrounding region 1. This small domain had a hexagonal shape. However, an HRTEM image not obtained, so its actual crystal structure could not be determined. Figure 4.14(d) shows the entire cross-section and indicated the location of this nanowire.

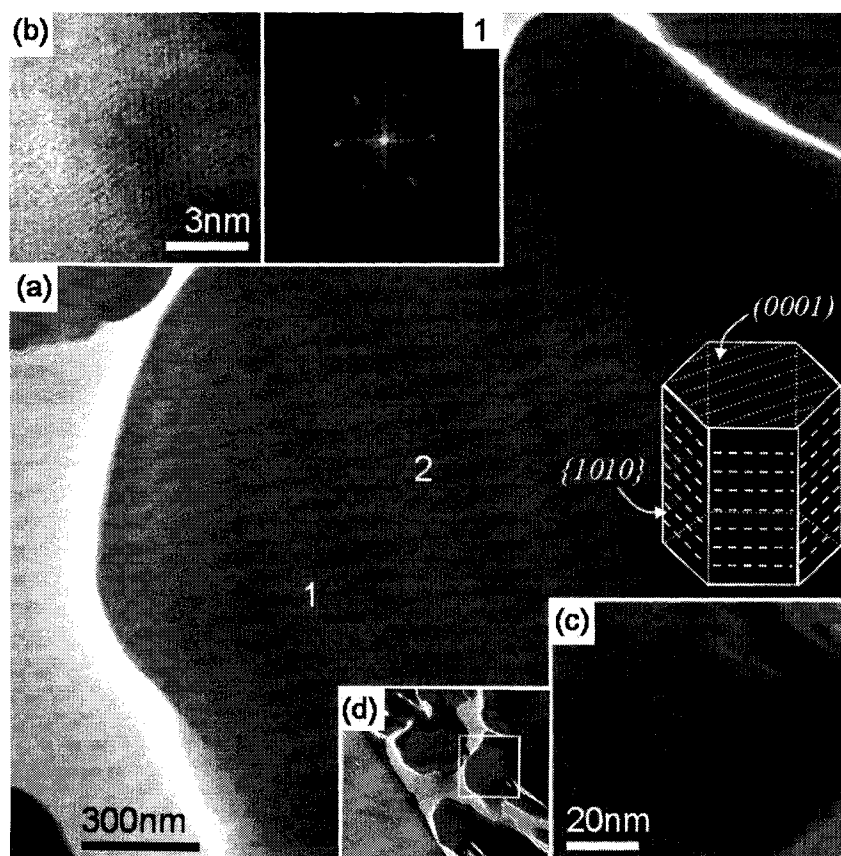


Figure 4.14. HRTEM images of the cross-section taken from the nanowire grown at 1000° C. (a) A large nanowire with a width of roughly 1.5 μm is shown. A wurtzite crystal model shows the facet planes parallel to the growth direction, $\{10\bar{1}0\}$, that resulted in the hexagonal cross-section shape, and the growth plane, (0001), perpendicular to the growth direction. (b) A high-resolution image of region 1 showing the high crystallinity of the nanowire. An FFT of region 1 that could be solved for the wurtzite crystal structure in the [0001] direction is shown in the inset. (c) A close up image of region 2 revealed a dark contrast wurtzite domain. (d) TEM image of the entire cross-section indicating where this nanowire cross-section was located. Images and interpretation: B.W. Jacobs

Figure 4.15 shows details of a smaller nanowire, roughly 200 nm in width. The nanowire was divided into three regions, as shown in figure 4.15(a). Regions 2 and 3 at the center of the nanowire were areas of lighter contrast relative to the surrounding region 1. FFTs of each region shown on the right hand side of this figure all indicated that the nanowire was single-phase wurtzite growing along the [0001] direction. Figure 4.15(b) shows the entire cross-section and indicates the location of this nanowire. Figure 4.15(c) shows an HRTEM image of regions 2 and 3. These regions were observed to be hexagonal in shape. The FFTs of these two regions were in the same orientation of

region 1 and no detectable interfaces were observed between these regions. Figure 4.15(d) shows an HRTEM image of region 1 with a well-resolved lattice that indicated the high crystal quality of the nanowire.

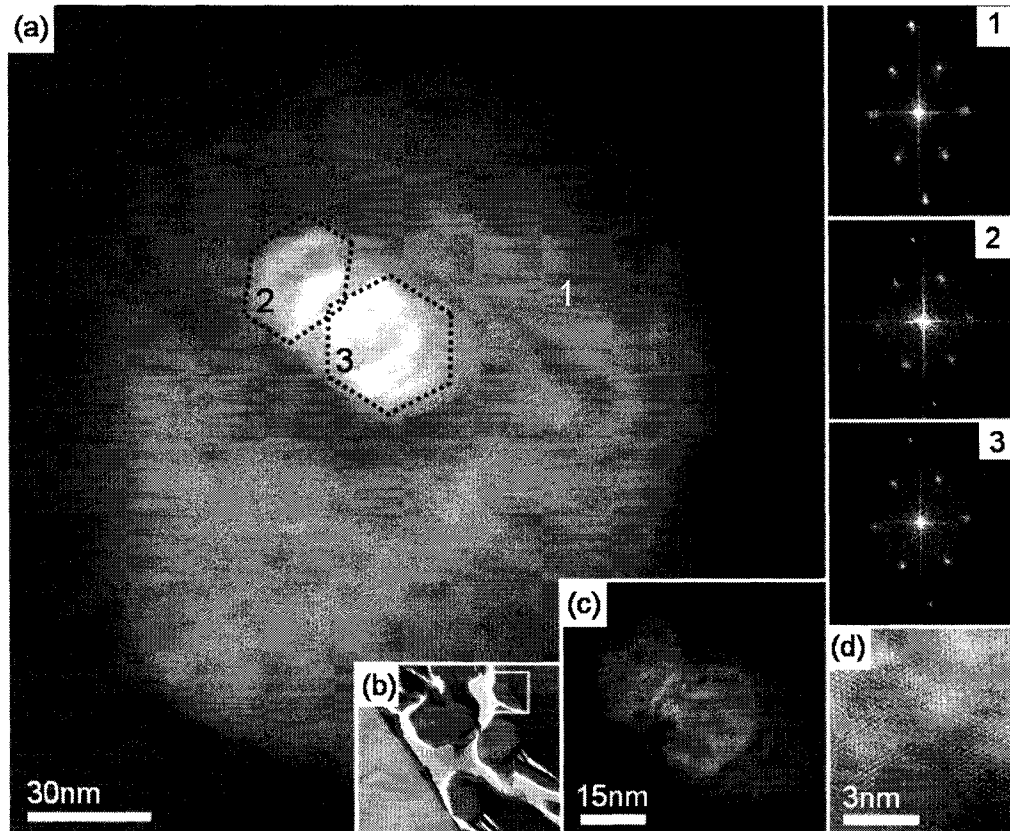


Figure 4.15. HRTEM images of the cross-section taken from the nanowire grown at 1000° C. (a) A small nanowire with a width of roughly 200 nm is shown here. It grew in the same direction as the nanowire shown in figure 4.15. It was divided into three regions. Regions 2 and 3 were lighter in contrast relative to the surrounding region 1. The FFTs shown on the right were all solved for the wurtzite structure along the [0001] direction. They were all in the same orientation. (b) A TEM image of the entire cross-section showing where this nanowire cross-section was located. (c) A close up of region 2 and 3 revealed that the light contrast regions were both hexagonal in shape. (d) A high-resolution image of region 1 showed the high crystallinity of the nanowire. Images and interpretation: B.W. Jacobs

Figure 4.16 shows details of a larger “double” nanowire, roughly 2 μm in width at its widest point. The nanowire was divided into four regions, as shown in figure 4.16(a). Regions 1 and 2 comprised the left and right nanowires that made up the double nanowire, respectively. FFTs of regions 1 and 2 are shown at the bottom of this figure.

They were solved for the wurtzite structure along the [0001] direction. They were also in the same orientation. Figure 4.16(b) shows the entire cross-section and indicated the location of this nanowire. Figure 4.16(c) shows an HRTEM image of region 3. This image shows a small platelet that seemed to partially cover a hole in the center of the nanowire. If the small platelet were to be removed, the hole would be hexagonal in shape, indicating that it faceted on the {1010} planes, the same facet planes as on the external surface of the nanowire. Figure 4.16(d) shows an HRTEM image of region 4. This region also had a hole surrounded by an area of light contrast that is probably due to a thinner area.

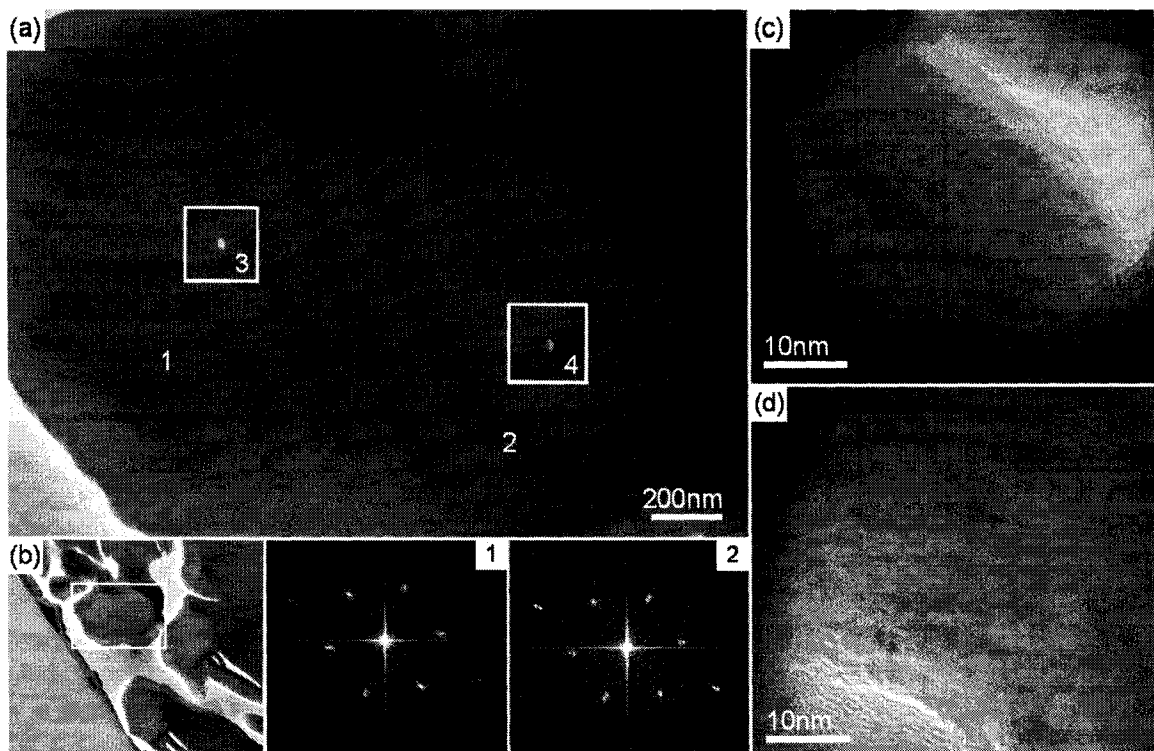


Figure 4.16. HRTEM images of the cross-section taken from the nanowire grown at 1000° C. (a) A large “double” nanowire with a width of roughly 2 μm at its widest point is shown here. It grew in the same direction as the nanowire shown in figure 4.15 and 4.16. It was divided into four regions. Regions 1 and 2 are the left and right nanowires that made up the double nanowire. Regions 3 and 4 were areas with lighter contrast relative to the surrounding regions 1 and 2. The FFTs shown on the bottom of the image were taken from regions 1 and 2, and were solved for wurtzite structure along the [0001] direction. They were in the same orientation. (b) A TEM image of the entire cross-section indicates where this nanowire cross-section was located. (c) A close up of region 3 indicated that the light contrast region was hexagonal in shape. A small platelet was partially covering a hole in the center of the nanowire. (d) A close up of region 4 also shows an area of lighter contrast with a hole at its center. Images and interpretation: B.W. Jacobs

Each cross-section investigated with HRTEM revealed a somewhat different nanowire structure. The cross-sections taken from nanowires grown at 850° C and 950° C were different in the domain orientations as well as the wurtzite to zinc-blende ratios. Each crystalline phase in these nanowires, however, grew in the same direction and faceted on the same planes. The nanowires grown at 1000° C had more similarities in their structure but were different than the nanowires grown at the lower two temperatures. The nanowires were single-phase wurtzite, with growth along the [0001] direction. There were subtle differences between these nanowires also. Small anomalous domains with

light or dark contrast were observed that can not as yet be fully explained. They may be due to thickness variations or slightly different crystal domain orientations resulting in contrast differences.

The evidence for a new multiphase crystalline homostructure in GaN nanowires based on the analysis by HRTEM with SAED, FFT, EDS, EELS, and cross-section analysis has been confirmed. Wurtzite and zinc-blende domains were observed with coherent and incoherent interfaces between the domains. Facet planes were identified that are responsible for the cross-sectional shape of each nanowire. Reliable growth of the multiphase nanowires as well as single-phase nanowires is a result of vapor solid growth, and will be discussed next.

4.2 Nanowire Matrix Investigations

In order to understand how the multiphase and single-phase nanowires grow, the matrix on which the nanowires nucleate was investigated. Using SEM, nanowires have been shown to nucleate from the sides and points of hexagonal platelets that form early in the growth process as previously reported^{22,23,24}. The SEM investigations presented in this thesis agreed with those previously reported findings for matrix that formed at 850° C, 950° C and 1000° C, in that nanowires nucleated from the sides of hexagonal platelets. Further investigations of matrix that formed at 1000° C revealed three distinct regions of matrix with different feature sizes. In the matrix that formed at 1000° C, in addition to the nucleation sites on the sides of the hexagonal platelets, a second type of nucleation site was identified. This nucleation site was located on the tops of hexagonal platelets.

After SEM investigations established where nanowire nucleation was occurring, at the sides of hexagonal platelets, HRTEM investigations were carried out to determine if the nucleation sites had features smaller than those resolved in the SEM. The HRTEM investigations revealed a network of structures on the sides of many hexagonal platelets in the form of nanoscale ledges that were in the same orientation and coherent with the hexagonal platelet.

The SEM and HRTEM investigations of the matrix proved essential in understanding the growth mechanisms involved for multiphase and single-phase nanowire formation. Without the study of the growth matrix, most information about the mechanism involved in multiphase nanowire growth would be unknown.

4.2.1 SEM

Matrix features and nanowire nucleation sites that formed at 850° C, 950° C and 1000° C were investigated with SEM. Distinct differences in the matrix features that formed from each temperature were noted and will be discussed.

Matrix features that formed at 850° C are shown in the SEM images in figure 4.17. These feature sizes were around 200 nm to 1 μm in size. Figure 4.17(a) shows an SEM image of the matrix at low magnification. Figure 4.17(b) shows another SEM image at higher magnification so that subtle features could be resolved. A range of feature sizes is apparent in this image. Two nanowires, indicated by the arrows, have nucleated from the matrix.

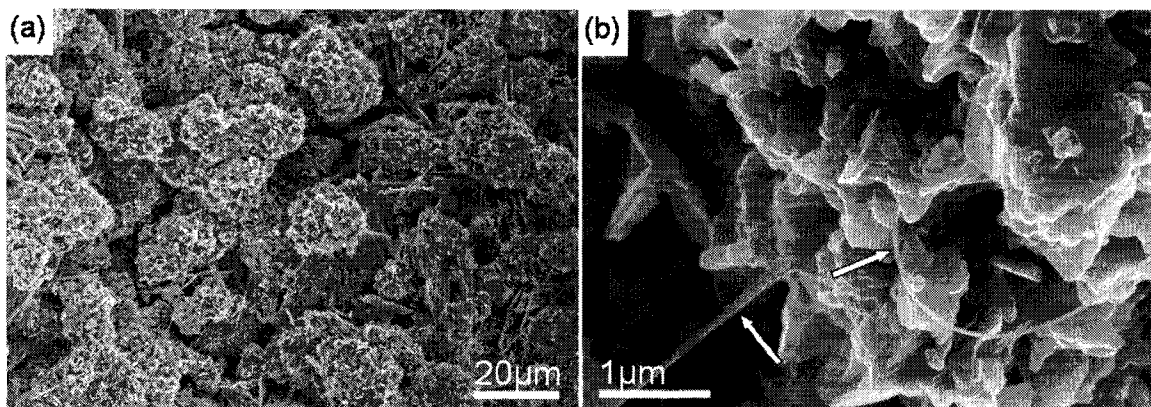


Figure 4.17. SEM images of the matrix that formed at 850° C. (a) The matrix is relatively uniform with feature sizes of around 200 nm to 1 μm in size. (b) A close up image shows the features in detail. There are many small and medium sized GaN crystal formations. Two nanowires in this image, as indicated by the arrows, have nucleated from the matrix. Images: K. McElroy

Figure 4.18 shows SEM images of nanowire nucleation sites on the matrix that formed at 850° C. In figure 4.18(a) a nanowire has nucleated from the corner of a hexagonal platelet. In figure 4.18(b) a nanowire has nucleated from the side of a hexagonal platelet. Although the nanowires shown in these images have nucleated from

different areas of the platelet, they grew in the same direction relative to the hexagonal platelet orientation, assumed to be along the $\langle 2\bar{1}\bar{1}0 \rangle$ direction.

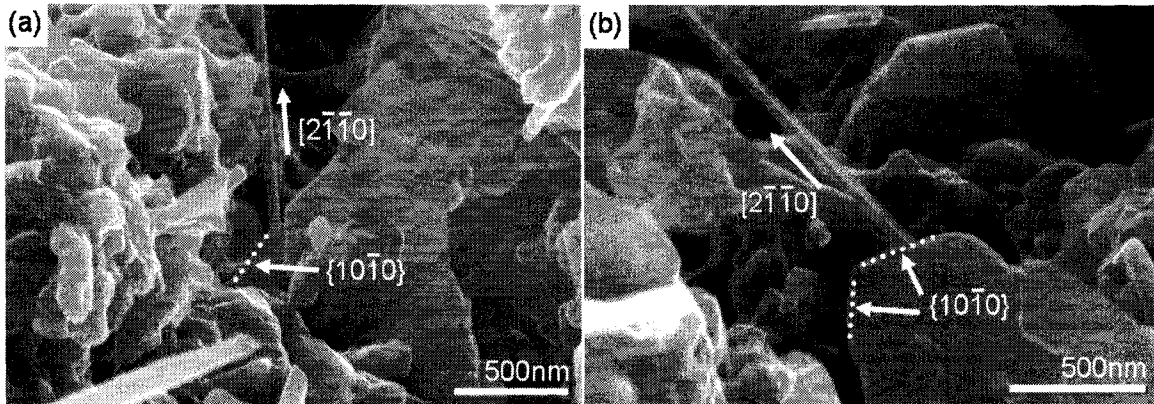


Figure 4.18. SEM images of the matrix that formed at 850° C. (a) A nanowire nucleated from the side of a hexagonal platelet. The arrows show the probable nanowire growth direction, $[2\bar{1}\bar{1}0]$ and the sides of the hexagonal platelet, $\{10\bar{1}0\}$. (b) A nanowire nucleated from the side of a hexagonal platelet. The arrows show the nanowire growth direction and sides of the platelet. Images: B.W. Jacobs

Matrix features that formed at 950° C are shown in the SEM images in figure 4.19. These feature sizes were around 200 nm to 1 μm in size. Matrix that formed at this temperature was very similar to the matrix that formed at 950° C. Figure 4.19(a) shows an SEM image of the matrix at low magnification. Figure 4.19(b) shows another SEM image at higher magnification so that subtle features could be resolved. A range of feature sizes is apparent in this image. A nanowire, indicated by the arrow, has nucleated from the matrix.

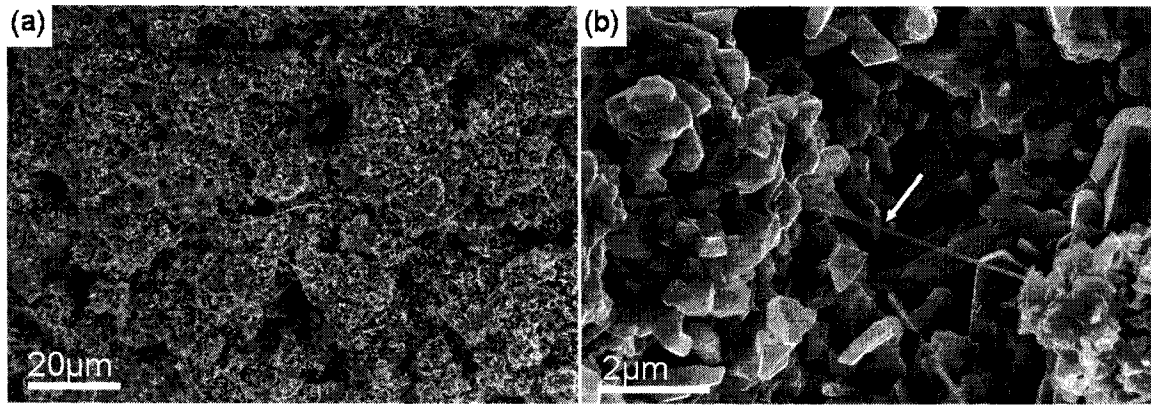


Figure 4.19. SEM images of the matrix that formed at 950° C. (a) The matrix is relatively uniform with feature sizes of around 200 nm to 1 μm in size, and similar to the matrix features formed at 850° C. (b) A close up image shows the features in detail. There are many small and medium sized GaN crystal formations. One nanowire in this image, as indicated by the arrow, has nucleated from the matrix. Images: K. McElroy

Figure 4.20 shows SEM images of nanowire nucleation sites for matrix that formed at 950° C. In figure 4.20(a) a nanowire has nucleated from the side of a hexagonal platelet. The arrows show the probable nanowire growth direction, $[2\bar{1}\bar{1}0]$, and the sides of the hexagonal platelets, $\{10\bar{1}0\}$. In figure 4.20(b) a nanowire has also nucleated from the side of a hexagonal platelet. The arrows show the probable nanowire growth direction, $[2\bar{1}\bar{1}0]$, and the sides of the hexagonal platelets, $\{10\bar{1}0\}$. These nucleation sites are very similar to those found for matrix that formed at 850° C.

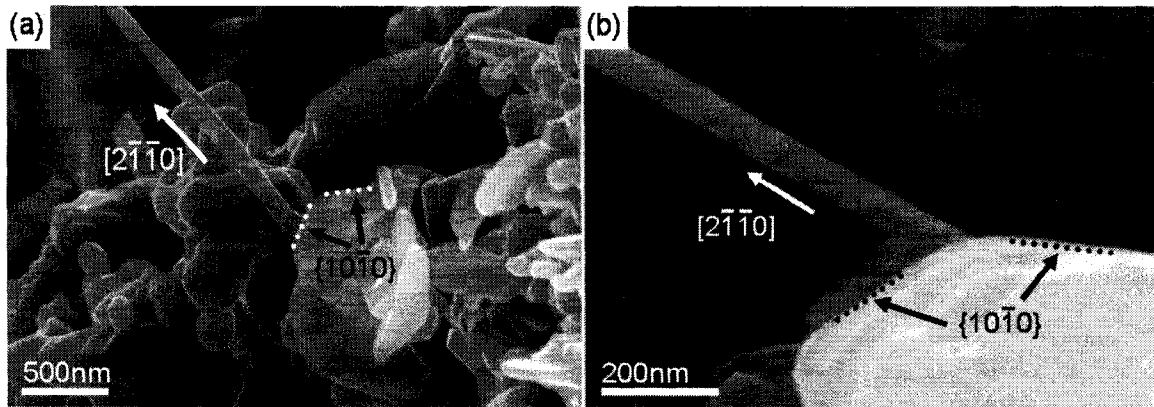


Figure 4.20. SEM images of the matrix that formed at 950° C. (a) A nanowire nucleated from the side of a hexagonal platelet. The arrows show the probable nanowire growth direction, $[2\bar{1}\bar{1}0]$ and the sides of the hexagonal platelet, $\{10\bar{1}0\}$. (b) A nanowire is also shown to have nucleated from the side of a hexagonal platelet. The arrows show the nanowire growth direction and sides of the platelet. Images: B.W. Jacobs

The matrix features that formed at 1000° C were quite different from the matrix features that formed at the lower two temperatures. Three distinct matrix regions were divided according to their feature size, as shown in figure 4.21. The smallest features of around 100 nm to 200 nm in size were observed in region 1. Larger features of around 200 nm to 1 μm in size, similar to the feature sizes found in the matrix that formed at 850° C and 950° C, were observed in region 2. The largest features of around 1 μm to 5 μm in size were observed in region 3. In figure 4.21(a) an SEM image shows how all three regions can form together in one small area. Figure 4.21(b) shows an SEM image of region 1 in the foreground and region 3 in the background to give a sense of scale of how different these matrix features are in size. The arrow denotes where a nanowire nucleated from region 1. Figure 4.21(c) shows an SEM image of region 2 located atop an area of region 3 matrix. This region was comprised of similar features and sizes found in matrix that formed at 850° C and 950° C. The arrows denote where nanowires nucleated from this region. Figure 4.21(d) shows an SEM image of region 3. Large micron size structures are readily seen. This figure shows a large rod that was not found

at the lower growth temperatures. This type of rod is frequently seen in the matrix that forms at 1000° C.

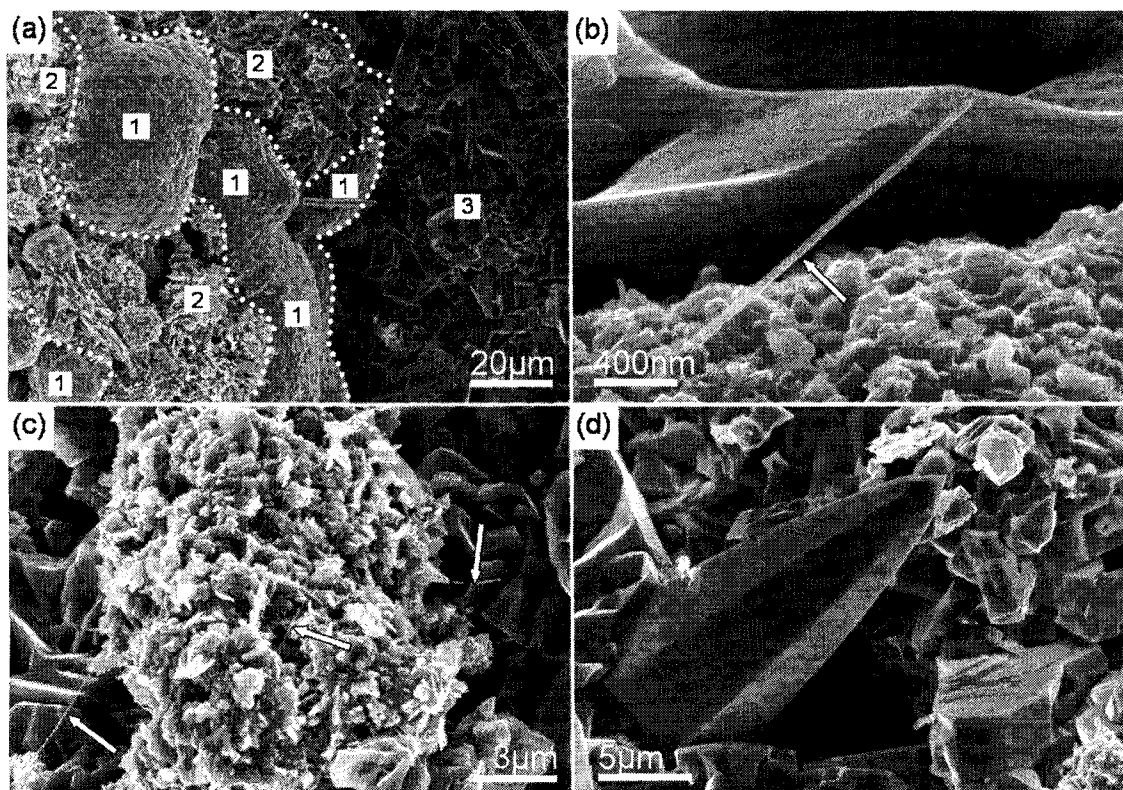


Figure 4.21. SEM images of the matrix that formed at 1000° C. (a) The matrix formed distinct features that could be divided into three regions. Region 1 indicates where the smallest features formed, region 2 the larger features, similar to those found in the matrix that formed at 850° C and 950° C and region 3 with the largest features. (b) A higher magnification image of regions 1 and 3 shows the features in more detail. The small features of region 1, in the foreground, are compared to the larger features of region 3, in the background. One nanowire in this image, as indicated by the arrow, has nucleated from region 1. (c) A higher magnification image of region 2 shows the features in more detail. This region is very similar to the matrix found to form at 850° C and 950° C. Three nanowire in this image, as indicated by the arrows, have nucleated from this region. (d) A higher magnification image of region 3 shows the features in more detail. The large crystal formations are easily seen here. A large rod is seen in the center of the image. These rods were observed in the matrix that formed at 1000° C and not in the matrix that formed at the lower two temperatures. Images: K. McElroy

Figure 4.22 shows SEM and TEM images of nanowire nucleation sites on matrix that formed at 1000° C. The nucleation sites shown in this figure were unique to this growth temperature. Nanowires shown in the SEM image in figure 4.22(a) have nucleated from the top of hexagonal platelets, instead of from the side as shown in the

figures above. Figure 4.22(b) shows an SEM image of what may be a nanowire that started to nucleate from the top of a hexagonal platelet. Figure 4.22(c) and 4.22(d) shows a TEM image where large and small hexagon-shaped light contrast regions can be seen, denoted by arrows. These are identified as holes in the platelet, which can result from TEM sample preparation during which the matrix is sonicated to release the nanowires. Large and small hexagon-shaped holes were observed.

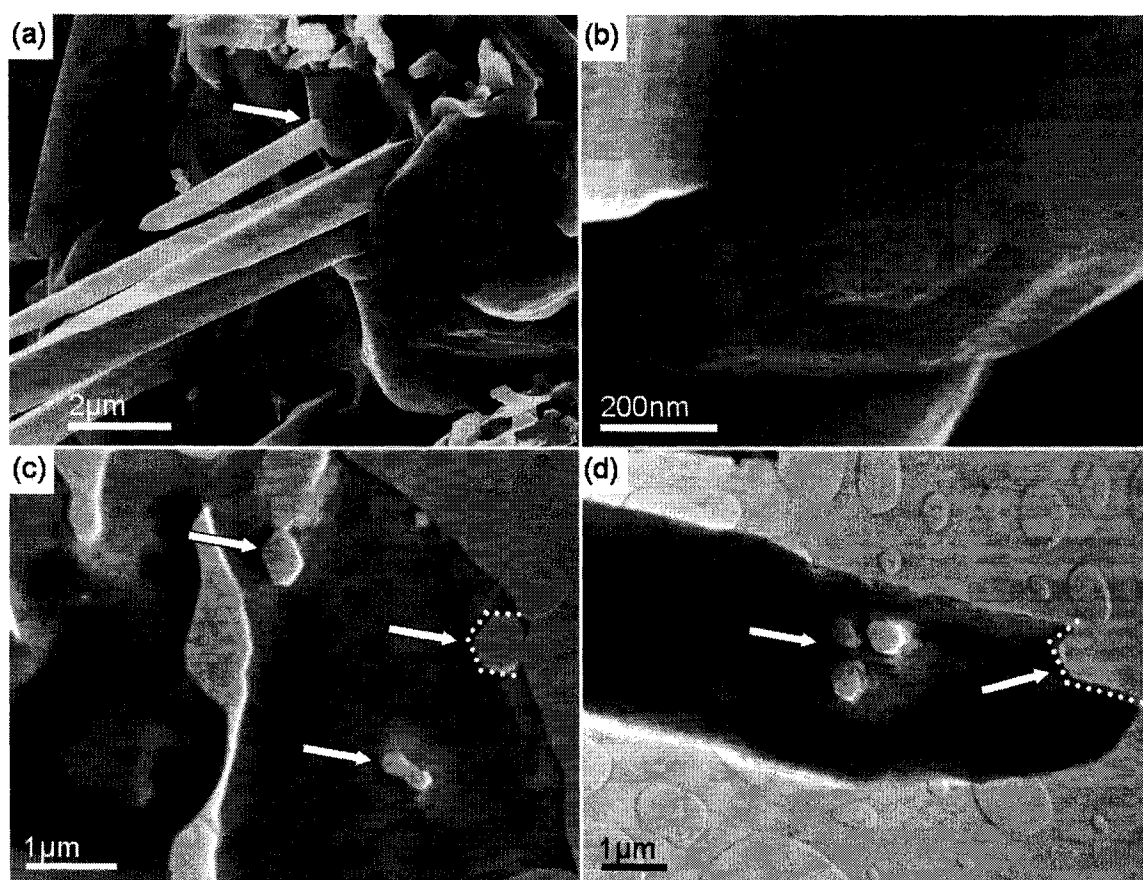


Figure 4.22. SEM and TEM images of the matrix that formed at 1000° C. (a) A SEM image of multiple nanowires that grew from the matrix. The arrow indicates where a nanowire nucleated from the top of a hexagonal platelet. (b) A SEM image of a possible nanowire nucleation site on the top of a hexagonal platelet. (c) A TEM image of the matrix showing large and small hexagonal holes, which may be sites where nanowires nucleated and broke off. (d) A TEM image of the matrix also showing large and small hexagonal holes indicating possible nanowire nucleation sites. Images: (a),(b) K. McElroy, (c),(d) B.W. Jacobs

Nanowire nucleation sites on the sides and corners of hexagonal platelets were also observed in the matrix that formed at 1000° C, not shown. As discussed next, features that were common to matrix formations from each temperature that give rise to similar multiphase nanowire growth were identified.

4.2.2 HRTEM

Further investigation of the matrix with HRTEM revealed features on the sides of the hexagonal platelets that were not resolvable in the SEM. These features consisted of a network of nanoscale ledges as shown in figure 4.23. A typical hexagonal GaN platelet from matrix that formed at 850° C is shown in figure 4.23(a). A close up HRTEM image shown in figure 4.23(b) of the area indicated in 4.23(a) revealed the nanoscale features that were present on the sides of the hexagonal platelet.

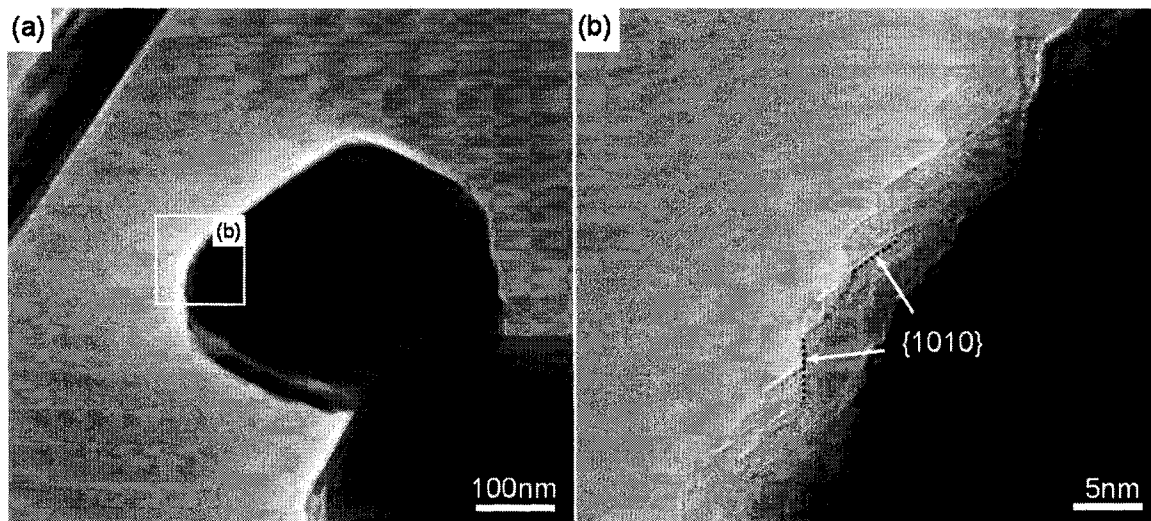


Figure 4.23. TEM images of a hexagonal platelet and its nanoscale ledges from matrix that formed at 850° C. (a) A TEM image shows a typical GaN hexagonal platelet. (b) HRTEM image of the indicated area in (a) revealed a network of nanoscale ledges. Images: B.W. Jacobs

Figure 4.24 shows HRTEM analysis of the nanoscale ledges from hexagonal platelets that formed at 850° C. FFTs and HRTEM images indicated that the nanoscale ledges were in the same orientation and coherent with the hexagonal platelets. Figure 4.24(a) shows an HRTEM image of nanoscale ledges and their orientation. The nanoscale ledges formed peak-like structures that resembled a row of teeth on a saw blade. The two edges of each nanoscale ledge corresponded to the $\{10\bar{1}0\}$ planes as indicated in each image in figure 4.24. The $\langle 2\bar{1}\bar{1}0 \rangle$ directions are also shown because this was the wurtzite growth direction in the multiphase nanowires. The significance of this will be discussed in section 4.3. Figure 4.24(b) shows an HRTEM image of nanoscale ledges that were on the same platelet as those shown in 4.24(a). These platelets were in a different but equivalent orientation. Not all platelets had nanoscale ledges on their sides, however. Figure 4.24(c) shows an HRTEM image of a smooth platelet with no observable nanoscale features in the form of ledges. Figure 4.24(d) is an HRTEM image taken in a slightly different area but on the same platelet where it intersected another hexagonal platelet. Smooth edges are readily seen with no indication of nanoscale ledges.

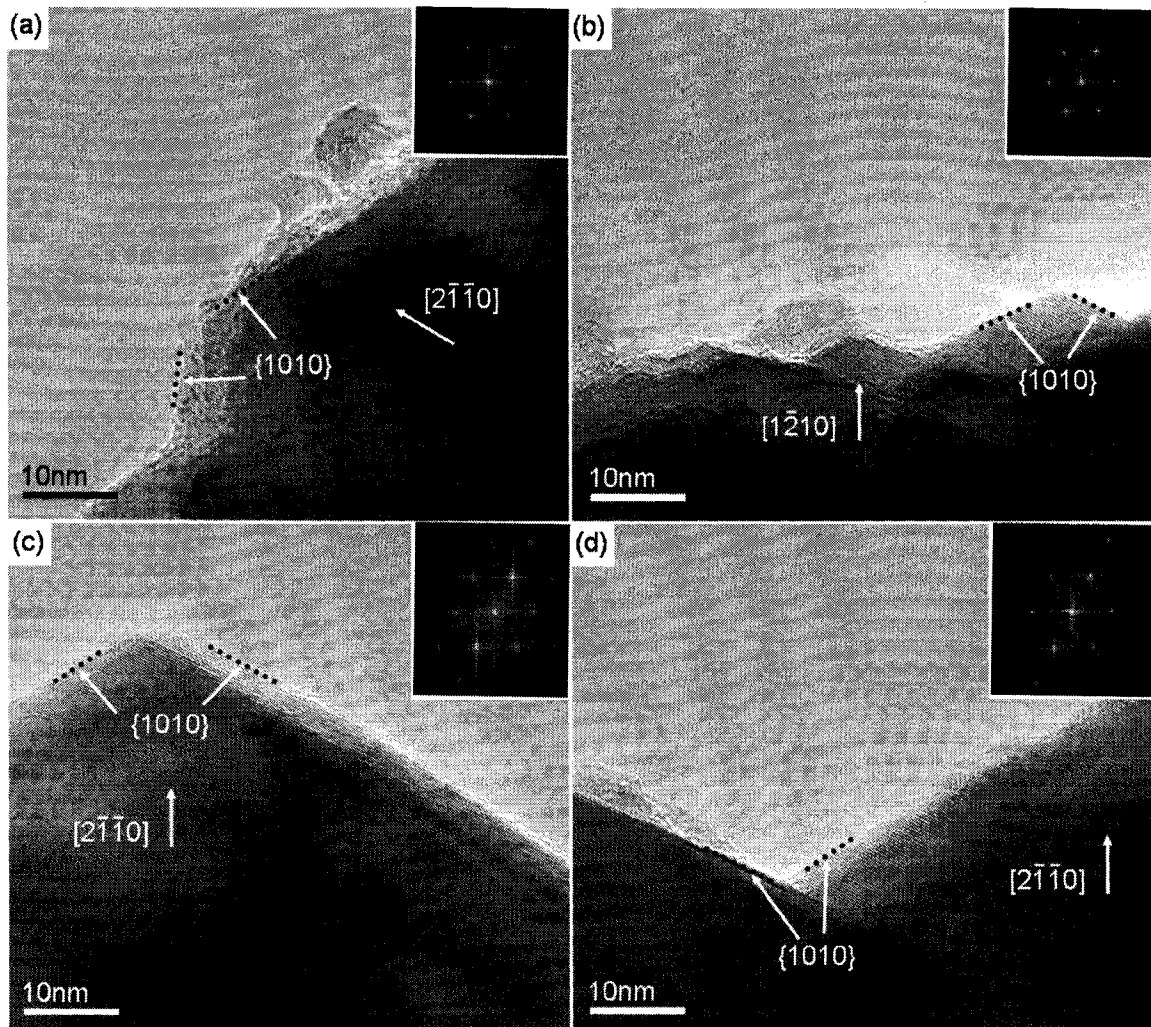


Figure 4.24. HRTEM images of the nanoscale ledges from matrix that formed at 850° C. (a) An HRTEM image shows the side of a hexagonal platelet revealing the orientation of the nanoscale ledges. (b) An HRTEM image taken from a different area of the same hexagonal platelet revealed nanoscale ledges in a different but equivalent orientation as the ledges shown in (a) (c) An HRTEM image of a different platelet shows no nanoscale ledges revealing that not all hexagonal platelets have these features. (d) An HRTEM image of a different area on the same platelet in (c) shows the smooth edges of this platelet. Images: B.W. Jacobs

Figure 4.25 shows TEM and HRTEM analysis of the nanoscale ledges from hexagonal platelets that formed at 1000° C. Figure 4.25(a) is a TEM image showing evidence of hexagonal platelet decomposition leading to the formation of nanoscale ledges. Platelet decomposition will be further discussed in section 4.3. Figure 4.25(b) is an HRTEM image of the boxed area in (a). This image shows the nanoscale ledge orientations relative to the hexagonal platelet. Each ledge was in the same orientation

and coherent with the platelet. An FFT of the nanoscale ledge, shown in the inset, confirmed its orientation. Figure 4.25(c) shows the side of a different platelet. It shows that the nanoscale ledges can form on the long edges of hexagonal platelets. This leads to very asymmetric nanoscale ledges with one $\{10\bar{1}0\}$ plane much longer than the other similar to a staircase rather than a saw blade.

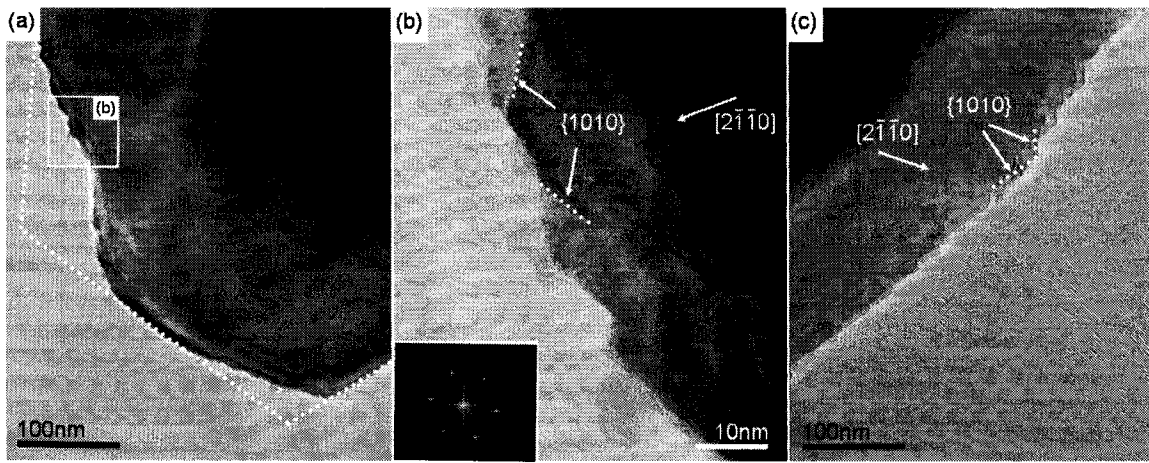


Figure 4.25. TEM images of hexagonal platelets and nanoscale ledges from matrix that formed at 1000°C . (a) Decomposed platelet resulting in the formation of nanoscale ledges. The dotted line indicates a fully formed platelet. (b) An HRTEM image of the area indicated in (a) shows the features and orientation of the ledges. (c) A TEM image of a different platelet indicates that nanoscale ledge formation can occur on the sides of platelets leading to a roughened edge. Images: B.W. Jacobs

These nanoscale nucleation sites were key in understanding how the nanowires nucleated. This type of nucleation site was expected to lead to the formation of multiphase nanowires with multi-domain structures extending in the longitudinal direction. Details of nanowire nucleation on the nanoscale ledges will be discussed next.

4.3 Nanowire Growth and Discussion

SEM investigations of the growth matrix indicated that the multiphase nanowires grew from the sides and corners of hexagonal platelets. It was later discovered that the hexagonal platelets formed at all three growth temperatures had networks of nanoscale ledges in the same orientation and coherent to the hexagonal platelets. The edges and points of the nanoscale ledges were expected to be active and responsible for nanowire nucleation. The peaks of the nanoscale ledges were oriented in the $\langle 2\bar{1}\bar{1}0 \rangle$ direction, the same direction as the wurtzite phase in the multiphase nanowire growth, as shown in figures 4.7-4.9 and in figure 4.26. However, if only the point contributes to nanowire nucleation, the nanowire should be much thinner than it was observed to be.

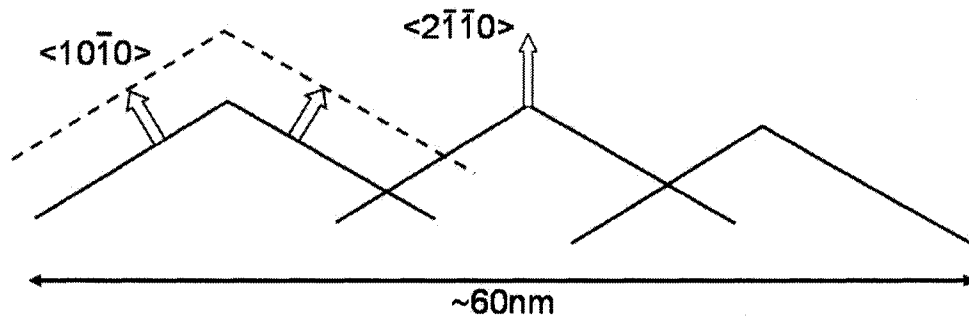


Figure 4.26. Model showing the nanoscale ledges. The edges are the $\{10\bar{1}0\}$ planes and the peaks point in the $\langle 2\bar{1}\bar{1}0 \rangle$ direction. Nanoscale ledge growth occurred on the $\{10\bar{1}0\}$ planes and nanowire growth occurred along the $\langle 2\bar{1}\bar{1}0 \rangle$ direction. Image: B.W. Jacobs

Growth was likely along the active $\{10\bar{1}0\}$ ledges as well as at the field-enhanced active points, as shown in figure 4.26. However, NH_3 is known to break down at step edges²⁷, and nitrogen may be abstracted forming molecular nitrogen, leading to a decomposition process on the surface of the nanoscale ledges, as shown in figure 4.25. These processes are known to occur in GaN thin films. Bombardment of the nanoscale ledges by energetic gallium atoms may also contribute to the decomposition process.

This in turn leads to a line of dangling bonds on the $\{2\bar{1}\bar{1}0\}$ planes, which is expected to be very active, possibly resulting in nanowire nucleation.

Competitive $\{10\bar{1}0\}$ wurtzite growth versus $\langle 011 \rangle / \langle 2\bar{1}\bar{1}0 \rangle$ nanowire growth, such as is shown in figure 4.27, was typical near the nanowire nucleation sites. Platelet and nanowire orientations are inferred from the shape of the platelet and direction of the nanowire, which for the wurtzite phase has always been observed to grow along the $\langle 2\bar{1}\bar{1}0 \rangle$ direction at this growth temperature. However, growth along the $\langle 011 \rangle$ and $\langle 2\bar{1}\bar{1}0 \rangle$ directions eventually dominate growth.

Nucleation at multiple nanoscale ledge sites can also explain the multiple wurtzite domain orientations because multiple nanoscale ledges could contribute to a single nanowire. These observations support the hypothesis that the nanoscale ledges act as the nucleation sites. All nanoscale ledges observed have been wurtzite. Therefore evidence of zinc-blende nucleation from wurtzite GaN was inferred, rather than directly shown.

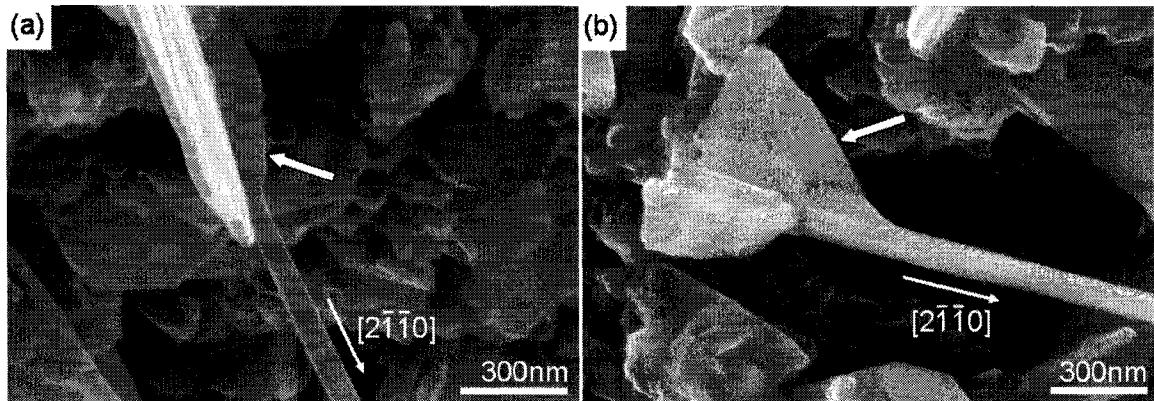


Figure 4.27. SEM images indicating the evidence of the $\{10\bar{1}0\}$ growth. (a) The arrow indicates where the $\{10\bar{1}0\}$ platelet growth occurred, near the nanowire nucleation site, and the nanowire continuing to grow from there. (b) The arrow indicates a similar platelet growth in this image. The nanowire is shown to continue to grow from the base formation. Images: K. McElroy

In the multiphase nanowires, the observed triangular wurtzite domains within the nanowires form regions with $\{10\bar{1}1\}$ and (0001) faces. However, only the $\{10\bar{1}1\}$ planes were observed as external facet planes. The (0001) planes have typically been observed to terminate within the internal nanowire volume. Further, a tapered tip is observed on nanowires that grew along the $[0001]$ direction at 1000°C , as shown in figure 4.14 and 4.28. The external facet planes at the tip are the $\{10\bar{1}1\}$ planes based on the angle relative to the $[0001]$ growth direction.

GaN (0001) planes are known to have multiple surface reconstructions^{28,29}. In the multiphase nanowire system the instability of the (0001) planes may be compensated through the incorporation of the zinc-blende phase, as a second stabilizing aspect of the multiphase configuration. This is readily apparent in the cross-sections in figures 4.12 and 4.14, where the zinc-blende phase could be a convenient option for internal nanowire domain configurations. Also as previously mentioned, nanowires with multiple wurtzite domains could nucleate off multiple nanoscale nucleation sites. The instability of the (0001) planes could cause the wurtzite domains to twist inward after nucleation resulting in (0001) planes that only terminate internally.

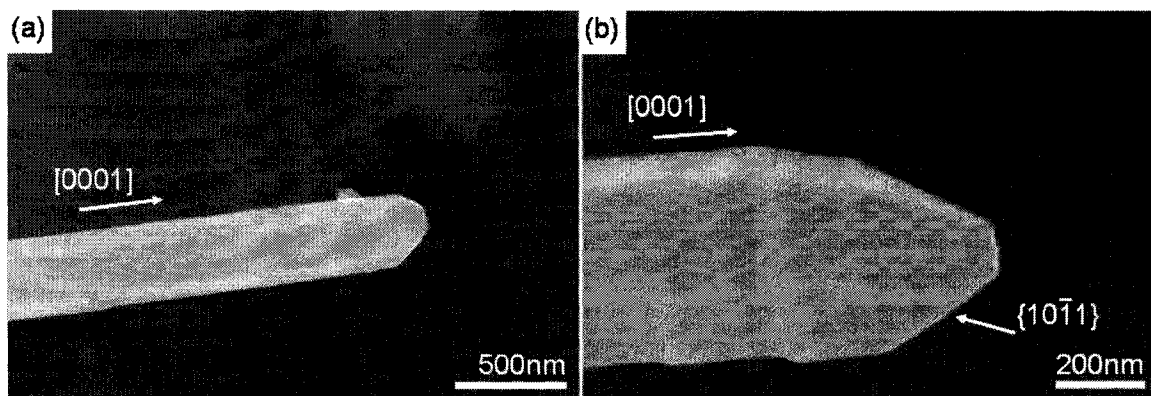


Figure 4.28. SEM images showing the tapered tips of nanowires that grew at 1000°C along the $[0001]$ direction. The tips faceted on the $\{10\bar{1}1\}$ planes. Images: K. McElroy Interpretation: B.W. Jacobs

The multiphase nanowires and nanoscale ledges that acted as nucleation sites were found at all growth temperatures investigated. This can explain the presence of the multiphase nanowires observed at each growth temperature. However, at 1000° C single-phase wurtzite nanowires with growth along the $[2\bar{1}\bar{1}0]$ direction, in addition to the multiphase nanowires, were observed, as shown in figure 4.12. These single-phase nanowires were typically skinnier than the multiphase nanowires. The single-phase nanowire growth may have to do with growth kinetics in addition to the type of nucleation site.

A second type of nucleation site developed at 1000° C, located on the (0001) plane of the hexagonal platelets. Nanowires from this type of nucleation site grew along the [0001] direction, and had hexagonal cross-sections. The reason for nanowire nucleation at these sites is as yet not known, and further investigations are underway in order to understand how nanowires nucleate of the tops of hexagonal platelets.

A formation with a difference in contrast in the HRTEM images was also typically observed at the middle of each nanowire, as shown in figures in section 4.2. Contrast differences may be due to a small variation in thickness with respect to the rest of the nanowire cross-section or a slight crystal domain orientation difference. These features are common in nearly all nanowire cross-sections observed. Continuing investigations are underway to determine if these features propagate the entire length of the nanowire.

Details of the nanowire nucleation sites, including the formation of nanoscale ledges whose orientation dominates the nanowire growth direction, has been discussed. The formation of a totally coherent interface between the zinc blende and wurtzite

phases, which was sustained over the entire length of the nanowire, may provide stability that renders the multiphase configuration energetically attractive. There are several implications associated with this newly discovered ability to consistently grow zinc-blende/wurtzite multiphase GaN nanowires. Multiphase nanowires represent a new class of waveguide structures with important applications in quantum transport and phase specific transport, as will be discussed in the next section. Temperature has been shown to be an important factor in nucleation site formation. Nucleation site control leads to single and multiphase GaN nanowires with high crystalline quality that have tailored and reproducible crystallographic growth directions, which is essential in producing high performance devices. The vapor-solid one-step method described here simplifies growth, making new and complex nanowire structures easier to achieve.

4.4 Electronic Properties

4.4.1 Electronic Investigations of Multiphase GaN Nanowire-Based GaNFETs

Gallium nitride nanowire-based field effect transistors (GaNFETs) have been shown to possess interesting electronic and optical properties due to their wide, direct band gap as discussed in the introduction of this chapter. GaNFETs using multiphase nanowires as active elements were fabricated using electron beam lithography (EBL) and their electronic properties tested.

A highly doped p-type silicon wafer (5 m Ω -cm) was used as the GaNFET substrate and back gate. A 100 nm layer of thermally grown silicon dioxide was used as the gate dielectric, as shown in figure 4.29. The backside of the wafer was stripped of silicon dioxide using diluted HF and Ti/Au (10/70 nm) was thermally evaporated to form a layer of high conductivity for the back gate contact of the GaNFET³⁰. GaN nanowires were then dispersed from an ethanol solution onto the substrate, and source and drain contacts were patterned via EBL. Ti/Au (10/30 nm) was thermally evaporated for the conducting source and drain contacts after being exposed to a 100 W oxygen plasma (March Instruments PX-250) for 30 s to 1 min to remove any electron beam resist residue. Subsequent metal lift-off was performed in heated acetone.

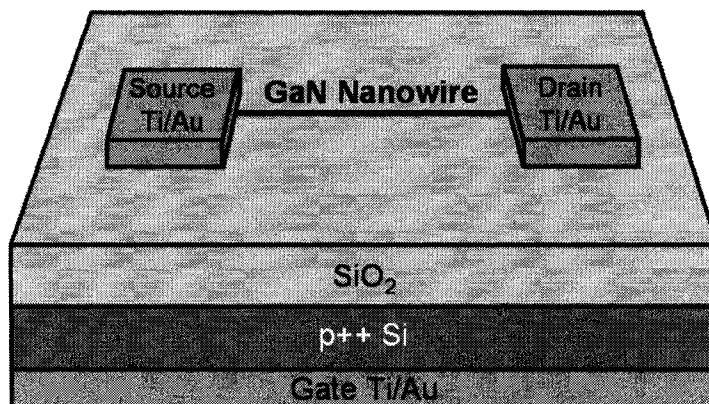


Figure 4.29. A typical GaNFET configuration. A highly doped silicon wafer was used as the substrate. SiO₂ was grown as the gate dielectric and a layer of metal was thermally evaporated on the backside of the wafer for the gate electrode. Nanowires were dispersed on top of the wafer and source and drain contacts were patterned with EBL. Image: B.W. Jacobs

Current–voltage (I-V) measurements of a GaNFET were done using a Keithley 4200-Semiconductor Characterization System (SCS)³¹. The GaNFET was connected to the 4200-SCS through macroscopic probes via photolithographically patterned contact pads, with EBL patterned electrodes contacting the nanowire. The global back gate was contacted to the probe station chuck. Measurements were done in ambient air at room temperature in a shielded enclosure.

During these measurements the drain–source (DS) voltage was continually swept from -5 to $+5$ V_{DS} as the gate–source (GS) voltage stepped from -30 to $+30$ V_{GS} in steps of 10 V. I–V curves, figure 4.30(a), indicated Schottky barrier behavior since the current changed non-linearly as V_{DS} was swept and V_{GS} stepped. Current modulation from $+2$ to $+12.6$ μ A was observed as V_{GS} was stepped from -30 to $+30$ V_{GS} at $+5$ V_{DS}. Current modulation from -6 to -13.7 μ A was observed as the gate voltage was stepped from -30 to $+30$ V_{GS} at -5 V_{DS}. This behavior was typical for an n-type device. Figure 4.30(b) shows V_{GS} swept as V_{DS} was stepped, and was extracted from the V_{DS} swept data in

figure 4.30(a). V_{DS} was stepped in increments of 1 V. The calculated transconductance, g_m , for this device was ~ 4 nS, where $g_m = \Delta I_{DS} / \Delta V_{GS}$.

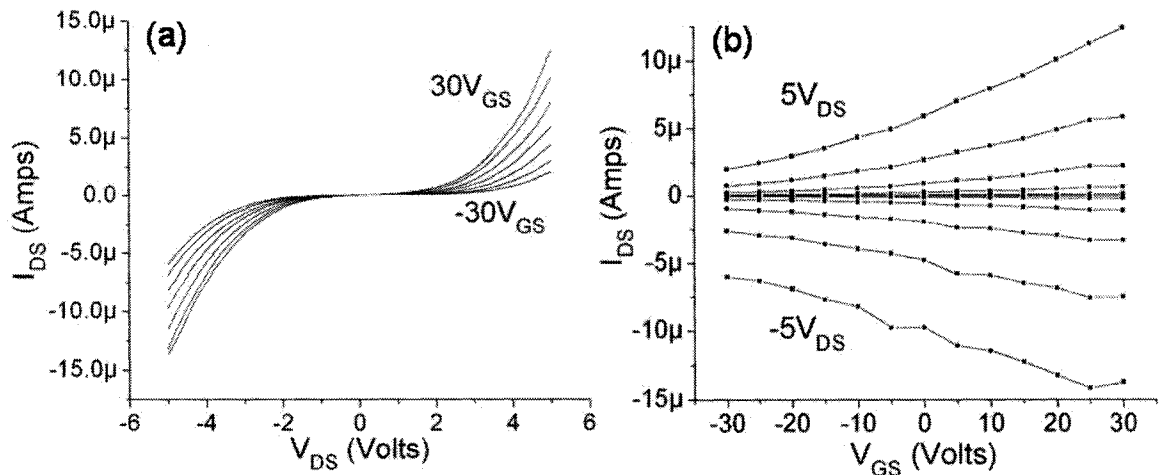


Figure 4.30. I-V characteristics of a GaNFET. (a) The current was measured as V_{DS} was swept and V_{GS} stepped. The nonlinearity of the curves indicated Schottky barrier behavior. (b) This graphs emphasizes the change in current as a result of the change in V_{GS} . These data were extracted from the data in (a). I-V Characteristics: B.W. Jacobs *et al. Nanotechnol.*, **18**, 475710 (2007) with permission.

Additional I-V characteristics of GaNFETs were measured at NASA Goddard Space Flight Center. V_{DS} was varied and the resulting current was measured, but the gate terminal was not contacted in these experiments. Figure 4.31(a) shows a typical I-V curve of a circuit investigated in this study. Over $70 \mu\text{A}$ was measured at $6 V_{DS}$. The nonlinearity of the curve can be attributed to the Schottky barrier that formed at the nanowire-metal junction as mentioned above and further discussed below. Figure 4.31(b) shows an SEM image of the actual circuit. The nanowire was on top of a SiO_2 insulating layer and Ti/Au contacts were thermally evaporated on top of the nanowire and SiO_2 layer. The arrow shows the path of the induced current through the Ti/Au contacts and the nanowire.

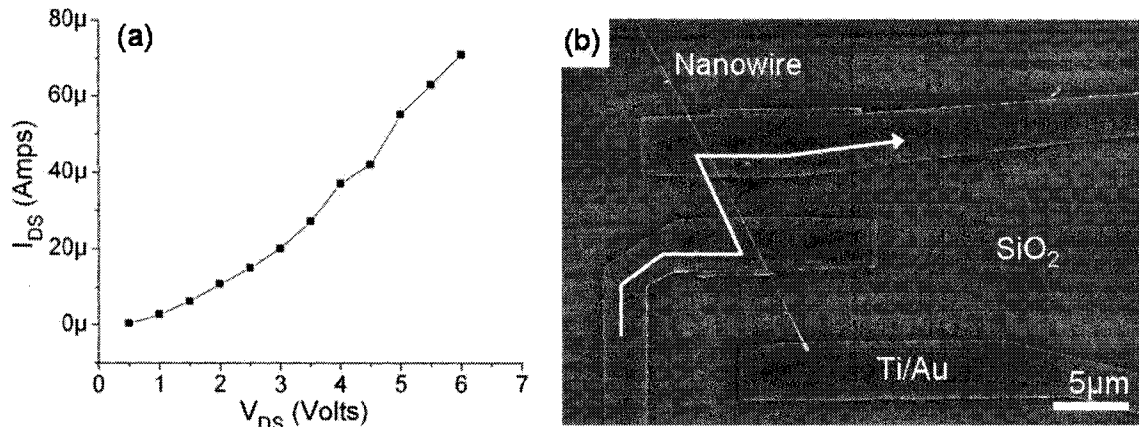


Figure 4.31. I-V characteristics of the circuit shown in the SEM image. (a) The nonlinear curve indicated that the nanowire-metal junction formed a Schottky barrier. At 6 V_{DS} over 70 μA of current was passing through the nanowire. (b) An SEM image shows the actual circuit. The SiO_2 insulating layer and Ti/Au contacts are labeled. The arrow shows the path current takes through the circuit. I-V characteristics, image and interpretation: B.W. Jacobs

The circuit shown in figure 4.32 was fabricated with three nanowires contacted in parallel. This showed that the current roughly scaled accordingly with the addition of two nanowires. Over 400 μA was measured at 6 V_{DS} , as shown in 4.32(a). Figure 4.32(b) shows the entire circuit and gives an overall picture of how the circuit was fabricated. First the large Ti/Au pads were patterned with photolithography (PL). The nanowires were then deposited on the surface, and the Ti/Au contacts were patterned with EBL. Figure 4.32(c) shows two contacted nanowires. The EBL contact on the right was on top of the PL pad, thereby completing the circuit. Figure 4.32(d) shows the third nanowire contacted with EBL.

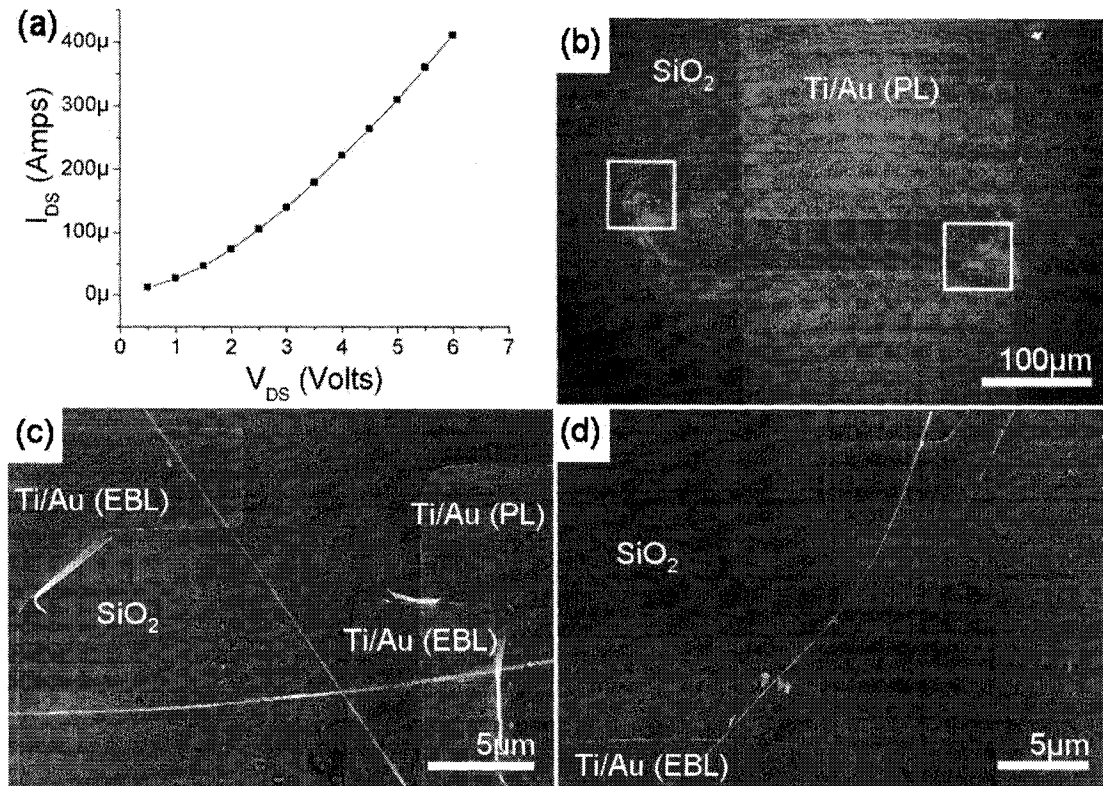


Figure 4.32. I-V characteristics of a GaNFETs with three nanowires hooked in parallel. (a) The measured current was very high, over 400 μA , at 6 V_{DS} . (b) An SEM image shows the entire circuit. Photolithography (PL) was used to define the large contact pads where the contact probes were placed. The left and right boxes denote where close ups were taken in (c) and (d), respectively. (c) An SEM image showing two nanowires contacted in parallel. EBL was used to define the areas where metal was deposited on top of the nanowires. The bottom left pattern created with EBL is seen on top of an PL defined pattern. (d) A SEM image shows the third nanowire hooked in parallel and the EBL defined patterns that connected it. I-V characteristics, images and interpretation: B.W. Jacobs

Investigations by some groups suggest that it is the Schottky barriers between the Ti/Au source and drain and the GaN nanowire that are the source of the transistor behavior^{32,33,34}. A putative model for similar devices utilizing carbon nanotubes has also been developed^{35,36,37}. In the case of these GaNFETs, raising and lowering of the barrier through an electrostatic interaction between the source and drain contacts and the back gate electrode explain the ability of the gate to modulate the current. The current arises from both tunneling and thermionic emission injection in varying proportions, and was dependent upon the height and thickness of the barrier³⁸.

In the FET experiments the current was modulated via the gate voltage, with less current flowing when $-30 V_{GS}$ gate was applied, $2 \mu A$, relative to the current flowing when $+30 V_{GS}$ gate was applied, $12.6 \mu A$, both at $+5 V_{DS}$. The gate voltages needed to significantly modulate the current were somewhat high, and the on-off ratio was therefore low. This may be due to the high contact resistance between the nanowire and Ti/Au contact, as will be discussed in the two and four-point probe investigations. This resistance may be improved with further processing steps such as rapid thermal annealing.

The electronic transport characteristics between metal electrodes and GaN nanowires in such devices are of great importance when maximizing device performance, as these junctions play a critical role in device behavior. Therefore, two and four-point probe investigations were carried out to quantify the contact resistances in a GaNFET device using a state-of-the-art probing instrument, as discussed next. However, carrier injection into nanowires has yet to be completely explained at a fundamental level, which impedes the effectiveness of device design.

4.4.2 Electronic Investigations of an Individual Multiphase GaN Nanowire

The electronic characteristics of an individual GaN nanowire were investigated using two-point and four-point probe techniques. A GaNFET was used as the test sample in these experiments. The back gate was not used. The experiments were performed using a Zyvex KZ100 Nanomanipulator system. The KZ100 is a hybrid instrument interfacing the Keithley 4200-SCS and the Zyvex S100 Nanomanipulator, as shown in figure 4.33. It is equipped with probes that are electrochemically etched tungsten

polycrystalline wires with a nominal tip diameter of 50 nm. The KZ100 is capable of probe positioning resolution under 5 nm. This small tip diameter and precise probe positioning allows direct probe-nanowire connections. The electronic characterization with the KZ100 was performed in a LEO 1530 FESEM at room temperature, allowing real-time, visual inspection with the SEM during the experiments. During measurements the SEM electron beam was turned off, and during visual inspection a low energy beam was used to minimize charge penetration effects. The tungsten probes were electrically cleaned *in situ* to provide a clean tungsten surface for measurements.

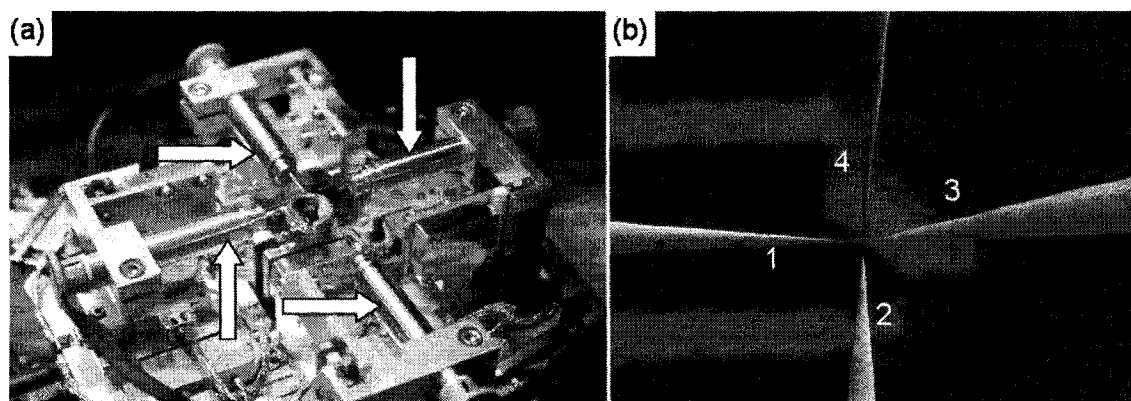


Figure 4.33. The Zyvex S100 Nanomanipulator System. (a) The entire probing system is mounted in an SEM for high resolution imaging essential for nanoprobng and nanomanipulation. The arrows point out the four piezoelectrically controlled tungsten nanomanipulators. Images: R. Stallcup, A. Hartman and V.M. Ayres

4.4.2.1 Four-Point Probe

In the four-point probe measurements, the intrinsic nanowire resistance and the Ti/Au-nanowire contact resistances were determined³¹. This was done using floating voltage sense probes that were situated between two current source probes. This configuration is used to eliminate probe contact resistance effects, as described in chapter 2, so that the intrinsic nanowire resistance can be measured. The nanoscale voltage

probes are important for four-point probe measurements of single-nanowire systems since they are less invasive than macroscopic probes and contacts. The 4200-SCS is also ideally suited for measurements in such nanoprobe configurations because it can make measurements with very low noise and can have input impedances greater than $10^{16} \Omega$.

Four separate four-point probe configurations were carried out to determine both total system and intrinsic nanowire resistance, as shown in figure 4.34. In configuration A, the current source and voltage sense probes were placed on the Ti/Au contacts, as shown in figure 4.34(a), to measure the total system resistance. In configuration B, the current source probes were placed on the Ti/Au contacts and voltage sense probes were directly contacted to the nanowire, as shown figure 4.34(b), to investigate the nanowire resistance. In configuration C, the current source and voltage sense probes were directly contacted to the nanowire, as shown in figure 4.34(c), also to investigate the nanowire resistance. In configuration D, one current source probe was directly contacted at one end after breaking the nanowire, the voltage sense probes directly contacted the nanowire, and the other current source probe was placed on the Ti/Au contact, as shown in figure 4.34(d). The open nanowire end contact was achieved through probe impact on the nanowire top surface, which resulted in a brittle fracture. This configuration was possible due to the probe tip diameter, which is around 50 nm, as it is comparable to the open nanowire cross-section width.

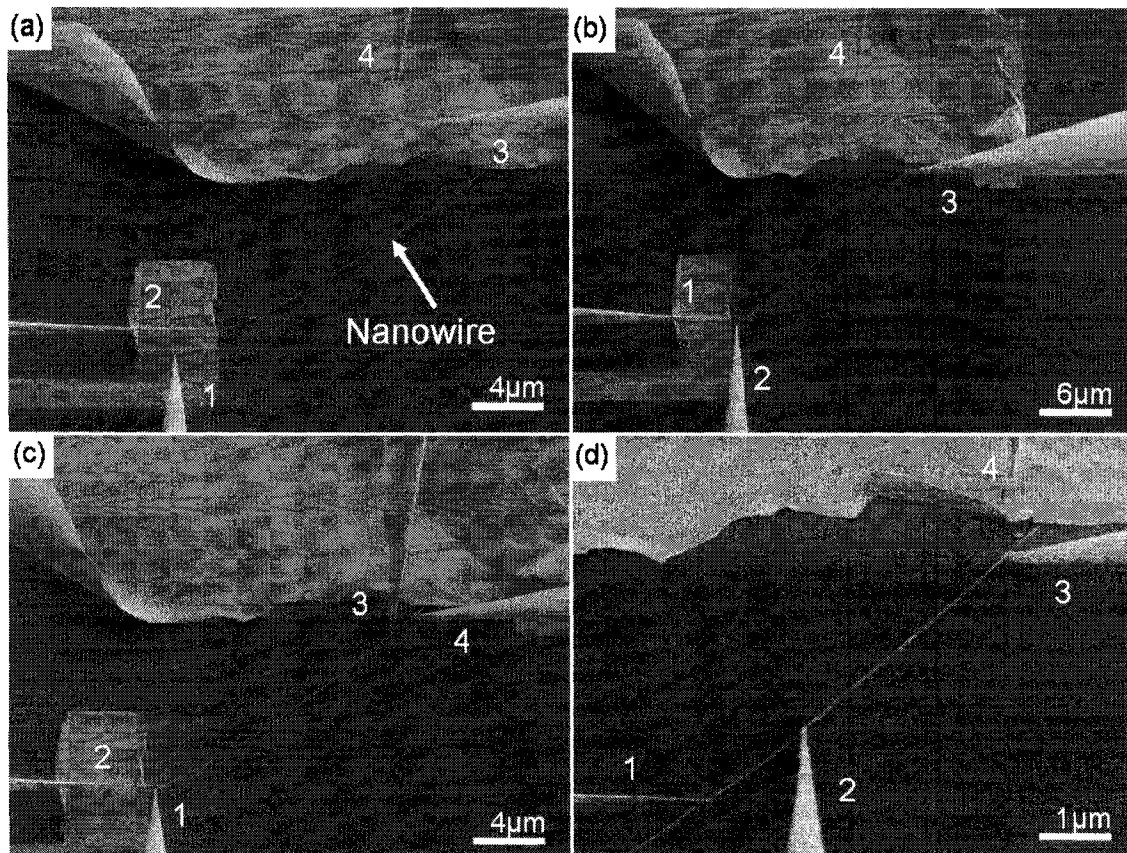


Figure 4.34. SEM images showing the four-point probe configurations. Probes 1 and 4 were the current source probes, 2 and 3 were the voltage sense probes. (a) Configuration A, all probes were contacted to the contact pads. (b) Configuration B; current source probes were contacted to the contact pads, while the voltage sense probes were contacted to the nanowire. (c) Configuration C; all probes were contacted to the nanowire. (d) Configuration D; one current source probe was contacting the end of the nanowire and the other the contact pad, while the voltage sense probes were contacted to the nanowire. Images: B.W. Jacobs *et al. Nanotechnol.*, **18**, 475710 (2007) with permission.

The four-point resistance measurements from configuration A, used to determine the total system resistance, consistently produced a resistance of between 3 and 6 M Ω , as shown in figure 4.35(a), which is comparable to other reported findings³⁹. The graph also shows “negative” resistance, however this was a result of taking measurements in the opposite direction, i.e. a negative voltage, not a negative resistance. Measurements made in configurations B and C were used to determine the intrinsic nanowire resistance. In both configurations the nanowire resistance was between 500 and 800 k Ω , as shown in figure 4.35(b). Probe coupling directly to the nanowire in these configurations appeared

noisy at low source currents, but resistance values reduced to more consistent values at higher source currents. For a length of $16\ \mu\text{m}$ between the voltage sense probes, and using a triangular base width and height of $100\ \text{nm}$, the resistivity was calculated to be $15.6\ \text{m}\Omega\text{-cm}$. Configuration D was also used to determine nanowire resistance. After the nanowire fracture, the voltage sense probes were situated closer together at $10\ \mu\text{m}$, and the nanowire resistance was between $375\ \text{k}\Omega$ and $3\ \text{M}\Omega$, as shown in figure 4.35(c). It was noted that these data were the noisiest among all configurations, and was like a result of the end-contacted configuration where coupling may be somewhat different than in the side-contacted configuration.

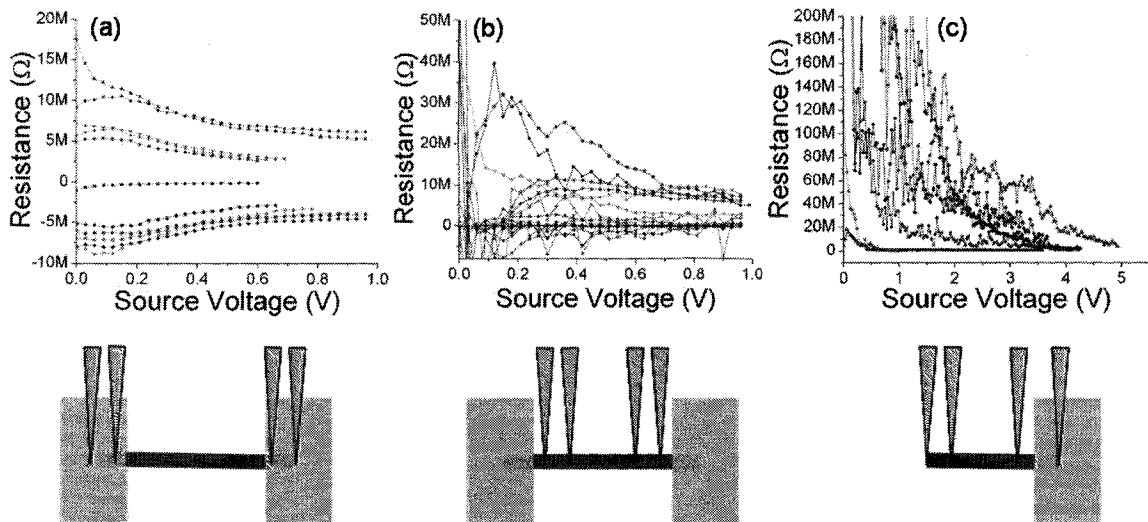


Figure 4.35. Four-point probe resistance measurements. (a) Configuration A, total system resistance measurement. Resistance values were between 3 and 5 $\text{M}\Omega$. Negative values corresponded to current sourced in the opposite direction. (b) Configuration C, NW resistance measurement, side contact. Resistance values were between 500 and 800 $\text{k}\Omega$. (c) Configuration D, NW resistance measurement, end contact. Resistance values were between 375 $\text{k}\Omega$ and 3 $\text{M}\Omega$. Below the resistance diagrams are the corresponding nanomanipulator nanoprobe placements for each configuration. Resistance measurements and diagrams: R. Stallcup, A. Hartman, V.M. Ayres and B.W. Jacobs

4.4.2.2 Two-Point Probe

Two-point probe experiments were also conducted in configurations A, C, and D.

The purpose was to study the change in dynamic resistance in each configuration due to size differences of the probe tips and the Ti/Au contacts. The dynamic resistance of the total system including the probe–Ti/Au–nanowire contact was investigated in configuration A. The dynamic resistance of the probe–nanowire contact was investigated in configuration C. Two-point probe–nanowire breakdown investigations were conducted in configuration D.

In configuration A, two-point probe measurements were conducted to investigate the dynamic resistance, $R = \Delta V/\Delta I$, of the total system. The nonlinear character observed for the I – V characteristics corresponded to a total system resistance, R , which was comprised of the contact, R_{C1} and R_{C2} , nanowire, R_{NW} , and probe, R_{P1} and R_{P2} , resistances, where

$$R = R_{P1} + R_{C1} + R_{NW} + R_{C2} + R_{P2}.$$

The probe resistances, R_{P1} and R_{P2} , were assumed to be negligible in configuration A since the tungsten probes and Ti/Au contacts should couple well due to the metal on metal contact. This was confirmed in the four-point probe measurements in this configuration, where the source voltage and sense voltage were close in value. The total dynamic resistance measured in this configuration followed a power law as shown in figure 4.36, where

$$I(V) \propto V^{1.7}.$$

In configuration C, two-point probe measurements were conducted to investigate the dynamic resistance of the probes and nanowire. R_{C1} and R_{C2} were omitted by directly contacting the probes to the nanowire. Therefore R_{NW} , R_{P1} , and R_{P2} were measured. The total dynamic resistance in this case followed a different power law, also shown in figure

4.36, where

$$I(V) \propto V^{2.2}$$

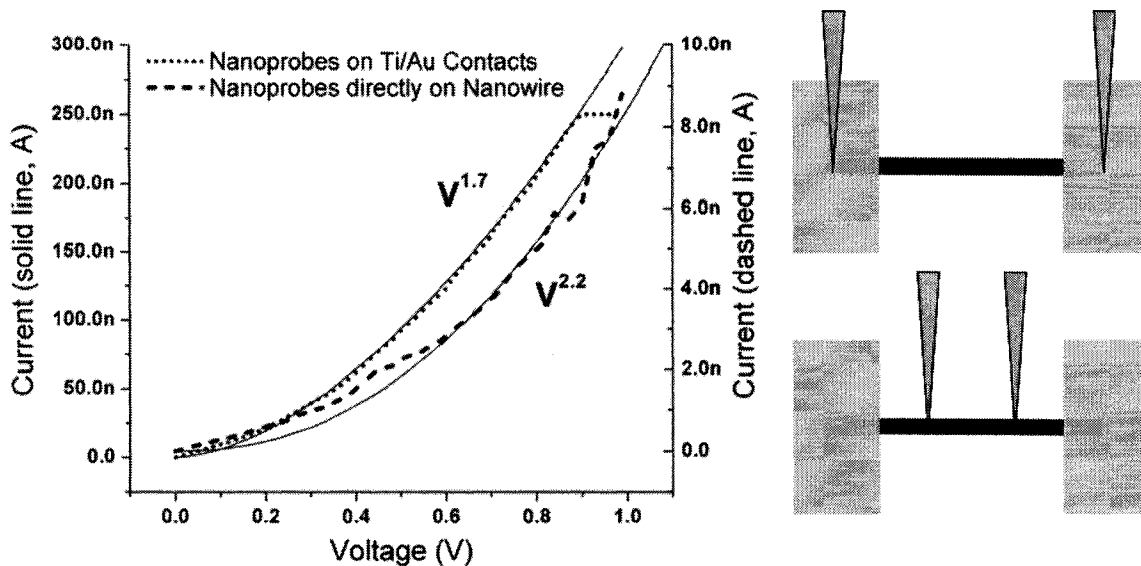


Figure 4.36. Two-point probe results. The graph shows the different voltage dependences of the current when the probes are on the Ti/Au contacts (dotted line, compliance was set to 250 nA) and directly on the nanowire (dashed line). Diagrams of the probe configurations are shown on the right. I-V characteristics and diagrams: K. McElroy and B.W. Jacobs

The dynamic resistance behavior from the two-point probe investigations suggests the formation of a Schottky barrier at the probe–nanowire contact as well as at the Ti/Au–nanowire contact. The different exponents could result from variations in coupling, and indicate different barriers between the probe–nanowire and Ti/Au–nanowire interfaces. It has also been shown that for a carbon nanotube system a smaller metal contact area concentrates the electric field at the junction³⁶. Electron conduction channel variations through the contact may also play a role in contact resistance, where microscopic to microscopic contacts may increase the carrier injection efficiency⁴⁰.

After measurements were made in configuration D, where the nanowire was broken in the middle, as shown in figure 4.37(a), the breakdown behavior was investigated. The source current was increased from 10 nA through 50 μ A, with

breakdown occurring around 50 μA . After each measurement the nanowire was visually inspected with the SEM. After breakdown, a pull-apart of the nanowire at a point approximately midway between the voltage sense probes was observed in the SEM, figure 4.37(b). Also, a new phenomenon was observed prior to breakdown. A liquid protrusion formed at the directly contacted end while the external structure remained intact. A small liquid ball was clearly observable by 10 μA , as shown in figure 4.37(c), and continued to grow in size to over 100 nm in diameter, as shown in figure 4.37(d). The liquid nature of the protrusion was verified by mechanically pushing into it with the probes.

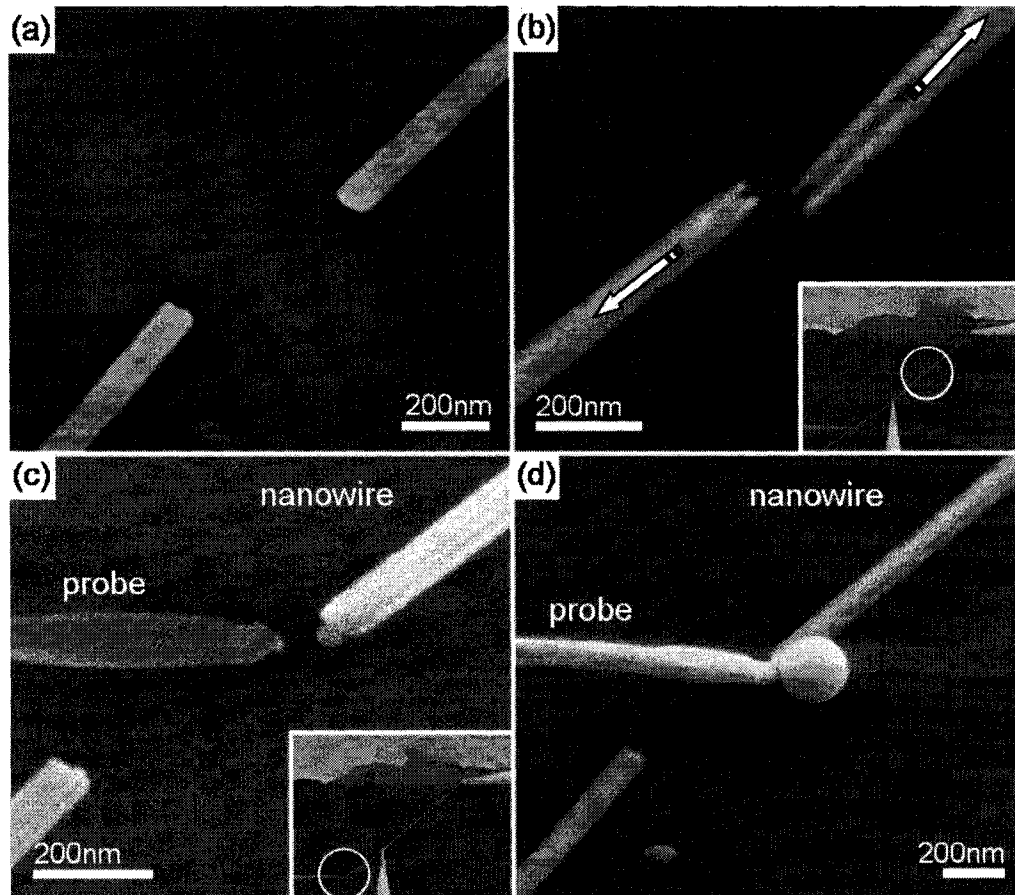


Figure 4.37. SEM images of the breakdown measurements, in configuration D. (a) The fractured nanowire. (b) The pull-apart between the voltage probes. The location of the pull-apart is shown in the inset. (c) Simultaneous onset of the single-phase melt. The location of the melt is shown in the inset. (d) A larger amount of material melted and formed a protrusion outside the nanowire. Images: B.W. Jacobs *et al. Nanotechnol.*, **18**, 475710 (2007) with permission.

The observed structural disintegration may be a result of the multiphase nature of the GaN nanowire. A single-phase volume was observed to melt while an outer layer retained its structural integrity. The diameter of the initial melt formation, which progressed smoothly, as observed in the SEM, to the final melt formation was consistent with melting of a single phase. The electronic structure of the multiphase interface and the possibility of phase specific electron transport and phonon confinement are currently under investigation by our group.

The multiphase nanowire has the ability to carry high current densities as shown

in the GaNFET and two and four-point probe experiments. This may be due to the multiphase nature of the nanowire. The actual path electrons take in the nanowire is still an open question. They could flow in equal amounts throughout the nanowire, however the two-point breakdown experiments indicated that current might follow a specific crystalline phase. The interfaces that exist in the nanowire as shown by the cross-sections may have barriers high enough to confine electrons in one phase. They may also form a longitudinal quantum well at the interface, into which the electrons can fall and travel in. Further theoretical and experimental investigations may answer this question. However, the multiphase structure opens possibilities for enhanced device performance due to its ability to carry high current and if single-phase transport can be reliably achieved, the implications would be significant.

4.4.3 Cathodoluminescence

Cathodoluminescence (CL) experiments were performed to investigate the electronic structure of the multiphase GaN nanowires, including the band gap and if a significant number of impurities exist in the nanowire. The experiments were performed in a LEO Supra 50 VP SEM in conjunction with a GatanMono CL system with a low-noise Peltier-cooled Hamamatsu R5509 photomultiplier detector. The GaN signature in the 290-360 nm wavelength range was used to optimize the CL signal. The best peak-to-background ratio was achieved at approximately 10 keV incident electron energy. The slit widths were set at 1 mm, which was the optimum for achieving high count rates, while maintaining sufficient resolution to differentiate between the wurtzite and zinc-blende band gaps. Narrower slits did not change the peak widths significantly. In these

initial investigations, detailed analysis of the near band gap exciton electronic structure was not considered, and the experiments were carried out at room temperature.

The CL spectra of various GaN nanowires exhibited either a single peak, ascribed to the wurtzite structure, or two distinct peaks, implying the simultaneous presence of both wurtzite and zinc-blende structures. It should be noted that the spectra had no observable contribution from luminescence that could be attributed to defects (stacking faults or impurity mediated), which indicated high-quality samples. The observed CL spectrum shown in Figure 4.38, indicated the coexistence of zinc-blende and wurtzite structures in a single isolated GaN nanowire. The peak maxima, observed at 3.64 and 3.88 eV, were identified as the zinc-blende and wurtzite peaks based on their similarity to those observed for bulk GaN. The increase in energy of ~ 0.4 eV, measured by CL, relative to bulk values, may be attributed to both electron confinement and strain effects as discussed below.

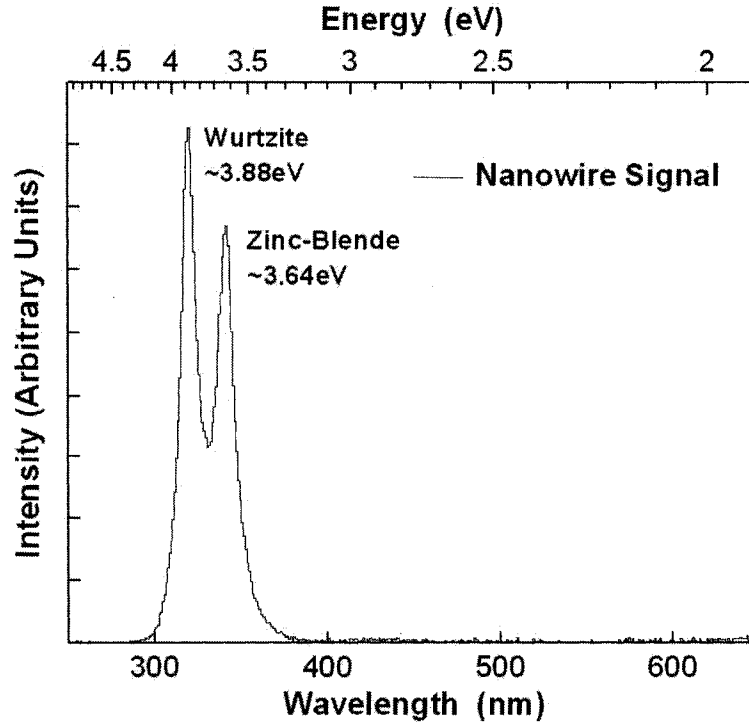


Figure 4.38. Cathodoluminescence spectrum showing the double peak indicating the wurtzite and zinc-blende phases present in the nanowire. The band gap energies for each phase is blue-shifted on the order of 0.4 eV. Spectra: B.W. Jacobs *et al. Nano Lett.* 7, 1435-1438 (2007) with permission.

A 0.4 eV band gap shift was observed in the CL measurements. An electron confinement calculation for the nanowires based on an infinite potential well model accounts for only a few meV of the observed band gap shift. Calculations based on experiments for pure wurtzite GaN nanowires have identified band gap shifts as high as 0.3 eV due to compressive and tensile stresses^{41,42}. Therefore the band gap shift observed in the present experiments may have more contribution from stress than from electron confinement, but confinement effects may still play a significant role due to the multiphase nanowire structure, and their effects are under further investigation.

The discovery of the multiphase GaN nanowire was a significant step forward in the field of nanowires. It is a new structure with properties that may augment or be superior to single phase nanowires. The plain-view HRTEM investigations identified the

two phases of the nanowires and the cross-section HRTEM investigations identified their orientations and revealed details about how this structure can form. SEM and HRTEM investigations of the matrix revealed details on how they form and how nanowires with different growth directions can grow. Electronic properties showed that these nanowires have a large amount of strain and electron confinement effects based on the blue shifted band gap results. The multiphase nanowires may have phase specific transport, begging the question of how and where electron transport actually occurs in these nanowires. The ability to carry high currents could lead to high power devices. Their radiation resilience was also tested as discussed in the next section, which may open up many new application possibilities for these unique structures.

References

1. Y. W. Heo, D. P. Norton, L. C. Tien, Y. Kwon, B. S. Kang, F. Ren, S. J. Pearton, J. R. LaRoche, "ZnO nanowire growth and devices," *Mater. Sci. Eng. R*, **47**, 1-47 (2004)
2. Y. Shan, A. K. Kalkan, C-Y. Peng, S. J. Fonash, "From Si Source Gas Directly to Positioned, Electrically Contacted Si Nanowires: The Self-Assembling "Grow-in-Place" Approach," *Nano Lett.*, **4**, 2085-2089 (2004)
3. A. B. Greytak, L. J. Lauhon, M. S. Gudiksen, C. M. Lieber, "Growth and transport properties of complementary germanium nanowire field-effect transistors," *Appl. Phys. Lett.*, **84**, 4176-4178 (2004)
4. A. I. Persson, M. W. Larsson, S. Stenstroöm, B. J. Ohlsson, L. Samuelson, L. R. Wallenberg, "Solid-phase diffusion mechanism for GaAs nanowire growth," *Nat. Mater.*, **3**, 677-681 (2004)
5. S. Vaddiraju, A. Mohite, A. Chin, M. Meyyappan, G. Sumanasekera, B. W. Alphenaar, M. K. Sunkara, "Mechanisms of 1D Crystal Growth in Reactive Vapor Transport: Indium Nitride Nanowires," *Nano Lett.*, **5**, 1625-1631 (2005)
6. L. J. Lauhon, M. S. Gudiksen, C. M. Lieber, "Semiconductor nanowire heterostructures," *Phil. Trans. R. Soc. A*, **362**, 1247-1260 (2004)
7. C. P. T Svensson, W. Seifert, M. W. Larsson, L. R. Wallenberg, J. Stangl, G. Bauer, L. Samuelson, "Epitaxially grown GaP/GaAs_{1-x}P_x/GaP double heterostructure nanowires for optical applications," *Nanotechnol.*, **16**, 936-939 (2005)
8. J. Goldberger, R. He, Y. Zhang, S. Lee, H. Yan, H-J. Choi, P. Yang, "Single-crystal gallium nitride nanotubes," *Nature*, **422**, 599-602 (2003)
9. J. Q. Hu, Y. Bando, J. H. Zhan, F. F. Xu, T. Sekiguchi, D. Golberg, "Growth of Single-Crystalline Cubic GaN Nanotubes with Rectangular Cross-Sections," *Adv. Mater.* **16**, 1465-1468 (2004).
10. I. Vurgaftman, J. R. Meyer, "Band parameters for nitrogen-containing semiconductors," *J. Appl. Phys.*, **94**, 3675-3696 (2003)
11. R. G. Powell, N. E. Lee, Y. W. Kim, J. E. Greene, "Heteroepitaxial wurtzite and zinc-blende structure GaN grown by reactive-ion molecular-beam epitaxy: Growth kinetics, microstructure, and properties," *J. Appl. Phys.*, **73**, 189-204 (1993)
12. P. Bogusławski, E. L. Briggs, J. Bernholc, "Native defects in gallium nitride," *Phys. Rev. B*, **51**, 17255-17258 (1995)

-
13. Y. Huang, X. Duan, Y. Cui, C. M. Lieber, "Gallium Nitride Nanowire Nanodevices," *Nano Lett.*, **2**, 101-104 (2002)
 14. Y. Huang, X. Duan, Y. Cui, L. J. Lauhon, K. H. Kim, C. M. Lieber, "Logic Gates and Computation from Assembled Nanowire Building Blocks," *Sci.*, **294**, 1313-1317 (2001)
 15. H-M. Kim, T. W. Kang, K. S. Chung, "Nanoscale ultraviolet-light-emitting diodes using wide-bandgap gallium nitride nanorods," *Adv. Mater.*, **15**, 567-569 (2003)
 16. Z. Zhong, F. Qian, D. Wang, C. M. Lieber, "Synthesis of p-Type Gallium Nitride Nanowires for Electronic and Photonic Nanodevices," *Nano Lett.*, **3**, 343-346 (2003)
 17. C. Y. Nam, P. Jaroenapibal, D. Tham, D. E. Luzzi, S. Evoy, J. E. Fischer, "Diameter-Dependent Electromechanical Properties of GaN Nanowires," *Nano Lett.*, **6**, 153-158 (2006)
 18. X. Duan, C. M. Lieber, "Laser-assisted catalytic growth of single crystal GaN nanowires," *J. Am. Chem. Soc.*, **122**, 188-189 (2000)
 19. H. Y. Peng, X. T. Zhou, N. Wang, Y. F. Zheng, L. S. Liao, W. S. Shi, C. S. Lee, S. T. Lee, "Bulk-quantity GaN nanowires synthesized from hot filament chemical vapor deposition," *Chem. Phys. Lett.*, **15**, 263-270 (2000)
 20. C. C. Chen, C. C. Yeh, C. H. Chen, M. Y. Yu, H. L. Liu, J. J. Wu, K. H. Chen, L. C. Chen, J. Y. Peng, Y. F. Chen, "Catalytic Growth and Characterization of Gallium Nitride Nanowires," *J. Am. Chem. Soc.*, **123**, 2791-2798 (2001)
 21. M. Law, J. Goldberger, P. Yang, "Semiconductor Nanowires and Nanotubes," *Annu. Rev. Mater. Res.*, **34**, 83-122 (2004)
 22. M. He, P. Zhou, S. N. Mohammad, G. L. Harris, J. B. Halpern, R. Jacobs, W. L. Sarney, L. Salamanca-Riba, "Growth of GaN nanowires by direct reaction of Ga with NH₃," *J. of Cryst. Grow.*, **231**, 357-365 (2001)
 23. M. He, I. Minus, P. Zhou, S. N. Mohammed, J. B. Halpern, R. Jacobs, W. L. Sarney, L. Salamanca-Riba, R. D. Vispute, "Growth of large-scale GaN nanowires and tubes by direct reaction of Ga with NH₃," *Appl. Phys. Lett.*, **77**, 3731-3733 (2000)
 24. B. W. Jacobs, V. M. Ayres, M. P. Petkov, J. B. Halpern, M. He, A. D. Baczewski, K. McElroy, M. A. Crimp, J. Zhang, H. C. Shaw, "Electronic and Structural Characteristics of Zinc-Blende Wurtzite Biphase Homostructure GaN Nanowires," *Nano Lett.*, **7**, 1435-1438 (2007)

-
25. D. B. Williams, C. B. Carter, "Transmission Electron Microscopy," Plenum Press, New York, 1996.
 26. <http://rsb.info.nih.gov/ij/>
 27. R. Held, B. E. Ishaug, A. Parkhomovsky, A. M. Dabiran, P. I. Cohen, "A rate equation model for the growth of GaN on GaN (0001) by molecular beam epitaxy," *J. Appl. Phys.*, **87**, 1219-1226 (2000)
 28. K. Rapcewicz, M. B. Nardelli, J. Bernholc, "Theory of surface morphology of wurtzite GaN (0001) surfaces," *Phys. Rev. B*, **56**, 12725 (1997)
 29. J. Fritsch, O. F. Sankey, K. E. Schmidt, J. B. Page, "Ab initio calculation of the stoichiometry and structure of the (0001) surfaces of GaN and AlN," *Phys. Rev. B*, **57**, 15360 (1998)
 30. J. Appenzeller, J. Knoch, R. Martel, V. Derycke, S. J. Wind, P. Avouris, "Carbon nanotube electronics," *IEEE T. Nanotechnol.*, **4**, 184-189 (2002)
 31. B. W. Jacobs, V. M. Ayres, R. E. Stallcup, A. Hartman, M. A. Tupta, A. D. Baczewski, M. A. Crimp, J. B. Halpern, M. He, H. C. Shaw, "Electron transport in zinc-blende wurtzite biphasic gallium nitride nanowires and GaNFETs," *Nanotechnol.*, **18**, 475710 (2007)
 32. C. Y. Nam, D. Tham, J. E. Fischer, "Disorder effects in focused-ion-beam-deposited Pt contacts on GaN nanowires," *Nano Lett.*, **5**, 2029-2033 (2005)
 33. H. Y. Yu, B. H. Kang, C. W. Park, U. H. Pi, C. J. Lee, S. Y. Choi, "The fabrication technique and electrical properties of a free-standing GaN nanowire," *Appl. Phys. A*, **81**, 245-247 (2005)
 34. M-H. Ham, J-H. Choi, W. Hwang, C. Park, W-Y. Lee, J-M. Myoung, "Contact characteristics in GaN nanowire devices," *Nanotechnol.*, **17**, 2203-2206 (2006)
 35. F. Leonard, A. A. Talin, "Electrical contacts to nanotubes and nanowires: why size matters *ArXiv Preprint* cond-mat/0602003 (2006)
 36. R. Martel, V. Derycke, C. Lavoie, J. Appenzeller, K. K. Chan, J. Tersoff, P. Avouris, "Ambipolar electrical transport in semiconducting single-wall carbon nanotubes," *Phys. Rev. Lett.*, **87**, 256805 (2001)
 37. S. Heinze, J. Tersoff, R. Martel, V. Derycke, J. Appenzeller, P. Avouris, "Carbon nanotubes as Schottky barrier transistors," *Phys. Rev. Lett.*, **89**, 106801 (2002)
 38. J-Y. Yu, S-W. Chung, J. R. Heath, "Silicon nanowires: preparation, device fabrication, and transport properties," *J. Phys. Chem.*, **104**, 11864-11870 (2000)

-
39. J-R. Kim, H. M. So, J. W. Park, J-J. Kim, J. Kim, C. J. Lee, S. C. Lyu, "Electrical transport properties of individual gallium nitride nanowires synthesized by chemical-vapor-deposition," *Appl. Phys. Lett.*, **80**, 3548-3550 (2002)
 40. S. Datta, *Electronic Transport in Mesoscopic Systems*, (Cambridge: Cambridge University Press) 1995
 41. H. W. Seo, S. Y. Bae, J. Park, H. N. Yang, K. S. Park, S. Kim, "Strained gallium nitride nanowires," *J. Chem. Phys.*, **116**, 9492-9499 (2002)
 42. T. Kuykendall, P. J. Pauzauskie, Y. Zhang, J. Goldberger, D. Sirbuly, J. Denlinger, P. Yang, "Crystallographic alignment of high-density gallium nitride nanowire arrays," *Nat. Mater.*, **3**, 524-528 (2004)

5. Fundamentals of Radiation Interactions in Reduced Dimensionality Systems

The candidate's research has been supported by grants and contracts from NASA and by the award of a NASA Graduate Student Researchers Program Fellowship with two subsequent competitive renewals. NASA's interest is in circuit and material resilience in the extreme environment of space. The candidate's research is also relevant for other extreme environment situations.

5.1 The Space Radiation Environment

The harsh radiation conditions in space have been a formidable problem in designing suitable electronic devices that are able to sustain desired operation in such environments. The environment close to the Earth is somewhat more protected due to its magnetic field that deflects most of the harmful radiation away from the Earth, and serves to shield life on Earth as well as electronic devices. Figure 5.1 is an exaggerated illustration of how the magnetic field effects incoming solar radiation and galactic cosmic rays, where incoming radiation hits the field and is swept past Earth. As one ventures beyond the realm of this protective magnetic field, the threat of harmful radiation dramatically increases. This radiation is highly energized and highly penetrating, which even the thickest of radiation shielding is helpless to stop. Sources of this radiation emanate from across the universe as well as close to home in our own galaxy and solar system.

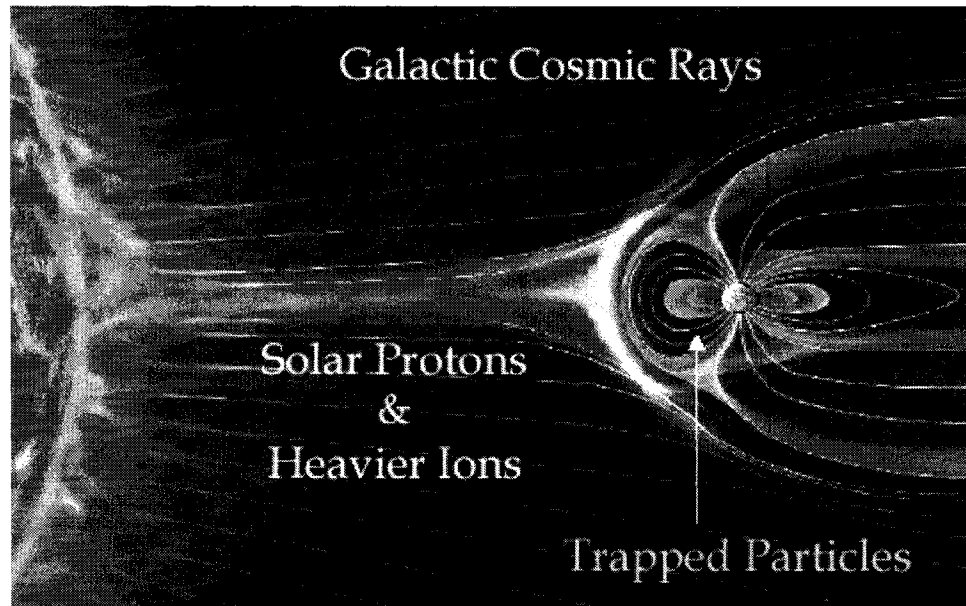


Figure 5.1. The Space Radiation Environment. Galactic cosmic rays constantly bombard the Earth and surrounding space. The Earth's magnetic field, as indicated by the lines surrounding the Earth, protects it from harmful radiation. Image: NASA

5.1.1 Single Event Effects and Total Ionizing Dose

Since space based systems and solar system exploration began in the mid 20th century, space radiation effects have been of primary concern in system design. Radiation effects on electronic systems has been an ongoing research issue at space agencies and institutions across the globe. Due to this focused research effort, radiation effects on electronic systems is well defined and is divided into two categories, total ionizing dose (TID) and single event effects (SEEs). TID is a long-term measure of the degradation of an electronic device exposed to ionizing radiation. SEEs are the effect that one particle of ionizing radiation has on a device. SEEs can be further broken down into subgroups, delineating specific affects SEEs can induce. These subgroups fall into two main categories, hard errors and soft errors^{1,2}. Hard errors consist of SEEs that cause unrecoverable damage to the device. Soft errors consist of SEEs that can be corrected in flight, through a power reset, error correction, etc.

Hard Errors

Single-Event Hard Error (SEH) – An unalterable change of operation that is typically associated with permanent damage to one or more of the device elements.

Single-Event Burnout (SEB) – A single ion induced condition that results in the destruction of the device due to the activation of a localized high current state that results in catastrophic failure.

Single-Event Gate Rupture (SEGR) – A single ion induced condition that results in a breakdown and subsequent conducting path through the gate oxide. Typically seen in a MOSFET device.

Soft Errors

Single-Event Latchup (SEL) – A loss of device functionality due to a single-event. When SEL occurs a power cycle is needed to return to normal operation.

Single-Event Upset (SEU) – A single latched logic state from one to zero, or vice versa, i.e. a bit flip.

Single-Event Functional Interrupt (SEFI) – The loss in functionality of the device that does not require cycling of the device's power to restore operability, unlike SEL, and does not result in permanent damage as in SEB.

These two categories, TID and SEEs, provide the framework in which electronic devices can be tested and benchmarked. The entities that cause these errors are also subdivided into well defined categories and are now discussed.

5.1.2 Cosmic Rays

Cosmic rays are the primary source of harmful radiation found in space. These rays come in a variety of forms and species and are the source for many upsets in space based, as well as terrestrial electronic systems. Cosmic rays can be grouped into two categories, galactic, originating in the Milky Way including the Sun, and extragalactic,

radiation originating from outside the Milky Way³. The atomic composition of galactic and intergalactic cosmic rays consists of about 90% protons, 9% helium nuclei and 1% heavier nuclei. Other species of radiation include electrons and photons, such as gamma and x-rays.

Radiation sources are scattered throughout the universe, with our Sun being the primary source of high-energy protons and heavy ions in the Solar System⁴. The Sun is constantly spewing highly energized heavy ions, protons, neutrons and photons from its surface that travel through the Solar System and out to interstellar space. Radiation flux emanating from the Sun varies with the 11-year solar cycle with higher levels of harmful radiation occurring during the solar maximum. It is during the solar maximum that orbiting satellites, interplanetary space probes, and other space based electronic systems are especially susceptible to SEEs. Despite the Earth's protective magnetic field, communication and global positioning (GPS) satellites have been prone to failure during solar maximums. At times these solar events are so energetic that electronic systems on Earth, such as the power grid, are affected.

Non-solar galactic cosmic rays, emanating from sources within the Milky Way, also cause damaging high-energy radiation upsets. These species of radiation are similar to solar rays, which include protons, electrons, heavy ions, and photons. There are significant differences in non-solar rays, however. Their energies are significantly higher due to the speed at which these particles travel, which is often highly relativistic. Therefore, they are usually completely ionized, i.e. the electrons are completely stripped from the nucleus, due to the high the speed at which the particle is traveling. The energies of these particles can range from GeV to as high as PeV, or quadrillions of

electron volts⁵. These high energies are a consequence of the highly energetic events occurring in interstellar space. Originating from such cataclysmic events as supernovae, these particles generally travel freely in the high vacuum of space, once free of local magnetic fields. These two forms of radiation, which emanate from galactic and intergalactic sources, are of primary concern when designing systems. They are highly penetrating and highly destructive.

5.2 Electronics in Space

Current silicon based integrated circuits in interplanetary exploration probes and satellites within Earth's magnetic field must be designed with SEE and TID effects in mind. High levels of redundancy and radiation hardening are usually employed to cope with the effects of highly energized radiation species. Radiation hardening includes several techniques for increasing a circuit's resiliency in radiation. Using an insulator, such as sapphire, as a substrate can greatly increase the circuit's lifetime in radiation environments. Using static random access memory (SRAM) instead of dynamic RAM (DRAM) for memory modules is also a common practice, since DRAM is more susceptible to SEEs. Error checking design schemes have proved highly effective in reducing upset, where added circuit elements, for example, check bit parity or identical redundant elements are queried and checked against each other for errors. Even with these techniques, problems still persist.

The primary building block used in current device design is the metal-oxide-semiconductor field effect transistor (MOSFET), which have become ubiquitous in the electronics industry due to its low power and large scale integration capabilities. MOSFETs as well as other devices such as metal semiconductor FETs (MESFETs) and bipolar junction transistors (BJTs) have a high susceptibility to radiation^{6,7,8}. There are several key areas of these devices that are especially sensitive and are discussed below.

5.2.1 Silicon Based Electronics

MOSFETs, MESFETs and BJTs rely on charge separated regions, or junctions, to operate. It is well documented that these junctions are prone to radiation damage,

whereby heavy ions⁹, protons¹⁰, electrons¹¹, photons¹², cause a buildup of charge resulting in the malfunction of the transistor. This malfunction can vary in terms of the degree of damage caused, and these different malfunctions are described in the subcategories of SEEs and TID as described above. Radiation may only cause a temporary soft error remedied by a reset, or do significant physical damage, resulting in a hard error, rendering the transistor useless.

SEEs, as well as TID, affect these sensitive regions through two basic mechanisms, lattice displacement and ionization. Lattice displacement frequently occurs in highly energized heavy ions and device interactions. These high-energy heavy ions are especially problematic because they are highly penetrating and in most cases shielding is not effective. One SEE upset with a heavy ion and the device could be rendered inoperable. As the heavy ion interacts with the device it leaves charged ions in its wake due to displacement damage. This line of charged atoms can occur directly through sensitive components of the device. This displacement damage is usually permanent, significantly altering device operation characteristics.

Ionization damage can occur with all types of radiation, but significant device operation alterations generally take longer periods of time. While heavy ion lattice displacement damage can happen nearly instantly, ionization effects can take years to accumulate. Ionization effects limit the lifetime of a device and design considerations are essential to limit these effects. However, even with modern designs, ionization, as with heavy ion damage, can alter the device characteristics so drastically that the functionality of the device can be irrevocably altered.

5.2.2 An Example: A MOSFET in Radiation

There are many ways that a device can be affected by lattice and ionization damage. MOSFETs are by far the most popular choice in devices today, so they will be used as an example. A MOSFET is comprised of three terminals, a source, drain, and gate, and is simply an amplifier acting as an on/off switch. The on/off states of the MOSFET are determined by the voltage applied to the gate and drain relative to the source, which is usually regarded as the ground terminal, or reference. The gate can induce a conduction channel between the source and drain via an electric field, and is separated from the channel by a thin insulating material, usually silicon dioxide. By applying a voltage across the drain and source, and across the gate and source, a current can be modulated.

Using this basic three terminal design, two variations of MOSFETs have primarily been used in devices: the n-type and p-type MOSFET. In an n-type MOSFET electrons are used to conduct current, and in a p-type MOSFET holes are used to conduct current. Holes can be thought of as the opposite of electrons, as they have an opposite, positive, charge. For n-type conduction to occur, a positive gate voltage relative to the source is applied, and for p-type conduction, a negative voltage is applied. This provides the fundamental ingredients for modern complimentary metal oxide semiconductor, or CMOS, technology, which forms the basis for most electronic systems in operation today.

In MOSFET operation, the MOS, which is comprised of the metal or polysilicon gate, the silicon dioxide insulating layer, and the conducting channel, is the essential element in the on/off functionality of the device. The MOS layer is extremely thin to

maximize device response to applied voltages. The oxide layer is usually less than 10nm thick and the induced conduction channel is around 10nm to 20nm thick. These elements are highly sensitive to variations in the materials. The gate voltage induced conduction channel can be affected by substrate dopant atoms, which can scatter electrons. Surface states between the gate oxide and conduction channel can also cause scatter electrons. The gate oxide can be affected by unwanted charge, usually due to impurities such as sodium atoms. Therefore, current MOSFET technologies require an extremely stringent, highly reproducible fabrication processes to mitigate these unwanted impurities and defects in devices.

Due to these stringent criteria the MOS area is highly prone to radiation induced upset. Charged particles of radiation can cause ionization and lattice displacement damage in this area in a variety of ways. Radiation can cause arcing over the gate oxide, essentially shorting out the gate terminal to the substrate, activate oxide impurities, increase surface states between the oxide, and conducting channel and cause deterioration of the gate oxide itself. Figure 5.2 shows an illustration of an energetic heavy ion passing through sensitive areas in a MOSFET leaving behind displaced atoms and a line of dangling bonds. In effect all these factors play a roll in shifting the threshold voltage, V_T , of the transistor, above which in an n-type device is considered on and below which the device is considered off, and vice versa for a p-type device. In general this radiation damage will push the threshold voltage down, making it easier to turn n-type devices on and harder to turn p-type devices off. The threshold voltage¹³ for n-type transistors is given by

$$V_T = \Phi_{ms} - \frac{Q_i}{C_i} - \frac{Q_d}{C_i} + 2\phi_F;$$

where Φ_m is the metal-semiconductor work function potential difference, ϕ_f is the Fermi level relative to the center of the semiconductor band gap, and C_i is the MOS interface capacitance. Q_i and Q_d , the effective MOS interface charge and depleting region charge, respectively, are the values directly affected by radiation. These values tend to increase when the transistor is exposed to radiation, causing the threshold voltage decrease. For CMOS devices this threshold voltage shift is very sensitive, and is compounded by the inherent design of CMOS: the use of both p-type and n-type transistors.

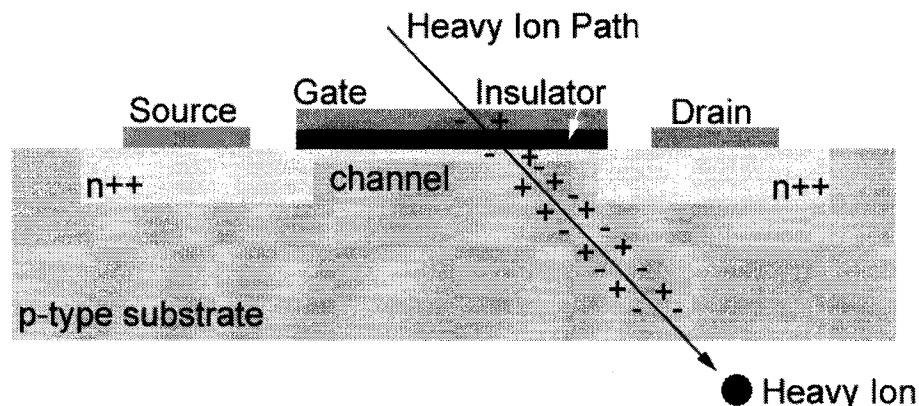


Figure 5.2. n-type MOSFET. Radiation induced damage by an energetic heavy ion. As the heavy ion traverses through the semiconductor, it leaves a trail of defects. Image: B.W. Jacobs

Other sensitive areas in the MOSFET include junctions between dissimilar materials. These junctions, comprised of lattice-mismatched material films and metal on semiconductors, are very thin and the accumulation of surface states is favorable. This situation can sometimes cause a physical disruption of the interface resulting in a loss of adhesion. This build up of interface charge can also result in shifts in the threshold voltage.

As MOSFETs continue to decrease in size, they become more susceptible to SEE and TID upset. Gate oxide thicknesses are becoming extremely thin, just a few nanometers, so the conduction channel modulation is more sensitive to changes in gate voltage. Any small disruption in this ultra thin gate oxide area may result in erroneous functionality. Transistor operating voltages are also concurrently decreasing, which increases the sensitivity of threshold voltage shifts due to radiation upset. Therefore silicon technology is not only reaching its size limits in modern transistors, but its viability in space applications is becoming increasingly compromised. Space-based silicon electronics have come a long way, with redundant systems, radiation hardened devices and shielding, but problems still persist. Therefore, new materials that are inherently radiation resilient that can be used in electronic devices that meet or exceed the current state-of-the-art silicon technologies are needed.

5.3 The National Superconducting Cyclotron Laboratory

The need to test new nanomaterials and nanocircuits in simulated space conditions is essential to determine their viability in such environments. There are only a handful of terrestrial facilities that can simulate the energies and representative species of heavy ion radiation found in space. One such facility is the National Superconducting Cyclotron Laboratory (NSCL) at Michigan State University¹⁴. The NSCL is particularly suited for these studies because its available beam energies and species are a good approximation of the energy spectra of abundant charged particles in cosmic rays. The ability to accelerate any element on the periodic table makes it highly versatile for a variety of heavy ion radiation experiments.

5.3.1 The Coupled Cyclotron

The NSCL uses a coupled cyclotron system, and is a truly unique design. Each cyclotron uses large superconducting magnets that bend charged particles accelerated by the cyclotron radiofrequency system. The first cyclotron used in acceleration is the smaller K500, which was the world's first cyclotron to use superconducting magnets. The second, larger cyclotron is the K1200, which until very recently was the most powerful in the world, also uses superconducting magnets. Since 2001 these coupled cyclotrons have produced highly energized, high current particle beams.

In order to achieve such highly uniform particle beams that are accelerated to relativistic velocities, near the speed of light, a complex array of state-of-the-art instruments, many of which were first designed and developed at the NSCL, are used for

initial particle preparation, acceleration, and beam delivery. These instruments must work in precise synchronicity for the entire process to work.

The first step in preparing a beam includes extracting a particular element from a source. This source is usually purchased in highly pure gas form, such as oxygen or nitrogen. Sources that are initially in solid form are heated into a gas. These atoms are usually electrically neutral and if an atom with a neutral charge, with the same number of positively charged protons in the atom's nucleus as negatively charged electrons surrounding the nucleus, enters a magnetic field nothing happens. This is similar to touching a magnet to a non-magnetic material such as wood or plastic. There must be a charge on the material that the magnetic field can influence. Therefore, initial steps in ionizing the atom, or stripping electrons to give it an overall positive charge, must be taken so that it can interact with the magnetic field.

This initial electron stripping is done using electron cyclotron resonance (ECR) ion sources. In an ERC source the movement of electrons is used to prepare a particular species of heavy ion gas. The movement of electrons can be influenced by magnetic fields due to the Lorentz force. Electrons will move in a helical pattern around static magnetic field lines at a certain frequency given by:

$$\omega_{ce} = \frac{eB}{m};$$

where e is the charge of a single electron, 1.6×10^{-19} C, B is the magnetic field strength and m is the mass on an electron, 9.1×10^{-31} kg. An ERC ion source takes advantage of this and introduces microwaves at the ECR frequency equal to ω_{ce} to heat the electrons.

The heated electrons will collide with the gas inside the chamber, which is the element to be accelerated, and begin to strip electrons of the atoms, ionizing them. This group of

ionized atoms is called a plasma. After sufficient ionization has occurred, a strong electric field pushes the plasma out of the ECR source down a beam pipe to the first cyclotron so the acceleration process can begin. The ECR source produces ions with many charge states, and usually intermediate charge states are the most abundant and are sent to the K500 to maximize the beam current.

Once inside the K500, a magnetic field perpendicular to the trajectory of the ions confines them while an oscillating electric field accelerates them. In this process the charged ion accelerates in a spiral trajectory running through the accelerating electric field many times over each time gaining more energy. As the particle increases in velocity, the radial path of the particle grows while the frequency of oscillation remains constant. The equation for circular motion for a particle having charge q and mass m in a uniform magnetic field of strength B is given by,

$$\frac{E}{A} = \frac{(BR)^2}{2} \frac{q^2}{m^2}.$$

E is the kinetic energy of the particle, A is the atomic number, B is the magnetic field, R is the radius of the particle's path, q is the charge of the particle, and m is the mass.

$\frac{(BR)^2}{2}$ is called the bending power. The increase in kinetic energy can either be compensated by increasing the radius of the particle or by increasing the magnetic field. However, in order to keep the cost and size of equipment down, a small radius is required. Therefore the magnetic field must increase if high-energy particles are needed for experiments. Note, higher values of q/m , result in higher values of E/A .

It was the discovery of the superconductor that has made high-energy, compact cyclotrons possible. A superconductor is able to carry very large currents with no

resistance. Employing Faraday's law of induction, which states that an electric current will induce a perpendicular magnetic field, small, high-power magnets can be realized by utilizing superconducting coils that carry extraordinary amounts of current with no resistance. The superconducting coils that produce the magnetic fields, however, must be kept very cold. Liquid helium at 4.2 K or -452° F is used to cool the coils so that they maintain their superconducting properties.

After injection from the ECR ion source into the K500 superconducting magnet, which can be tuned to between 3 and 5 Tesla (T), the charged particles are accelerated to around 10% the speed of light, or around 20 MeV/nucleon. After the ions exit the K500, they are injected into the larger K1200 cyclotron for further acceleration. The K1200 has a stripper foil near the entrance of the beam line from the K500 cyclotron, which typically increases the charge of the particle 2.5 times. The ion is accelerated from 10% the speed of light to around 50% the speed of light, or from around 20 MeV/nucleon to around 200 MeV/nucleon. The K1200 utilizes the higher charge state of the particle in acceleration. With a higher charge, the electric field used for acceleration can further boost the ions to higher energies while the stronger magnetic fields can effectively confine the ions during its acceleration. After the acceleration process is complete, the highly energized ions are extracted and can be sent down a variety of beam lines where different experiments take place.

5.3.2 The Single Event Effects Testing Facility

Multiple beam lines, which steer the beam to application specific vaults, allow for a wide variety of experiments to be done¹⁵. One such beam vault is specially designed

for ion radiation experiments on electronics for space applications. The Single Event Effects Testing Facility (SEETF)^{16,17} is a NASA sponsored facility where energetic heavy ions can be delivered to a remote controlled testing system. Figure 5.3 shows how a beam of ions begins from the ECR source and is conditioned and steered to the SEETF vault. The beam passes through a series of attenuators and apertures before it reaches its destination.

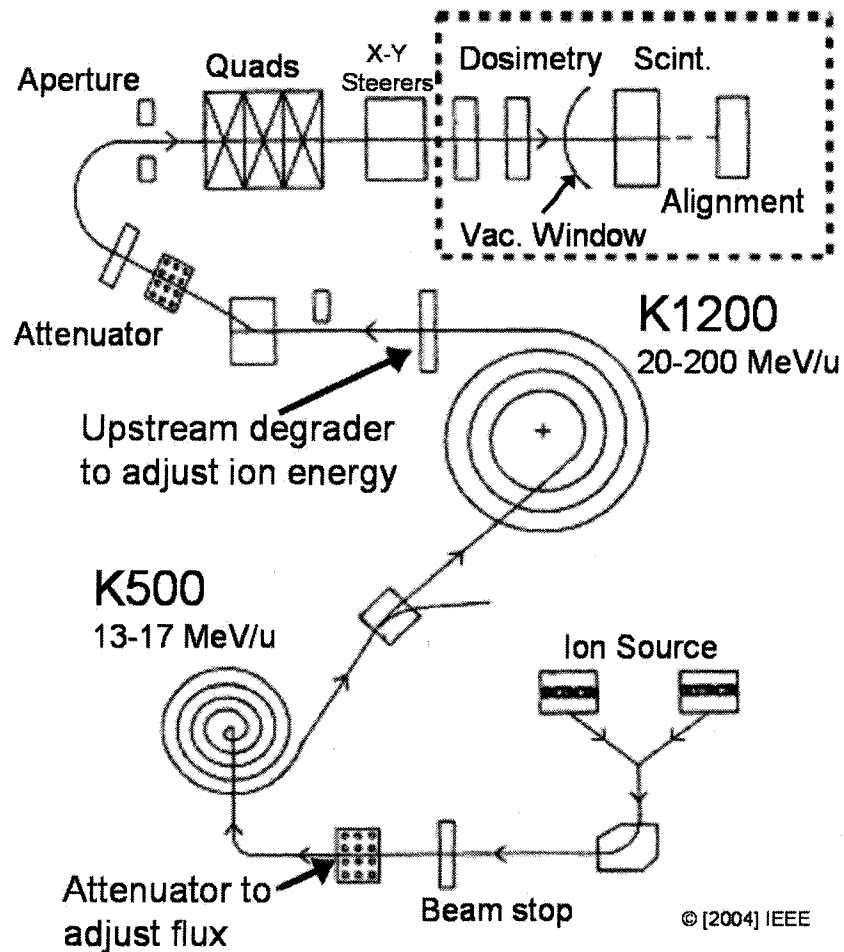
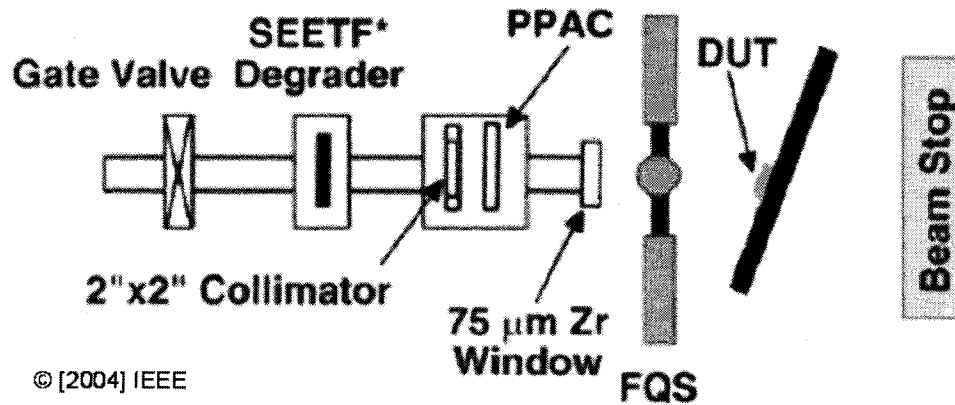
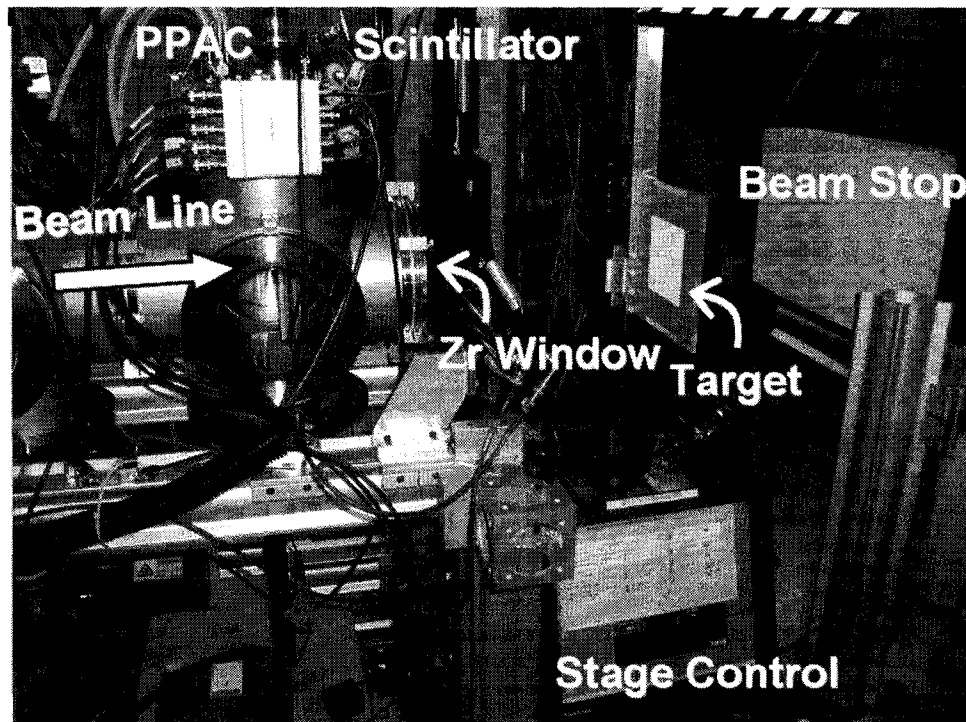


Figure 5.3. Illustration of the particle acceleration process at the NSCL. Ions are sent from the source through attenuators to adjust the beam current. They are then injected into the K500 cyclotron and then the K1200 for acceleration. Degraders and attenuators adjust the beam properties, which is sent to the specified beam vault for experiments. The boxed area in the upper right represents the SEETF vault and its components. Image: adapted from R. Ladbury et al. IEEE T. Nucl. Sci. 51, 3664 (2004) with permission.

There are several components to the SEETF used for beam preparation, delivery and analysis. First the beam must be of the correct energy and be uniform. Aluminum degraders are used to lower the beam energy and make it uniform. The parallel plate avalanche counter (PPAC) is used to obtain beam details. In order to achieve a desired dose, the flux, uniformity and position of the beam are all important for a successful experiment. The PPAC is used to count beam particles and obtain position and uniformity information, essential for beam tuning. The ions then travel out of vacuum into air through a thin zirconium foil. After exiting, the particles pass through a plastic scintillator, which is similar to the PPAC in that it counts the particles passing through it and notes their position. The scintillator verifies beam uniformity and particle flux without significantly degrading the beam. It can be used during experiments to obtain real time beam information to determine target dose throughout the run. If the maximum particle flux possible is desired, the scintillator can also be retracted. The particles then travel through air to reach the beam target. The on target beam size is usually determined by the user, with a maximum size of 5 cm by 5 cm. If a larger beam is needed, rastering the beam is also possible to achieve a larger irradiated area. The target is mounted on a stage capable of moving 10 inches in the x-direction and 20 inches in the y-direction with 70° of rotational freedom, and can be controlled by an adjacent laptop computer or a remote computer using LAPLINK¹⁸. Target positioning is determined by a laser crosshair that denotes the center of the beam. If the beam passes through the target and stage it will hit a graphite block, stopping the beam. Figure 5.4 shows the equipment setup in the SEETF. A photo shows the primary equipment components. The illustration below the photo also shows the components in a more readable form.



© [2004] IEEE

Figure 5.4. Image of the NSCL SEETF. Each main component of the SEETF is noted. The ion beam runs through the PPAC for analysis, exits through a zirconium foil, runs through the plastic scintillator, hits the target, and hits the graphite beam stop. Top image: B.W. Jacobs Bottom image: R. Ladbury *et al.*, *IEEE T. Nucl. Sci.*, **51**, 3664 (2004) with permission.

When testing devices in the SEETF, electronic characterization equipment can be placed inside the vault near the target. The beam will not disrupt the characterization equipment, usually supplied by the user, since it is highly focused on the target sample. Several electrical outlets are available within the vault for all required equipment.

User and SEETF equipment can be controlled remotely through the NSCL Ethernet. This significantly enhances the capabilities of the facility. Multiple target samples can be irradiated by remotely moving the stage. A remote camera allows precise target placement using a laser crosshair as a reference. Characterization equipment controlled via LabVIEW, for example, can also be remotely controlled using the LabVIEW software or Windows Remote Desktop. This adds increased capability for real time testing and data acquisition while the beam is on target.

The versatility of the SEETF also lends itself to other possible user built test environments. A low or high temperature system could be integrated into the stage system, or a small vacuum device could also be incorporated. With these add-ons, the SEETF could better simulate conditions found in space. Given the SEETF capabilities and experiment possibilities, along with the high quality primary heavy ion beams available at the NSCL, an ideal terrestrial setting for electronic and material testing and benchmarking for current and promising systems for use in space environments, as well as radiation environments found on Earth, can be realized.

5.4 Reduced Dimensionality Materials in High Radiation Environments

Novel reduced dimensionality materials, or nanomaterials, have already changed the face of modern science. In recent years a wide variety of materials with inherent or engineered reduced dimensionality components have gained significant interest. The quantum phenomena the small spatial dimensions invoke can lead to enhanced device performance. Many of these systems closely resemble theoretical reduced dimensionality systems and provide excellent experimental evidence of many quantum theories.

Nanomaterials may open up a wide array of electronic as well as mechanical applications for use in space environments. They have been shown to possess an inherent increased radiation resiliency, whereby damage propagation mechanisms that meet fundamental conservation law requirements change in reduced dimensionality systems in ways that may result in enhanced radiation resilience¹⁹. Therefore, the use of nanomaterials in electronics devices and mechanical systems may result in overall enhanced system performance without the need for heavy shielding and high redundancy.

Experiments to test nanomaterials and devices in a heavy ion radiation environment was essential in assessing how well these materials could maintain their structural integrity in a space environment. Candidates chosen for radiation testing represented nanomaterials with a high likelihood of success in harsh environments and nanomaterials that were very versatile for potential use in variety of applications. These three candidates were carbon nanotubes, single and multi walled, gallium nitride nanowires and carbon onions. The properties of these materials will first be discussed and then the results of the material testing in heavy ion radiation will be presented.

5.4.1 Materials

5.4.1.1 Gallium Nitride Nanowires and GaNFETs

Multiphase gallium nitride nanowires were chosen as potential candidates due to their pseudo one-dimensional structure that leads to the variety of promising electronic and optical properties as discussed in chapter 4. The bond between gallium and nitrogen is strong and its radiation resiliency has been shown to be high compared to other semiconductor materials such as gallium arsenide²⁰. The nanowires used were the same as described in chapter 4. The GaNFETs were also fabricated using the methods described in chapter 4.

5.4.1.2 Carbon Nanotubes

Carbon nanotubes have sparked much interest since their discovery in 1991²¹, as they possess remarkable electrical, mechanical and chemical behavior²². A carbon nanotube (CNT) is essentially a rolled up single sheet of graphite, or graphene, consisting of hexagonal rings of carbon atoms arranged in a honeycomb lattice. The wall of a CNT is only one atom thick, with a diameter of ~1 nm. It can reach millimeters in length, and possibly longer, resulting in very large aspect ratios. This system is therefore very close to a theoretical one-dimensional system.

Although CNTs are grown as tubes, it is convenient to describe a CNT based on how it is “rolled up” from a sheet of graphene, as shown in figure 5.5. The chiral vector, C_h , points down the axis of the nanotube, and defines the orientation of the hexagonal carbon rings with respect to the nanotube axis. Perpendicular to C_h is the translation vector, T , which defines the tube axis. The C_h and T vectors also define the unit cell of the CNT, or the basic building block of the tube. C_h is a combination of the unit vectors

of graphene, and is a multiple of these vectors, where, $C_h = na_1 + ma_2 \equiv (n,m)$. Generally only the (n,m) notation is used to describe a CNT structure.

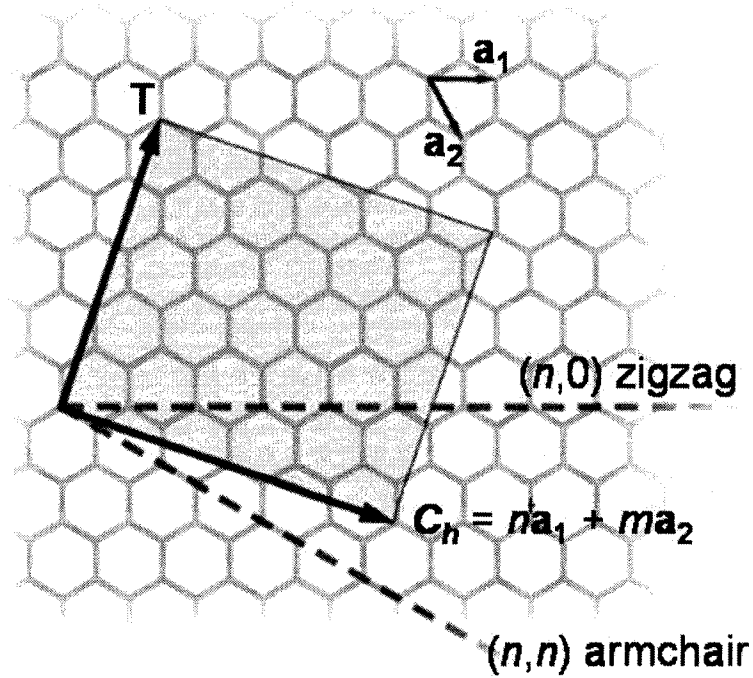


Figure 5.5. The (n,m) CNT labeling system. T is the tube axis. C_h is the chirality vector and describes how to roll up the graphene sheet. a_1 and a_2 are the unit vectors of graphene. $(n,0)$ and (n,n) are special chirality vectors denoting zig-zag and armchair CNTs, respectively. The shaded box denotes the unit cell of the nanotube.

CNTs can be characterized as being achiral or chiral based on their structural symmetry²³. There are only two types of achiral nanotubes, zig-zag and armchair, corresponding to $C_h = (0,n)$ and $C_h = (n,n)$, respectively. All other nanotubes are chiral. Figure 5.6 shows three examples of specific nanotubes including a $(0,10)$ zig-zag, a $(10,10)$ armchair and a $(7,10)$ chiral. C_h can also be used to calculate the diameter, d_t , of a nanotube with,

$$d_t = \frac{C_h}{\pi} = \sqrt{3}a_{c-c}(m^2 + mn + n^2)^{1/2} / \pi;$$

where a_{C-C} is the nearest neighbor carbon-carbon bond distance (1.421 Å in graphite) and C_h is the length of C_h . These two nanotube properties, chirality and diameter, influence the behavior of nanotubes in significant ways. With only subtle changes in these variables, a nanotube can have quite different and surprising properties. For instance, the band gap of the nanotube is dependent on its chirality. For a given (n,m) nanotube, when n-m is a multiple of 3 it is metallic, if it is not a multiple of 3 it is semiconducting. The band gap of semiconducting nanotubes can also vary and depends on the nanotube diameter.

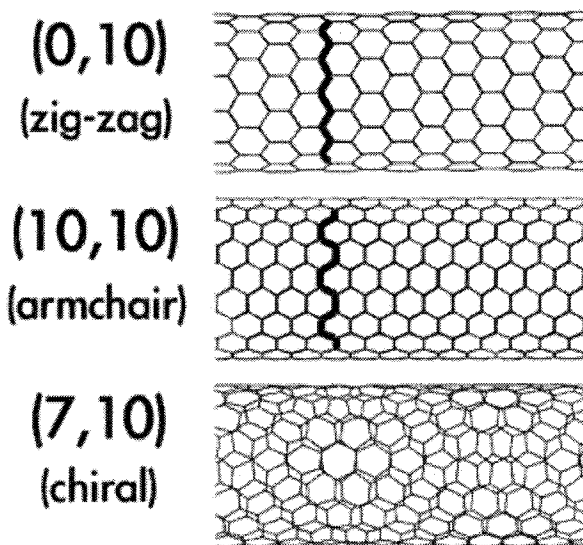


Figure 5.6. Types of CNTs. There are three main types of CNTs, zig-zag, armchair, and the rest, chiral nanotubes.

Carbon nanotubes are being investigated for use in high strength materials²⁴, metallic interconnects in integrated circuits^{25,26}, and chemical sensors^{27,28}. Simple carbon nanotube logic circuits^{29,30} have been fabricated and have shown levels of performance that meet or exceed those of state-of-the-art integrated silicon based logic devices³¹.

CNTs are very promising candidates for use in space applications due to their versatility in many devices and systems. The carbon-carbon bond in the sp^2 configuration as found in nanotubes is possibly the strongest bond found in nature. Therefore physical durability of a CNT is inherently high. It has also been theoretically shown that carbon nanotubes can self-heal after irradiation damage^{32,33}. In heavy ion radiation, damage in CNTs occurs via a direct knock on and secondary knock on displacement of carbon atoms³⁴. Atomic vacancies are filled through dangling bond saturation and the lattice is reorganized to compensate for the loss of an atom.

Both single walled carbon nanotubes (SWCNT), which consist of one atomic layer of graphene as described above, and multi walled carbon nanotubes (MWCNT), multiple SWCNTs in a nested coaxial structure, were tested. MWCNTs share many properties of the SWCNT in their high strength and electron conduction ability. Figure 5.7 shows HRTEM images of typical single, 5.7(a) and multi walled CNTs 5.7(b).

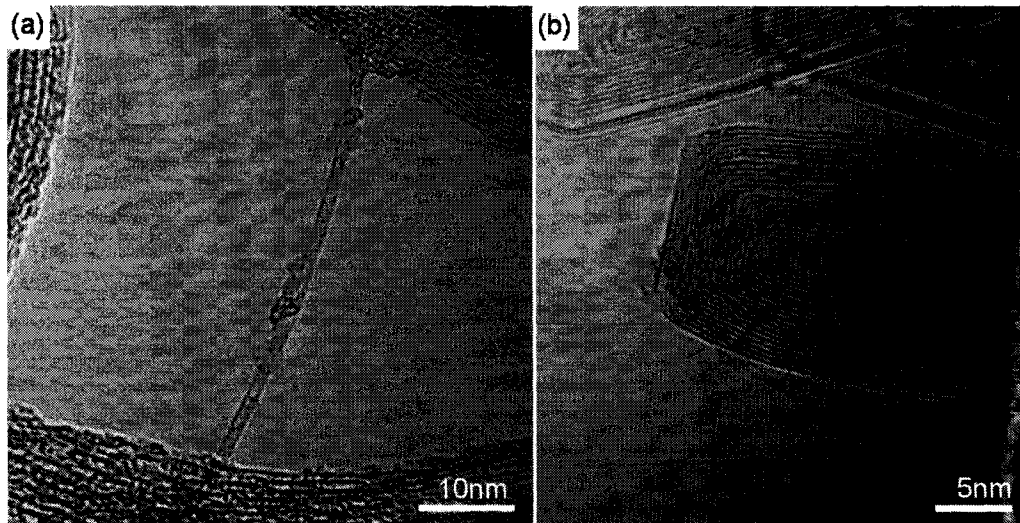


Figure 5.7. HRTEM images of SWCNTs and MWCNTs. (a) A single SWCNT can be seen in the middle of the image running nearly vertically. The single wall structure is easily seen. Disordered carbon is also seen on the surface of the nanotube. (b) The nested MWCNT structure is seen in this figure where each line indicates a wall. Images: B. W. Jacobs.

SWCNTs obtained from Tubes@Rice, now Carbon Nanotechnologies, Inc.³⁵ and NASA Johnson Space Center were grown via the high-pressure carbon monoxide conversion (HiPco) method³⁶. This method uses heated, high-pressure CO as the source of carbon and uses a catalyst particle, usually a transition metal, to initiate nanotube growth. The HiPco method yields high quality nanotubes with only small amounts of disordered carbon and catalyst impurities. The sample from Tubes@Rice came in the form of buckypaper, which is a thin sheet of CNTs around 10 mm² in area and 1 mm thick. This ensured maximum heavy ion beam-sample interactions due to the relatively large cross-sectional area of the buckypaper.

Multi walled CNTs were obtained from NASA Goddard Space Flight Center and were grown via a catalyst-free arc discharge method³⁷. In this growth method a welder creates an electric arc across a carbon anode and carbon cathode causing the carbon anode to vaporize. An inert gas is pumped through the area of vaporization so that oxygen does not interfere with the process causing oxidation of the carbon samples. During vaporization the cathode is cooled in water. This method, while creating abundant multi walled CNTs, also creates a large amount of amorphous carbon in which the CNTs are embedded. A post-growth treatment can be done to reduce the amount of amorphous carbon using nitric acid or toluene, but no such treatment was done for these MWCNT samples. The MWCNTs were of high quality as shown by the HRTEM image above.

5.4.1.3 Carbon Onions

A carbon onion is a similar form of carbon as a MWCNT in that it consists of nested single layers of graphene rolled into a ball, as shown in figure 5.8. These graphene balls that make up an onion are called buckyballs, and are variations on the C₆₀ molecule, which is shown in figure 5.8(a) in the inset. Carbon onions, like CNTs, consist of carbon-carbon bonds the *sp*² configuration, which may be the strongest bond in nature. In radiation carbon onions may exhibit self-healing effects seen in nanotubes due to the similar structure.

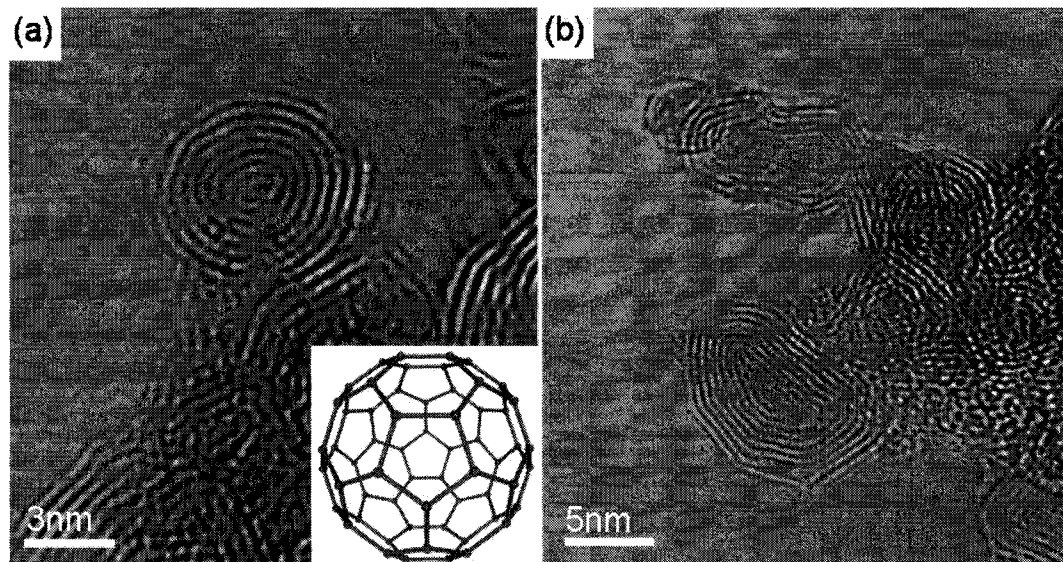


Figure 5.8. HTREM image of carbon onions. (a) A single round carbon onion is shown in this figure. The inset shows a model of a C₆₀ molecule, which is the basis of carbon onions. (b) These carbon onions formed polygonal sides with some faceting on the outer layers. Images: B.W. Jacobs

Carbon onions were chosen as potential candidates for space applications because they exhibit excellent lubrication properties³⁸. Lubricants in space must be able to maintain a low coefficient of friction over a long period of time in very harsh conditions. Lubricants in space-based systems cannot be easily changed in the event of material failure due to their remote locations. Radiation is but one factor effecting lubricants in

space-based systems, drastic temperature change and the vacuum environment are also primary factors effecting lubrication performance. Carbon systems such as nanotubes and onions have been shown to respond very well to temperature variations due to their high thermal conductivity and durability. Carbon onions also act as a solid lubricant so the vacuum environment does not affect the onions like it does with liquid lubricants, where leaks can sometimes occur.

Vacuum conditions have been shown to affect the performance of carbon onions. Studies have shown that carbon onions maintain low coefficients of friction in air^{39,40}. However, when tested in vacuum, the coefficient of friction increases. A loss in film stability is also seen, where the carbon onions slide away from the moving surfaces, resulting in very high coefficients of friction. Treatment in hydrogen peroxide (H₂O₂) drastically improved the lubrication performance of carbon onions in vacuum, reducing the coefficient of friction and increasing film stability⁴⁰. Graphite is also a potential candidate for use as a solid lubricant in space, but the increase of the graphite friction coefficient in vacuum is a well-known effect, and heavy metal compounds are usually added for solid lubrication applications in vacuum conditions. Carbon onions do not require heavy metal additives, therefore representing a more environmentally benign solid lubricant.

Carbon onion samples were produced at Tokyo Institute of Technology from nanocrystalline diamond with diameters of around 5 nm, as shown in figure 5.9. The nanocrystalline diamond was heated to temperatures between 1700° C to 2300° C in an infrared radiation furnace in argon at atmospheric pressure. This procedure can produce relatively large amounts of carbon onion sample quickly and easily. Thermogravimetric

analysis revealed that onions produced at higher temperatures have a higher vaporization temperature meaning onions with fewer defects or amorphous carbon were produced.

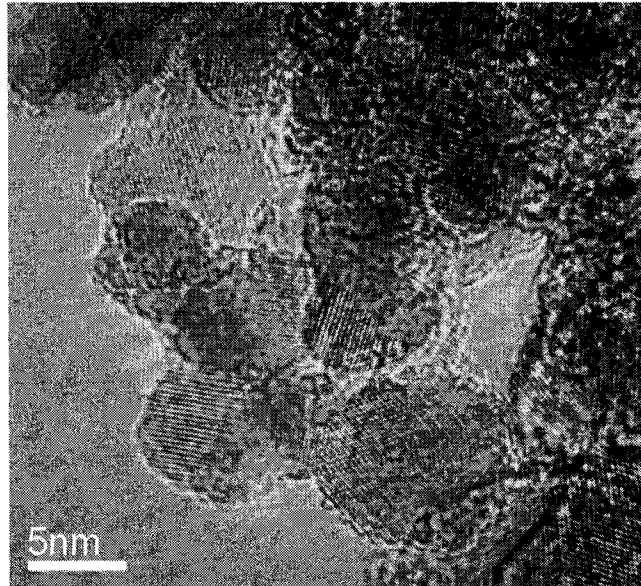


Figure 5.9. HRTEM image of nanocrystalline diamond with diameters of 5 to 10 nm. This is used as a starting material for producing carbon onions. Image: B.W. Jacobs

Each material investigated for heavy ion radiation resilience has potentially high impact return if they can consistently perform in heavy ion radiation. These three types of materials have a wide array of potential applications. GaN nanowires and carbon nanotubes can be used in electronic, optical, mechanical, and sensor applications. Carbon onions could be used as a solid lubricant for moving parts on mechanical space based systems such as a moving antenna or a roll out mechanism for solar panels. Each material, however, must be tested in real world radiation conditions. These materials must maintain high levels of performance in harsh environments before they can be implemented in space-based devices and systems.

5.4.2 Experiments

Heavy ion radiation experiments carried out at the NSCL consisted of a series of experiments done to investigate the low to high Z heavy ion interactions with nanomaterials and electronic devices with integrated nanomaterials as active elements. This series of experiments was funded through an NSCL internal competitive grant that included 92 hours beam time and collaboration with two senior NSCL physicists. Three separate radiation experiments were done at the NSCL with three different heavy ion beams: krypton-86, krypton-78 and calcium-48 at energies that were close to the energy spectra of heavy ions found in space.

5.4.2.1 Krypton-86: The First Experiment

In the first experiment a buckypaper sample consisting of SWCNTs and a powder sample consisting of MWCNTs embedded in amorphous carbon were irradiated with a krypton-86 beam at 142 MeV/nucleon, or 12.212 GeV/atom. The experiment was done in the N4 vault at the NSCL. The beam was focused to uniformly irradiate an area having dimensions of 20 x 20 mm, as measured from known dimensional markings on the beam-viewing scintillator placed at the beam line exit vacuum window. The vacuum window was a 0.022 mm thick zirconium foil. In this experiment carbon samples were put in close packed in quartz tubes, as shown in figure 5.10, and placed as close as possible to the zirconium exit window in the beam line. Thin walled quartz tubes were used in order to minimize secondary ion production. Each individual quartz tube had an outer diameter of 3 mm and an inner diameter of 2 mm. The beam current was measured at the exit point using a Faraday cup, which measured a stable current of 0.3 particle

picoamps (ppA), or 1.87×10^6 particles per second (pps). Therefore, the particle flux was 4.68×10^3 pps/mm².

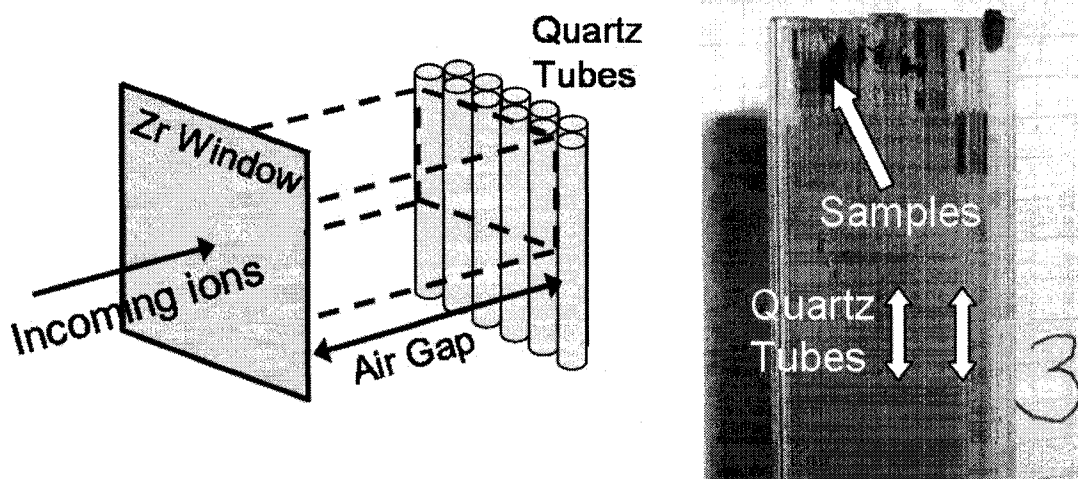


Figure 5.10. The carbon samples were placed in quartz tubes and put in a close packed configuration. These samples were irradiated simultaneously. The heavy ions exited into air through a thin zirconium window and passed through the quartz tubes with an on target beam energy of over 11 GeV, as shown in the left image. The samples packed in the quartz tubes are shown on the right. Images: B.W. Jacobs

To quantify the amount of radiation a sample receives, a dose calculation is done. The total dose of radiation depends upon incident beam energy, beam current, sample volume and density and all losses. The fluence of the beam determines the number of particles passing through a cross-section of the beam per unit time. In conjunction with the cross-sectional area of the samples, this determines the number of particles passing through the sample under test per unit time. From this and the energy loss per nucleon, the amount of energy deposited in the sample for each ion passing through the cross-section of the sample can be determined, giving an effective dose per unit time for a given beam fluence and energy. From the dose per unit time, the duration of the exposure of the target to the beam for a desired total dose of radiation can be determined.

To estimate the on target beam energy, the energy loss in each stage of the beam line was calculated using Stopping and Ranges of Ions in Matter (SRIM)⁴¹. The energy loss due to the Zr exit window was about 63.13 MeV/atom. In the 63 mm air gap between the vacuum window and the first target samples, the energy loss was about 502.3 MeV/atom. The energy loss after traversing the first 0.5 mm of quartz (density = 2.65 g/cm³) was 359.2 MeV/atom. The on target beam energy for the first row of material was approximately 11.29 GeV/atom or 131.2 MeV/nucleon. The irradiated area of each sample was estimated to be 16.92 mm². The density of CNTs was estimated to be 2.24 g/cm³, which is the density of single crystal hexagonal planar graphite.

5.4.2.2 Krypton-78: The Second Experiment

In the second experiment, SWCNTs, MWCNTs, GaN nanowires, and GaNFETs were irradiated with a krypton-78 beam at 140 MeV/nucleon, or 10.92 GeV/atom. The beam was focused to uniformly irradiate an area having dimensions of 20 (height) x 10 mm (width). The estimated beam current during the experiment was .3 ppA and the current was varied from 1.6×10^5 - 10^6 pps. The particle flux was calculated to be 5×10^3 pps/mm².

Samples were packed between a silicon wafer and thin (~0.25 mm) mica covers that were glued to the wafer using silicone and placed in the beam line, as shown in figure 5.11. The silicon wafer was glued to a piece of particleboard that was mounted to the SEETF movable stage. This sample configuration proved much easier to work with than the quartz tube samples. The beam passed through a 0.27 mm four-quadrant plastic scintillator plate, used to continuously monitor the incoming beam current, a .075 mm Zr

exit window, a 432 mm air gap, and the 0.25 mm mica sheets. The energy loss was calculated to be 226.2 MeV/atom through the Zr foil, 210.6 MeV/atom through the scintillator plate, 358.8 MeV/atom through the air gap, and 421.2 MeV/atom through the mica cover. This resulted in an on target beam energy of 9.703 GeV/atom or 124.4 MeV/nucleon.

In this experiment the sample dose calculations were more carefully considered. Given the ability to irradiate each sample individually, a more accurate dose could be imparted on each sample. Therefore, doses based on the on target beam energy and each individual sample mass, accurately measured with a highly precise scale (Denver Instruments M-220D), and cross-sectional area were used to calculate the time needed to reach the predetermined dose.

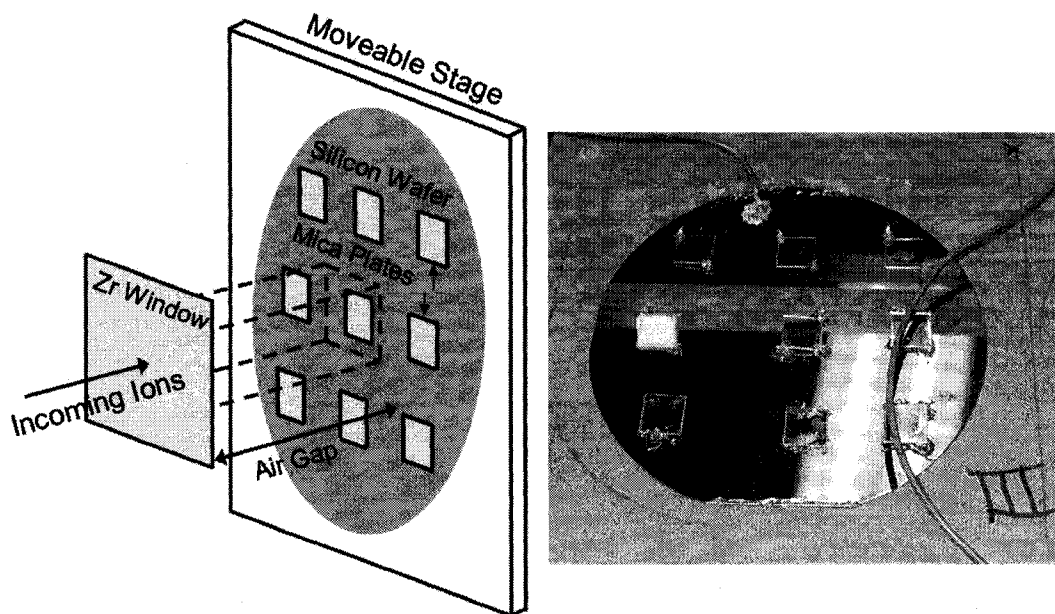


Figure 5.11. The carbon and gallium nitride nanowire samples were placed on a silicon wafer that was attached to a piece of particleboard with silicone adhesive. The particleboard was then screwed onto the SEETF movable stage. The samples were held in place by a small mica sheet that was attached to the silicon wafer with silicone adhesive. Each sample could then be separately irradiated with a specific dose. The heavy ions exited into air through a thin zirconium window and passed through the mica sheets with an on target beam energy of over 9.7 GeV, as shown in the left image. The samples that were placed on the silicon substrate are shown on the right. Images: B.W. Jacobs

A GaNFET was also tested in the krypton-78 beam. Its electronic characteristics were measured in real time while the circuit was being irradiated by energetic heavy ions. This was made possible by the NSCL Ethernet and LabVIEW computer control of the characterization equipment. Using Windows Remote Desktop, the computer running LabVIEW in the vault was remotely controlled and parameters such as the gate-source voltage and drain-source voltage were varied at will during irradiation. The GaNFET was fabricated as described in chapters 2 and 4. It was placed in ceramic package and wire bonded. Wire bonding was done at Howard University. David Liu at NASA Goddard Space Flight Center wrote the LabVIEW program.

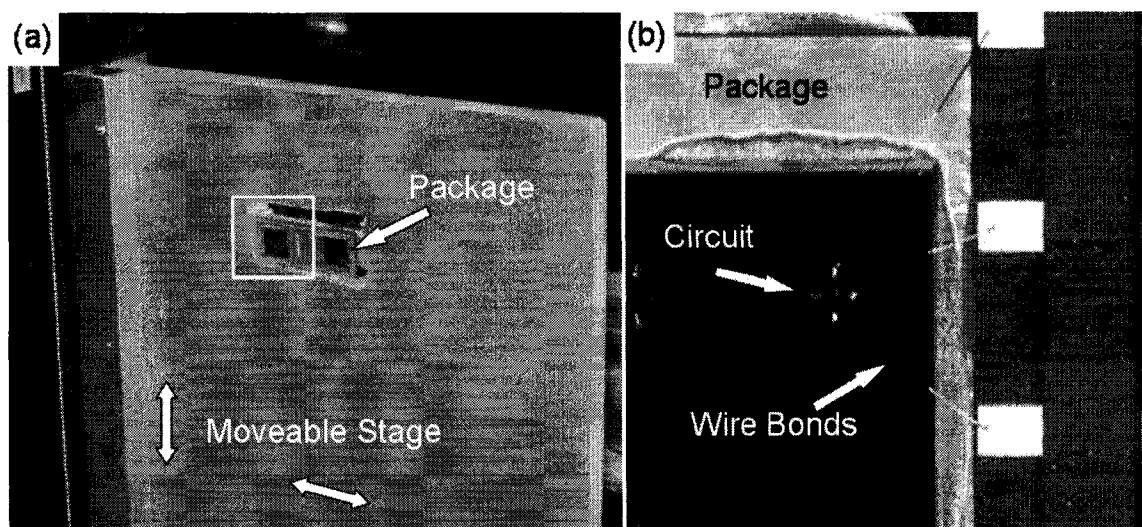


Figure 5.12. The electronic characteristics of a GaNFET in radiation were measured. (a) The circuit was mounted in a ceramic package and mounted on particleboard and attached to the SEETF moveable stage. (b) A close up of the circuit shows its wire bonds. Images: B.W. Jacobs Wire bonding and package mount: James Griffin, Howard University

The I-V characteristics of the GaNFET were tested before, during and after heavy ion irradiation (Keithley 487 Picoammeter/Voltage Source and HP 6633A DC Power Supply). In measuring the I-V characteristics the drain-source voltage was continually swept from 0 V to 22 V, while the gate-source voltage was stepped through from 0 V,

3V, 6V and 9V. No dose was calculated for the GaNFET but rather a fluence of the beam was started low at 10^2 pps over a beam area of 200 mm^2 and was gradually increased to 10^4 pps, 10^5 pps and finally 10^6 pps, corresponding to 3×10^4 to 3×10^7 particles/cm². The beam was on target for 600 s for each fluence.

5.4.2.3 Calcium-48: The Third Experiment

In the third experiment, SWCNTs and MWCNTs in addition to carbon onions were irradiated with a calcium-48 beam at 140 MeV/nucleon and 70 MeV/nucleon, or 6.72 GeV/atom and 3.36 GeV/atom, respectively. This experiment was also done in the SEETF.

The SWCNT, MWCNT and carbon onion samples were individually mounted in a similar configuration as the previous experiment behind thin 0.2 mm quartz cover slips on a silicon substrate with a native oxide layer. The SEETF beam path passed through a 0.075 mm zirconium foil vacuum exit window, a 432 mm air gap, and the 0.2 mm quartz cover slips. Beam energy calculations were performed using the SRIM software package. At an incident beam energy of 140 MeV/nucleon, SRIM indicated a loss of 430 MeV/atom, across the zirconium foil vacuum exit window, the air gap, and the quartz restraining sheet. This loss was 759.84 MeV/atom for the 70 MeV/nucleon beam. The resulting on target beam energies were 6.29 GeV/atom or 131.04 MeV/nucleon and 2.6 GeV/atom or 54.17 MeV/nucleon.

There are no published guidelines for high-energy heavy ion beam exposure times for nanomaterials and nanocircuits. The experiments were therefore conducted with doses and exposure times comparable to those that can be expected to damage or destroy

current state-of-the-art silicon circuits. The failure under irradiation for a diverse range of silicon devices and technologies indicate that damage thresholds are at about 10 Gray (Gy), where 1 Gy = 1 Joule/kg. Thresholds for radiation-hardened devices are at about 1000 Gy. Almost all devices will fail before doses reach 10^5 Gy. Therefore, 100 Gy, 1,000 Gy and 10,000 Gy were set as the target doses. Corresponding times to achieve these doses were calculated based on the estimated on target beam energy, sample weight, density and cross sectional area. The density of each nanomaterial is also essential in calculating an accurate dose. These nanomaterials do not have well defined densities and are many times very fluffy and difficult to work with. Therefore a rough estimation of the density of each nanomaterials was used in calculating the dose.

5.4.3 Experimental Results and Discussion

5.4.3.1 Gallium Nitride Nanowires and GaNFETs

GaN nanowires were irradiated at the SEETF with highly energetic krypton-78 heavy ions with an on target energy of 128.4 MeV/nucleon. After irradiation, GaN nanowires were analyzed with HRTEM and exhibited minimal radiation coupling. The majority of nanowires analyzed showed no radiation damage. When damage was observed radiation coupling occurred via a previously unreported short track mechanism. This radiation coupling took the form of a crystalline to amorphous transition in the outer layer of the nanowire, as shown in figure 5.13. An amorphous plume was observed and was attributed to heavy ion radiation damage. An FFT of this and the surrounding areas, shown in figure 5.13(b), show ring patterns as well as spot patterns, indicating that some crystallinity was retained after irradiation. Not all nanowires irradiated, however, showed

damage. Only a minority of the nanowires observed via HRTEM showed the crystalline to amorphous transition.

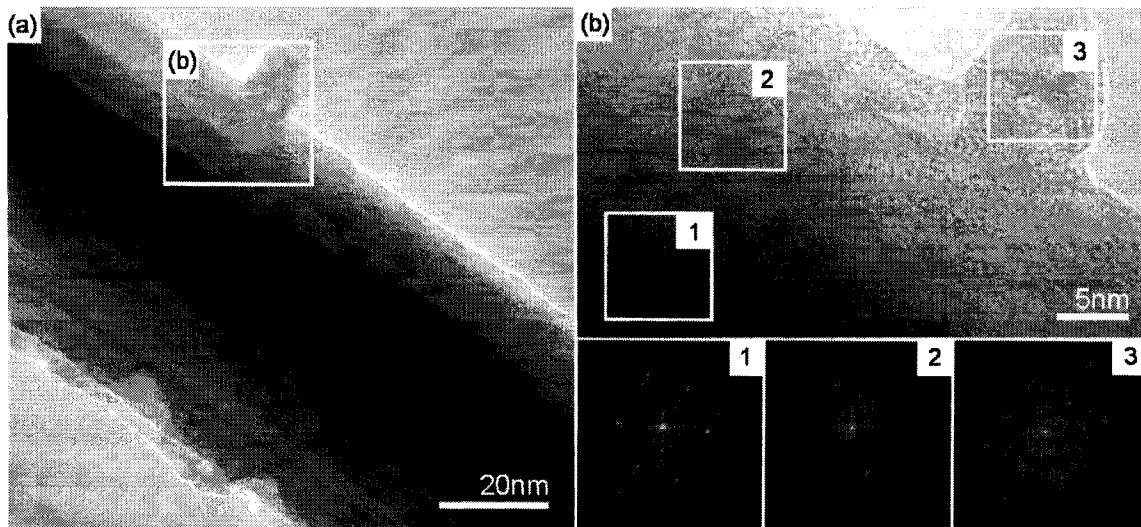


Figure 5.13. TEM images of irradiated GaN nanowire. (a) A TEM image shows a plume of material, which may have resulted from heavy ion radiation. (b) An HRTEM image of the plume showing its amorphous character. The FFTs of the indicated areas show the ring structure associated with amorphous or polycrystalline material. Images: B.W. Jacobs

A second nanowire observed with the TEM after heavy ion radiation shows rough outer layers that may have been caused by the radiation, as shown in figure 5.14(a). HRTEM analysis indicated that the rough surface was comprised of amorphous plumes of GaN, as shown in figure 5.14(b), where the high crystallinity of the nanowire normally seen in the non-irradiated samples was not observed. An FFT of the boxed area has a ring pattern and a spot pattern indicating that the crystallinity in this area was retained. Other images of the internal structure of the nanowire, shown in figure 5.14(c), revealed what looked to be areas not affected by the heavy ions. The coherent interface between the zinc-blende and wurtzite phase normally seen in these nanowires was not damaged in any observable way. FFTs that did not have significant ring patterns confirmed the high crystallinity of these areas.

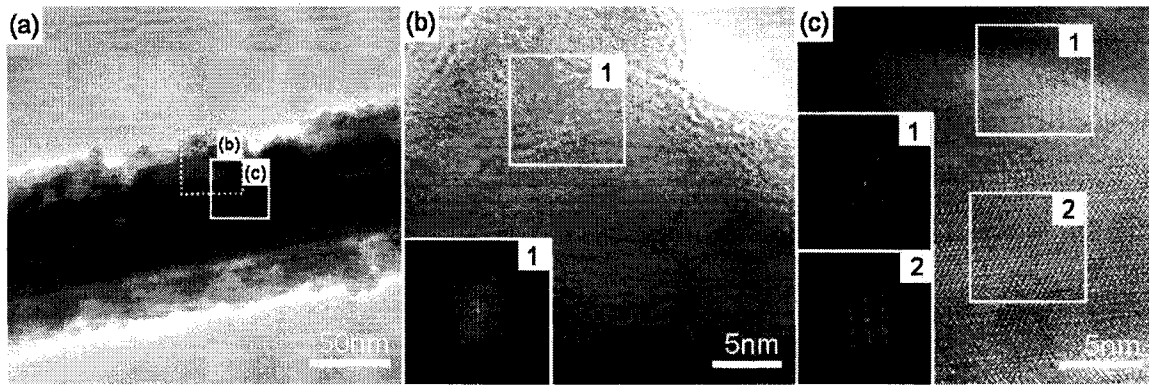


Figure 5.14. TEM images of an irradiated nanowire. (a) The TEM image shows a nanowire with a rough outer surface, which may have resulted from heavy ion radiation. (b) HRTEM image of the boxed area in (a). An amorphous plume is shown here. An FFT taken from the boxed area shows a ring pattern associated with an amorphous and polycrystalline region. (c) HRTEM image taken from the boxed area in (a). The zinc-blende/wurtzite coherent interface is shown here. No damage is observed in this picture and FFTs do not show significant ring patterns. Images: B.W. Jacobs

The GaN nanowire sample was exposed to a uniform 2 cm^2 beam centered on a $\sim 0.16 \text{ cm}^2$ sample using the laser alignment. The highest radiation dose was 6.4×10^5 pps irradiation for 900 s. As shown in the GaN matrix SEM images in chapter 4, the nanowires were somewhat dispersed throughout the matrix. Therefore, an actual dose for the nanowires was roughly estimated to be about 300-400 Gy.

The heavy ion radiation damage mechanisms in nanowires are also not well defined. Damage in traditional semiconductors is usually seen through a long track of displaced atoms and dangling bonds in the material corresponding to the path of the energetic heavy ion. No tracks were observed in the nanowires, only local areas of disordered material, and some nanowires did not show indications of heavy ion radiation damage. This could be a result of the strong bond gallium and nitrogen form in GaN, or the nanowire cross-section could be small enough that heavy ion interactions do not frequently occur.

GaN FETs were also irradiated in a krypton-78 heavy ion beam in order to study device operation in real time under radiation. The GaN FET was exposed to highly

energetic heavy ion radiation that would cause traditional silicon based MOSFETs to malfunction. No dose was calculated for the GaNFET but rather a fluence of the beam was started low at 10^2 pps over a beam area of 200 mm^2 and was gradually increased to 10^4 pps, 10^5 pps, and finally 10^6 pps, corresponding to 3×10^4 to 3×10^7 particles/cm². The beam was on target for 600 s for each fluence. While the beam was on target, real time I-V curves were measured. The GaNFET showed minimal damage after every radiation exposure and continued to operate after irradiation was complete, see figure 5.15.

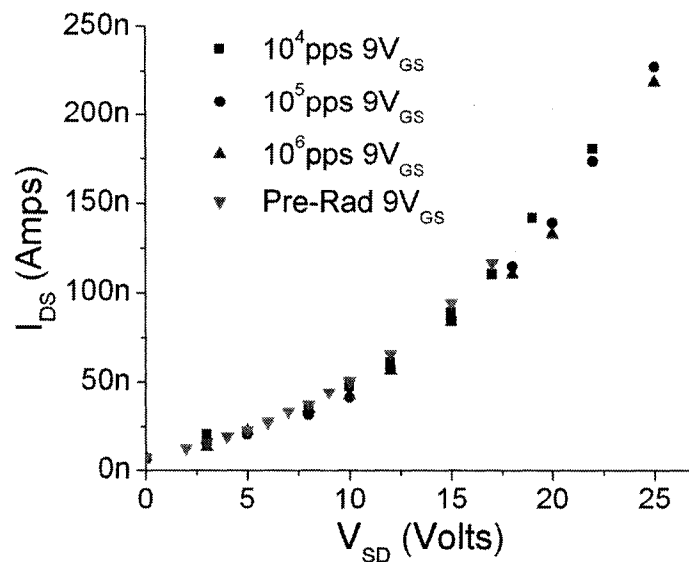


Figure 5.15. Multiple V_{DS} sweep of a GaNFET in radiation. V_{GS} was kept constant at 9V. I-V Characteristics: V.M. Ayres *et al. Diam. Relat. Mater.*, **15**, 1117-1121 (2006) with permission.

In addition to the material and small size of the nanowire, the GaNFET design may also make it inherently radiation resilient. When comparing a GaNFET to a traditional silicon based MOSFET design, there are several key differences in architecture that may enhance its radiation resilience. There are fewer junctions in a GaNFET that are susceptible to radiation damage. The gate oxide layer is not as sensitive to radiation damage in a GaNFET. Since modern MOSFETs employ a very thin gate

oxide layer to modulate an inversion layer directly underneath it, it is very sensitive to current leakage through the gate oxide. It is therefore very sensitive to ionizing damage. GaNFET operation is different in that it uses the gate field to modulate the height of the Schottky barrier formed between the metal-nanowire junctions. This junction is, however, susceptible to radiation damage, as is any junction of dissimilar materials. Combined with the radiation resilience of GaN nanowires, and their excellent material properties GaNFETs may be a viable solution for space-based electronics.

5.4.3.2 Single Walled Carbon Nanotubes

SWCNTs were irradiated with krypton-86, krypton-78 and calcium-48. Post irradiation analysis using Raman spectroscopy, HRTEM and SEM indicated that the samples sustained no observable damage. Raman spectroscopy studies across all samples showed the characteristic double peak at $\sim 1580\text{ cm}^{-1}$ corresponding to semiconducting and metallic nanotubes, as shown in figure 5.16. This showed that the CNTs retained their overall tubular structure. The $\sim 1330\text{ cm}^{-1}$ peak is the disorder carbon peak (D-peak), and after large doses of heavy ions, was expected to increase as the nanotube structure was broken down due to heavy ion knock on displacement damage. This did not occur, and in every instance, only a small disordered peak was observed, with no correlation between the peak characteristics, including the number of counts or its full width half max (FWHM), and the radiation dose. Subtle variations in the double peak structure were observed, but these variations are as yet unexplained. Figure 5.16(a) shows the SWCNTs Raman spectra before and after the krypton-78 irradiation. The characteristic double peak is still present after both doses. Figure 5.16(b) shows the SWCNTs Raman

spectra before and after the calcium-48 irradiation. The characteristic double peak is still present after both doses. These doses were much higher and the SWCNT structure was maintained. The SWCNTs from the krypton-86 experiment are not shown, because the calculated dose was much smaller, and very similar spectra to those shown below resulted.

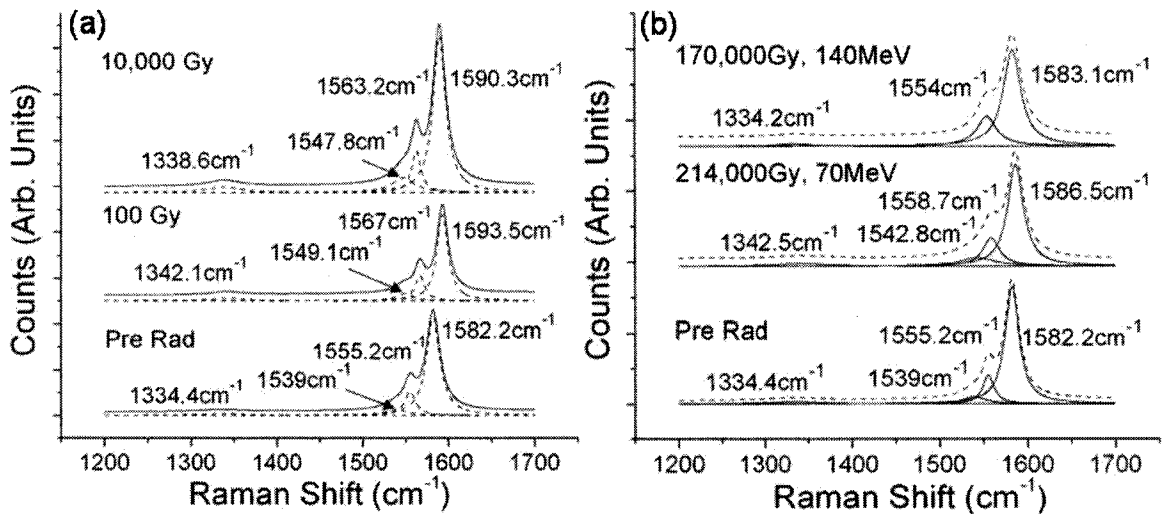


Figure 5.16. Raman spectra of irradiated SWCNTs. (a) Before and after krypton-78 irradiation. (b) Before and after calcium-48 irradiation. After all irradiation the SWCNTs indicated no observable damage. Spectra: B.W. Jacobs

SEM and HRTEM images shown in figure 5.17 also showed no observable structural damage after krypton-78 irradiation. Figures 5.17(a) and 5.17(b) are SEM and HRTEM images of SWCNTs before radiation. Figures 5.17(c) and 5.17(d) are SEM and HRTEM images of SWCNTs after a 1000 Gy dose of krypton-78 radiation. Figures 5.17(e) and 5.17(f) are SEM and HRTEM images of SWCNTs after a 10,000 Gy dose of krypton-78 radiation. The images show pristine nanotube structures.

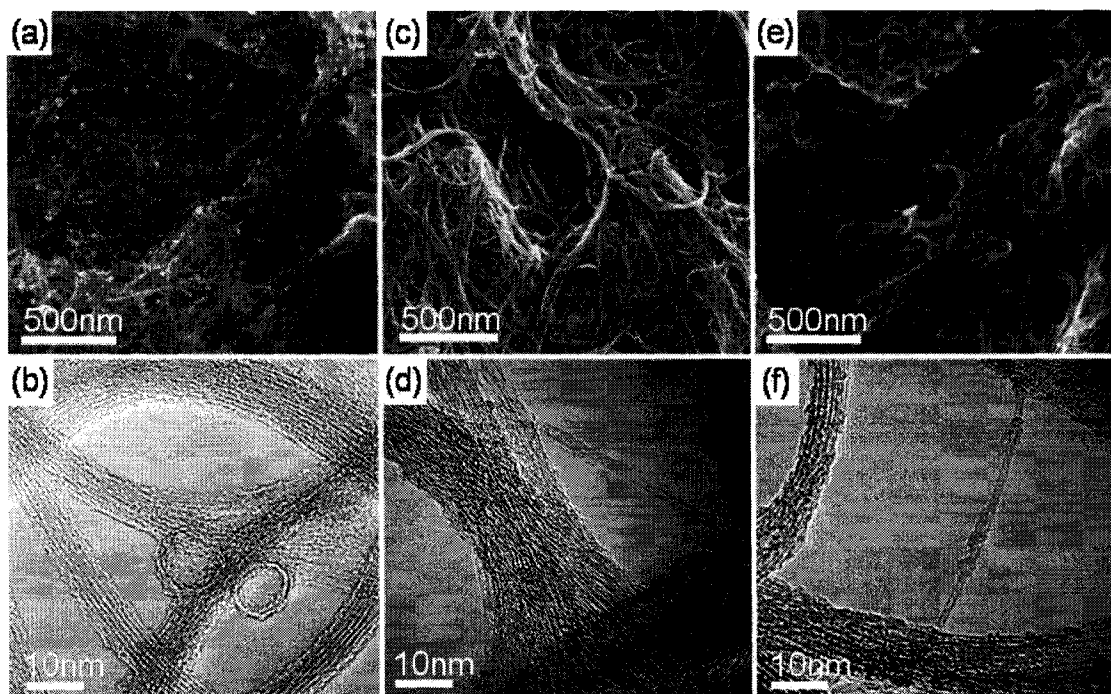


Figure 5.17. SEM and HRTEM images of single walled CNTs before and after irradiation. (a) SEM before irradiation. (b) HRTEM before irradiation. (c) SEM after 1,000Gy krypton-78 irradiation. (d) HRTEM after 1,000Gy krypton-78 irradiation. (e) SEM after 10,000Gy krypton-78 irradiation. (f) HRTEM after 10,000Gy krypton-78 irradiation. Images: B.W. Jacobs

One single walled CNT observed, however, did show one alteration. After a high dose of krypton-78 ion irradiation, the nanotube was packed with C_{60} molecules, see figure 5.18. When buckyballs are packed within nanotubes they are called peapods. It is believed that these peapods may be a direct result of ion irradiation. This result is under further investigation.

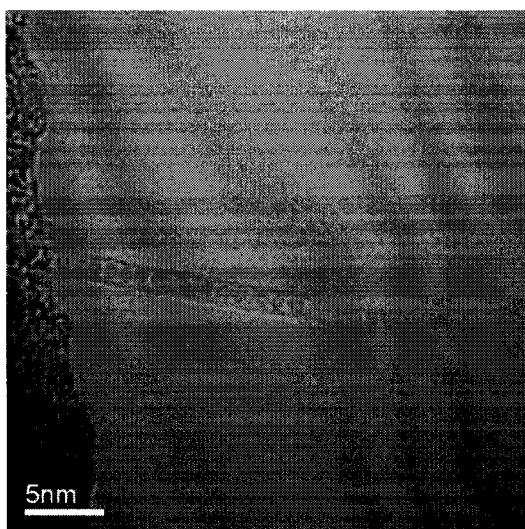


Figure 5.18. HRTEM image of SWCNT after 10,000Gy krypton-78 irradiation. This image shows carbon-60 packed into a SWCNT, a peapod, possibly due to heavy ion irradiation. Image: B.W. Jacobs

The cylindrical wall structure of the SWCNTs held up very well at all radiation doses, with doses exceeding 200 kGy of calcium-48 radiation as indicated by the HRTEM images and the Raman spectra. This is very high radiation resiliency. These results are very promising for possible integration of carbon nanotubes in a wide variety of devices for space applications.

5.4.3.3 Multi Walled Carbon Nanotubes

Multi walled CNTs were also irradiated with krypton-86, krypton-78 and calcium-48 heavy ion beams. The results of these experiments closely parallel those of the single walled CNTs in that no beam damage has thus far been observed using Raman spectroscopy, HRTEM, and SEM analysis.

Figure 5.19 shows Raman spectra of MWCNTs before and after krypton-78 heavy ion radiation. The D-peak in these spectra, $\sim 1337 \text{ cm}^{-1}$, is much larger than in the SWCNT case. This was due to the process in which these MWCNTs were grown, where a by-product was amorphous carbon. This amorphous carbon can be removed with an

acid treatment, but no such treatment was done on these samples. The graphitic peak (G-peak) at $\sim 1580 \text{ cm}^{-1}$ is observed after all radiation doses. This is a characteristic of the multi walled tubular structure of this material. Overall, the Raman spectra do not change significantly indicating that the MWCNTs held up very well in heavy ion radiation.

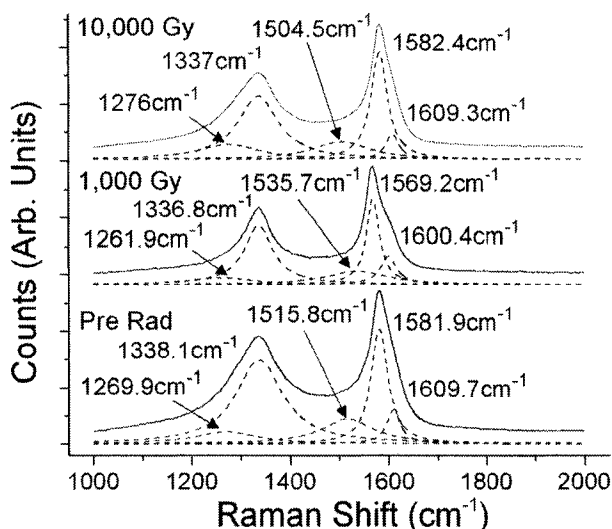


Figure 5.19. Raman spectra of MWCNTs before and after krypton-78 radiation. The D and G-peaks do not change significantly after each radiation dose compared to the un-irradiated sample. This indicates that the MWCNTs held up very well in the krypton-78 radiation and retained their multi walled structure. Spectra: B.W. Jacobs

SEM and HRTEM images shown in figure 5.20 also showed no observable structural damage after krypton-78 irradiation. Figures 5.20(a) and 5.20(b) are SEM and HRTEM images of MWCNTs before radiation. The nanotubes can be seen sticking out of the amorphous carbon material. Figures 5.20(c) and 5.20(d) are SEM and HRTEM images of MWCNTs after a 1000 Gy dose of krypton-78 radiation. Figures 5.20(e) and 5.20(f) are SEM and HRTEM images of MWCNTs after a 10,000 Gy dose of krypton-78 radiation. All images show pristine nanotube structures, but some amorphous carbon can be seen on the surface of some nanotubes.

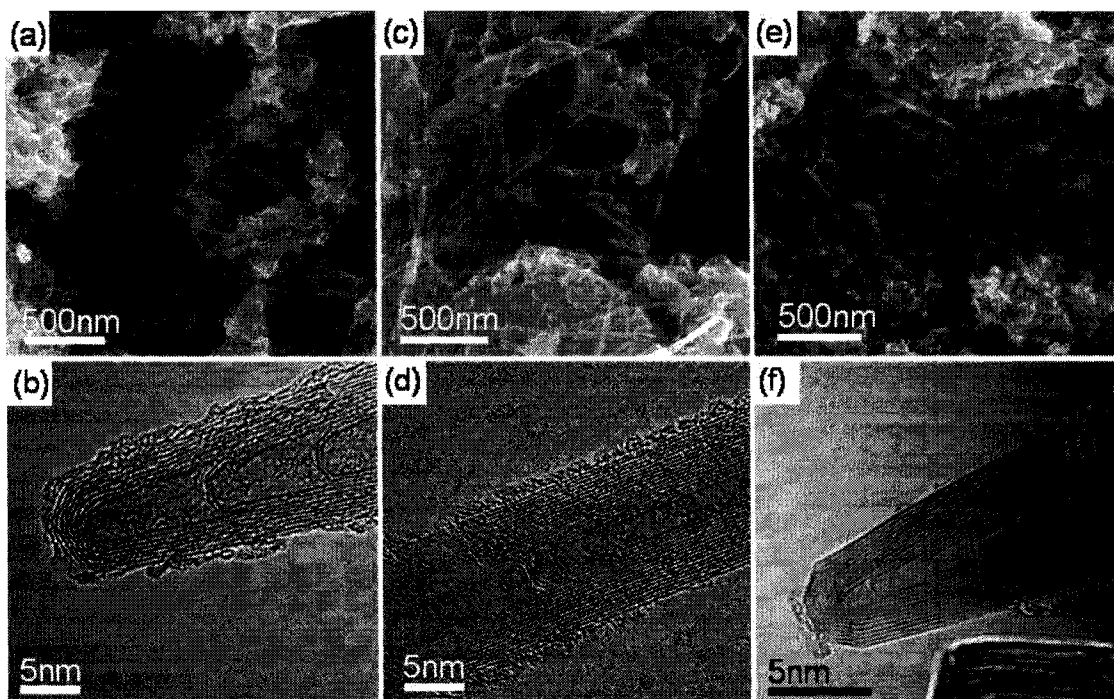


Figure 5.20. SEM and HRTEM images of multi walled CNTs before and after irradiation. (a) SEM before irradiation. (b) HRTEM before irradiation. (c) SEM after 1,000Gy krypton-78 irradiation. (d) HRTEM after 1,000Gy krypton-78 irradiation. (e) SEM after 10,000Gy krypton-78 irradiation. (f) HRTEM after 10,000Gy krypton-78 irradiation. Images: B.W. Jacobs

The resiliency of the MWCNT was also a surprising result. All observed samples retained their wall structure with no detectable damage. Results may indicate that the heavy ion radiation possibly reduced the amount of amorphous carbon surrounding the MWCNTs. This is immediately apparent in figure 5.20(f), where only a small amount of amorphous carbon is seen on the outer walls of the pristine MWCNT. Like SWCNTs, MWCNTs are excellent candidates for potential applications in high radiation environments.

5.4.3.4 Carbon Onions

Carbon onions were irradiated with a calcium-48 heavy ion beam. Post irradiation analysis using Raman spectroscopy and HRTEM indicated that the sample

sustained some observable damage. The Raman spectra of irradiated carbon onions, shown in figure 5.21, indicated that the onions retained their cylindrical shape and multi wall structure. Comparing before and after irradiation Raman spectra of onions that did not receive an oxidation treatment and onions that did receive an oxidation treatment, the D and G-peaks remained similar after all radiation doses.

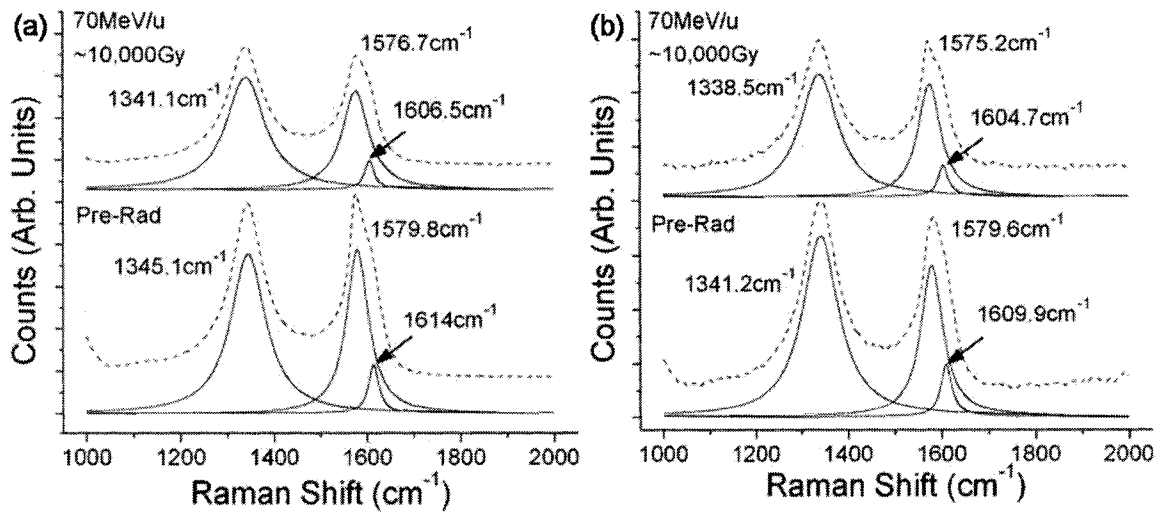


Figure 5.21. Raman spectra of untreated and treated carbon onions before and after calcium-48 irradiation. (a) Untreated carbon onions. (b) Treated carbon onions. Spectra: B.W. Jacobs

HRTEM investigations of irradiated onions coincided with the Raman results indicating that the onions retained their overall spherical shape. Figure 5.22 shows HRTEM images of irradiated onions that did not receive an oxidation treatment, figure 5.22(a) and 5.22(b), and onions that did receive an oxidation treatment, figure 5.22(c) and 5.22(d). The overall onion shape is preserved after heavy ion irradiation, with only minor changes in onion structure. The arrows in figures 5.22(b) and 5.22(d) point out some modifications that took the form of onion coalescence.

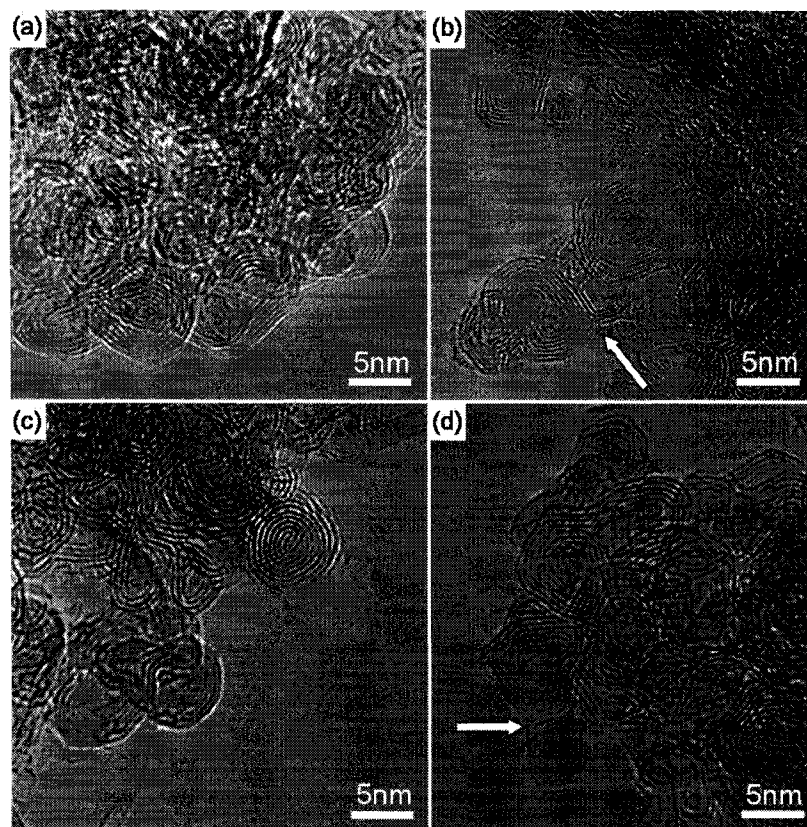


Figure 5.22. HRTEM images of carbon onions before and after calcium-48 irradiation. (a) and (b) compares the before and after irradiation of the untreated carbon onions. (c) and (d) compares the before and after irradiation of the carbon onions with oxidation treatment. The arrows in (b) and (d) denote modifications due to radiation that took the form of onion coalescence. Images: B.W. Jacobs

Figure 5.23 shows additional carbon onions after heavy ion radiation and the structural modifications that resulted for untreated, figure 5.23(a), and treated, figure 5.23(b), onions. Arrows in figure 5.23 denote these modifications. Faceting on the outer carbon onion layers was frequently seen as well as onion coalescence where two carbon onions began to form one larger onion. Carbon onion coalescence is shown in both insets in figure 5.23.

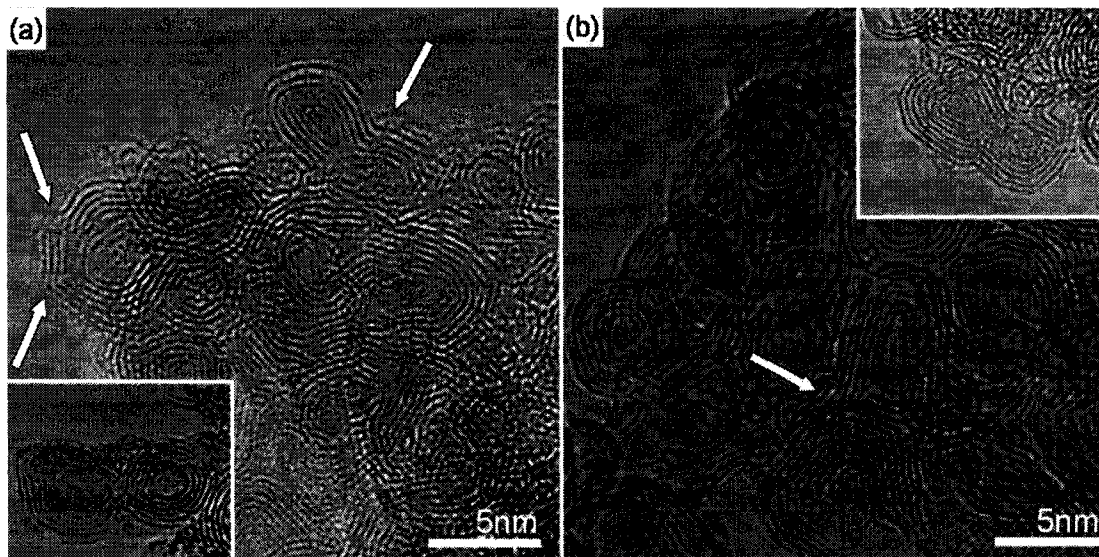


Figure 5.23. HRTEM images of carbon onions after calcium-48 irradiation. (a) Oxidation treated onions. The left most arrows point out outer layer discontinuities and the right points out onion coalescence. The inset also shows onion coalescence. (b) Untreated carbon onions. The arrow points out onion coalescence. The inset also shows onions coalescence. Both images indicate that that the overall onion structure was maintained. Onion structure modifications are consistent for both treated and untreated samples. Images: B.W. Jacobs

When comparing HRTEM images of carbon onions before radiation, onions that underwent a high dose of radiation resembled onions grown at 2300°C, as shown in figure 5.24(c). At this high growth temperature onion faceting and onion coalescence occurred. Ribbons of graphite could also be seen in the post irradiated onions as well as in the onions grown at 2300°C. Onions grown at lower temperatures are also shown in figure 5.24(a) and 5.24(b) for comparison and to highlight the structural changes as a result of growth temperature. This suggested that heavy ion radiation reduced the disordered carbon component of the carbon onions, or the carbon onion structure changed and annealed, or possibly a combination of both.

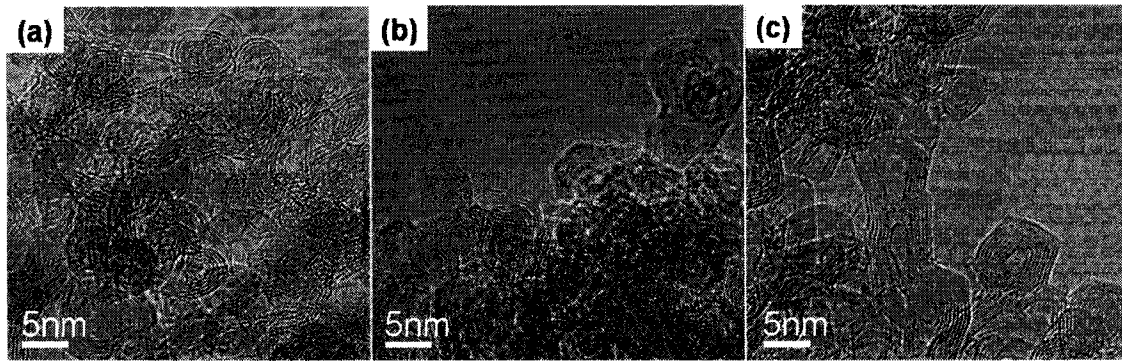


Figure 5.24. HRTEM images of untreated carbon onions grown at temperatures (a) 1700°C (b) 2000°C and (c) 2300°C show the evolution from spherical to polyhedral onions. The increased onion coalescence and outer layer discontinuities can be seen in (c). Images: B.W. Jacobs

The nanomaterials performed very well under each radiation species and energies at all doses. The carbon nanotube samples had no damage that could be observed with Raman spectroscopy or HRTEM. The peapods found in one nanotube could be attributed to heavy ion radiation, and is a new result, but warrants further investigation. The carbon onions did have minor damage in the form of outer layer discontinuities and carbon onion coalescence. This result was identified with HRTEM. Raman spectroscopy did not indicate significant peak alterations before and after radiation. Thermogravimetric analysis could also be used to further quantify the damage of carbon onions incurred through radiation.

The radiation damage in GaN nanowires occurred through a short track mechanism where highly crystalline material turned amorphous. This was identified with HRTEM and FFTs of HRTEM images. Not all nanowires observed were damaged. The GaNFETs tested also performed well in radiation with minimal deviation from normal operation.

These results are significant. Heavy ion radiation has been a serious problem in space-based systems. These materials represent a great leap forward toward the solution

of this problem. Shielding in space-based applications could be minimized, and the need for redundant systems mitigated. Reliable electronic and mechanical operation of space-based systems would be greatly increased. These materials could revolutionize space applications as they have already revolutionized many fields of science and engineering.

References

1. K. LaBel "Single Event Effect Criticality Analysis," conference of single event effect criticality analysis, <http://radhome.gsfc.nasa.gov/radhome/papers/seecai.htm>.
2. EIA/JEDEC Standards No. 57, "Test procedures for the measurement of single event effects in semiconductor devices from heavy ion irradiation," Electronic Industries Association, 1996.
3. J. Barth, "Ionizing Radiation Environment Concerns," conference of single event effect criticality analysis, <http://radhome.gsfc.nasa.gov/radhome/papers/seeca3.htm>.
4. D. V. Reames, "Solar Energetic Particles: Sampling Coronal Abundances," *Space Sci. Rev.*, **85**, 327-340 (1998)
5. J. Cronin, T. K. Gaisser, S. P. Swordy, "Cosmic rays at the energy frontier," *Sci. Amer.*, **276**, 44-49 (1997)
6. H. J. Barnaby, S. K. Smith, R. D. Schrimpf, D. M. Fleetwood, R. L. Pease, "Analytical model for proton irradiation effects in bipolar devices," *IEEE T. Nucl. Sci.*, **49**, 2650-2649 (2002)
7. P. Lenahan, J. F. Conley, Jr., "A comprehensive physically based predictive model for radiation damage in MOS systems," *Appl. Phys. Lett.*, **71**, 2413-2423 (1998); A. Y. Yang, P. M. Lenahan, J. F. Conley, Jr., "The radiation response of the high dielectric-constant hafnium oxide/silicon systems," *IEEE T. Nucl. Sci.*, **49**, 2844-2851 (2002)
8. T. P. Ma, P. V. Dressendorfer, *Ionizing Radiation Effects in MOS Devices & Circuits*, chap. 1, John Wiley and Sons, Toronto, 1989
9. L. W. Massengill, B. K. Choi, D. M. Fleetwood, R. D. Schrimpf, K. F. Galloway, M. R. Shaneyfelt, T. L. Meisenheimer, P. E. Dodd, J. R. Schwank, Y. M. Lee, R. S. Johnson, G. Lucovsky, "Heavy-ion-induced breakdown in ultra-thin gate oxides and high-*k* dielectrics," *IEEE T. Nucl. Sci.*, **48**, 1904-1912 (2001)
10. E. Simoen, A. Mercha, A. Morata, K. Hayama, G. Richardson, J. M. Rafi, E. Augendre, C. Claeys, A. Mohammadzadeh, H. Ohyama, A. Romano-Rodriguez, "Short-channel radiation effect in 60 MeV proton irradiated 0.13 μm CMOS transistors," *IEEE T. Nucl. Sci.*, **50**, 2426-2432 (2003)
11. K. Kobayashi, H. Ohyama, M. Yoneoka, K. Hayama, M. Nakabayashi, E. Simoen, C. Claeys, Y. Takami, H. Takizawa, S. Kohiki, "Radiation damage of N-MOSFETS fabricated in a BiCMOS process," *J. Mater. Sci. Mater. Elect.*, **12**, 227-230 (2001)

-
12. B. Djeddar, A. Smatti, A. Amouche, M. Kechouane, "Channel-Length Impact on Radiation-Induced Threshold-Voltage shift in N-MOSFET's Devices at Low Gamma Rays Radiation Doses," *IEEE T. Nucl. Sci.*, **47**, 1872-1878 (2000)
 13. B. Streetman, S. Banerjee, *Solid State Electronic Devices, Fifth Edition*, Prentice Hall, Upper Saddle River, NJ, 2000.
 14. <http://www.nscl.msu.edu/tech/index.html>
 15. <http://www.nscl.msu.edu/tech/devices/index.html>
 16. R. Ladbury, R. A. Reed, Member, P. Marshall, K. A. LaBel, R. Anantaraman, R. Fox, D. P. Sanderson, A. Stolz, J. Yurkon, A. F. Zeller, J. W. Stetson, "Performance of the High-Energy Single-Event Effects Test Facility (SEETF) at Michigan State University's National Superconducting Cyclotron Laboratory (NSCL)," *IEEE T. Nucl. Sci.*, **51**, 3664-3668 (2004)
 17. N. Anantaraman, "NSCL Single Event Effects Test Facility Users Manual," National Superconducting Cyclotron Lab., Michigan State Univ., East Lansing, MI.
 18. <http://www.laplink.com>
 19. R. Leon, S. Marcinkevicius, J. Siegert, B. Cechavicius, B. Magness, W. Taylor and C. Lobo, "Effects of proton irradiation on luminescence emission and carrier dynamics of self-assembled III-V Quantum dots," *IEEE T. Nucl. Sci.*, **49**, 2844-2851 (2002)
 20. A. Ionascut-Nedelcescu, C. Carlone, A. Houdayer, H. J. von Bardeleben, J.-L. Cantin, S. Raymond, "Radiation Hardness of Gallium Nitride," *IEEE T. Nucl. Sci.*, **49**, 2733-2738 (2002)
 21. S. Iijima, "Helical microtubules of graphitic carbon," *Nature*, **354**, 56-58 (1991)
 22. R. H. Baughman, A. A. Zakhidov, W. A. de Heer, "Carbon Nanotubes - the Route Toward Applications," *Science*, **297**, 787-792 (2002)
 23. R. Saito, G. Dresselhaus, M. S. Dresselhaus, *Physical Properties of Carbon Nanotubes*, London, Imperial College Press, 1998.
 24. R. Andrews, D. Jacques, A. M. Rao, T. Rantell, F. Derbyshire, Y. Chen, J. Chen, and R. C. Haddon, "Nanotube composite carbon fibers," *Appl. Phys. Lett.*, **75**, 1329-1331 (1999)
 25. Z. Chen, J. Appenzeller, Y-M. Lin, J. Sippel-Oakley, A. G. Rinzler, J. Tang, S. J. Wind, P. M. Solomon, P. Avouris, "An Integrated Logic Circuit Assembled on a Single Carbon Nanotube," *Science*, **311**, 1735 (2006)

-
26. S. Li, Z. Yu, S-F. Yen, W. C. Tang, P. J. Burke, "Carbon Nanotube Transistor Operation at 2.6 GHz," *Nano Lett.*, **4**, 753-756 (2004)
 27. P. W. Barone, S. Baik, D. A. Heller, M. S. Strano, "Near-infrared optical sensors based on single-walled carbon nanotubes," *Nat. Mater.*, **4**, 86-92 (2005)
 28. E. S. Snow, F. K. Perkins, E. J. Houser, S. C. Badescu, T. L. Reinecke, "Chemical Detection with a Single-Walled Carbon Nanotube Capacitor," *Science*, **307**, 1942-1945 (2005)
 29. P. R. Bandaru, C. Daraio, S. Jin, A. M. Rao, "Novel electrical switching behaviour and logic in carbon nanotube Y-junctions," *Nat. Mater.*, **4**, 663-666 (2005)
 30. S-H. Hur, M-H. Yoon, A. Gaur, M. Shim, A. Facchetti, T. J. Marks, J. A. Rogers, "Organic Nanodielectrics for Low Voltage Carbon Nanotube Thin Film Transistors and Complementary Logic Gates," *J. Amer. Chem. Soc.*, **127**, 13808-13809 (2005)
 31. P. Avouris, "Supertubes [carbon nanotubes]," *IEEE Spect.*, **41**, 40-45 (2004)
 32. A.V. Krasheninnikov and K. Nordlund, "Irradiation effects in carbon nanotubes," *Nucl. Instrum. Meth. B*, **216**, 355-366 (2004)
 33. A.V. Krasheninnikov, K. Nordlund, and J. Keinonen, "Production of Defects in Supported Carbon Nanotubes under Ion Irradiation," *Phys. Rev. B.*, **65**, 165423-1, (2002)
 34. F. Banhart, "Irradiation effects in carbon nanostructures," *Rep. Prog. Phys.*, **62**, 1181-1221 (1999)
 35. <http://www.cnanotech.com>
 36. M. J. Bronikowski, P. A. Willis, D. T. Colbert, K. A. Smith, R. E. Smalley, "Gas-phase production of carbon single-walled nanotubes from carbon monoxide via the HiPco process: A parametric study," *J. Vac. Sci. Technol., A*, **19**, 1800-1805 (2001)
 37. J. M. Benavides, "Method for manufacturing high quality carbon nanotubes," US Patent 7,008,605 (2006)
 38. A. Hirata, M. Igarashi, T. Kaito, "Study on solid lubricant properties of carbon onions produced by heat treatment of diamond clusters or particles," *Tribo. Inter.*, **37**, 899-905 (2004)

-
39. K. W. Street, M. Marchetti, R. L. Vander Wal, A.J. Tomasek, "Evaluation of the tribological behavior of nano-onions in Krytox 143AB," *Tribol. Lett.*, **16**, 143-149 (2004)
40. A. Hirata, R. Yamada, B. W. Jacobs, A. D. Baczewski, V. M. Ayres, "Correlation of Fundamental Properties with Tribological Performance of Carbon Onions with Oxidation Treatment," *accepted for publication in Japanese Journal of Applied Physics*
41. J. F. Ziegler, "SRIM-2003," *Nucl. Instrum. Methods Phys. Res., Sect. B*, **219-220**, 1027-1036 (2004)

6. Future Work

The research presented in this thesis represents an ongoing research effort with long-term goals. There are still many possible research avenues that can be taken in order to understand the properties of the multiphase GaN nanowires and fundamental heavy ion interactions with nanomaterials. Further experimental investigations using the discussed techniques and largely unexplored techniques, discussed below, may uncover more interesting properties of the multiphase nanowires and heavy ion-nanomaterial interactions.

6.1. Gallium Nitride Nanowires

Cross-section HRTEM analysis will be essential in further investigations of the structure and growth of the multiphase as well as the single-phase nanowires. Observations of nanowires in the SEM and TEM have shown a variety of different features that are unique to each individual nanowire. The nanowire may have different features based on the nucleation site characteristics. Since the multiphase characteristic is an important feature for many possible future applications, the ability to control how zinc-blende and wurtzite form, would have considerable implications. Cross-sections of the nanowires grown at different conditions would also be beneficial to understand how these conditions affect nanowire growth. Additional cross-sections of nanowires grown along the [0001] direction could help determine the nature of the anomalous features in the center of these nanowires, including the holes and dark and light contrast areas discussed in chapter 4. The origins of the light and dark contrast areas may shed light on

how these nanowires nucleate and grow. If holes do occur along the entire length of the nanowire, the application possibilities would be intriguing.

The investigations with the Zyvex Nanomanipulator system only scratched the surface of what can be done with this instrument. Thorough electronic transport studies of individual nanowires could be carried out to determine if single-phase transport is reproducible. The transport characteristics of the nanowires that grew along the [0001] direction should also be investigated because the transport characteristics might be different due to the different growth direction. Single-phase wurtzite nanowires that grew along the $[2\bar{1}\bar{1}0]$ direction could be studied to see how its transport differs from the single-phase nanowires that grew along the [0001] direction and the multiphase nanowires. The probes could be used to study the mechanical properties of the different nanowires.

The electronic structure of these nanowires are very intriguing, and as yet have not been investigated in detail. The large band gap shift measured using CL showed that these nanowires can absorb and emit light in the UV range. Further investigations with CL could be done to ascertain whether the band gap shift varies from nanowire to nanowire or if it persists in all multiphase and single-phase nanowires.

Photoluminescence could also uncover a wide variety of properties. With the ability to vary the wavelength of light, PL could pick out subtle mid-gap luminescence mechanisms in the nanowire. These luminescence mechanisms could be traced to the interface states between domains. PL could also further assess the feasibility of multiphase nanowires in optical devices.

X-ray diffraction (XRD) could be used to investigate the structure of the nanowire and matrix material. It is in many ways similar to electron diffraction in the TEM. Instead of using electrons, an XRD utilizes the wave nature of photons to interact with a crystal structure. The photons are diffracted from planes in the crystal and strong reflections result when the Bragg condition is satisfied. An XRD system has some advantages compared to using a TEM for diffraction, in that the size of the sample is not as restricted and X-rays are not nearly as destructive as a high-energy electron beam.

An XRD system creates and displays diffraction information somewhat differently than the TEM. Figure 6.1 shows a typical XRD system. On the right the X-ray source emits photons that are directed at the sample, in the center. A detector on the left side collects the diffracted X-rays. The detector is swept out in a circular path while the source remains stationary. As the detector sweeps out it detects diffracted beams that satisfy the Bragg condition and records the associated angle at which the reflections occur. This information is then graphed on a computer. In the generated graph the x-axis is the swept angle and the y-axis is the measured intensity. Certain crystals will diffract more strongly at certain angles resulting in strong peaks at those angles. The angle is based on the interplanar spacing of a given crystal material and the wavelength of the X-ray, just as in electron optics in the TEM. A XRD system can measure the interplanar spacing of a given crystal sample to a high degree of accuracy. Due to this high-resolution many crystal systems are measured for possible strain in the material. By measuring the shift in the angles of diffraction peaks the amount of strain present in a material can be quantified.

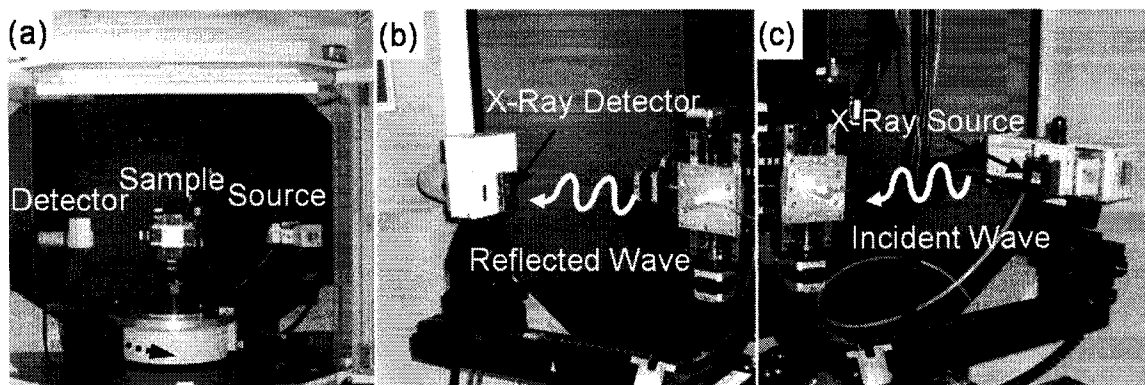


Figure 6.1. Bruker AXS high resolution XRD at the W. M. Keck Microfabrication Facility at Michigan State University. (a) The X-ray beam originates from the right. It hits the sample and is detected on the left. The detector sweeps in a counterclockwise direction and records the reflected beam. (b) The X-ray detector. A reflected beam from the sample is detected. (c) The X-ray source. X-rays travel from the source to the sample. Images: B.W. Jacobs

The XRD could further quantify the amount of strain present in the multiphase nanowires. CL detected a large amount of strain in the nanowires through the measure of a large blue shift in the band gap of the nanowires. XRD could provide a more accurate measure of this strain.

Further investigations of the GaNFET characteristics, including the behavior of the metal-nanowire junction, would be very beneficial for nanowire circuit design. This junction is not well understood, and the nature of the Schottky barrier that forms there has not been well defined. Using a STM, a special capability called scanning probe recognition microscopy and ballistic electron emission microscopy, the Schottky barrier of a metal-nanowire junction can be directly measured. These techniques are discussed below.

Scanning Probe Recognition Microscopy is a new scanning probe capability developed by the Ayres' research group in partnership with Veeco Instruments^{1,2}. A standard Veeco Instruments Nanoscope IIIa scanning probe microscope system is equipped with a special modification developed by the Ayres' research group by which the SPM

system itself is given the ability to auto-focus on regions of interest through incorporation of recognition-based tip control. This is described as Scanning Probe Recognition Microscopy (SPRM). The recognition capability is realized using algorithms and techniques from computer vision, pattern recognition and signal processing fields. Adaptive learning and prediction are also implemented to make detection and recognition procedures quicker and more reliable. The integration of recognition makes the SPRM system more powerful and flexible in investigating specific properties of samples.

Ballistic electron emission microscopy is a promising technique that is used with a STM^{3,4}. When determining the Schottky barrier between a metal and semiconductor, a thin layer of metal is deposited on top of a clean semiconductor surface. The sample is placed in the STM metal side up, i.e. the metal side interacts directly with the tip. Connections to the metal, called the base, and to the semiconductor, called the collector, are made. One ammeter is connected to the collector and another to the base, see figure 6.2. The STM tip is then brought down to the surface and normal STM imaging commences. Electrons tunnel through the barrier between the tip and sample, and when the emitted electrons hit the metal surface they can either pass through the metal without scattering, or scatter and lose energy and pass through the attached ammeter. The electrons can pass through the metal without scattering because the metal is thinner than the mean free path of the electron, which is the average distance an electron travels through a material before scattering and losing a significant portion of its energy. If the un-scattered electron has enough energy to overcome the metal-semiconductor Schottky barrier, eV_b , the electron can enter the semiconductor and will eventually pass through

the attached ammeter. The Schottky barrier is determined by the measured currents, I_t and I_c .

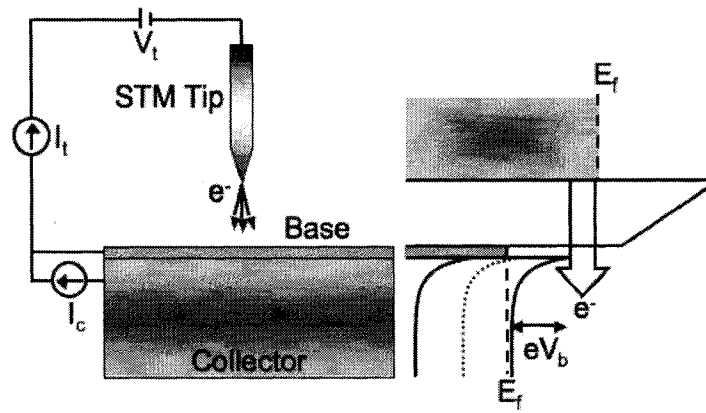


Figure 6.2. Diagram of BEEM operation. The left image shows the physical setup of a BEEM. The tip interacts with the base metal surface passing electrons through gap between the tip and surface. I_c is the current coming out of the semiconductor collector, I_t is the current from the base metal resulting from electrons that were scattered in the metal and did not have enough energy to surmount the barrier, plus the collector current. The right image shows the energy diagram indicating each barrier. Electrons originate in the metal STM tip, tunnel through the vacuum gap and pass through the metal and into the semiconductor collector. E_f is the Fermi level of each material, and eV_b is the height of the metal-semiconductor Schottky barrier. The figure is not to scale. The vacuum gap is usually on the order of a few nanometers, and the metal base thickness is usually around 10nm. Image: B.W. Jacobs

Used in conjunction with SPRM the STM will be able to automatically track the nanowire/metal interface creating a spatial map as well as an energy spectrum of the Schottky barrier present at the interface. Investigations on the nanowire-metal junctions could be studied in different designs, and different contact metals could be deposited to see how the Schottky barrier and carrier injection differs.

Using STM to image the electronic surface states of the nanowire would also help understand the energy landscape of the nanowire. Surface investigations as well as cross-section STM investigations would shed light on the electronic states of the nanowire surface, which is important information for understanding the nature of nanowire-metal junctions. STM of the cross-section would help uncover electronic properties of the

interface and provide information on the electronic barrier characteristics of the interface. The SPRM modality of the STM would also prove highly effective in these investigations, because it would be able to track an interesting feature, such as an interface between a zinc-blende and wurtzite phase, at will, mapping out the energy landscape at that interface along the way. These experiments would further assess the viability of the multiphase GaN nanowires used in real world devices.

6.2 Fundamentals of Radiation Interactions in Reduced Dimensionality Systems

The radiation resilience of nanomaterials and nanocircuits is a very promising area of research with high probability of success. The ideas and results presented in this thesis were critical in getting this project off the ground, but more experimental as well as theoretical testing can still be explored with different devices, materials and radiation beams.

First, further heavy ion radiation investigations of the nanomaterials already tested must be done. An in depth analysis of low to high Z heavy ions with multiple charge-to-mass-ratios should provide further details of nanomaterial-heavy ion interactions. A future experiment using oxygen-16 is currently being planned. Sample density, weight and area must be highly precise so that dose calculations are accurate. Standard methods and calculations for irradiating nanomaterials should be developed. A reproducible procedure must be followed so accurate results are continually produced. Since the nanomaterials were not significantly damaged, higher radiation doses should be administered. Without significant damage to the materials, the mechanism in which they interact with the heavy ion beam cannot be described.

X-ray Photoelectron Spectroscopy (XPS) could also be utilized as an additional carbon structure characterization technique for before and after irradiation analysis. XPS is a surface characterization technique used to determine the elemental composition, chemical or electronic state of a given material. In an XPS system X-rays are at high enough energy to interact with core electrons in sample atoms. These core electrons in the sample can gain enough energy through the absorption of the incident X-rays to overcome the work function of the material, see figure 6.3. The removal of an electron

from a material through the absorption of a photon is called the photoelectric effect. Core electron energies are highly specific to each element in the periodic table. Therefore, measuring the energy of the emitted electrons, called photoelectrons or photo-emitted electrons, specific elements and their bonds can be detected and characterized in a given material. The beam of incident X-rays penetrate into the material up to several microns, however only surface electrons are usually emitted, generally up to 10 nm in depth, due to recombination within the material. Therefore, this technique is only used to analyze surfaces.

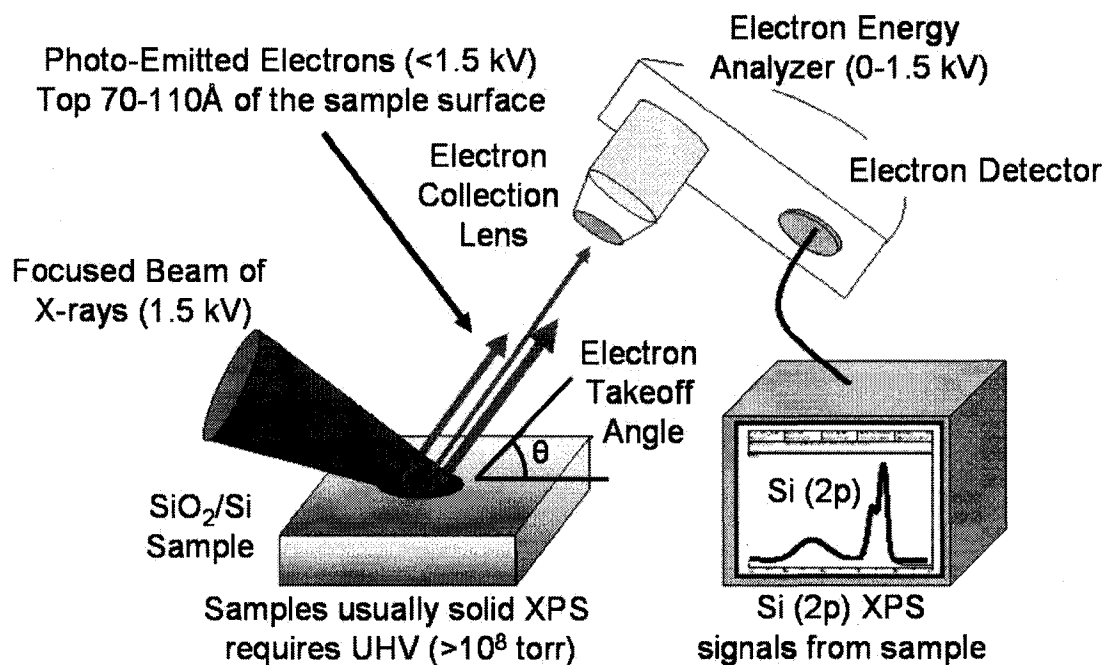


Figure 6.3. Basic method of XPS sample spectrum acquisition. The X-rays are aimed at the sample surface at a known angle and interact with the surface inducing photo-emitted electrons. The photo-emitted electrons are collected and analyzed to determine their energy. A spectrum of the photo-emitted electrons is then created indicating what materials are on the sample surface, and the electronic state they are in.

An XPS system uses one of two X-ray sources: a monochromatic aluminum source or a non-monochromatic magnesium source, both of which are often integrated

into the same system. The Al source emits X-rays with energy of 1486.7 eV, and because the energy spread of X-rays emitted from this source is quite small, 0.4-0.6 eV, it is used for high-resolution XPS. The intensity is rather small compared to the Mg non-monochromatic source, so the time required to gather a spectrum with an acceptable signal-to-noise ratio is longer. The Mg source emits X-rays with energy of 1253 eV, and has a larger energy spread of around 1 eV. Therefore, it has a lower resolution but more intense source. Since the photoelectron detector is far from the sample surface, the sample chamber must be under ultra-high vacuum, 10^{-8} - 10^{-10} Torr. This allows the photoelectrons to travel to the detector without losing much energy. After the electrons have been detected they are sent to a computer where an energy spectrum is created.

XPS is a powerful technique that can provide very beneficial information about sample surfaces. Acquiring spectra is usually very quick, only a few minutes, after the lengthy sample preparation and pump down procedures have been completed. Some samples, however, can take several hours if the monochromatic Al source is used.

In this thesis research, the XPS system was used to determine carbon onion properties. XPS can distinguish between the sp^2 and sp^3 hybridizations and determine if oxygen exists in the carbon system. When taking a XPS spectrum of the carbon onions, sample preparation is of great importance. Many times samples will be placed on a metal such as copper with an adhesive layer on one side. This adhesive layer contains carbon and oxygen and therefore interferes with the spectrum. An adhesive that does not contain carbon and oxygen should be used, or if an alternate powder sample mounting technique could be developed, it would create more reliable XPS spectra.

GaN FET operation in heavy ion radiation must also be further explored. Many circuits must be tested so that the failure mechanisms of the GaN FETs as a result of irradiation can be identified and improved upon. The optical properties of the GaN nanowires are thought to be conducive to operation in UV detectors and LEDs. Therefore, real time operation in the heavy ion beam testing the optical properties of GaN nanowires might also yield promising results.

6.2.1 Other Candidate Materials for High Radiation Environments

6.2.1.1 Quantum Dots

Quantum dots represent a relatively new device concept. A quantum dot is a zero-dimensional system where electrons in the system are confined in every direction. Quantum dots are primarily used for optical applications since they are very efficient due to their high quantum yield⁵. This allows for bright light emitting devices, which do not require much electrical power.

Ion irradiation experiments on quantum dots have shown the possibility of an inherently reduced dimensionality radiation resilient system⁶. When the optical performance of a quantum well (two-dimensional) structure was compared to a quantum dot structure in phosphorus radiation, the quantum dot substantially outperformed the quantum well in optical emission⁷. These results are very promising for quantum dot performance in radiation. This result for the zero-dimensional performance reinforces the results obtained with the one-dimensional systems described in this research. Reduced dimensionalities do seem to play a role in radiation resilience.

6.2.1.2 Semiconducting Nanowires of Various Materials

There have been many reports of successful growth of a variety of different semiconducting nanowires. These nanowires, like their bulk material counterparts, possess a variety of different band gaps, electron and hole mobilities and mechanical properties making them highly versatile. This versatility could be used for radiation resilient devices. GaN nanowires have shown a high resilience in radiation either due to its material properties, its small size, or both. Since radiation interactions in nanomaterials may fundamentally change as discussed in chapter 5, this opens up a wide variety of application possibilities that exploit the versatility of semiconducting nanowires.

6.2.2 Other Candidate Devices for High Radiation Environments

6.2.2.1 Carbon Nanotube-Based Field Effect Transistors

Carbon nanotubes showed very high heavy ion radiation resilience in all experiments discussed in chapter 5. The results are promising in that carbon nanotubes can be used for a variety of electronic, optical and chemical devices. It is probable that these devices that integrate carbon nanotubes as the primary element will be radiation resilient. To date, however, no carbon nanotube-based device has been tested in this research effort. Therefore, nanotube devices must be tested in heavy ion radiation, as they may outperform GaNFETs already tested.

6.2.2.2 High Electron Mobility Transistors

High electron mobility transistors have also been fabricated⁸ using a two-dimensional GaN thin film as a quantum well conduction channel, and are being used in high power, high frequency microwave communications applications. They operate via source, drain and gate voltage modulation with a gate modulated conduction channel consisting of a thin intrinsic semiconductor layer sandwiched between two insulating layers. In a GaN/AlGaN HEMT a heavily doped AlGaN layer, connected to a source and drain voltage, is the electron source. Since AlGaN has a larger band gap than GaN, when electrons enter the GaN conduction channel they will be trapped at the interface. They are drawn to the interface because the conduction band energy is reduced due to the band bending resulting from Fermi level alignment, and a triangular quantum well forms as a result. Although there are only a few allowed energy levels in the quantum well, electrons are able to move with very high motilities due to the reduced number of scattering centers, which are normally present in most devices due to dopants. With no dopants acting as scattering centers, the electrons scatter less and very high levels of current can be achieved. The HEMT can also operate at very high frequencies.

This conduction channel represents a two-dimensional system with a constricted z-direction of only ~10nm. Electrons are confined in the z-direction so they can only have certain quantized values on energy, but are free to move in both the x- and y- directions. With this configuration, HEMTs and their reduced dimensionality may be more resilient in radiation.

This ongoing project that assesses the viability of reduced dimensionality systems for heavy ion radiation environments will need further investigation. This thesis has laid

the groundwork for future studies of these materials and systems. The materials and methods discussed in this chapter may uncover applications and properties that were previously unknown, taking these materials and systems a step closer to real world applications.

References

1. <http://www.nsf.gov/awardsearch/showAward.do?AwardNumber=0400298>
2. Y. Fan, Q. Chen, V. M. Ayres, A. D. Baczewski, L. Udpa S. Kumar, "Scanning Probe Recognition Microscopy Investigation of Tissue Scaffold Properties", *in press Int. J. Nanomed.*, **2**, (2007)
3. V. Narayanamurti, M. Kozhevnikov, "BEEM imaging and spectroscopy of buried structures in semiconductors," *Phys. Rep.*, **349**, 447-514 (2001)
4. R. E. Martínez II, I. Appelbaum, C. V. Reddy, R. Sheth, K. J. Russell, V. Narayanamurti, J-H. Ryou, U. Chowdhury, R. D. Dupuis, "Electron transport through strongly coupled AlInP/GaInP superlattices," *Appl. Phys. Lett.* **81**, 3576-3578 (2002)
5. I. Gryczynski, J. Malicka, W. Jiang, H. Fischer, W. C. W. Chan, Z. Gryczynski, W. Grudzinski, J. R. Lakowicz, "Surface-Plasmon-Coupled Emission of Quantum Dots," *J. Phys. Chem.*, **109**, 1088-1093 (2005)
6. S. Marcinkevicius, J. Siegert, R. Leon, B. Cechavicius, B. Magness, W. Taylor, C. Lobo, "Changes in luminescence intensities and carrier dynamics induced by proton irradiation in In_xGa_{1-x}As/GaAs quantum dots," *Phys. Rev. B*, **66**, 235314 (2002)
7. P. G. Piva, R. D. Goldberg, I. V. Mitchell, D. Labrie, R. Leon, S. Charbonneau, Z. R. Wasilewski, S. Fafard, "Enhanced degradation resistance of quantum dot lasers to radiation damage," *Appl. Phys. Lett.*, **77**, 624-626 (2000).
8. H. Xing, S. Keller, Y-F. Wu, L. McCarthy, I. P. Smorchkova, D. Buttari, R. Coffie, D. S. Green, G. Parish, S. Heikman, L. Shen, N. Zhang, J. J. Xu, B. P. Keller, S. P. DenBaars, U. K. Mishra, "Gallium nitride based transistors," *J. of Phys.: Cond. Matt.*, **13**, 7139-7157 (2001)

7. Conclusion

A significant discovery was made during the exploration of nanomaterials for use in space applications. GaN nanowires were thought to possess high radiation resilience due to their bond strength as well as their small size. In analyzing the nanowire with HRTEM, a multiphase structure was uncovered with longitudinal crystal domains that extended the entire nanowire length.

The matrix on which the nanowires grew was analyzed with SEM and TEM. Nanowire growth from the sides of GaN hexagonal platelets that formed on the matrix was observed. At different temperatures different matrix formations led to nanowires with different growth directions and morphologies. Nanowires that grew at lower temperatures always exhibited a zinc-blende/wurtzite multiphase structure with growth along the $\langle 011 \rangle / \langle 2\bar{1}\bar{1}0 \rangle$ direction. HRTEM analysis linked nanoscale platelets, which formed on the hexagonal platelet sides in the same orientation and coherent to the platelets, to the multiphase nanowire nucleation. However, when the growth temperature was increased, two additional types of nanowires were observed. Single-phase wurtzite nanowires were identified with growth in the same direction as the wurtzite phase in the multiphase nanowires, $\langle 2\bar{1}\bar{1}0 \rangle$. Nanoscale nucleation sites were linked this single-phase nanowire growth. Single-phase wurtzite nanowires were identified with growth along the $[0001]$ direction. Hexagonal platelet tops were linked to nucleation sites for this single-phase nanowire.

Cross-section HRTEM analysis revealed how the multiphase structure formed and the orientations of the longitudinal crystalline domains. Several coherent and incoherent interfaces formed between crystalline domains. A coherent interface was seen in all

multiphase nanowire cross-sections analyzed and explained the coherent interface seen in the plain-view HRTEM analysis. This coherent interface could provide a stabilization mechanism that renders the multiphase nanowire energetically attractive. The (0001) face was always observed to terminate on an internal interface, possibly due to its instability. In the multiphase nanowire system, the instability of the (0001) planes may be compensated through the incorporation of the zinc-blende phase as a second stabilizing aspect of the multiphase configuration. The growth directions identified in plain-view HRTEM analysis corresponded to the on axis FFTs from each crystalline domain found in the cross-sections. Cross-section analysis revealed holes in the center of some single-phase nanowires.

The electronic properties of a multiphase nanowire were tested using a nanomanipulator. Two and four-point probe investigations were carried out to determine the resistance of an individual nanowire with non-invasive probes, and to study coupling differences between nanoscale probes and macroscopic metal contacts. Differences in coupling were linked to macroscopic vs. microscopic contacts to the nanowire, where microscopic probes that had a tip diameter on the order of the nanowire width, injected carriers more effectively.

Using two-point probe techniques the nanowire was end-contacted and breakdown measurements were carried out. As a result of passing a large current through the nanowire, a round agglomeration of material formed at nanowire end where the probe was contacted and began to grow. This material looked as though it came from the internal structure of the nanowire, while an external structure remained intact. Probing the agglomeration showed that it was liquid. This was evidence of possible phase-

specific transport, and has significant implications on the question of how and where electron transport actually occurs within the multiphase nanowires.

GaN nanowire-based transistors were fabricated using electron beam lithography. I-V measurements of these devices showed that multiphase nanowires were viable in devices. Gate modulation of the current was achieved in measurements. I-V characteristics indicated Schottky barrier behavior. Two-point probe and I-V measurements of a GaN device showed the ability of the nanowire to carry very high currents, important for high power applications.

The radiation resilience of nanomaterials and devices were investigated using multiple heavy ion radiation beams including krypton-86, krypton-78, and calcium-48 at the NSCL at Michigan State University. The nanomaterials tested include single and multi wall carbon nanotubes, GaN nanowires, carbon onions and GaN nanowire-based FETs. Each nanomaterial performed very well after each radiation dose. The carbon nanotubes did not exhibit any observable damage as a result of heavy ion radiation. Carbon onions had some structural modifications as a result of heavy ion radiation including increased outer layer discontinuities and multiple onion coalescence. GaN nanowires showed damage in the form of a short track crystalline to amorphous transition. All materials performed above expectation and are very promising candidates for future space-based systems.

The results presented in this thesis mark significant steps forward in understanding GaN nanowire multiphase growth and applications, and fundamental radiation interactions with nanomaterials and devices that incorporate a reduced dimensionality system. This thesis research also laid the groundwork for further study of

the multiphase nanowire system and radiation experiments, and suggested future experiments and analysis methods. The nanomaterials and devices that incorporate them have great promise for high performance devices and systems as well as extraordinary potential for future space as well as terrestrial applications.